DEVELOPMENT OF ACCURATE COMPUTATIONAL METHODS FOR SIMULATIONS OF ADSORPTION AND DIFFUSION IN ZEOLITES

A Dissertation

Presented to

The Academic Faculty

By

Rohan V. Awati

In Partial Fulfillment

of the Requirements for the Degree

Doctor of Philosophy in the
School of Chemical and Biomolecular Engineering

Georgia Institute of Technology

May 2016

DEVELOPMENT OF ACCURATE COMPUTATIONAL METHODS FOR SIMULATIONS OF ADSORPTION AND DIFFUSION IN ZEOLITES

Approved by:

Dr. David S. Sholl, Advisor

School of Chemical and Biomolecular Engineering

Georgia Institute of Technology

Dr. Sankar Nair

School of Chemical and Biomolecular Engineering

Georgia Institute of Technology

Dr. William J. Koros

School of Chemical and Biomolecular Engineering

Georgia Institute of Technology

Dr. Seung Soon Jang

School of Materials Science and Engineering

Georgia Institute of Technology

Dr. Krista S. Walton

School of Chemical and Biomolecular Engineering

Georgia Institute of Technology

Date Approved: December 11, 2015

To friends & family

ACKNOWLEDGEMENTS

My childhood dream of becoming a scientist was fulfilled when I got admitted as a PhD student to Georgia Institute of Technology in the Fall of 2010. The 5 years I spent at Georgia Tech have been a wonderful journey that has prepared me for the future challenges and opportunities. This memory will forever be cherished due to the people I met at Georgia Tech and became friends with over the years.

To begin with, I am heartily thankful to my advisor, Dr. David S. Sholl, whose continuous encouragement, guidance, and support throughout enabled me to develop a better understanding of the life. Not only is he a great mentor but he is also a passionate teacher. I learnt important lessons from him about time management, research philosophy, and the meaning of patience which will prove fruitful in my professional as well as personal life. Even after being in his group for 5 years, I am still amazed by his dedication to the students and his involvement in the technical details of their work. For all this and much more, I shall always be indebted...

I have been very fortunate to have a group of excellent researchers as a part of my thesis committee. I would like to thank Dr. William J. Koros, Dr. Krista S. Walton, Dr. Sankar Nair, and Dr. Seung Soon Jang for their guidance and genuine interest in my PhD work. I express my special gratitude to Dr. Peter Ravikovitch and Dr. Preeti Kamakoti from Exxon Mobil Research and Engineering. The weekly teleconferences shall always be fondly remembered. Their experimental knowledge provided a very useful perspective in my PhD work.

During my time at Georgia Tech, I had the pleasure of directly working with many members of the Sholl group. Specifically, I would like to thank Hanjun, Salah,

Ambarish, Nita, Emmanuel, Iyad, Kelly, Jason, Ji, Taku, Dalar, Jeff, and Ross for all the discussions, technical and otherwise.

I am very fortunate to have wonderful friends like Ambarish, Paras, Nitesh, Gautami, Gaurav, Shricharan, Himanshu, Jaya, Pradnya, Shweta, Sireesha, Anshuman, Lalit, Souryadeep, Shilpa, Mayank, Anusha, Aritra, and Akil. I will always remember the time we spent together for the dinners, the movies, the birthday celebrations, the weekend plans, the potlucks, and the road trips. I am also very thankful to my Georgia Tech seniors- Pramod , Dhaval, Prashant, and Prabuddha who guided and steered me in right direction in my early days of PhD life.

Last but not the least, I cannot express my gratitude in words for my parents who stood by me my entire life. Their constant encouragement in times, good or bad, helped me endure every difficulty I faced and stand where I am today. I am eternally grateful for all that they have done and the compromises that they have made to ensure my happiness and my success.

-Rohan Awati, Georgia Tech, December 2015

TABLE OF CONTENTS

LIST OF TABLES

LIST OF FIGURES

LIST OF SYMBOLS AND ABBREVIATIONS

AlPO	Aluminiphosphate
CBMC	Configurational Bias Monte Carlo
CC	Coupled cluster
DFT	Density Functional Theory
FF	Force Field
GCMC	Grand Canonical Monte Carlo
LJ	Lennard-Jones
MC	Monte Carlo
MD	Molecular Dynamics
PES	Potential Energy Surface
TST	Transition State Theory

SUMMARY

The overall objective of this thesis has been to develop accurate computational methods for the diffusion and adsorption of small gases in zeolites. Firstly, the effect of the zeolite framework flexiblity on the single component and binary diffusion of various gases were discussed. Results indicate that for tight fitting molecules the rigid framework approximation can produce order(s) of magnitude difference in diffusivities as compared to the simulations performed with a fully flexible framework. We proposed two simple methods in which the flexible structure of a zeolite is approximated as a set of discrete rigid snapshots. Both methods are orders of magnitude more efficient than the simulations with the fully flexible structure. Secondly, we use a combined classical and quantum chemistry based approach to systematically develop the force fields based on DFT calculations for interactions of simple molecules like CH_4, N_2, linear alkanes, and linear alkenes in zeolites. We used a higher level of theory known as the DFT/CC method to correct DFT energies that were used in the periodic DFT calculations to develop force fields. Our results show that DFT-derived force fields give good predictions of macroscopic properties like adsorption isotherms in zeolites. The force fields are transferrable across zeolites and hence can be further used to screen materials for different storage and separation applications.

CHAPTER 1

INTRODUCTION

1.1 Nanoporous Materials

Porous materials have been widely used in the chemical industry for a variety of applications including separations, catalysis, sensing, and gas storage. Porous materials are organic or inorganic frameworks that are commonly classified based on their pore size as macroporous (> 50 nm), mesoporous (2 - 50 nm) and microporous (< 2 nm). As the pore sizes associated with microporous materials is comparable to many common molecules, they are commonly referred to as nanoporous materials.[1] Due to their small pore sizes and narrow channels, these materials show interesting properties for a variety of separations and catalysis.[2]

Depending on the ordered or disordered nature of the underlying framework, nanoporous materials can be further classified as being amorphous or crystalline. Amorphous materials like activated carbons do not have a well-defined crystal structure but have a distribution of pore sizes. In contrast, crystalline nanoporous materials such as zeolites consist of a periodic and ordered structure that makes them amenable to computational modeling studies. A brief overview is presented below.

1.2 Zeolites

A zeolite structure is formed by tetrahedral units (primary building units), with one oxygen atom at every vertex and one T atom at the center, (see Fig. 1.1 (a)). The T atom is usually a silicon or aluminum atom, although some structures have been

synthesized in which some of the T-atoms are replaced by Ge, P, Mg, Mn, Co or Zn.[3-4] Aluminosilicates are the class of zeolites which contain Al and Si as T atoms while aluminophosphates are class of zeolites containing Al and P as T atoms. The generally accepted Löwenstein rule states that Al-O-Al sequences are energetically forbidden, although structures that violate this rule have been recently synthesized at high temperatures.[5] Due to the constraints imposed by the bond lengths and angles within the tetrahedral building blocks, only a limited number of primary building unit association geometries are available.

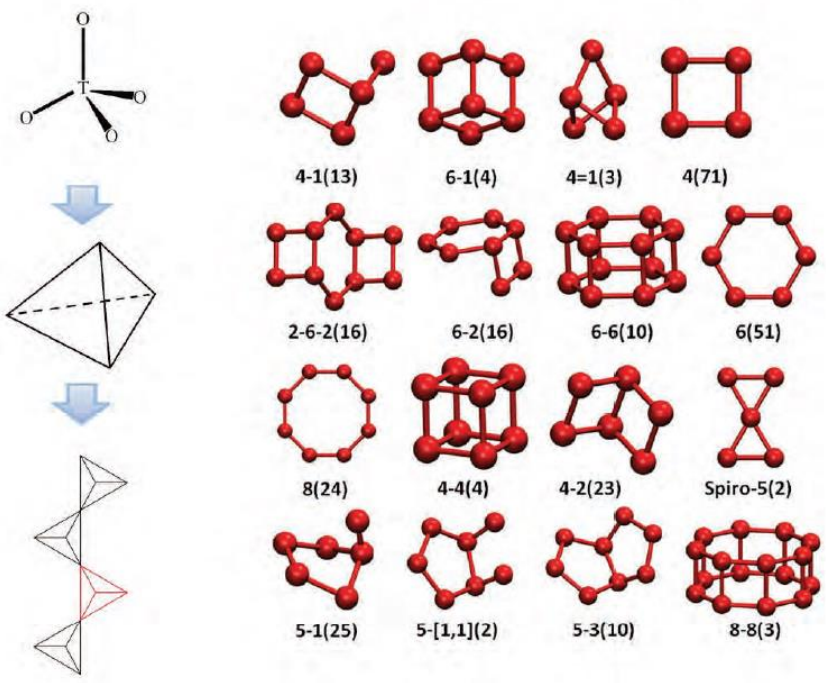

Figure 1.1 (a) Primary building units (PBUs) in zeolites and an example of linking, (b) some examples of secondary building units (SBUs) present in zeolites. T atoms are represented by beads. The oxygen atoms are located approximately at the middle each line joining T atoms. The first numbers are the description code of the SBU, and the number in parenthesis the frequency of occurrence in zeolites.[6] The figure is adapted from Sanchez *et al.*[7].

In Fig. 1.1 (b), the secondary building units (SBUs), or different arrangement of tetrahedral units, that have been found in zeolites are shown. Zeolites can be completely described by the asymmetric unit cell of the particular zeolite and its space group, from which every atom position of the symmetric unit cell can be generated. A perfect, infinite zeolite crystal is obtained by copying the symmetric unit cell in all three directions in space. In reality, perfect zeolite crystals do not exist. Zeolite crystals often consist of complex inter-grown structures with internal grain boundaries and varying pore orientation[8]. One common defect in zeolites is the rupture of one of the Si-O-Si bonds to form silanol groups (Si-O-H), altering the crystal structure and the hydrophobic character of the zeolite[9].

Zeolite structures contain micropores in one or more dimensions, with diameters between 3 and 10 Å[10]. These micropores are responsible for most of zeolite's interesting properties. According to their pore arrangement, zeolites are usually classified in three different categories: straight channels, intersecting channels, and cages. Some typical examples are shown in Fig. 1.2. In pure siliceous zeolites, the number of oxygen atoms is twice as large as the number of silicon atoms, and the electrostatic charge is perfectly balanced so that the zeolite is charge neutral. In the cases where framework silicon atoms are substituted by aluminum, the aluminum atoms introduce a net negative charge. This net negative charge has to be counterbalanced by non-framework cations in the zeolite pores. One important property of zeolites is the possibility of exchange of non-framework cations from solution[11]. This property makes zeolites ideal candidates for water purification and softening. The selectivity of a zeolite for one specific cation depends on

several factors such as temperature, pH, size and charge of the cation, the concentration of the cations in the solution, and the particular structure of the zeolite[12].

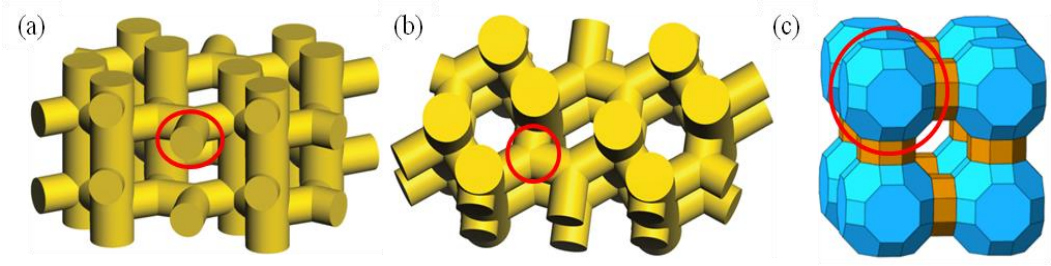

Figure 1.2 Classification of zeolites with their pore network, (a) zig-zag channel shown inside red circle[13], (b) intersection of zig-zag channel shown inside red circle[13], and (c) cages connected by small pores[13] known as windows shown inside red circle.

The large surface area of zeolites, as well as their excellent thermal and chemical stability, makes them suitable materials for a large number of applications. Specific zeolites have to be chosen for a particular use depending on their characteristics such as hydrophilic character, pore volume, surface area, pore size, non-framework cations present in the structure, and cost. Zeolites are used as molecular sieves to separate gases for different applications. For example, in the Parex™ process developed by UOP, zeolites are used to separate p-xylene from mixed xylenes.[14] Also, they are used to produce highly purified medical oxygen or to remove water, carbon dioxide, and Sulphur compounds from natural gas streams.[15-16] In the petrochemical industry, cation exchanged zeolites are used as solid state Lewis acids that can act as catalysts for isomerisation, alkylation, and cracking reactions[17]. As a source of potassium or ammonium, the natural zeolite clinoptilolite (CLI) is used as a soil treatment[18]. Zeolites are added to concrete to reduce its manufacture and laying temperature, providing easier compaction and improving break strength[19].

Given the huge diversity of available zeolites, it is a difficult task to identify high performing materials for a specific application. Even within zeolites which have been under study since 1950s, it is impractical to study the properties of each material and every possible variation using detailed experiments. Additionally, it is likely that only a handful of the studied candidate materials will be useful for the given application. Thus, a method of quickly and cheaply screening through a library of prospective materials is required. Computational molecular modeling and process simulation approaches are ideally suited for this scenario and offer a very powerful tool towards accelerated materials discovery and process development. The strengths, the limitations and the utility of different modeling methods are outlined below.

1.3 Classical Atomistic Simulations

Classical simulations describe the interaction of individual gas molecules with the adsorbent framework at the atomic level. The intermolecular forces and interaction energies are represented by mathematical equations called force fields; and the macroscopic properties such as adsorption isotherms, heat of adsorption, and diffusivities are obtained from statistical mechanics. In particular, Grand Canonical Monte Carlo[20] (GCMC) is used to predict adsorption properties, while diffusivities are calculated from Molecular Dynamics (MD) simulations.[20] Classical methods can be used to describe systems as large as 1 million atoms for a few nanoseconds of simulation time.

The accuracy of the GCMC and MD predicted properties are highly dependent on the quality of force fields used to describe the energetics of the system. Traditional or generic force fields are not transferrable and are found to be severely lacking in correctly describing the complex chemical environments in nanoporous materials. Moreover, force

fields fitted to one set of experimental data are unable to predict adsorption in similar materials, rendering them unsuitable for material screening. For the atomistic simulations to be useful for screening applications, it is essential for the force field to have predictive capabilities.

At a given temperature, atoms in a zeolite crystal vibrates around their mean crystallographic position making zeolite a flexible structure. However, atomistic simulations in zeolites are often carried out with a assumption of rigid framework to reduce the vast computational time associated with the flexible framework. A number of previous studies have examined the effect of framework flexibility on adsorption and diffusion of molecules with conflicting outcomes.[21-24] Thus, it is a new direction for atomistic simulations to understand when a rigid framework approximation is justified and when, in contrast, framework flexibility is important for correctly describing adsorbate adsorption and diffusion.

1.4 DFT and Computational/Quantum Chemistry Methods

Quantum chemistry methods provide a better description of intermolecular interactions than classical simulations but are generally impractical for use in the large scale GCMC or MD simulations required for calculating macroscopic properties. Within quantum mechanics (QM), different methods of varying computational cost and accuracies can be used for calculating various properties of the systems. Typically, highly accurate methods such as coupled cluster (e.g. CCSD(T)) and Moller-Plesset (e.g. MP2) [26,70,128] can only be used for studying systems consisting of about 10 - 50 atoms. Moreover, these methods are only applicable for small representative clusters of the zeolite and cannot be used for studying the periodic crystal structure of the framework.

A good compromise between accuracy and computational cost is provided by Density Functional Theory (DFT). Within DFT, the properties of the many-electron system is described by functionals that depend on the electron density. DFT has been widely used to study nanoporous materials, semi-conductors, bulk metals and surfaces.[25-26] In many cases, DFT provides a sufficiently accurate description of the intermolecular interactions for the adsorption systems of interest.[27]

1.5 Thesis Summary

The overall objective of this work is to study and understand the adsorption and diffusion processes for different adsorbates in zeolites using the computational methods outlined above. In Chapter 2 and 3, we discuss the effect of the zeolite framework flexiblity on the diffusion of various gases. This study presents the first detailed analysis of different types of zeolite framework flexibilities and how they depend upon the zeolite topology. In Chapter 4, we use a combined classical and quantum chemistry based approach to systematically develop force fields based on DFT calculations for interactions of simple molecules like CH_4 and N_2 with zeolites. Our results show that DFT-derived force fields give good predictions of macroscopic properties in zeolites and can be further used to screen materials for different storage and separation applications. These methods are extended to derive force fields for more complex adsorbates like olefin and paraffin interactions with zeolites in Chapter 5. Here we use periodic DFT calculations to develop force fields similar to chapter 4, for modeling adsorption in zeolites. Finally, we outline and discuss the main challenges and opportunities of molecular simulations for studying nanoporous materials in Chapter 6. This study

provides a framework for understanding the different aspects of adsorption and diffusion processes using a multiscale computational approach.

CHAPTER 2

Efficient and Accurate Methods for Characterizing Effects of Framework Flexibility on Molecular Diffusion in Zeolites: CH_4 Diffusion in 8MR Zeolites[1]

Molecular dynamics (MD) and transition state theory (TST) methods are becoming efficient tools for predicting diffusion of molecules in nanoporous materials. The accuracy of predictions, however, often depends upon a major assumption that the framework of the material is rigid. This saves considerable amount of computational time, and is often the only method applicable to materials for which accurate force fields to model framework flexibility are not available. In this chapter, we systematically characterize the effect of framework flexibility on diffusion in four model zeolites with typical cage-window structures (LTA, CHA, ERI, and BIK) that exhibit different patterns of window flexibility. We show that for molecules with kinetic diameters comparable (or larger) to the size of the window the rigid framework approximation can produce order(s) of magnitude difference in diffusivities as compared to the simulations performed with a fully flexible framework. We also show that simple recipes to include the effect of framework flexibility are not generally accurate.

---

[1] Portions of this chapter have been previously published as Awati, R. V.; Ravikovitch, P. I.; Sholl, D. S., Efficient and Accurate Methods for Characterizing Effects of Framework Flexibility on Molecular Diffusion in Zeolites: CH_4 Diffusion in Eight Member Ring Zeolites. *J. Phys. Chem. C* **2013**, *117*, 13462-13473.

To account for framework flexibility effects efficiently and reliably, we introduce two new methods in which the flexible structure is approximated as a set of discrete rigid snapshots obtained from simulations of dynamics of an empty framework, using either classical or, in principle, *ab-initio* methods. In the first method, we perform MD simulations of diffusion in a usual manner but replace the rigid structure with a new random snapshot at a certain characteristic frequency corresponding to the breathing motion of the window, while keeping positions of adsorbate molecules constant. In the second method, we directly compute cage to cage hopping rates in each rigid snapshot using TST and average over a distribution of snapshots. Excellent agreement is obtained between diffusivities predicted with these two new methods and direct MD simulations using fully flexible structures. Both methods are orders of magnitude more efficient than the simulations with the fully flexible structure. The new methods are broadly applicable for fast and accurate predictions of both infinite dilution and finite loading diffusivities of simple molecules in zeolites and other nanoporous materials.

2.1 Introduction and Literature Review

To study adsorption and diffusion processes in zeolites and other nanoporous materials, molecular simulation methods[28-30,21, 31-38] are important tools alongside experimental studies.[39] One area in which molecular diffusion is especially important is for zeolites with pore sizes that are comparable with the kinetic diameters of the molecules. In particular, small pore eight member ring (8MR) zeolites (pore size ~ 3-4 Å) are important materials for separations of small molecules.[39-40]

Molecular simulations in zeolites are often carried out with a rigid framework in which atoms are kept fixed at their crystallographic positions. This approach ignores any

vibrations of the zeolite's framework atoms. Including framework flexibility is in principle preferable if a force field (FF) is available that accurately represents the zeolite degrees of freedom. When approximating the zeolite as rigid, however, calculations of adsorbate diffusion can be performed much faster than when framework flexibility is included.[41-42] It is therefore useful to understand when a rigid framework approximation is justified and when, in contrast, framework flexibility is crucial for correctly describing adsorbate diffusion. A number of previous studies have examined the effect of framework flexibility on adsorption and diffusion of molecules of size comparable to the pore size of the zeolites.[21-24, 32, 43-44] The topics of this earlier work are summarized in Table 2.1.

Generally, omission of framework flexibility does not significantly affect equilibrium properties such as the adsorption isotherms in zeolites.[21, 44] Similarly, it does not affect the diffusion of molecules that are significantly smaller than the pore size of the zeolite. Hence, simulations with rigid frameworks are typically sufficient in such cases. However, there is much less clarity regarding the effect of framework flexibility on diffusion of the molecules with sizes comparable to or larger than the nominal zeolite pore size. Garcia *et al.* and Leroy *et al.* observed higher diffusivities when the framework was treated as flexible and concluded that framework flexibility plays an important role in diffusion of molecules of size comparable to or greater than the pore size of zeolites.[21, 24] Krishna *et al.* suggested that framework flexibility can be effectively taken into account by performing simulations with a different rigid structure, the so-called time-averaged (TA) structure.[22, 32] They concluded that the time averaged structure is sufficient to capture the

effect of framework flexibility. More details about simulations with time averaged structures are discussed below.

Table 2.1 Summary of the previous work examining framework flexibility in zeolites.

Reference	FF for framework flexibility	System studied	Properties reported
Deem *et al.*[45]	Deem	Frameworks only	Window flexibility
Demontis *et al.*[43]	Demontis	CH_4 in LTA	Single component D_s
Vlugt *et al.*[44]	Demontis	Hydrocarbons in silicalite	Heat of adsorption; Henry's coefficient
Leroy *et al.*[24]	Demontis & Bougeard	n-alkanes in silicalite	Single component D_s
Garcia *et al.*[21]	Nicholas[46], Hill-Sauer[47-48]	CH_4 in LTA	Single component D_s
Krishna *et al.*[22, 32]	BKS[49], PMM[50]	CH_4,CH_4/H_2,CH_4/CO_2 in LTA and CHA	Single- and multi-component D_s ; Diffusion selectivity (S_{diff})
Combariza *et al.*[23]	BKS, PMM	C_3H_8/C_3H_6 in Si-CHA, Si-SAS	Single component D_s
Huth *et al.*[51]	Nicholas	H_2, N_2, O_2, CO_2, CH_4 in DDR	Single component D_s

The aim of this study is to assess the effect of framework flexibility for molecular diffusion on the example of siliceous 8MR zeolites. We show that the time averaged approach introduced by Krishna *et al.*[22] is able to correctly account for flexibility effects in some but not all the materials. We then introduce two new methods that allow the effect of framework flexibility to be described efficiently and accurately. These methods are applicable not only to zeolites but also to related materials such as metal-organic

frameworks[52-53] and glassy polymers[54] where molecular hopping through narrow pores is important. The chapter is organized as follows. In section 2.2, we discuss the zeolite structures, force fields and simulation methods used in our calculations. In section 2.3, we discuss in detail the effect of framework flexibility on diffusion in selected 8MR zeolites. In section 2.4, we introduce two new efficient methods to predict self-diffusivities in flexible structures, and discuss the main advantages of these new methods.

2.2 Models and Simulation details

2.2.1 Adsorbate and zeolites

Throughout this chapter, we focus on the diffusion of CH_4 in 8MR silica zeolites. Results will be presented for four 8MR zeolites, CHA, ERI, LTA, and BIK. The rationale for selecting these specific four examples is described further below. The window dimensions of energy minimized geometries of each zeolite are shown in Fig. 2.1. Energy minimization was carried out starting from structures taken from the IZA database using methods described further below. Window dimensions were defined using the convention from the IZA database[10], namely the atom to atom distance across the window minus 2.7 Å. LTA has two equivalent minimum window dimensions, while CHA, BIK, and ERI have a single minimum dimension due to the asymmetry of their 8MR windows. The asymmetry of CHA is small and hence when the dynamics of a flexible structure is included it has two dimensions that can define the minimum window dimension. We show below that this distinction has implications for the role of flexibility on molecular diffusion.

2.2.2 Force fields

Previous studies of framework flexibility in zeolites have used various flexible FFs.[21-24, 32, 43-44] For simplicity, we focus on a single FF throughout this work, namely the Hill- Sauer FF developed for silica materials.[47-48] In the Hill-Sauer FF, zeolite degrees of freedom (DOF) consist of one type of bond (Si-O), two types of angles (Si-O-Si, O-Si-O), one type of torsion (O-Si-O-Si) and coupling between these DOF. Further details on this potential are summarized in Tables A1 and A2 in Appendix A. The adsorbate of interest, CH_4, was modeled as a spherical united atom[55] (UA) with zero net charge. CH_4-CH_4 and CH_4-framework interactions are defined using Lennard-Jones[55] (LJ) potentials from the literature. Details are given in Table A3 in Appendix A. LJ potentials were cut and shifted using a cutoff radius of 12 Å.

2.2.3 Simulation details

For consistency, prior to performing MD simulations, the structure of each zeolite was energy minimized using the Hill-Sauer FF. Energy minimized structures are also denoted as optimized structures and abbreviated OPT below. The lattice parameters obtained in this way are listed in Table 2.2. Unless otherwise specified, all calculations below were performed using the lattice constants obtained from these energy minimized structures. These lattice constants are slightly larger than the lattice constants listed in the IZA database.

The temperature-dependent time averaged structures of each zeolite were obtained by MD simulation of empty frameworks using the Hill-Sauer FF in the canonical ensemble (constant NVT). Starting with the energy minimized structures, framework atom positions were averaged over their position recorded every 1 fs from

trajectory 10 ps in length. Tests with longer trajectories indicated that this approach gave well converged results. It should be noted that in performing calculations at different temperatures we ignore the temperature dependence of the unit cell volume. Such calculations, while potentially important, are outside of the scope of the present work.

Table 2.2 Lattice parameters for a single unit cell of energy-minimized zeolite structures. Numbers in brackets in the first column indicate number of unit cells along each cell vector used in the simulation. Unit cell parameters taken from IZA database are also shown in parentheses in the respective columns.

Zeolites	a (Å)	b (Å)	c (Å)	α (°)	β (°)	γ (°)
LTA (2×2×2)	12.1190 (11.9190)	12.1190 (11.9190)	12.1190 (11.9190)	90 (90)	90 (90)	90 (90)
BIK (4×2×5)	7.5950 (7.5400)	16.3405 (16.2222)	5.2944 (5.2560)	90 (90)	90 (90)	90 (90)
CHA(2×2×2)	13.7875 (13.6750)	13.7595 (13.6750)	14.8885 (14.7670)	90 (90)	90 (90)	120 (120)
ERI (2×2×2)	13.1900 (13.0540)	13.1560 (13.0540)	15.3330 (15.1750)	90 (90)	90 (90)	119.74 (120)

Molecular Dynamics (MD) calculations of flexible zeolites were performed using LAMMPS[56] and the FFs described above. For calculations using rigid zeolites, an in-house MD code that uses grid interpolation for the potential energy surface of zeolite was used; this approach requires far less computational effort than calculations that explicitly compute the potential energy at each time step.[57] We verified that the two codes give equivalent results for calculations using rigid structures. Time steps of 0.1 fs and 1 fs were used in simulations of flexible and rigid structure, respectively. Test calculations in

the microcanonical ensemble verified the validity of these time steps. The shorter time step required to treat flexible frameworks is one of the reasons why simulations of rigid structures have a large advantage in computational speed. Initial adsorbate configurations were obtained from Grand Canonical Monte Carlo (GCMC) simulations for the rigid structures using an in-house GCMC code. For flexible structures, initial adsorbate configurations from GCMC using the time averaged structure were used. Simulations in the NVT ensemble were performed using a Nosé-Hoover thermostat and the velocity Verlet integrator.

For each simulation, a simulation box was chosen to ensure that the minimum length in each of the direction was larger than 24 Å (twice the cutoff radius of the LJ potentials). The mean square displacement (MSD) of CH_4 molecules was recorded every 1000 MD steps. This data was then used to calculate self-diffusivity D_s, of CH_4 using,

$$D_s = \frac{1}{6}\lim_{t\to\infty}\frac{d}{dt}\left\langle |r(t)-r(0)|^2 \right\rangle \qquad (2.1)$$

where, r(t) denotes the positions of the adsorbates at time t. The total length of the simulation varies with temperature, type of zeolite, and loading, and was typically in the range of 1-50 ns to achieve diffusive regime. For simulations at low temperatures we made sure that the minimum MSD achieved is at least the square of distance between two adjacent cages (144, 90, and 36 $Å^2$for LTA, CHA, and ERI respectively), or adjacent unit cells in the case of 1-dimensional BIK (58 $Å^2$). Sample MSD plots are shown in Fig. A1 for calculating diffusion of CH_4 in all the four zeolites at conditions mentioned.

2.3 Results and discussion

2.3.1 Justification for selection of LTA, CHA, BIK, and ERI

Before examining adsorbate diffusion, it is useful to characterize several properties of the flexible frameworks for the four zeolites we examined. As shown in Fig. 2.1, there are four distances (d_1, d_2, d_3, d_4) that can be defined as window dimensions in 8MR zeolites. The minimum window dimension among these four distances for the energy minimized structure is denoted d_{min}^{OPT}. The minimum window dimension for the time averaged structure is denoted d_{min}^{TA}. For the flexible structure, the minimum window dimension of any given window is a function of time, $d_{min}(t) = \min[d_1(t), d_2(t), d_3(t), d_4(t)]$. The distribution of window dimensions and its mean $\langle d_{min}(t) \rangle$ was obtained for each material from a MD simulation of the empty framework in the NVT ensemble. All these characteristic window dimensions for all four zeolites are shown in Fig. 2.1 along with the tail of the distribution corresponding to larger window dimensions ($> d_{min}^{TA}$). This tail region differentiates the time averaged and flexible structures. For BIK and ERI, the minimum window dimension of the time averaged structure, d_{min}^{TA}, is equal to the mean of the full distribution from the flexible structure, $\langle d_{min}(t) \rangle$. In contrast, $\langle d_{min}(t) \rangle < d_{min}^{TA}$ for LTA above 0 K and for CHA above ~300 K (below 300 K CHA has $\langle d_{min}(t) \rangle \approx d_{min}^{TA}$). As shown in Appendix A, this is a direct result of the number of directions that can define the minimum window dimension in the flexible structures; only structures for which a single direction defines the minimum window dimension at all times have $\langle d_{min}(t) \rangle \approx d_{min}^{TA}$. Consequently, in approximating the flexible structure as a time averaged structure, one neglects the effect of the large tail

of the distribution on D_s is neglected, and hence the time averaged structure may not accurately predict the diffusivity behavior in the fully flexible structure. This tail of the window size distribution can play a crucial role in enhancing D_s of the tight fitting molecules, as discussed later in this chapter. On the other hand, in the structures with multiple minimum window dimensions, the time averaged structure comes close to capturing the diffusivity in the fully flexible structure as the condition $\langle d_{min}(t)\rangle < d_{min}^{TA}$ results in a smaller tail region.

A second way to classify the zeolites we have chosen was motivated by considering differences that can exist between the time averaged and energy minimized structures. If these two structures were calculated for a perfectly harmonic solid they would be identical, because the time averaged position of any harmonic degree of freedom is equal to its energy minimum. This argument indicates that if the O atom vibrations of 8MR windows in zeolites are nearly harmonic (anharmonic) within a given temperature range, then the energy minimized and time averaged structures will be almost the same (different) resulting in similar (different) values of d_{min}. To quantify the anharmonicity of zeolite vibrations, a method used previously to study the anharmonic motions of the proteins[58-60] was used. In this method, the mean square displacement (MSD) of the oxygen atoms in 8MR windows was calculated as a function of temperature. If the MSD varies linearly (non-linearly) with temperature then the system is harmonic (anharmonic) in that temperature range.[59] For harmonic structures, the initial slope of the temperature dependence remains constant throughout the temperature range in which a given structure is harmonic. The results are shown in Fig. 2.2 (a). Using the definition just given, LTA and ERI are anharmonic while CHA and BIK are harmonic. At

each temperature, the magnitude of the MSD is BIK < CHA ≈ LTA ≈ ERI. This ranking does not correlate in a simple way with the effect of framework flexibility as this data does not tell us about the dynamics of the 8MR oxygen or whether a diffusing molecule is tight fitting.

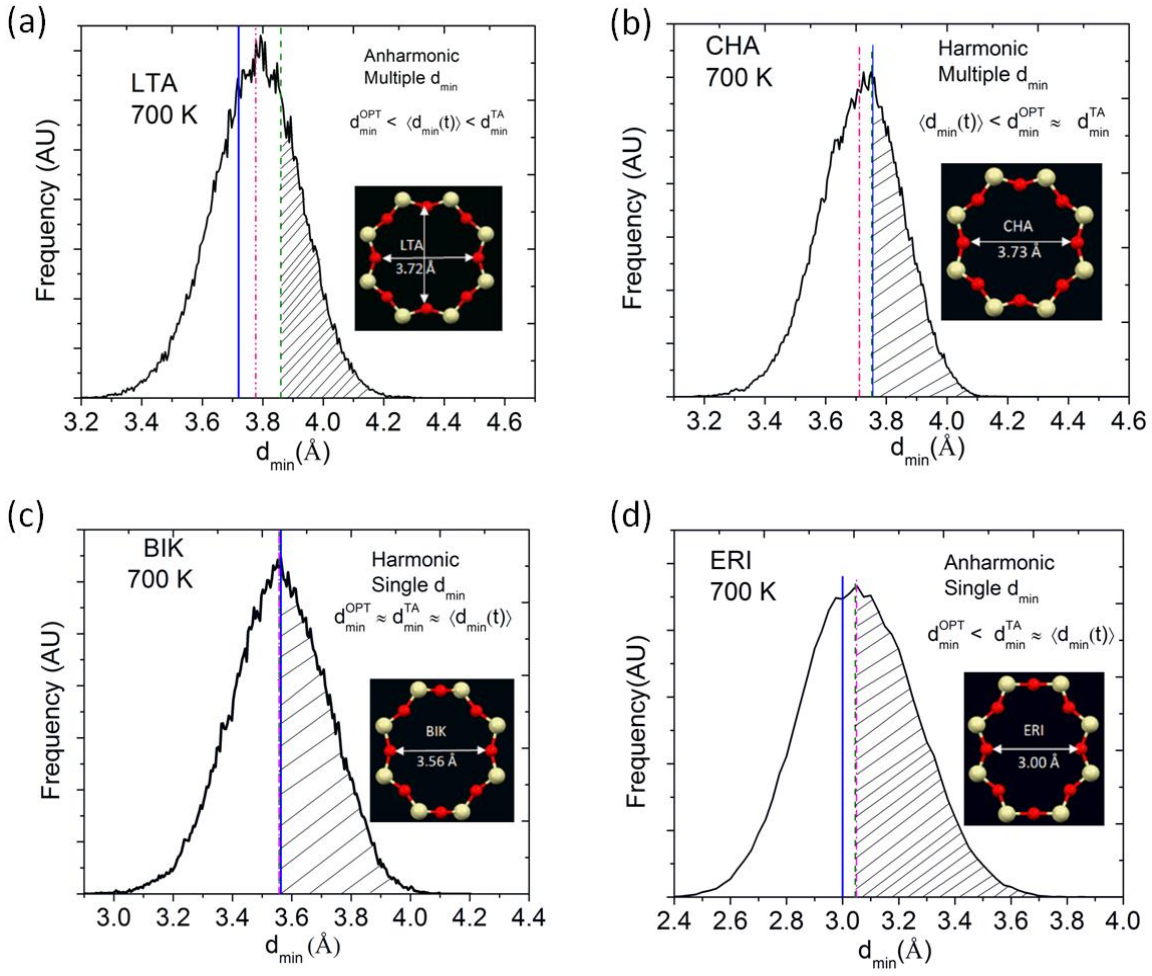

Figure 2.1 Window size distribution, $\mathbf{d_{min}^{OPT}}$(solid, blue), $\mathbf{d_{min}^{TA}}$ (dash, green), $\langle \mathbf{d_{min}(t)} \rangle$ (dot-dash, pink), and the tail of the distribution (shaded region) are shown for a) LTA, b) CHA, c) BIK, and d) ERI. Some of the characteristic dimensions are not visible because they overlap. In the insets, 8MR windows of the zeolites in their energy minimized geometries are shown with $\mathbf{d_{min}^{OPT}}$ labeled. Si (O) atoms are shown as yellow (red) spheres.

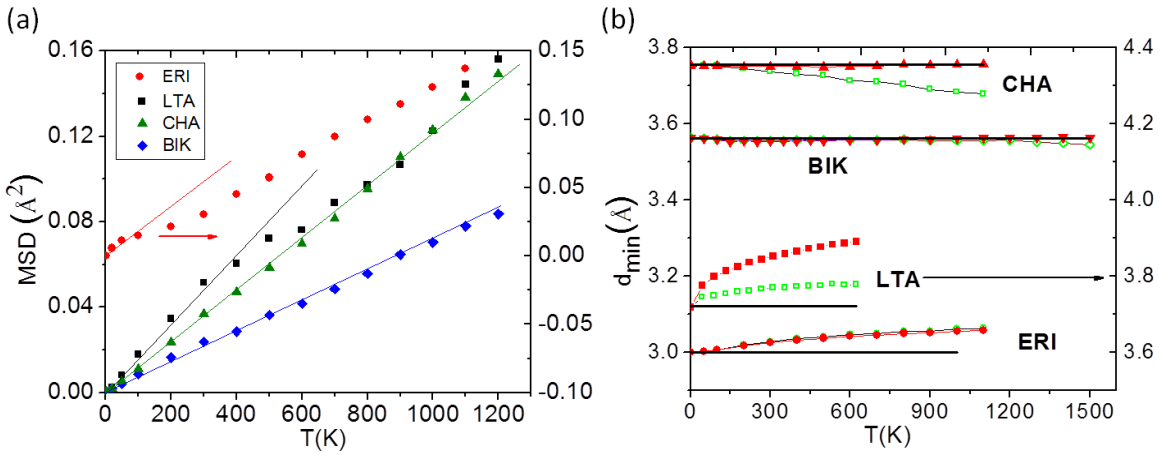

Figure 2.2 (a) MSD plots as a function of T for CHA, BIK, LTA, and ERI (note that for the ERI, vertical axis is on right hand side). The lines are guides to the eyes; (b) $\mathbf{d_{min}^{OPT}}$(black line), $\mathbf{d_{min}^{TA}}$(red), and mean of the distribution of window sizes (light green) for each zeolite. In our NVT calculations we did not consider the temperature dependence of the unit cell, thus this information does not enter into our conclusions regarding harmonicity/anharmonicity of the zeolites considered in this work.

The connection between the harmonicity of the 8MR atoms and d_{min} is shown in Fig. 2.2 (b). For the harmonic structures, BIK and CHA, the energy minimized and time averaged d_{min} are essentially equal at all temperatures. This immediately implies that using the time averaging procedure will not be effective in accounting for the framework flexibility in these materials. For the two anharmonic materials, LTA and ERI, the time averaged and energy minimized minimum window dimensions are unequal, and the former is temperature dependent. For BIK, the energy minimized d_{min} and the mean of the window size distribution are equal at all temperatures as seen from Fig. 2.2 (b). This result is combination of BIK being harmonic and having a single direction that defines the minimum window dimension.

The discussion above has shown that two properties are important to characterize the effect of framework flexibility: (a) the number of distinct directions that can be associated with the minimum window dimension in a fluctuating structure, and (b) the harmonicity of the vibrations associated with the atoms in the windows. The four silica zeolites we have examined, LTA, CHA, ERI, and BIK, were selected to give one example each of the four possible behaviors seen when considering this pair of properties.

2.3.2 Effect of framework flexibility

As an initial example of the effect of framework flexibility, we consider CH_4 diffusion in LTA, an example that has also been used in previous studies.[21-22, 32, 43] NVT MD simulations were used to compute D_s in the energy minimized, time averaged, and flexible structures of LTA at 700 K at different CH_4 loadings as shown in Fig. 2.3. Similar calculations were performed previously by Krishna *et al.*[22, 32] at 500 K in the LTA structure taken from IZA database without energy minimization. Our results agree qualitatively with Krishna *et al.* Calculations with the energy minimized structure underpredict D_s relative to the fully flexible structure; while the time averaged structure gives results in good agreement with the fully flexible structure. This is because LTA has multiple d_{min} at 700 K, causing a narrow tail region. At such a high temperature, D_s is already high, and any additional enhancement in D_s due to the tail region is small. On the other hand, the energy minimized structure has a lower d_{min} than the time averaged structure. This gives rise to the large deviation in results between the energy minimized and fully flexible structures. The largest discrepancy between the diffusivities from the

energy minimized and flexible structures is roughly a factor of 2 at a loading of 9 molecules/unit cell.

To judge whether this effect can be considered large, it is useful to compare this discrepancy with those obtained from different experimental measurements of D_s in zeolites. There are well documented examples where different experimental techniques give vastly different values of D_s.[33, 39, 61-62] If the difference in D_s obtained via calculation in the three structures is within the typical range of several experiments, then the impact of framework flexibility cannot be tested explicitly by comparison with experimental data. This suggests that changes of at least an order of magnitude should be observed due to the framework flexibility before the effect of flexibility can be considered significant.[61-62]

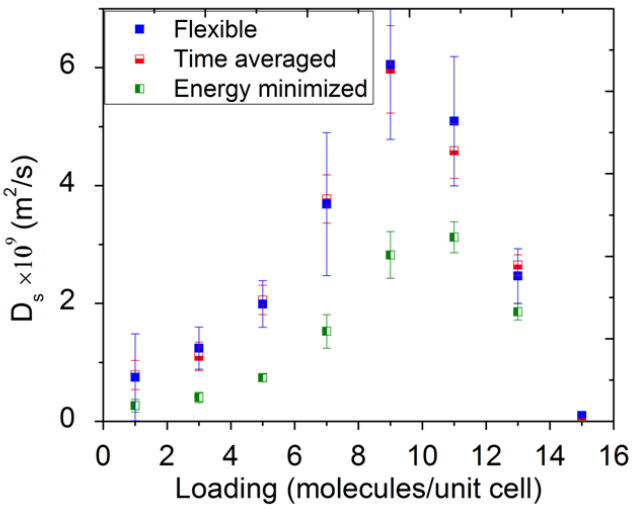

Figure 2.3 Comparison of D_s of CH_4 at 700 K in the flexible, time averaged, and energy minimized structures of LTA as a function of adsorbate loading.

In order to explore whether variation of an order of magnitude or more in D_s is possible due to framework flexibility, we considered the temperature dependence of D_s in

several materials. D_s was calculated in the energy minimized, time averaged, and flexible structures of LTA, CHA and ERI with the following temperature ranges and loadings: 300-1050 K and 9 molecules/unit cell for LTA, 250-1100 K and 10 molecules/unit cell for CHA, and 1100-2100 K, 1.5 molecules/unit cell for ERI. These conditions were chosen so that D_s were readily measurable in our MD simulations in each case. We recognize that many of these temperatures are not relevant to experimentally accessible conditions. The results in Fig. 2.4 (a) show an Arrhenius behavior in all three structures. In each material, the deviation between the diffusivities in the fully flexible structure and the energy minimized structure becomes larger as T decreases. For both ERI and CHA, the lower temperatures examined in our MD simulations show approximately an order of magnitude difference in diffusivities between the energy minimized and flexible structures. These are clear examples where accounting for the framework flexibility is critical to making accurate predictions about the molecular diffusion.

It is useful to note that with two materials shown in Fig. 2.4 (a) using the time averaged structure instead of the energy minimized structure does not accurately capture the impact of the flexibility. For CHA, the time averaged and energy minimized structure are almost identical as a result of the harmonicity of the O atoms in the 8MR windows, as discussed above. As a result, using the time averaged structure does not capture any of the impact of framework flexibility. For ERI, using the time averaged structure captures some of the impact of the flexibility, but the results in Fig. 2.4 (a) show that this approach does not reach the goal of accurately predicting the outcome for the fully flexible material.

An important point noticed at lower T (~300 K), is that the ratio $\frac{D_S^{Flexible}}{D_S^{TA}}$ is higher for CHA (~5.4) compared to that for LTA (~1.6) even though they have similar window sizes. This is because CHA has single d_{min} at 300 K, causing a wide tail region. This results in larger $\frac{D_S^{Flexible}}{D_S^{TA}}$ because the time averaged approach neglects the contribution from the tail region in enhancing D_s. On the other hand, multiple d_{min} in LTA, at 300 K cause smaller tail region, and hence smaller $\frac{D_S^{Flexible}}{D_S^{TA}}$ ratio.

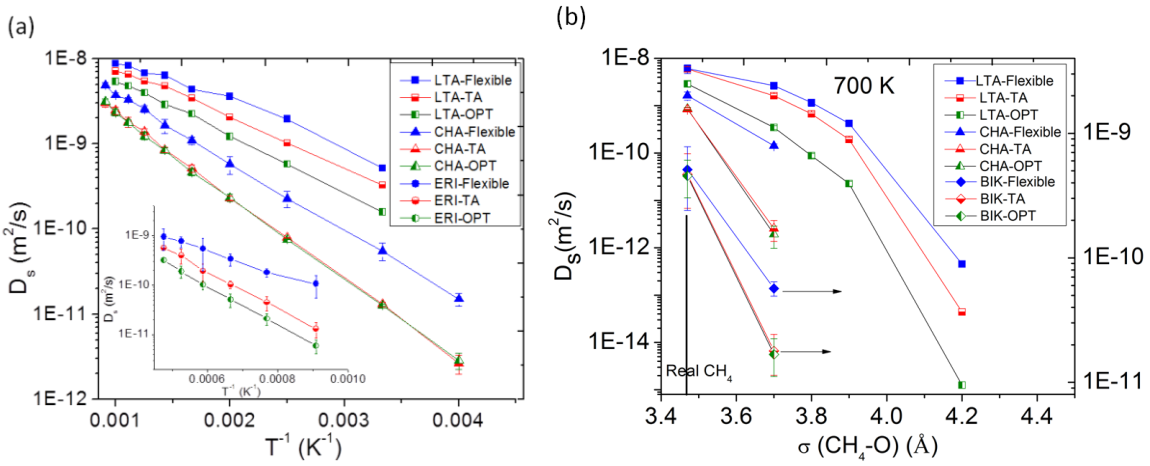

Figure 2.4 (a) NVT-MD simulation of CH_4 in energy minimized (green), time averaged (red), and flexible structures (blue) of LTA (squares), CHA (triangles), and ERI (circles). The loadings are 9 molecules/unit cell for LTA, 10 molecules/unit cell for CHA, and 1.5 molecules/unit cell for ERI; (b) NVT-MD simulation of hypothetical CH_4 in energy minimized (green), time averaged (red), and flexible structures (blue) of LTA (squares), CHA (triangles), and BIK (diamonds) showing the effect of the framework flexibility for the tight fitting molecules. The loadings are 9 molecules/unit cell for LTA, 10 molecules/unit cell for CHA, and 0.25 molecules/unit cell for BIK.

2.3.3. Impact of adsorbate size

The examples above relied on MD simulations to assess the role of framework flexibility on molecular diffusion. To understand these effects over a wider range of temperatures, it is useful to examine the same materials from the standpoint of transition state theory (TST). LTA, ERI, and CHA are cage type 8MR zeolites where CH_4 adsorbs within cages and diffusion occurs by hopping through the 8MR windows.[63] We can expect that TST will lead to a diffusivity with an Arrhenius form,

$$D_s = k_0 \exp(-E_a / RT) \qquad (2.2)$$

where k_0, T, and R are the pre-exponential factor, temperature, and gas constant, respectively. Haldoupis *et al.*[52] showed that for tightly fitting adsorbates, the activation energy depends approximately exponentially on window dimensions. With this approximation,

$$E_a \approx a \exp(-b d_{\min}) \qquad (2.3)$$

where, *a* and *b* are the fitted parameters and d_{min} is the minimum window dimension. Combining equations (2.2) and (2.3) gives

$$D_s \approx k_0 \exp(-a \exp(-b d_{\min}) / RT) \qquad (2.4)$$

This supports the qualitative idea that diffusion coefficients can be very sensitive to the window dimensions for tight fitting molecules.[32, 52, 62] For diffusion in the flexible structures, the distribution of the window dimensions results in the distribution of the activation energies for hopping events. The tail of the distribution corresponding to larger window dimensions can play a crucial role in increasing D_s relative to approximations based on rigid structures. As a result, self-diffusion of tight fitting molecules will be significantly affected by the tail of the window size distribution. One example of this

outcome shown above is the diffusion of CH_4 ($\sigma_{CH_4-O} = 3.47$ Å) in ERI ($d_{min}^{OPT} = 3$ Å) where $\frac{D_S^{Flexible}}{D_S^{TA}}$ is high even at high temperatures, as seen from Fig. 2.4 (a).

To test this concept in the zeolites other than ERI, the tight fitting adsorbates were generated by artificially increasing the LJ-size parameters, $\sigma_{CH_4-CH_4}$ and σ_{CH_4-O}. These molecules are referred to as hypothetical CH_4 molecules below. These two size-parameters are interdependent and hence for subsequent discussion only σ_{CH_4-O} is used. The energy parameters $\varepsilon_{CH_4-CH_4}$ and ε_{CH_4-O} were kept constant. MD simulations in the NVT ensemble were carried out at 700 K with hypothetical CH_4 molecules in the flexible, time averaged, and energy minimized structures of BIK, LTA, and CHA. Loadings of 0.25, 9, and 10 molecules per unit cell were used in BIK, LTA, and CHA respectively. The results are shown in Fig. 2.4 (b) for the molecules with σ_{CH_4-O} up to 3.7 Å for BIK and CHA and up to 4.2 Å for LTA. In case of LTA, for the molecule with $\sigma_{CH_4-O} = 4.2$ Å, D_s cannot be accurately calculated by classical NVT-MD simulation because of the slow diffusion. To avoid this limitation, TST was employed as given by Eq. (2.2), where E_a and k_0 were obtained by fitting Eq. (2.2) to the MD data at higher temperatures. Deviations in D_s can be clearly observed between the flexible and rigid structures for LTA, BIK, and CHA. This deviation is approximately an order of magnitude when $\sigma_{CH_4-O} = 3.7$ Å in CHA, and larger for larger molecules. For LTA, an order of magnitude deviation is observed at $\sigma_{CH_4-O} = 3.9$ Å with the energy minimized structure and at $\sigma_{CH_4-O} = 4.2$ Å with the time averaged structure. Again, larger deviations are predicted for larger diffusing molecules.

The effect of framework flexibility at lower temperatures for hypothetical CH_4 molecules with $\sigma_{CH_4-O} = 3.7$ Å was also studied in the same zeolites at the loadings defined above. The results obtained are shown in Fig. 2.5. Large differences can be seen between the results from the rigid and flexible structures. For BIK and CHA, it is clear that the time averaged structure does not capture any of the effects of framework flexibility. The impact of framework flexibility is, not surprisingly, larger for these hypothetical molecules than for CH_4 described using realistic potential parameters. For example, in CHA at 700 K, for CH_4 with $\sigma_{CH_4-O} = 3.7$ Å, the ratios $\frac{D_S^{Flexible}}{D_S^{TA}} \approx 60$ and $\frac{D_S^{Flexible}}{D_S^{OPT}} \approx 60$ are much larger than corresponding ratios (1.9 and 1.95 respectively) for CH_4 with $\sigma_{CH_4-O} = 3.47$ Å.

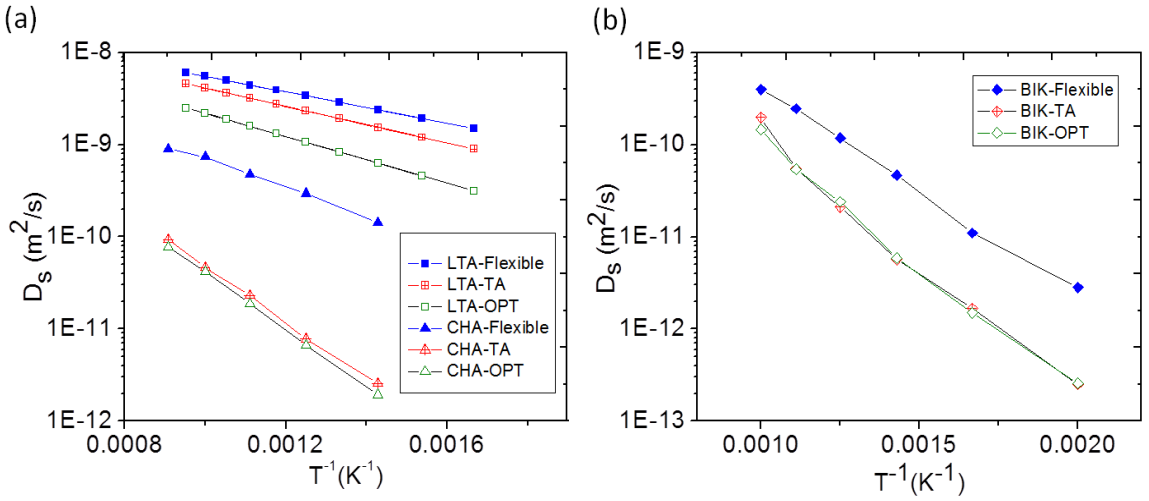

Figure 2.5 NVT-MD simulation results for hypothetical CH_4($\boldsymbol{\sigma_{CH_4-O} = 3.7}$ **Å**) in the energy minimized (green), time averaged (red), and flexible structure (blue) of LTA (square), CHA (triangles), and BIK (diamonds) zeolites showing combined effect of low T and large adsorbate size.

2.4 New efficient methods to simulate framework flexibility

The results above indicate that the framework flexibility can be an important factor in molecular diffusion in zeolites. They also show that the time averaged structure approach proposed by Krishna *et al*. cannot always capture these effects even qualitatively. It clearly would be useful to have methods that can efficiently and reliably account for framework flexibility effects. In the remainder of this chapter, we introduce two new methods with this goal. These methods are motivated by recent work by Haldoupis *et al*.[52], who proposed a method in which the flexible structure can be approximated as a set of discrete rigid structures. These discrete rigid structures, or snapshots, can be generated from a classical MD simulation of the empty framework or, alternatively, from *ab initio* MD trajectories.[52] The latter idea would allow framework flexibility to be considered even in complex materials where a reliable classical force field for the framework degrees of freedom is not available. The process of recording snapshots is a computationally inexpensive process when a flexible force field is available. We have simulated flexible empty frameworks in the NVT ensemble, and recorded 200 snapshots at each temperature of interest from a trajectory of 10 ps in length. We have developed two new methods to calculate diffusivity using a set of rigid snapshots. Both of these methods make the assumption that the presence of adsorbed molecules has a negligible influence on the window size distribution.

2.4.1 Method 1: Direct NVT-MD in a set of rigid structures

2.4.1.1 Description of the method

In our first method, molecular diffusion is simulated using NVT MD at the adsorbate loading of interest in a rigid framework picked at random from the set of

snapshots. After a certain period of time the adsorbate positions are held fixed while the rigid framework is replaced by another randomly chosen framework from the set of pre-recorded snapshots. The MD simulation is then continued with the adsorbates in the new rigid structure. This procedure is repeated at fixed time intervals during the overall MD trajectory. To implement this method, an in-house MD code was used after being modified to perform MD in a continuous manner with a series of rigid framework structures. For each temperature, a set of 200 snapshots from simulations of a flexible framework was used. A new set of structures was generated at every temperature simulated. The adsorbate-zeolite potential energy surface (PES) was recorded on finely spaced grids for each snapshot in the set. Initial adsorbate configurations were obtained from Grand Canonical Monte Carlo (GCMC) simulations in the first rigid snapshot. Apart from using a randomized set of rigid structures during a simulation, MD simulations with this method were performed with the same thermostat, time step etc. as the other rigid structure calculations described earlier.

While switching between rigid structures it is possible that overlap with framework atoms can occur as the positions of adsorbates are kept constant. We detected this situation by checking if the total adsorbate-framework potential became positive. In our tests this occurred in a very small number of framework swaps. The percentage of overlaps that occurred while swapping frameworks are shown in Table A4 for different zeolites. When this situation arose, small canonical MC moves were used to move the adsorbate to a position with a negative framework-adsorbate potential.

The method just outlined inherently assumes that vibrations of the zeolite framework are decoupled from the adsorbate degrees of freedom. If this assumption is a

reasonable approximation, then our approach will give accurate results provided that the swapping frequency chose for the simulations gives a series of structures that approximates the true ensemble of framework configurations sampled by a diffusing adsorbate in a calculation with a fully flexible structure. Below, we discuss the selection of the swapping frequency.

2.4.1.2 The choice of switching frequency

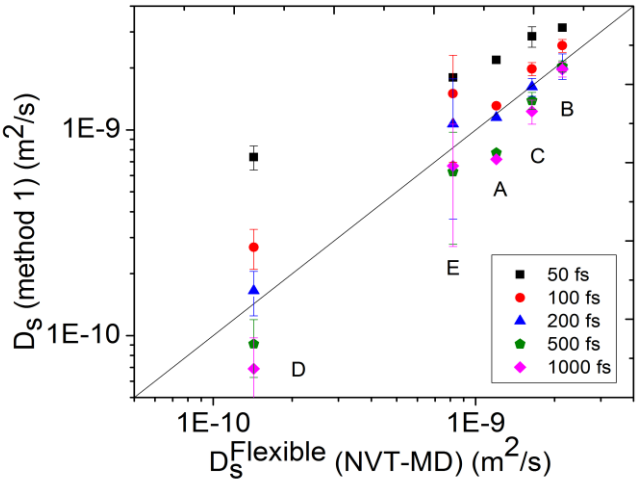

Figure 2.6 Comparison of D_s calculated using different time intervals from 50 fs to 1000 fs. Here, A, B, C, D, and E respectively indicate D_s of (A) CH_4 with 3 molecules/unit cell in LTA; (B) hypothetical CH_4 with 9 molecules/unit cell in LTA; (C) CH_4 with 10 molecules/unit cell in CHA; (D) hypothetical CH_4 with 10 molecules/unit cell in CHA; (E) CH_4 with 0.25 molecules/unit cell in BIK. All of the calculations were performed at 700 K.

The most important parameter in this method is the frequency at which the current snapshot should be replaced by a new structure. To determine this, we applied this method using frequencies of 50, 100, 200, 500, and 1000 fs in all four zeolites keeping

other variables constant. The results of this test are shown in Fig. 2.6, which shows that the diffusivity results with frequency of 200 fs agree with MD results in flexible structure better than other frequencies. An important observation from this figure is that using intervals considerably shorter or longer than 200 fs led to variation in the calculated diffusivities. The longer (shorter) switching frequencies, > 200 fs (< 200 fs) tend to give lower (higher) diffusivities. Nevertheless, we note that the calculated diffusivities are still within the factor of two for calculations performed with twice higher or twice lower frequencies or snapshot changes, thus the method is quite robust (Fig. 2.6).

Before we carry out additional calculations we need to understand why a switching frequency of 200 fs is appropriate. The frequency at which the new structure is selected should be correlated with the underlying flexibility of the framework. This means that the required frequency should be related to the characteristic vibrational frequency of the 8MR oxygen atoms corresponding to d_{min}. To quantify this, we obtained the vibrational density of states (VDOS) for one of the oxygen atoms in a single 8MR window corresponding to d_{min} via the velocity autocorrelation function (VACF) using

$$VACF(t) = \frac{v(0) \bullet v(t)}{v(0) \bullet v(0)} \qquad (2.5)$$

$$F(\omega) = \frac{1}{\sqrt{2\pi}} \int_{-\infty}^{\infty} VACF(t) e^{i\omega t} dt \qquad (2.6)$$

where v(t) is the velocity of the 8MR oxygen atom corresponding to d_{min} at time t and F(ω) is the VDOS at frequency ω. The VDOS obtained for LTA as well as CHA are shown in Fig. 2.7. The VDOS for BIK and ERI are also given in Fig. A2. The results for LTA and CHA show a peak highlighted by a red line at a frequency of ~150 cm^{-1} which

corresponds to 222 fs (~200 fs). The results for ERI and BIK also show the peak at around 150 cm^{-1}.

To understand the vibrational modes associated with this frequency we analyzed individual components of the VACF ($v_{xx}(t)$, $v_{yy}(t)$, $v_{zz}(t)$), and the corresponding components of the VDOS ($F_{xx}(\omega)$, $F_{yy}(\omega)$, $F_{zz}(\omega)$). LTA is the easiest example for this analysis because the 8MR windows lie in the coordinate planes of the unit cell (Fig. A3). The analysis shows that the frequencies around ~150 $cm^{-1}$are dominant in the projection of the VDOS on the axis corresponding to the "breathing" direction of the 8MR window, as well as out-of 8MR plane projection. On the other hand, the dominant frequencies in the projection perpendicular to the 8MR breathing direction are ~1000-1100 cm^{-1}, which corresponds to Si-O stretching.[64] Thus, we can justify that the frequency of ~150 cm^{-1} corresponds to the "breathing" motion of the 8MR window. It is thus not surprising from the point of view of diffusion that this frequency provides the most relevant flexibility mode.[65] In previous simulations of framework flexibility in zeolites performed with a different force field[45] the frequency of ~200 cm^{-1} was also associated with the breathing motion of the zeolite pores.

Another way to analyze framework flexibility is to perform the normal-mode analysis of vibrations within the harmonic approximation of the solid, in which case different vibrational modes can be unambiguously identified.[64] Normal-mode analysis of zeolite vibrations coupled with a Monte Carlo algorithm has been used to calculate free energy surface along the diffusion path for benzene in MFI.[66] Our results indicate that, at least for methane in 8MR zeolites, the low-frequency breathing motion of the windows is the most relevant vibrational mode that affects diffusion. It should be noted that our

method does not make assumption about the harmonicity of solid vibrations, and thus should in principle be applicable to a range of cage-window materials as long as the characteristic breathing mode of the window is identified.

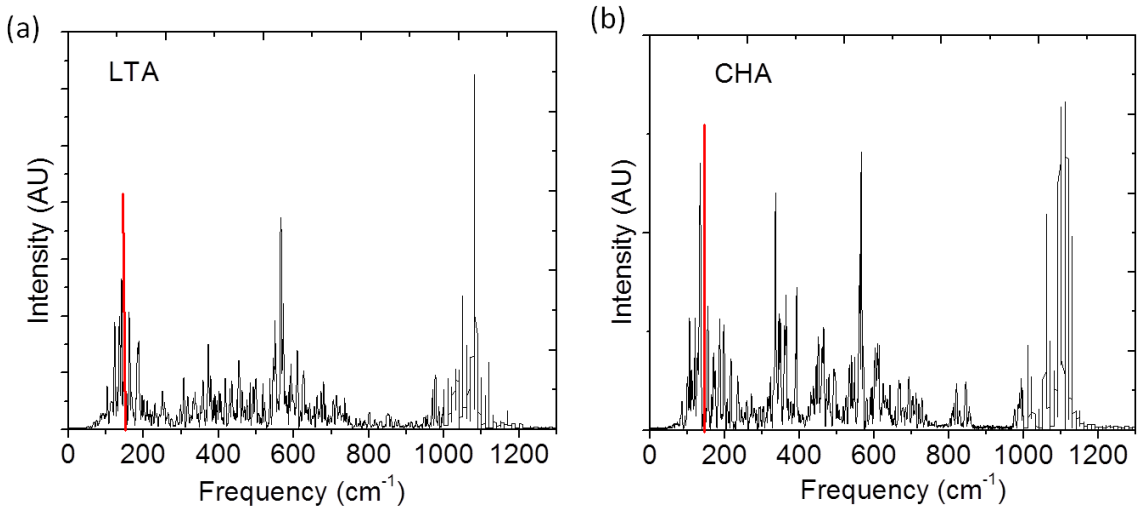

Figure 2.7 Vibrational density of states (VDOS) for one of the 8MR oxygen atoms from a single window belonging to d_{min} in (a) LTA and (b) CHA. The red line indicates the frequency of 150 cm^{-1}.

2.4.1.3 Examples

This method was applied to calculate D_s of CH_4 ($\sigma_{CH_4-O} = 3.47$ Å)in four zeolites with the following temperature ranges and loadings: 300-900 K and 9 molecules/unit cell for LTA, 300-900 K and 10 molecules/unit cell for CHA, 500-1100 K and 0.25 molecules/unit cell for BIK, and 1100-2100 K and 1.5 molecules/unit cell for ERI. Similar calculations were performed for hypothetical ($\sigma_{CH_4-O} = 3.7$ Å) CH_4 molecules at the same loadings as above zeolites at 500-900 K for LTA and CHA and 700-1100 K for BIK. Additional information is given in Table A5. In Fig. 2.8 (a), this method is compared to MD in the fully flexible structures. Diffusivities obtained in

different zeolites at different temperatures using method 1 are in excellent agreement with D_s in the fully flexible structure, demonstrating that this method can accurately predict diffusion in these materials.

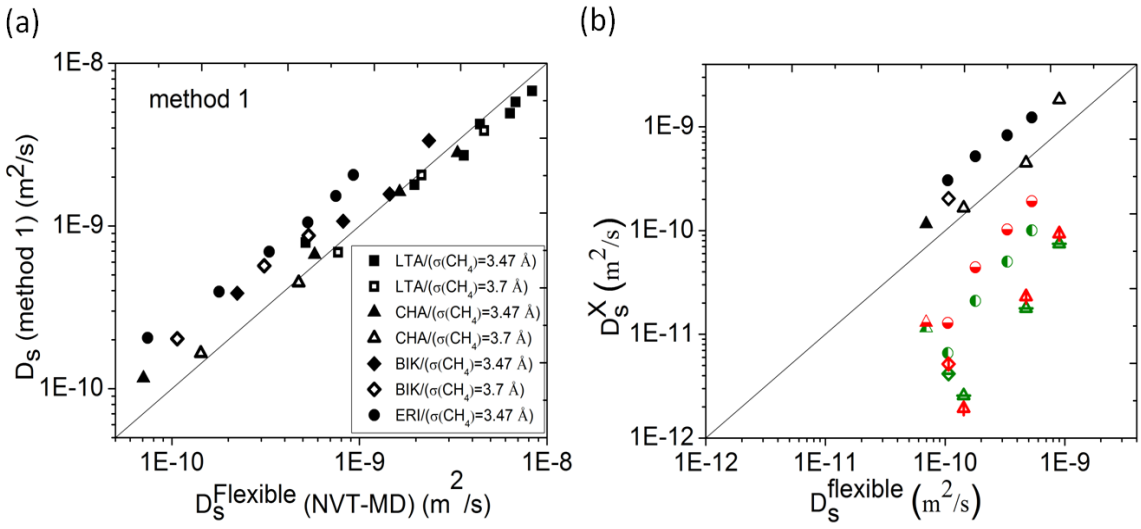

Figure 2.8 (a) Comparison of diffusivities obtained by Method 1 (vertical axis) with that obtained in the flexible structure (horizontal axis) for CH_4 (filled symbols) and hypothetical CH_4 (empty symbols). (b) Accuracy in predicting D_s of CH_4 (filled and half-filled symbols) and hypothetical CH_4 (empty symbols with and without line) in the flexible structure (horizontal axis) in CHA (triangle), BIK (diamonds), and ERI (circle) by different approximate methods X; where X is Method 1(● /▲ /△ /◇),time averaged(◒ / ◭ /◮ /◈),or energy minimized (◐/ ◭/ ◭/◈). Diagonal line indicates the equality of values on vertical axis with values on horizontal axis.

Specific examples at certain conditions (given in Table A5) were taken from Fig. 2.8 (a) where framework flexibility is important and hence the rigid energy minimized and time averaged structures cannot predict D_s correctly. These examples are shown in Fig. 2.8 (b), which compares D_s values predicted by Method 1 and by rigid structure

approximations with D_s in the fully flexible structure. Diffusivities obtained using Method 1 are in good agreement with corresponding diffusivities in the flexible structures while diffusivities in the energy minimized and time averaged structures show significant deviation from diffusivities in the flexible structures of CHA, BIK, and ERI. Although the predictions using this method for BIK and ERI are not perfect, they are better than the predictions using single rigid structure approximations. We stress that Method 1 can be applied to calculate diffusivity at any loading, not just at infinite dilution.

2.4.2 Method 2: Transition state theory in the infinite dilution limit

In the second method, we compute cage to cage hopping rates in each rigid snapshot using TST. We use an approach to TST for these systems that efficiently identifies the dividing surfaces between cages and does not rely on assumptions about the pre-factors for each hopping rate. Once these hopping rates have been found for each snapshot, an average of the resulting self-diffusivities gives the net self-diffusivity.

As an initial example, we consider the infinite dilution limit in all of these zeolites. The theory was explained in detail by June *et al*.[28] for infinitely dilute spherical sorbate molecules. Methods to extend TST to finite loadings exist,[36, 67-73] but we have not applied them here. In this method, the hopping rate, k^{TST}, through a window in the rigid snapshot was calculated using

$$k^{TST} = (2\pi\beta m)^{-1/2} \frac{\int_{S_i} \exp(-\beta u^p) dr^2}{\int_{V_j} \exp(-\beta u^q) dr^3} \qquad (2.7)$$

where, S_i and V_j are the area of dividing surface *i*, and the volume of cage *j* adjacent to the dividing surface *i*, u^p and u^q are the adsorbate-framework potential energy at grid points on the dividing surface and in the cage, and m, $\beta=1/k_bT$, and k_b are the adsorbate

mass, dimensionless inverse temperature, and Boltzmann constant, respectively. The hopping rate through each window in every individual framework in the set of structures was calculated. The average hopping rate, k_{avg}^{TST}, was obtained by taking the arithmetic mean of all these individual hopping rates. The self-diffusivity was then calculated using,

$$D_s = \frac{k_{avg}^{TST} \lambda^2}{2n} \qquad (2.8)$$

Here, λ is distance between centers of two adjacent cages and n is dimensionality of the pore network. This formulation makes no assumptions about adsorbate vibrations in the cage or on the dividing surface being harmonic. Below, we describe the algorithm used to compute the hopping rate for each transition state in each framework in the set of structures. This algorithm requires that the dividing surfaces and the location and size of the cages can be found in an efficient, automated way. It is also important that any inaccessible pockets where adsorbates cannot diffuse because of very small pore openings can be identified.

2.4.2.1 Description of the TST method

First, the simulation box was divided into discrete grid points spaced equally along each coordinate axis. The adsorbate-zeolite potential energy surface was recorded on a grid with ~0.1 Å spacing. Cages and inaccessible regions were identified using an in-house code. In this code, for every grid point, the distance from the nearest framework atom was calculated. The maximum among these distances and corresponding grid point give the radius and the center of the largest cage. Remaining cages and inaccessible regions were obtained by continuing the same process after excluding all the points present in the cavities already obtained. In the next step, all of the dividing surfaces present in a framework were obtained by analyzing the locations of the grid points in the

framework. In this step, the grid points present in the cages and inaccessible regions as well as the grid points which are very close to framework atoms were discarded to improve the efficiency of the method. For each of the remaining grid points, the cage where it belongs was obtained by moving in the direction of lower energy neighbor by neighbor as the grid points in the cages have lower energy. This process was continued until all the grid points were labeled by their respective cage numbers. The grid points with one of their neighbors labeled as a different cage number constitute the dividing surfaces. Once all the dividing surfaces and cages were obtained then the integrals in equation (7) were calculated numerically.

2.4.2.2 Results of the TST method

In order to validate this method, diffusivities were calculated first in individual rigid structures. Specifically, the energy minimized and time averaged structures were treated with TST and the results were compared to diffusivities from NVT-MD simulations. This approach was applied for CH_4 at 300-1000 K for LTA, 300-1000 K for CHA, and 1100-2100 K for ERI. For NVT-MD simulations, a low loading of 1 molecule/unit cell in LTA and CHA and 1.5 molecules/unit cell in ERI were used. These loadings are close to the infinite dilution limit. Additional information is given in Table A5. These MD simulations were performed with the same thermostat, time step, simulation box etc. as calculations described earlier. The results obtained are shown in Fig. 2.9 (a), which shows excellent agreement between the TST and MD results.

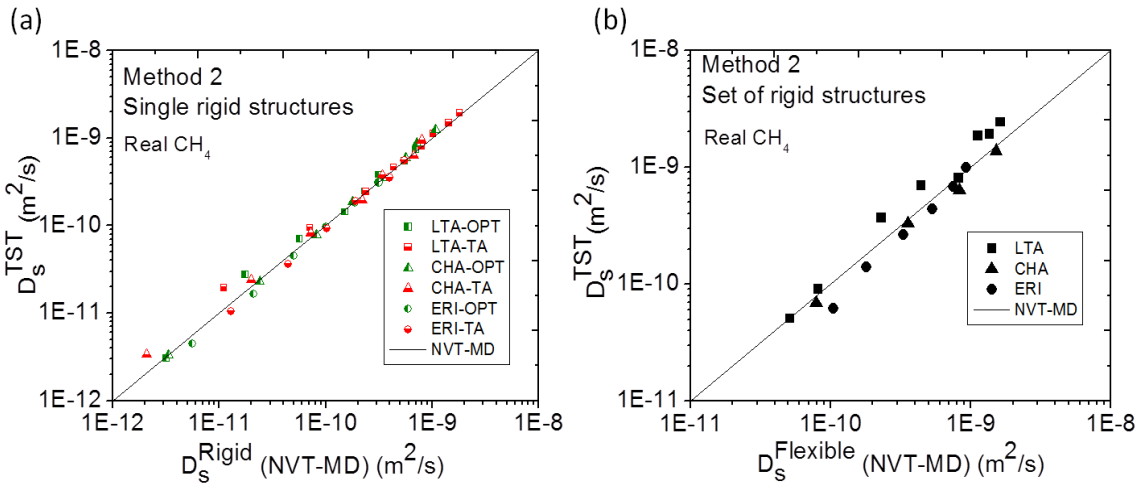

Figure 2.9 Comparison of diffusivities for CH_4 in LTA (square), CHA (triangle), and ERI (circle) obtained by Method 2 (vertical axis) with that obtained by NVT-MD (horizontal axis) (a) in energy minimized (green) and time averaged (red) for CH_4 and (b) in flexible structure.

Our TST method was then applied to the set of snapshots at different temperatures to calculate D_s for CH_4 in LTA, ERI, and CHA. The data in Fig. 2.9 (b) compares the results from TST to the MD results for the fully flexible structures. The TST results are in good agreement with the MD data, showing that TST can accurately predict diffusion in these materials. To compare this method with structures approximated by the energy minimized and time averaged rigid structures, specific examples were taken from Fig. 2.9 (b) (given in Table A5). This comparison is shown in Fig. 2.10, where agreement between Method 2 and MD in the fully flexible structure is unambiguous, while the results of calculations for single rigid structures show a large discrepancy from the results for the fully flexible structures.

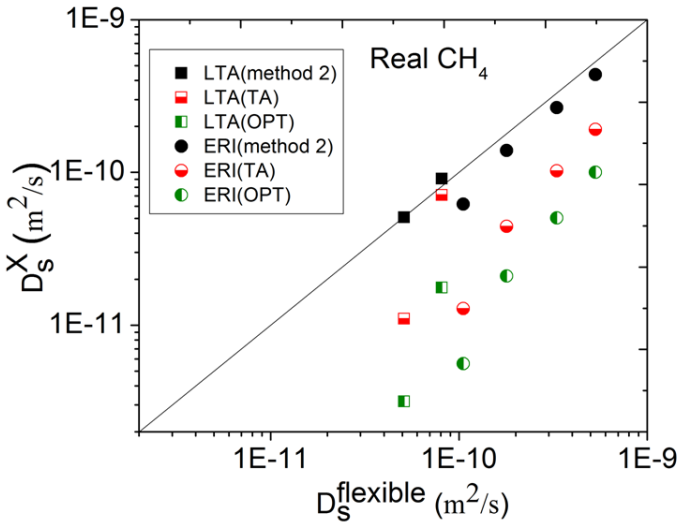

Figure 2.10 Accuracy in predicting D_s of CH_4 in flexible structure (horizontal axis) by different approximate methods X; where X is Method 2 (black), time averaged rigid structure (red), and energy minimized rigid structure (green).

With the TST based method, D_s at low temperatures can be obtained for which NVT-MD simulation cannot be used. This is one of the biggest advantages of this method. This method was applied to the energy minimized, time averaged, and the set of snapshots approximating fully flexible structure to obtain D_s of CH_4 in LTA and ERI and hypothetical CH_4 in CHA in the temperature range 50-300 K, 700-1000 K, and 200-300 K, respectively. The results are shown in Fig. 2.11. Here, diffusivities obtained in the energy minimized and time averaged structures are drastically lower compared to diffusivities obtained in the flexible structure. In LTA, for example, at 100 K $\frac{D_S^{Flexible}}{D_S^{OPT}} \approx 341$ while $\frac{D_S^{Flexible}}{D_S^{TA}} \approx 19$, indicating large effects of framework flexibility. This deviation increases as temperature decreases.

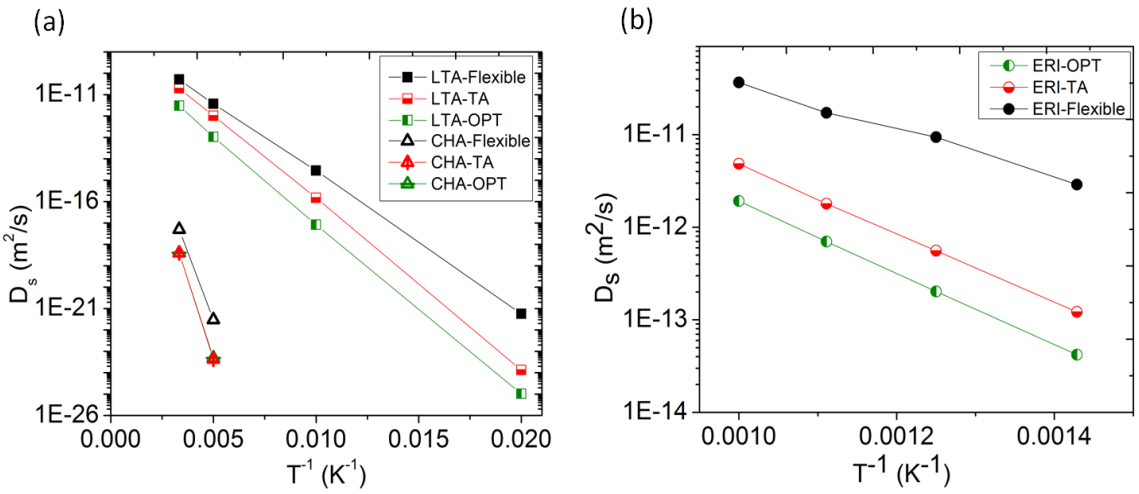

Figure 2.11 Low temperature D_s in the flexible (black), time averaged (red), and energy minimized (green) structure calculated using Method 2.

2.4.3 Computational costs of new methods

Finally, it is important to discuss the computational cost associated with the two methods introduced above. Typical comparisons are shown in Table 2.3 based on simulations in the LTA structure. Results are normalized with respect to computational cost of a single rigid structure at low and high loadings. The main factor that affects the computational cost is the adsorbate loading. At low loadings, these modified methods take time, somewhat longer than the single rigid structure methods although they are still much faster than the calculations utilizing the fully flexible structure. As the loading increases, the ratio $t^{\text{Method-1}}/t^{\text{Energy-minimized}}$ reduces considerably (Table 2.3) as the total time required for Method 1 remains almost constant, while the time taken for the energy minimized calculation increases linearly. This is because the dominant cost of Method 1 is the reading of pre-tabulated PES for all the snapshots, which is independent of the loading. For example, in LTA, this ratio decreases from 80 at low loading to ~5 at the higher loadings showing that Method 1 scales better than the conventional single

structure methods. Table 2.3 also shows that the relative time taken for method 2 calculations (1.3) is comparable to single rigid structure methods, as the TST calculations of the various snapshot can be carried out in parallel.

Table 2.3 Approximate computational costs associated with different methods normalized to the computational cost of MD in rigid structure to calculate D_s of CH_4.

Zeolites	**OPT** [a]	**TA** [a]	**Method 1** [§,a]	**Method 2** [†,b]	**Flexible** [c]
LTA (low loading, 1 molecules/unit cell)	1	1	80	1.3	7200
LTA (high loading, 9 molecules/unit cell)	1	1	5	-	600

[§] Method 1 is the method involving direct NVT-MD in the set of snapshots. [†] Method 2 is the transition state theory method applied to the set of snapshots, [a]Calculations using in-house MD code, [b]Calculations using in-house TST code, [c]Calculations using LAMMPS.

2.5 Conclusions

In this chapter, we have elucidated the role of the framework flexibility on diffusion of the small molecules (CH_4) in four representative 8MR zeolites with the cage-window type structures. While it is not surprising that the framework flexibility can play a crucial role when the size of the diffusing molecule approaches the size of the window, it is less clear how these effects can be captured accurately in the approximate methods without performing direct MD simulations with a fully flexible structure. We have shown that the magnitude of the framework flexibility effect is influenced by the number of distinct directions associated with the minimum window dimension in a fluctuating

structure, and harmonicity of the vibrations of the atoms forming 8MR windows. This is why a simple recipe of replacing the rigid structure with the time-averaged structure does not always work.

To account for the framework flexibility efficiently and reliably, we have introduced two new methods based on approximation of the flexible framework by the set of rigid snapshots obtained from the dynamics simulation of the empty framework. The first method is a modification of the MD in rigid frameworks where we periodically replace the rigid structure with a new one taken randomly from the pre-recorded set of snapshots while keeping positions of adsorbate molecules constant. The optimal frequency at which these swaps should be made corresponds to the characteristic vibrational frequency of oxygen atoms in the windows, or "breathing" frequency of the window, which can be determined from the analysis of the vibrational modes of the structure. The method is fairly robust with respect to the sensitivity to the exact switching frequency. The method is orders of magnitude more efficient than the simulations with the fully flexible structure. Another important advantage is that it can be used to calculate diffusivities at arbitrary loadings.

In the second method, we directly compute cage to cage hopping rates in each rigid snapshot using TST and average over a distribution of snapshots. The second method (as implemented) is applicable at infinite dilution but has an advantage that like other TST based methods it can predict diffusivities at low temperatures for slowly diffusing molecules where MD methods are not applicable. Excellent agreement has been obtained between diffusivities predicted with these two new methods and direct MD simulations using fully flexible structures.

Though these methods have been described for the 8MR zeolites, they can be applied to similar nanoporous materials such as Metal Organic Frameworks (MOF), glassy polymers etc. One limitation of the classical simulations in MOFs is that the computed diffusivities depend strongly on the intramolecular force field employed during the MD simulations. [74] This requires development and parameterization of new force fields for each new MOF to be studied. In such circumstances, one can use methods 1 or 2 that are efficient, reliable, and depend only on intermolecular interactions. If a reliable force field is unavailable, the set of snapshots can be generated using short *ab-initio* MD trajectories[52] and then methods 1 or 2 can be used to measure diffusivities at a given temperature and loading.

CHAPTER 3

Applying New Efficient Methods to Other Spherical Adsorbates in 8MR Zeolites: Extension to Binary Mixtures

In this chapter, we use the changing snapshot method and TST/snapshot method, as described in the previous chapter, to characterize the effects of zeolite framework flexibility on diffusion of spherical molecules in 8MR zeolites. These methods are applied to noble gases (Ne, Ar, Kr, Xe, Rn), and CF_4. We demonstrate the effect of the zeolite framework flexibility on diffusion by considering the size and loading of adsorbates and temperature. We studied in detail how the framework flexibility affects the loading dependence of diffusion. By looking at the computational costs, we demonstrated that both the methods are orders of magnitude more efficient than the fully flexible simulations. We then apply the changing snapshot method to binary mixtures of adsorbates to obtain accurate binary diffusivities and binary selectivities.

3.1 Introduction

Noble gases (He, Ne, Ar, Kr, Xe, and Rn) have applications in various fields. Noble gases have been used in many areas including radiotherapy, lighting, lasers[75], medicine[76], and as a inert carriers in flow systems. Ne, Ar, Kr, and Xe are typically obtained from air using cryogenic fractional distillation while He is obtained from the natural gas fields which are rich in He and separated by cryogenic gas separation techniques. These processes make the prices of noble gases high. Alternatives to cryogenic distillation may be useful to reduce the prices for these gases. One potential

alternative is adsorptive and/or diffusive separation using nanoporous materials like zeolites, metal-organic frameworks (MOFs), and activated charcoal.

There are a limited number of studies about separation and purification of noble gases using nanoporous materials. Most of the examples of experimental studies include zeolites[77-85] and MOFs[86]. Computational studies of adsorption and diffusion of inert gases in zeolites include work by Skoulidas et al.[87]; Krishna et al.[88], and Kopelevich et al[89] while in MOFs previous studies include work by Van Heest et al.[90], Demir et al.[91] and several other computational studies[92-94].

In adsorption based separations of inert gases, one adsorbate is selectively adsorbed over other components of the mixture. In such separations, the kinetic effects are negligible but quantifying diffusion in such materials is important to see if the adsorption sites are readily accessible. In addition to adsorptive separations, separations can also be diffusion-controlled.[95-97] One example of this kind is membrane separation using nanoporous materials.[98-102] In membranes, high selectivity values are a combination of diffusion selectivity (with one adsorbate diffusing through the material more quickly than another) and adsorption selectivity (with one species adsorbing more strongly than another). High diffusion selectivity, and hence high membrane performance, is most likely to be observed in materials where one of the adsorbed molecules is tightly confined. In these situations, the framework flexibility of the nanoporous materials can have a profound influence on molecular diffusion rates.[21, 24, 103] It is therefore helpful to have methods that can efficiently predict the diffusion of tight fitting molecules in materials like zeolites while accounting for framework flexibility. For this, we have

proposed two new efficient computational methods as described in previous chapter to deal with framework flexibility.

The aim of this chapter is to first show the accuracy of our two newly developed methods to deal with framework flexibility in 8MR zeolites. We then extend our methods to diffusion of adsorbed mixtures. Our results are illustrated by examining a range of spherical molecules in a variety of 8MR zeolites with different topologies. In section 3.2, we discuss the zeolite structures, force fields and simulation methods used in our calculations. Section 3.3 shows in detail the accuracy of newly developed methods for flexible frameworks as well as the effect of framework flexibility on diffusion of noble gases and CF_4 in selected 8MR zeolites.

3.2 Models and Simulation details

3.2.1 Adsorbates and zeolites

In previous chapter, we looked at the effect of the framework flexibility in pure silica 8MR zeolites on diffusion of spherical molecules like CH_4. In this chapter, we consider the diffusion of 6 additional spherical molecules, Ne, Ar, Kr, Xe, Rn, and CF_4, in pure silica 8MR zeolites.

There are 63 8MR zeolites in the International Zeolite Association (IZA) database[10] that have no significant distortions or terminal silanol groups and hence can be optimized using standard force fields (FF) for zeolite frameworks such as the Hill-Sauer FF[47-48]. A complete list of the 8MR zeolites is given in Appendix B in Table B2. We divided the list of 8MR zeolites into four categories based on two properties that are important to characterize the effect of framework flexibility[103]: a) the harmonicity of the vibrations associated with the atoms in the windows, and b) the number of distinct

directions that can be associated with the minimum window dimension in a flexible structure. Details about harmonicity (anharmonicity) as well as single (multiple) d_{min} and their connection with gas diffusion in zeolites are given in the previous chapter.

From the 63 known 8MR structures, 8 were chosen for study: CHA, ERI, LTA, BIK, SAS, RHO, DFT, and EAB. They were selected to give two examples each of the four possible behaviors seen when considering the abovementioned two properties, as shown in Table 3.1. Using multiple examples for each category helps to show that the results obtained in our previous study regarding the effect of these different 8MR window properties on diffusion are transferrable to other materials.

Table 3.1 8MR zeolites chosen for the study with their respective categories. The dimensionality of the pore structure is shown in the parentheses.

Multiple window dimensions		**Single window dimensions**	
Harmonic	**Anharmonic**	**Harmonic**	**Anharmonic**
CHA (3)	LTA (3)	BIK (1)	ERI (3)
SAS (1)	RHO (3)	DFT (3)	EAB (2)

Below, energy minimized structures are also denoted as optimized structures or OPT. The lattice parameters obtained in this way using the Hill-Sauer FF are listed in Table 3.2. All simulations were performed with the lattice constants obtained from these energy minimized structures. These lattice constants and the 8MR window dimensions are slightly different than the lattice constants listed in the IZA database.

Table 3.2 Lattice parameters for a single unit cell of the energy-minimized zeolite structures. Numbers in brackets in the first column indicate number of unit cells along each cell vector used in the simulation. Unit cell parameters taken from the IZA database are also shown in parentheses.

Zeolites	a (Å)	b (Å)	c (Å)	α (°)	β (°)	γ (°)
LTA (2×2×2)	12.1190 (11.9190)	12.1190 (11.9190)	12.1190 (11.9190)	90 (90)	90 (90)	90 (90)
BIK (4×2×5)	7.5950 (7.5400)	16.3405 (16.2222)	5.2944 (5.2560)	90 (90)	90 (90)	90 (90)
CHA(2×2×2)	13.7875 (13.6750)	13.7595 (13.6750)	14.8885 (14.7670)	90 (90)	90 (90)	120 (120)
ERI (2×2×2)	13.1900 (13.0540)	13.1560 (13.0540)	15.3330 (15.1750)	90 (90)	90 (90)	119.74 (120)
DFT (4×4×3)	7.1610 (7.0750)	7.1610 (7.0750)	9.1327 (9.023)	90 (90)	90 (90)	90 (90)
EAB (2×2×2)	13.3164 (13.178)	13.2900 (13.178)	15.1626 (15.005)	90 (90)	90 (90)	119.74 (120)
SAS (2×2×3)	14.3566 (14.349)	14.3566 (14.349)	10.4035 (10.398)	90 (90)	90 (90)	90 (90)
RHO (2×2×2)	15.11418 (14.919)	15.11418 (14.919)	15.11418 (14.919)	90 (90)	90 (90)	90 (90)

One of the methods we describe below uses time averaged structures for each zeolite. To get the time averaged structures, we performed MD simulation of empty frameworks using the Hill-Sauer FF in the canonical ensemble (constant NVT) at each temperature. Starting with the energy minimized structures, framework atom positions were averaged over their position recorded every 1 fs from a trajectory 10 ps in length. Test calculations indicated this approach gave well converged results. We ignore the

temperature dependence of the unit cell while examining diffusion at different temperatures. Such considerations, while potentially relevant in high resolution calculations, are outside of the scope of the present work.

3.2.2 Force fields

As in our previous chapter of CH_4 diffusion in flexible zeolites, we used the Hill-Sauer FF to describe the flexibility of all-silica zeolites.[47-48]

Table 3.3 LJ potential parameters and their references for adsorbate-adsorbate. A, Z indicates adsorbate and framework oxygen respectively.

Adsorbate	mass	ε_{AA} (K)	σ_{AA}(Å)	ε_{AZ} (K)	σ_{AZ}(Å)	Ref.
Ne	20.18	35.7	2.789	54.59	3.004	13
Ar	39.95	120	3.405	100.08	3.312	39
Kr	83.80	170	3.690	119.12	3.450	
Xe	131.30	211	4.100	132.71	3.660	
CF_4	88.00	134	4.660	105.76	3.940	40
Rn	222.00	300	4.170	158.24	3.690	41

We considered adsorption and diffusion of Ne, Ar, Kr, Xe, Rn, and CF_4. These adsorbate molecules are modeled as neutral spherical united atoms (UA). Adsorbate-adsorbate interactions were defined using Lennard-Jones (LJ) potentials from the literature as given in Table 3.3. The LJ potential parameters for framework oxygen-oxygen were extracted from CH_4-CH_4 and CH_4-framework oxygen interactions given by Dubbeldam et al.[55] assuming the Lorentz-Berthelot mixing rule. This assumption may or may not provide the accurate parameters, but the accuracy of the force field is not a

central concern of our work. It is useful to note that the parameters obtained using this way are very close to the standard CLAYFF oxygen-oxygen parameters.[104] The Lorentz-Berthelot mixing rule was applied to get adsorbate-framework oxygen interactions (see Table 3.3). Adsorbate LJ potentials were cut and shifted using a cutoff radius of 12 Å.

3.2.3 Simulation details

We performed five different types of calculations. First, we performed diffusivity calculations in fully flexible structures of zeolites using standard MD. Secondly, we obtained self-diffusivities using two efficient approximate methods, namely the changing snapshot method and the TST/snapshot method. We also performed MD simulations in the two types of rigid structures mentioned above, OPT and TA. Details about these simulations are given below.

a. Diffusion in flexible, OPT, and TA structures using MD

For Molecular Dynamics (MD) calculations in flexible zeolites, LAMMPS[56] was used. For calculations using rigid zeolites, an in-house MD code was used. This code is computationally efficient as it uses a grid interpolation technique for the potential energy surface of zeolite. This approach takes a far less computational effort than simulations that calculate the potential energy at each time step.[57] We verified that the two codes give equivalent results for calculations for rigid structures. Time steps of 0.1 fs and 1 fs were used in simulations of flexible and rigid structures, respectively. The shorter time step required to treat flexible frameworks is one of the reasons why simulations of rigid structures have a large advantage in computational speed. Simulations in the NVT ensemble were performed using a Nosé-Hoover thermostat and the velocity Verlet integrator. Initial adsorbate configurations were obtained from Grand Canonical Monte

Carlo (GCMC) simulations for the rigid structures using an in-house GCMC code. For flexible structures, initial adsorbate configurations from GCMC using the time averaged structure were used. For each simulation, a simulation box was chosen to ensure that the minimum length in each of the direction was larger than 24 Å (twice the cutoff radius of the LJ potentials). The mean square displacements (MSD) of adsorbate molecules were recorded every 0.1 ps. This data was then used to calculate self-diffusivity D_s, of adsorbate molecules using Einstein's relation,

$$D_s = \frac{1}{6}\lim_{t\to\infty}\frac{d}{dt}\left\langle |r(t)-r(0)|^2 \right\rangle \tag{3.1}$$

where, r(t) denotes the positions of the adsorbates at time t. The total length of the simulations and hence the computational time were varied with conditions in simulations like temperature, type of zeolites, and loading. Simulations times were 1-50 ns to achieve reliable D_s in MD calculations. For simulations at low temperatures we made sure that the minimum MSD achieved is at least the square of distance between two adjacent cages, or adjacent unit cells in the case of 1-dimensional zeolites like BIK or SAS.

b. Computing diffusion using the changing snapshot method and TST/snapshot method

We introduced two new methods in the previous chapter in which the flexible structure of zeolite can be approximated as a set of discrete rigid structures. These discrete rigid structures, or snapshots, can be generated from a classical MD simulation of the empty framework. The process of recording snapshots is a computationally inexpensive process when a flexible force field is available. We have simulated flexible empty frameworks of zeolite in the NVT ensemble, and recorded 200 snapshots at each

temperature of interest from a trajectory of 10 ps in length. It is also possible to collect data of this kind from *ab initio* MD simulations.[52-53] Both of these methods make the assumption that the presence of adsorbed molecules has a negligible influence on the window size distribution.

In first method, known as the changing snapshot method, molecular diffusion is simulated using NVT MD at the adsorbate loading of interest in a rigid framework picked at random from the set of snapshots. After 200 fs, the rigid framework is replaced by another randomly chosen framework from the set of pre-recorded snapshots while adsorbate positions are held fixed. The MD simulation is then continued with the adsorbates in the new rigid structure. This procedure is repeated at fixed time intervals during the overall MD trajectory. More details about this method as given in chapter 2.

We have shown in chapter 2 the reason and the robustness of using 200 fs as swapping frequency in the case of four 8MR zeolites, namely LTA, CHA, BIK, and ERI. Analysis of the vibrational modes of these zeolites showed that this frequency corresponds to the characteristic vibrational frequency of 8MR oxygen atoms in the plane of 8MR windows. This vibrational mode plays an important role in the diffusion of molecules from one cage to another through 8MR windows. We assumed that this frequency is applicable for all 8MR zeolites irrespective of their topology. As a result, in this work, we used a swapping frequency of 200 fs for all the 8MR zeolites.

In our prior use of the changing snapshot method, we used 200 grid files containing information about potential energy surfaces from 200 snapshots. Every time a snapshot was swapped, the MD code for the changing snapshot method read the new grid

file which took some time and hence increased computational cost. Since we only used 200 snapshots in this method, the code reads each grid file many times during a single simulation which was computationally inefficient. In this study, we modified our previous code to store all 200 grid files in memory during entire simulation, which reduced the time required to read each grid files many times. This enables us to use this method with computational cost almost equal to that of a MD simulation in a rigid structure.

In the second method, known as the TST/snapshot method, we compute cage to cage hopping rates in each rigid snapshot using TST. We use an approach to TST for these systems that efficiently identifies the dividing surfaces between cages and does not rely on assumptions about the pre-factors for each hopping rate. Once these hopping rates have been found for each snapshot, an average of the resulting self-diffusivities gives the net self-diffusivity. More details about this method are given in chapter 2. This method (as implemented) is applicable at infinite dilution but has an advantage that like other TST based methods it can predict diffusivities at low temperatures for slowly diffusing molecules where MD methods are not applicable.

3.3 Results and discussion

3.3.1 Accuracy of changing snapshot method (CSM) and TST/snapshot method

We showed that the changing snapshot method (CSM) and TST/snapshot method perform well for several spherical adsorbates in chapter 2. Excellent agreement was obtained between diffusivities predicted with these two methods and direct MD simulations using fully flexible structures. Before we proceed to use these two methods in variety of 8MR zeolites, we again want to show the accuracy of the methods. This can be

done by comparing diffusivities obtained using these two methods to that obtained from MD in the fully flexible structure.

Simulations in the fully flexible structures are time consuming. As a result, we decided to compare a limited number of adsorbate-zeolite pairs at a single temperature. We used low loadings for the changing snapshot method and the fully flexible method, while the TST/snapshot method, as defined earlier, is for the infinite dilution limit. Combinations of adsorbate-zeolite and temperatures for these simulations were chosen so that the window sizes of zeolites are comparable to or smaller than adsorbate size. There are no 8MR zeolites with window sizes comparable to or smaller than size of Ne; hence for Ne we used ERI, DFT, and EAB, which have smallest window sizes in available pool. We also chose temperatures for each example so the diffusivities are high enough to be obtained from MD simulations in reasonable computational time.

The list of zeolite-adsorbate-temperature combinations is given in Fig. 3.1. The system indices are arranged such that diffusivities go from low to high (as determined from MD with the fully flexible structure). Many of the temperatures used in Fig. 3.1 are unphysically high in order to make diffusion observable with straightforward MD. Despite these high temperatures, the window size distribution of the flexible structure during the simulation did not indicate any sort of collapse or damage of the zeolite framework. From Fig. 3.1, we can conclude that our two methods give self-diffusivities in a good agreement with that in the fully flexible structure.

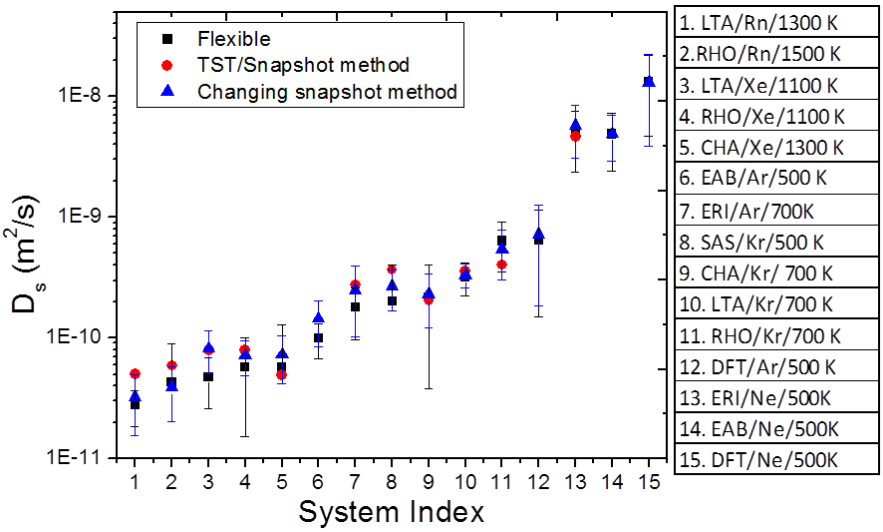

Figure 3.1 Comparison of D_s of different spherical adsorbates obtained from TST/snapshot method and changing snapshot method with fully flexible method in various 8MR zeolites. The loadings used in the changing snapshot method and in the fully flexible method are very small (1 molecule/unit cell) and hence close to infinite dilution (see Table 3.5 for saturation loading). The TST/snapshot method is applicable at infinite dilution limit. Numerical values of diffusivities are given in Table B3.

From Table 3.4, we can see that the normalized computational cost for the changing snapshot method is small compared to that for the fully flexible simulation and is comparable to the rigid structure simulations. The computational cost of the TST/snapshot method remains the same at all the temperatures while for methods based on MD, it increases as temperature decreases because of the need for longer adsorbate trajectories. This indicates that the CSM and TST/snapshot method can be used as an accurate and computationally efficient alternatives to the fully flexible simulations for all the spherical adsorbates under consideration.

Table 3.4 Approximate average computational costs for CSM and the fully flexible simulations per unit length of the MD trajectory normalized by the computational cost of MD in a rigid structure. The computational costs at high loadings are given in parenthesis. The variation in computational costs for the same zeolite is due to the variation in the machine efficiency.

System	CSM [a]	Flexible [b]	System	CSM [a]	Flexible [b]
1. LTA/Rn/1300 K	3 (2)	53000	9. CHA/Kr/ 700 K	3 (2)	64000
2.RHO/Rn/1500 K	3 (2)	108000	10. LTA/Kr/700 K	4 (2)	55000
3. LTA/Xe/1100 K	3 (1)	54000	11. RHO/Kr/700 K	3 (1)	113000
4. RHO/Xe/1100 K	6 (1)	110000	12. DFT/Ar/500 K	6 (1)	102000
5. CHA/Xe/1300 K	4 (1)	93000	13. ERI/Ne/500K	5 (1)	85000
6. EAB/Ar/500 K	3 (1)	75000	14. EAB/Ne/500K	5 (1)	65000
7. ERI/Ar/700K	4 (1)	80000	15. DFT/Ne/500K	6 (3)	83000
8. SAS/Kr/500 K	2 (1)	127000			

[a]Calculations using in-house MD code, [b]Calculations using LAMMPS.

3.3.2 The changing snapshot method (CSM)

Above, we showed how the changing snapshot method and TST/snapshot method can be used in place of time consuming fully flexible simulations for a large set of spherical molecules in variety of zeolites. In this section, we apply the CSM to study the effect of framework flexibility on a large set of spherical molecules including inert gases in 8MR zeolites. The main aim of this task is to demonstrate that the CSM can be applied to a large number of materials in reasonable computational time with high accuracy. To assess the effect of framework flexibility on single component D_s, we performed calculations as functions of temperature, adsorbate size, and adsorbate loading.

Table 3.5 Saturation loading (Sat.), mid loading, and high loading used in molecules/unit cell. In our simulations, the number of adsorbate molecules used was rounded to nearest integer.

Adsorbate/ Zeolite	Loading (mmol/g)			Adsorbate/ Zeolite	Loading (mmol/g)		
	Sat.	Mid	High		Sat.	Mid	High
Ne/ERI	27.6	9.1	18.2	Ar/ERI	12.0	4.0	7.9
Ne/DFT	22.3	7.3	14.7	Ar/DFT	8.4	2.8	5.5
Ne/EAB	28.9	9.5	19.1	Ar/EAB	13.1	4.3	8.7
Kr/CHA	8.4	2.8	5.5	Xe/CHA	7.1	2.3	4.7
Kr/LTA	10.4	3.4	6.9	Xe/LTA	7.6	2.5	5.0
Kr/SAS	9.4	3.1	6.2	Xe/SAS	6.3	2.1	4.2
Kr/RHO	12.5	4.1	8.3	Xe/RHO	8.4	2.8	5.5
Kr/BIK	5.6	1.8	3.7	CF_4/LTA	2.8	0.9	1.8
Rn/LTA	7.6	2.5	5.0	CF_4/SAS	4.3	1.4	2.8
Rn/SAS	5.3	1.7	3.5	CF_4/RHO	6.3	2.1	4.1
Rn/RHO	7.7	2.5	5.1				

Before performing any MD simulations, we first performed GCMC simulations at 300 K for the 21 adsorbate-adsorbent pairs listed in Table 3.5. The single component adsorption isotherms are given in Fig. B2. For each pair we chose three different loadings based on corresponding theoretical saturation loadings to study the effect of adsorbate loading on D_s in context of the effect of framework flexibility: a) close to infinite dilution (1 molecule/unit cell), b) mid, and c) high loadings. The theoretical saturation loading here is defined as the amount of gas molecules adsorbed at an extremely high fugacity (~ 10^{12} bar). The mid and high loading is defined as 33% and 66% of the saturation loading

respectively. The high loadings used in our calculations, though are not realistic at 300 K (and hence not shown in Fig. B2), are helpful for demonstrating the application of our methods to a wide range of loadings.

a. Effect of temperature

Temperature plays an important role in combination with flexibility effects for tight fitting molecules diffusing in zeolites. Depending upon the size and loading of the adsorbate and zeolite, there is a temperature region below which the effect of framework flexibility is significant and hence cannot be ignored. In the previous chapter, we have demonstrated this by showing the deviation between the diffusivities of CH_4 in the fully flexible structure and the rigid structures becomes larger as temperature decreases. This temperature region is higher for zeolites with smaller 8MR windows for an adsorbate at a given loading and it increases with increasing adsorbate size.

These temperature effects can be explained by considering the tail of the window size distribution (Fig. B1) for flexible structures. The tail region corresponding to wider windows and hence can increase D_s of tight fitting molecules. At high temperatures, D_s in a rigid structure is high enough that any enhancement in D_s due to the tail region is negligible. As temperature decreases, the D_s in rigid structures decrease exponentially and hence any addition in D_s due to the tail region for fully flexible structure is significant and is no longer negligible.

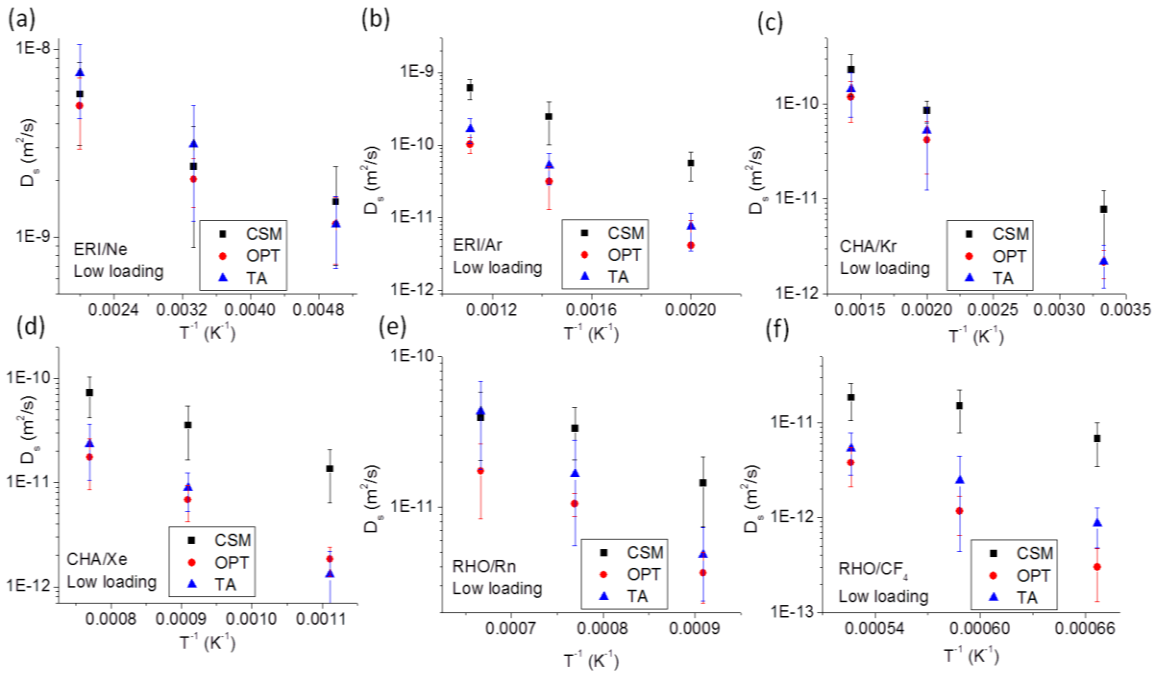

Figure 3.2 Self-diffusivities of (a) Ne in ERI, (b) Ar in ERI, (c) Kr in CHA, (d) Xe in CHA, (e) Rn in RHO, (f) CF_4 in RHO calculated using OPT, TA, and changing snapshot method (CSM) at 3 different temperatures at low loading (1 molecule/unit cell). Similar plots at low, mid, and high loadings for all adsorbate-zeolite systems can be obtained in Fig. B4 to B24 (a), (b), (c). Numerical values of diffusivities are given in Table B7.

We calculated D_s at three different temperatures for the three different loadings mentioned above. The specific loadings and temperature are listed in Tables 3.4 and B1 respectively. The temperatures were chosen after performing test calculations for each system to ensure D_s was readily measurable in our simulations in each case. D_s was calculated in the OPT and TA structures of the zeolites and compared with D_s calculated using the changing snapshot method.

The results for the temperature dependence of D_s in OPT, TA, and changing snapshot method for Ne and Ar in ERI, Kr and Xe in CHA, and Rn and CF_4 in RHO are

shown in Fig. 3.2 for low loading of gases. Similar results at low, mid, and high loadings for all the 21 adsorbate-zeolite systems are presented in Appendix B (Figs. B4 - B24). In all these materials, the deviation between the diffusivities obtained by changing snapshot method (approximating the fully flexible structure) and the optimized structure becomes larger as T decreases.

For Ne in ERI, simulations with the time averaged structure give D_s accurately at all the loadings (Fig. 3.2 (a), Fig. B4) as it is not a tight fitting molecule. The effect of the framework flexibility for Ar ($\sigma_{Ar-O} = 3.312$ Å) in ERI is shown in Fig. 3.2 (b) at low loading and in Fig. B7 at mid and high loading, in Fig. B8 for DFT, and in Fig. B9 for EAB. Large differences can be seen between D_s in the rigid and flexible structures, especially at low temperatures. Since all of these zeolites have a single window dimension, the time averaged structure does not capture the effects of the framework flexibility. Here, D_s in the OPT and TA structures are different because these zeolites are anharmonic.

The diffusivities for Xe are presented in Fig. 3.2 (d) for CHA, in Fig. B16 for LTA, in Fig. B17 for RHO, and in Fig. B18 for SAS. At the lower temperatures studied we can observe there is a difference of 1-2 orders of magnitude between D_s^{TA} and D_s^{CSM}. Even though CHA and LTA have similar window dimensions, the ratio $\frac{D_s^{CSM}}{D_s^{TA}}$ is higher for CHA (~10) than LTA (~3) at 900 K and low loading of Xe. This is because CHA is harmonic (i.e. $d_{min}^{TA} \sim d_{min}^{OPT}$), and therefore the TA structure does not perform better than OPT structure. On the other hand, in anharmonic LTA (i.e. $d_{min}^{TA} > d_{min}^{OPT}$), the TA structure narrows the tail region of the window size distribution and gets closer to the

fully flexible structure. Similar conclusions can be drawn for Kr diffusing in CHA (Fig. 3.2 (c) for low loading, Fig. B10 for mid and high loading) and LTA (Fig. B12) at the same temperature (e.g. 300 K) and loading. Parallel conclusions regarding the influence of the temperature on the framework flexibility effects on diffusion for other cases of adsorbates (Rn, CF_4) and zeolites (RHO, SAS, BIK) can be drawn based on the harmonicity and number of distinct window dimensions in the zeolite.

b. Effect of adsorbate size

Differences in adsorbate sizes play a pivotal role in kinetic separations using nanoporous materials like zeolites. In this section, we examine how framework flexibility affects D_s of inert gases of various sizes in the same zeolite and at low loading. Simulations for Ne ($\sigma_{Ne-O} = 3.005$ Å) and Ar ($\sigma_{Ar-O} = 3.312$ Å) in ERI (Fig. 3.2 (a)-(b), also Fig. B4 and B7 for mid and high loading), DFT (Fig. B5 and B8), and EAB (Fig. B6 and B9) indicate that the effect of framework flexibility is more pronounced for Ar than for Ne. For instance, in ERI at 200 K for Ar, the ratios $\frac{D_S^{CSM}}{D_S^{TA}} \approx 7$ and $\frac{D_S^{CSM}}{D_S^{OPT}} \approx 10$ are much larger than corresponding ratios (~1 and ~1 respectively) for Ne.

Similarly, the effect of the framework flexibility at different temperatures and loadings for Kr ($\sigma_{Kr-O} = 3.455$ Å) and Xe ($\sigma_{Xe-O} = 3.66$ Å) were studied in CHA, LTA, SAS, and RHO. The results obtained are shown in Fig. 3.2 (c)-(d) for CHA, Fig. B12 and Fig. B16 for LTA, Fig. B14 and Fig. B18 for SAS, and Fig. B13 and Fig. B17 for RHO. The results show that the framework flexibility affects D_s of the larger molecule, Xe, more significantly compared to Kr. For example, in SAS at 500 K, the

ratios $\frac{D_S^{CSM}}{D_S^{TA}} \approx 5-10$ and $\frac{D_S^{CSM}}{D_S^{OPT}} \approx 5-10$ are much larger than corresponding ratios (~1 and ~1 respectively) for Kr.

When we consider CF_4 and Rn, we have to use very high unphysical temperatures to observe diffusion. Simulations for Rn ($\sigma_{CF4-O} = 3.695$ Å) and CF_4 ($\sigma_{CF_4-O} = 3.94$ Å) in zeolites, RHO (Fig. 3.2 (e)-(f) for low loading, Fig. B19 and B22 for mid and high loading), LTA (Fig. B20 and B23), and SAS (Fig. B21, B24) indicate that the effect of framework flexibility is more significant for CF_4 compared to Rn. This can be highlighted when we look at D_s in RHO at 1500 K at low loading as the ratios $\frac{D_S^{CSM}}{D_S^{TA}}$ and $\frac{D_S^{CSM}}{D_S^{OPT}}$ are smaller for Rn (~1 and ~2) than for CF_4 (~10 and ~25).

c. Framework flexibility effects on loading dependence of D_s

It is well known that the adsorbate loading affects diffusion in zeolites. In the case of cage-type zeolites (ERI, EAB, CHA, LTA, SAS, and RHO), D_s increases with adsorbate loading up to a certain loading then decreases while in other zeolites (DFT, BIK), D_s continuously decreases.[88] In this section, we examine whether framework flexibility enhances the loading dependence of D_s. The results for the adsorbate loading dependence of D_s in OPT, TA, and the changing snapshot method for Ne and Ar in ERI, Kr and Xe in CHA, and Rn and CF_4 in RHO are shown in Fig. 3.3. Similar results at three different temperatures for all 21 adsorbate-zeolite systems are presented in Appendix B (Fig. B4 to Fig. B24).

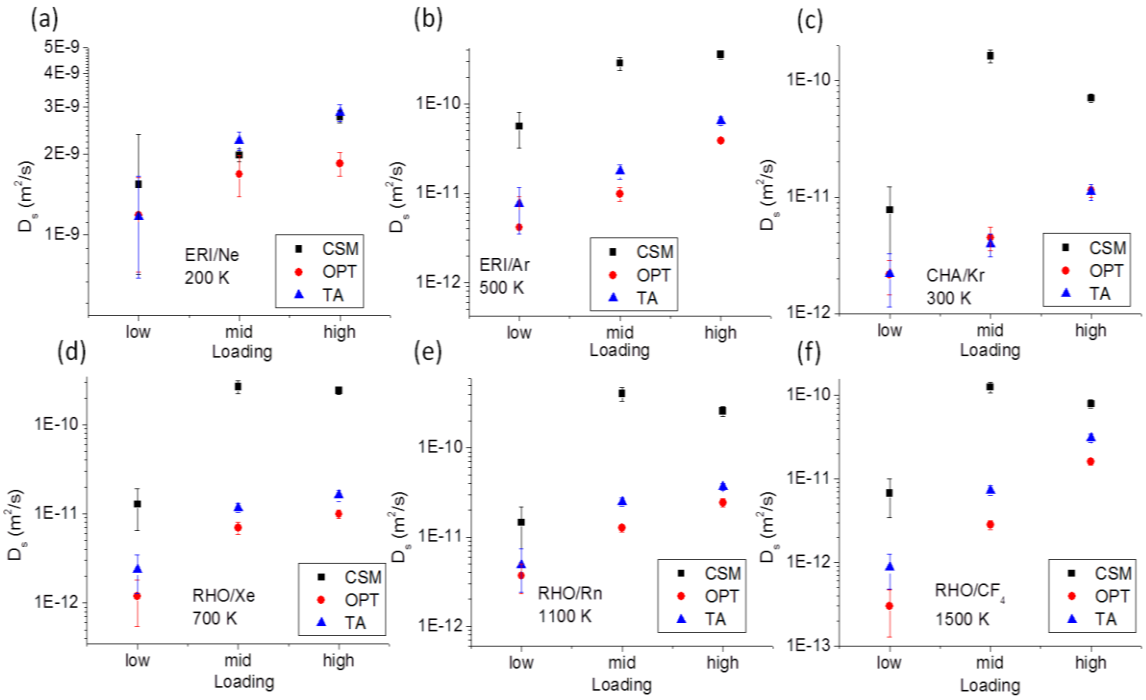

Figure 3.3 Self-diffusivities of (a) Ne in ERI, (b) Ar in ERI, (c) Kr in CHA, (d) Xe in RHO, (e) Rn in RHO, (f) CF_4 in RHO calculated using OPT, TA, and changing snapshot method (CSM) at 3 different loadings. Similar plots for all the adsobate-zeolite systems are shown in Fig. B4-24 (d), (e), and (f) at three temperatures. Numerical values of diffusivities are given in Table B5.

For small molecules like Ne, the framework flexibility does not affect loading dependence of D_s and hence, the rigid structures, OPT and TA, are sufficient for diffusion calculations. This can be seen, for example, for ERI (Fig.3.3a, Fig. B4), DFT (Fig.B5), and EAB (Fig. B6). Similarly, for Kr, which fits less tightly in SAS (Fig. B14), the framework flexibility effects on the loading dependence of D_s is negligible. For Ar, which fits tightly in the cage-type zeolites ERI (Fig. 3.3b, B7) and EAB (Fig. B9), $\frac{D_S^{CSM}}{D_S^{TA}}$ increases up to a certain loading and then decreases at high loading, even though the

D_s in rigid structures continue to increase. The ratio $\frac{D_s^{CSM}}{D_s^{TA}}$, for example, for Ar in ERI changes from ~6 at low loading to ~30 at mid loading and then decreases to ~5 at high loading at 500 K (Fig. 3.3b).

Similarly, for Kr in CHA (Fig. 3.3c), we can see that the ratio $\frac{D_s^{CSM}}{D_s^{TA}}$ at 300 K varies as 4→50→7. Here, the arrow indicates changing from low→mid→high loading. Framework flexibility influences the loading dependence of D_s more for more tight-fitting adsorbate in a given zeolite. For example, in RHO $\frac{D_s^{CSM}}{D_s^{TA}}$ changes 4→22→10 at 700 K for Xe (Fig. 3.3d), 4→20→8 at 1100 K for Rn (Fig. 3.3e) and 9→20→3 for CF_4 (Fig. 3.3f) at 1500 K.

In the case of diffusion of Ar in 3D channels of zeolites DFT (Fig. B8) or Kr in the 1D channels of BIK (Fig. B11), the D_s in the optimized and time averaged structures decrease with loading at all the temperatures as expected. However, the diffusion in the changing snapshot method either remains constant and then decreases or decreases continuously with loading. However, $\frac{D_s^{CSM}}{D_s^{TA}}$ shows the same qualitative behavior as above i.e. it first increases and then decreases with loading, just like any other cases of tight fitting molecule.

It can be concluded in general after looking at the examples above that if $\frac{D_s^{CSM}}{D_s^{TA}}$ ~ 1 at low loading (e.g. small molecule) at a given temperature for a given adsorbate then it is safe to assume $\frac{D_s^{CSM}}{D_s^{TA}}$ ~ 1 at higher loading also. As a result, we can neglect the effect of framework flexibility at higher loadings to save computational time. If $\frac{D_s^{CSM}}{D_s^{TA}}$ >> 1 at low

loading (e.g. tight fitting molecules), the framework flexibility will typically be even more important for higher loadings. At very high loading the framework flexibility effects on D_s diminishes because of adsorbate crowding.

3.3.3 TST/snapshot method

We have shown above in Fig. 3.1 that the diffusivities calculated using the TST/snapshot method are comparable to diffusivities in the fully flexible structure at low loading by studying few examples. We applied the TST/snapshot method for large number of adsorbate-zeolite systems to illustrate the potential of this method for screening materials for the kinetic separations.

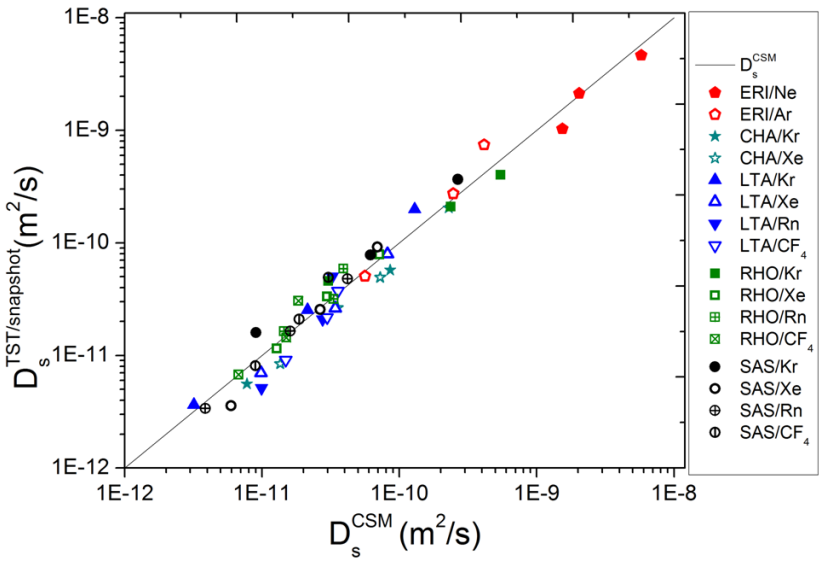

Figure 3.4 Comparison of TST/snapshot method with changing snapshot method for different adsorbate-zeolite systems at 3 different temperatures per system. Numerical values of diffusivities are given in Table B8.

Our TST based method was applied to the set of snapshots to calculate D_s for inert gases and CF_4 in the 8MR zeolites listed in Fig. 3.4. To calculate D_s at a particular

temperature, we used snapshots of zeolite at that temperature. Additional information about the specific temperatures used in simulations is given in Table B1. Figure 3.4 shows an excellent agreement between the TST/snapshot method and the changing snapshot method for systems where both the methods are applicable. This establishes that the conclusions we drew for the CSM above regarding the effect of temperature, adsorbate size on framework flexibility are equally applicable for TST/snapshot method.

The TST/snapshot method is useful to obtain D_s at low temperatures where MD simulations cannot be used. As already discussed, framework flexibility effects are particularly important in this regime. Hence, we used the TST/snapshot method to study the effect of framework flexibility at low temperatures. The TST/snapshot method was applied to the set of snapshots approximating fully flexible structures to obtain D_s of Ar, Kr, Xe, Rn, and CF_4 as shown in Fig. 3.5 and Fig. B25. We also applied the TST method to the optimized and time averaged structures for the comparison. For each adsorbate, we calculated D_s at two temperatures: 100 and 200 K for Ar, 50 and 100 K for Kr, 200 and 300 K for Xe and Rn both, 700 and 900 K for CF_4. The results for Ne are not shown as it is not tight fitting molecule and the effect of framework flexibility is negligible.

Here, diffusivities obtained in the optimized and time averaged structures are orders of magnitude lower than diffusivities obtained in the flexible structure approximated by TST/snapshot method, as expected. For example, the ratios $\frac{D_s^{snapshot/TST}}{D_s^{TA/TST}}$ ($\frac{D_s^{snapshot/TST}}{D_s^{OPT/TST}}$) for Ar in ERI at 100 and 200 K are ~300 (600) and ~50 (90) respectively. For Rn in LTA, $\frac{D_s^{snapshot/TST}}{D_s^{TA/TST}}$ ($\frac{D_s^{snapshot/TST}}{D_s^{OPT/TST}}$) ~$10^5$ (10^8) at 700 K and ~10^2 (10^4) at 900 K.

Similarly, we can also see such deviations of orders of magnitude in the case of Kr, Xe and CF_4 (Fig. B25). This divergence increases as temperature decreases.

As seen from Fig. 3.5, the TST method can access very low diffusivities; we show data as low as 10^{-25} m^2/s. Although these low diffusivities may not practically useful, it underlines the observation that this TST based method can be used to obtain D_s under conditions that are completely inaccessible using standard MD.

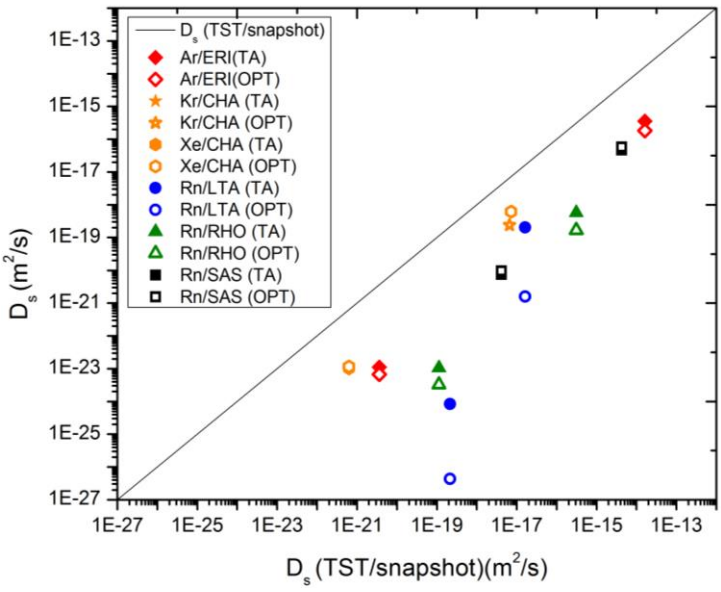

Figure 3.5 TST calculations of diffusivities at low temperatures in the time averaged and the optimized structures compared to D_s from TST/snapshot method for Ar, Kr, Xe, and Rn in respective 8MR zeolites. For harmonic zeolites (CHA, SAS), the data for OPT and TA structures overlaps and hence is hard to visualize in the figure for some cases. Numerical values of diffusivities are given in Table B6.

3.3.4 Effect of framework flexibility in binary mixtures

Above, we discussed the effect of framework flexibility on single component self-diffusion of spherical molecules. To screen materials for kinetic separations, it is of course desirable to obtain binary diffusion data. As a consequence, we extended our study to the diffusion of binary mixtures of spherical adsorbates in 8MR zeolites.

We first performed GCMC simulations using our in-house code for binary mixture for 8 adsorbates-adsorbent pairs: Ne/Ar in ERI and EAB, Ar/Kr in ERI and EAB, Kr/ Xe in LTA and CHA, Xe/Rn in LTA and RHO. The binary adsorption isotherms (at 50:50 gas phase composition) are given in Fig. B3. This is required to decide a reasonable mixture composition for our MD calculations. These 4 pairs of gases were chosen to give reasonable amount of adsorption for both gases. The respective zeolites are chosen so that the 8MR window dimensions comparable to both the adsorbates but one of the components of the mixture is a tight-fitting molecule while other can diffuse relatively rapidly. The main aim of this exercise is to show that the changing snapshot method works also for binary mixtures. We used the mixture composition obtained at 1000 bar at each temperature. The high loadings associated with these conditions are useful for illustrating the applications of our methods to a wide range of loadings.

Figure 3.6 shows the accuracy of the changing snapshot method for the binary mixture by comparing with standard MD simulations in all 8 systems. For the smaller molecules of each binary mixture, rigid structure simulations using the optimized and time averaged structures give results in a reasonable agreement with the fully flexible structures except for Ar-Kr in ERI, Ar-Kr in EAB, and Xe-Rn in LTA, where even the smaller molecules act as tight fitting at temperatures studied. For the larger molecules the

diffusivities predicted using single rigid structures, OPT and TA show significant deviation from diffusivities in the flexible structures and D_s in the changing snapshot method. D_s of the larger (hence slower) molecules of 4 binary mixtures (systems 1, 3, 4, and 5 in Fig. 6) in the optimized and time averaged structures are not reported because of very large computational time that would be required in these cases to observe cage to cage hopping.

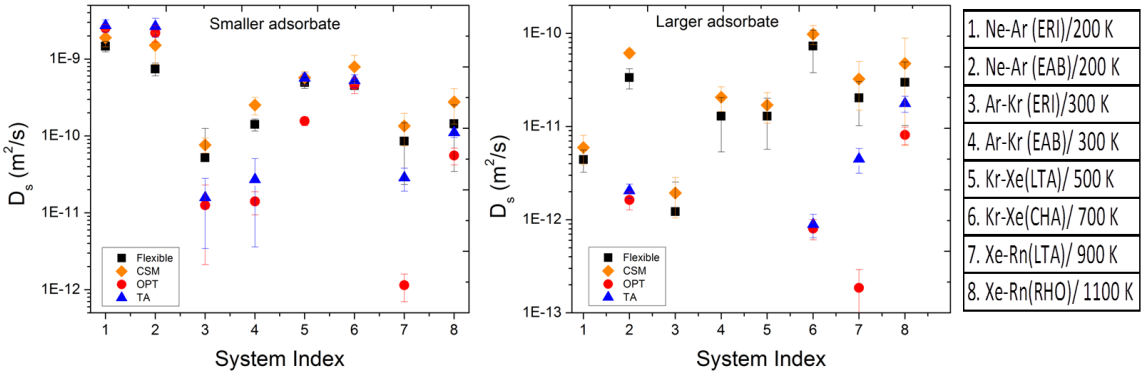

Figure 3.6 Binary self-diffusivities of (a) smaller molecules, and (b) larger molecules for 8 binary systems calculated using the changing snapshot method and compared with D_s in the fully flexible, optimized, and time averaged structures. Note that, some diffusivities of larger (hence slower) molecules in the optimized and time averaged structures are not reported because of a very large computational time. [Note: System index is arranged in the order of increasing size of adsorbates in the system]. Numerical values of diffusivities are given in Table B7.

The binary diffusion selectivity is an important quantity in deciding whether a material is suitable for a separation of mixture. Hence, we calculated the binary diffusion selectivity in the abovementioned 8 systems in the OPT, TA, and changing snapshot method. We also compared the selectivity with that obtained in the fully flexible structure

of zeolites. The results are given in Table 3.6, which indicate that the changing snapshot method performs very well in predicting the binary selectivity. The methods based on a single rigid structure, however, do not perform accurately. For systems 1, 3, 4, and 5, we calculated an upper bound on the D_s of larger molecules in the single structure calculations by assuming the total MSD of the adsorbate to be equal to a single hop from one cage to another in a given computational time.

Table 3.6 Binary diffusion selectivity data for 8 binary systems.

T (K)	Adsorbate Pair (Zeolite)	Diffusion selectivity			
		OPT	**TA**	**CSM**	**Flexible**
200	Ne-Ar (ERI)	>3506	>3792	318	332
200	Ne-Ar (EAB)	1344	1297	25	22
300	Ar-Kr (ERI)	>18	>22	40	43
300	Ar-Kr (EAB)	>71	>136	13	11
500	Kr-Xe(LTA)	>952	>3441	34	38
700	Kr-Xe(CHA)	570	589	8	6
900	Xe-Rn(LTA)	6.2	6.4	4	4.2
1100	Xe-Rn(RHO)	6.9	6.3	5.8	4.8

3.4 Conclusions

We have performed diffusivity calculations for 6 spherical molecules, Ne, Ar, Kr, Xe, Rn, and CF_4 using the changing snapshot and TST/snapshot methods in eight 8MR silica zeolites. We first demonstrated the accuracy of these methods by comparing results from these two efficient methods with diffusivities in the fully flexible structure. We then showed their applicability to obtain D_s at multiple temperatures and loadings. Both the methods are computationally efficient and hence can be used for screening of the

materials for separation processes. Throughout this work, we used a classical force field to describe flexibility of zeolites. An important advantage of the methods we have used is that they can also be used in conjunction with data from ab-initio MD simulations to accurately account for the effect of framework flexibility in the nanoporous materials where high quality classical force field are not available.

The changing snapshot method is applicable at any adsorbate loading. Using the changing snapshot method, we studied the effect of framework flexibility on adsorbate loading dependence of D_s. As expected, we concluded that the framework flexibility influences the loading dependence of D_s more for more tight-fitting adsorbates, irrespective of zeolite topology and structure. We also found that it is possible to use low loading calculations to see if the framework flexibility is important at any loading. The TST/snapshot method gives diffusivities at the infinite dilution limit and is useful for low temperature calculations where regular MD cannot be used due to time constraints.

In order to extend the changing snapshot method to binary mixtures, we performed simulations with the changing snapshot method with 8 binary noble gas pairs in 8MR zeolites. We have successfully demonstrated the applicability of the changing snapshot method for binary mixture of spherical molecules by comparing the diffusivities and diffusion selectivity with those in the fully flexible structures in all the cases. On the other hand, binary diffusivities and diffusion selectivities in rigid structures were incorrect by orders of magnitude for some cases.

Both of the methods we have used rely on the assumption that coupling between the adsorbate and the framework degrees of framework as the adsorbate passes through a

transition state are negligible. Our results show that there are many examples of physical interest where this approximation is well justified. There are situations, however, where this approximation may be less well founded. Two examples of systems of this kind include the hopping of geometrically extended molecules such as long chain hydrocarbons through narrow pores and the diffusion of adsorbate that are so large that they can only move due to structural deformation of pores. It would be useful to develop efficient and accurate methods to describe these situations that would complement the limited range of diffusivities that can be probed using standard MD.

CHAPTER 4

Prediction of CH_4 and N_2 adsorption in zeolites using force fields derived from periodic DFT-CC calculations

4.1 Introduction and literature review

Nanoporous materials such as zeolites, metal organic frameworks (MOFs), covalent organic frameworks (COFs), zeolitic imidazolate frameworks (ZIFs) have shown great potential for applications in storage, separation, purification, and catalysis.[105-108] Molecular simulations like Grand Canonical Monte Carlo (GCMC) and Molecular Dynamics (MD) are widely used to predict adsorption isotherms, heat of adsorption, diffusion, and other thermodynamic properties of adsorbate molecules in porous materials like zeolites.[57, 109-114] The accuracy of such predictions depends mainly on the accuracy of the Force fields (FFs) (i.e., interatomic potentials) for adsorbate-zeolite and adsorbate–adsorbate interactions. Molecular simulations of adsorption and diffusion in MOFs, COFs, and ZIFs typically use generic FFs (like UFF[115] and Dreiding[116]). While they have demonstrated success for many systems, these force fields were developed to treat a variety of molecules including organic, biological, and inorganic compounds, and their transferability is not always satisfactory for porous materials.[17,18] In simulations of adsorption in zeolites, force fields are usually obtained by fitting adsorption isotherms to existing experimental data.[55, 117-118] This parameterization strategy is empirical and lacks an explicit physical basis. When these force fields are

applied to other systems, their accuracy is questionable. In addition, the application of these force fields is not straightforward for new material types and compositions.

Developing FFs from first principle methods, however, can allow development of typically transferrable FFs without requiring initial experimental data. First-principles-based force fields have been proposed to predict adsorption properties of important gas molecules like H_2, CH_4, CO_2, N_2 etc. in nanoporous materials.[119-135] In this approach, force field parameters are obtained by fitting interaction energies calculated by first-principle methods and interatomic distances (usually at MP2 or Density Functional Theory levels) to classical potential functions. If they can be developed in a reliable way, first principles based force fields can provide an accurate description of adsorbate–adsorbent and adsorbate–adsorbate interactions. These studies typically used cluster models of the porous materials for quantum chemistry calculations and evaluated specific orientations of adsorbate molecules to fit classical potentials. This approach is appropriate if the configurations chosen for quantum chemistry calculations represent all of the important degrees of freedom on the overall potential energy surface (PES), but ensuring that this requirement is satisfied is challenging. In addition, cluster models cannot capture long range interactions which are important for some systems, like adsorption in zeolites. Recently, Fang *et al.*[27, 136] proposed an approach to developing first principles-based force fields for crystalline porous materials where they used the fully periodic framework to represent the adsorbent structure and performed quantum chemistry calculations for hundreds of adsorption configurations randomly scattered throughout the whole framework space. In that study, they illustrated the approach for adsorption of CO_2 in silica zeolites and showed that it could accurately predict

experimental adsorption properties and has good transferability.[27, 136] In this work, we extend the similar approach to molecules like CH_4 and N_2 in zeolites.

This chapter is organized as follows. In section 4.2, we discuss the computational feasibility and accuracy of various first-principles methods for describing CH_4 adsorption in periodic zeolites. Here, we have developed and tested other DFT-based FFs such as PBE-D2[137], PBE-D3[138], and VDW-DF2[139], which were found to overestimate adsorption isotherms. In section 4.3, we introduce our approach of DFT/CC (Density Functional Theory/Coupled Cluster) method[140] to developing force fields that account for CH_4–zeolite interactions. This approach uses Coupled-Cluster (CC) corrections to correct DFT energies for CH_4-zeolite, CH_4-aluminophosphates, CH_4-aluminosilicates, and N_2-zeolite/aluminosilicate. In section 4.4, we will discuss in detail the FF development procedure for CH_4 in the pure silica zeolite-CHA. A classical FF for CH_4 adsorption in silica zeolites was developed based on hundreds of DFT-CC calculations that probed the full range of accessible volume in purely silica chabazite (Si-CHA) via random as well as GCMC sampling. The methods demonstrated in this chapter will be broadly applicable in using molecular simulations to predict properties of adsorbed molecules in zeolites and other nanoporous materials. In section 4.5, we perform GCMC simulations to predict adsorption properties of CH_4 in different zeolites and compare the results with the experimental measurements to test the accuracy and the transferability of the developed FFs. We then extend the DFT/CC method to develop force field for CH_4 in aluminophosphates in section 4.6, for N_2 in silica zeolites in section 4.7, and both CH_4 and N_2 in cationic aluminosilicates in section 4.8. Our conclusions are summarized in section 4.9.

4.2 First-principles methods for describing CH_4 adsorption in silica zeolites

In previous developments of first-principles-based force fields, cluster models were usually built to represent local structures of porous adsorbents,[119-125, 128-135, 141-145] and Møller–Plesset second-order perturbation theory (MP2) was often used to describe interactions of guest molecules with adsorbent sites.[122-123, 125, 128-129, 131-132, 134-135, 145] The MP2 method can accurately predict adsorbate–adsorbent interaction energies where dispersion (or van der Waals) components play a dominant role. However, it is not computationally feasible to examine hundreds of adsorption configurations in periodic structures at this level of theory. Empirical dispersion corrections (D2[137] and D3[138]) have been recently used to develop force fields for various gas molecules in zeolites[27, 136, 146] and MOFs[144], giving good agreement between simulated results and experimental data.

Fang *et al.* considered several DFT methods that treated dispersion corrections either in an empirical or *ab initio* way, including DFT-D2 and various vdW-DF approaches.[27, 136, 146] Unlike high level cluster approaches, these methods are computationally inexpensive to use in periodic systems. The PBE-D2 approach was found to give the best agreement with the DFT/CC and experimental data, and then used in force field fitting for CO_2 adsorption in zeolites.[146] Excellent agreement was obtained between adsorption properties predicted with the fitted force field and experiments.[146] The PBE-D2 method, however, overestimates the adsorption energies in case of CH_4, which results in overestimated adsorption isotherms as seen from in Fig. 4.1. The adsorption isotherms obtained using DFT-D3 method is similar to that obtained using DFT-D2 and hence not shown in Fig. 4.1 for clarity. The VDW-DF2, VDW-DF-CC

methods are also used for comparison. VDW-DF2 overestimates the adsorption isotherm while VDW-DF-CC method underestimates the adsorption isotherms.

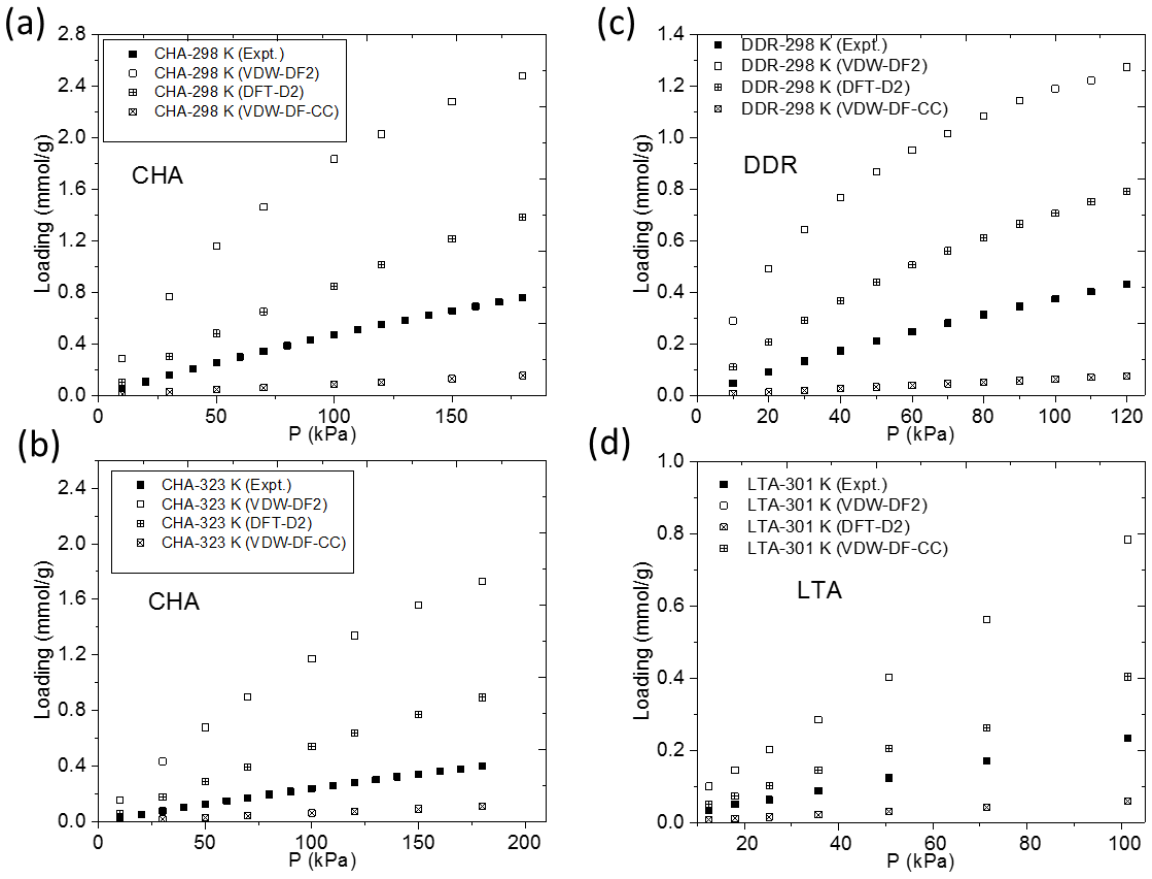

Figure 4.1 Comparison of computed adsorption isotherms using force fields derived from different DFT methods (PBE-D2, VDW-DF2 and VDW-DF-CC) and experimental adsorption isotherms in (a) CHA at 298 K, (b) CHA at 323 K, (c) DDR at 298 K, and (d) LTA at 301 K. Experimental data are taken from Maghsoudi *et al.*[147] for CHA, Himeno *et al.*[148] for DDR, and Hedin *et al.*[62] for LTA.

The possible reason for the poor performance of these dispersion corrected DFT methods (DFT-D methods) for CH_4 in zeolites can be explained as follows. The performance of the above DFT-D methods depends on the exchange-correlation

functional, training set, and the damping function used. Within these standard DFT-D schemes, the intermolecular interaction energy is calculated as $E_{DFT\text{-}D}=E_{DFT}+\Delta E$, where ΔE is an intermolecular energy correction (usually denoted as $E_{dispersion}$). The success or failure of the DFT-D model relies on the fit of R^{-6} term coefficients and damping function parameters. Within the DFT-D scheme, the ΔE term alone clearly does not account for the inability of the DFT to describe a dispersion interaction; rather, the R^{-6} term along with the damping function corrects the DFT functional for the description of weakly interacting systems like CH_4 in zeolites. As a result, the selection of a particular functional form may simplify the fitting procedure but introduces an artificial constraint on the parameter space resulting in poor performance. Hence, in order to derive accurate force fields for CH_4 in zeolites, it is necessary to use the more accurate method like DFT/CC for describing the interactions between CH_4 and zeolites.

4.3 DFT/CC method

4.3.1 Overview

The DFT/CC method was proposed by Nachtigall and co-workers for an accurate description of weakly bound molecular systems.[140] This method is based on estimating the DFT error, and then correcting the DFT energies for periodic systems. Here $\Delta E^{DFT/CC}$ is defined as the difference between DFT and accurate CCSD(T) interaction energies on molecular cluster. This method is similar to DFT-D class of methods but with a key difference: the artificial assumption about the particular form of the ΔE correction is removed. Instead, all the deficiencies of the DFT method for the description of weakly interacting systems are defined purely numerically (using an interpolation method), by correcting the DFT interaction energies to CCSD(T) accuracy.

The DFT/CC method has been successfully applied to a variety of systems where dispersion interactions are important including adsorption of various molecules on graphene and graphite surfaces,[149-150] water, CH_4, propane, and propene in the MOF CuBTC[151-153], as well as CO_2 in proton and cation exchanged zeolites[154-158]. Chen *et al.* derived potential energy surface (PES) for CH_4 in CuBTC using the DFT/CC method.[151] After implementing the PES in GCMC simulations, a good agreement between calculations and experiments for adsorption isotherms and adsorption mechanism were obtained.[151]

4.3.2 DFT/CC correction functions for CH_4--zeolite interaction

The main assumption of the method is that $\Delta E^{\mathrm{DFT/CC}}$ can be represented as pairwise representation using the following equation

$$\Delta E^{DFT/CC} = \sum_{i}^{N_a} \sum_{j}^{N_b} \varepsilon_{ij}(R_{ij}) \qquad (4.1)$$

where N_a and N_b are the numbers of atoms of the corresponding monomers, ε_{ij} are the DFT/CC correction functions, and R_{ij} is the intermolecular atomic distance between atom i and j. The correction functions are obtained from a set of energies calculated at CCSD(T)/CBS (CBS= complete basis sets) and DFT/AV5Z levels for a suitable reference set of molecules or clusters (CH_4--H_2, CH4--H_2O, and CH_4--$Si(OH)_4$ as shown in Fig. 4.2) by means of the Reciprocal Power Reproducing Kernel Hilbert Space Interpolation (RP-RKHS) as summarized below. In short, the RP-RKSH interpolation scheme is used to decompose ΔE into $\varepsilon_{CH}(R_{CH})$ and $\varepsilon_{HH}(R_{HH})$ for CH_4--H_2, $\varepsilon_{CO}(R_{CO})$ and $\varepsilon_{HO}(R_{HO})$ for CH4--H_2O, or $\varepsilon_{CSi}(R_{CSi})$, $\varepsilon_{HSi}(R_{HSi})$ for CH_4--$Si(OH)_4$. These reference sets are chosen

because precise calculations at the CCSD(T) level with sufficiently flexible basis sets are feasible.

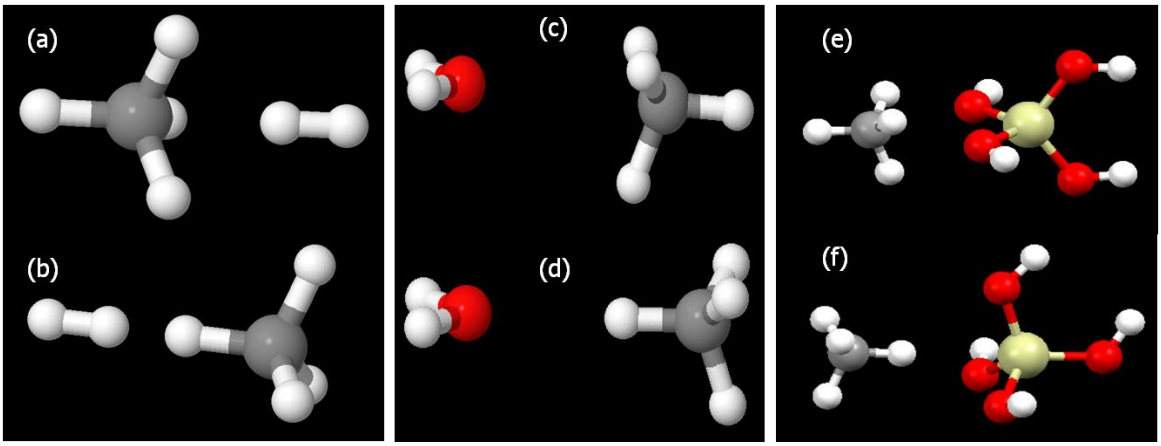

Figure 4.2 Definition of the reference set used for the generation of the DFT/CC correction functions: $CH_4\cdots H_2$ (a, b), $CH_4\cdots H_2O$ (c, d), and $CH_4\cdots Si(OH)_4$ (e, f). The *C2v* symmetry constraints were applied. The C, O, H, and Si atoms are depicted in grey, red, white, and yellow color, respectively.

Here, all calculations to get DFT and CCSD(T)/CBS energies were performed in the GAUSSIAN 09 program using the standard Dunning's augmented correlation-consistent valence-*X*-ζ basis sets with polarization functions, with *X*=double, triple, quadruple, or quintuple basis sets (designated as AVDZ, AVTZ, AVQZ, and AV5Z, respectively).[140, 151-154] All calculated interaction energies were corrected for the basis-set superposition error using the counterpoise correction method of Boys and Bernardi.[159] Before these calculations, the geometries of H_2 and CH_4 monomers were optimized at the CCSD(T)/AVQZ level of theory and the geometry of $Si(OH)_4$ monomer was optimized at the MP2/AVQZ level. The correction curve is represented by means of the RP-RKHS functional form[160-161],

$$\varepsilon_{ij}(R_{ij}) = \sum_k \alpha_k q(R_{ij}^2, R_k^2) \tag{4.2}$$

with a selected grid dependent kernel function q[140, 154]:

$$q(R_{ij}^2, R_k^2) = \frac{1}{3R_>^6} - \frac{R_<^2}{5R_>^8} \tag{4.3}$$

where R_{ij} are intermolecular atomic distances between i and j, R_k are yet unspecified grid points, $R_>$ = max(R_{ij} ,R_k), $R_<$ = min(R_{ij} ,R_k), and α_k are interpolation coefficients. The interpolation coefficients α_k and hence ε_{ij} were calculated as follows: For a fixed monomer-monomer orientation, we calculated the correction energies ΔE(R) on a selected grid in R [CH_4--H_2 (70 grid points), CH_4--H_2O (67 grid points), and CH_4--$Si(OH)_4$ (62 grid points)]. For each reference set, we have used 2 different orientations in order to obtain corrections functions for 2 interactions present in a system, one for C and other for H of CH_4. The corresponding RP-RKHS functional forms of ε_{ij} (Eq. (4.2)) along with calculated correction energies ΔE were substituted into the pairwise additive approximation (Eq. (4.1)). This led to a system of linear equations for α_k, which were solved numerically using the Tikhonov regularization[162-163] algorithm. Once α_k are known, the ε_{ij} can be easily obtained using equation (4.2). The correction functions are shown in Fig. 4.3, 4.4, and 4.5. The numerical values of ε_{ij} and α_k are reported in Appendix C.

The $CH_4 \cdots H_2$ reference system (Fig. 4.2 (a) and 4.2 (b)) provides the ε_{CH} and ε_{HH} correction functions as shown in Fig. 4.3. The $CH_4 \cdots H_2O$ reference system (Fig. 4.2 (c) and 4.2(d)) provides ε_{CO} and ε_{HO} correction functions shown in Fig. 4.4, using ε_{CH} and ε_{HH}

obtained previously for $CH_4\cdots H_2$. The $CH_4\cdots Si(OH)_4$ reference system (Fig. 4.2 (e) and 4.2 (f)) provided ε_{CSi} and ε_{OSi} correction functions shown in Fig. 4.5, using ε_{CH} and ε_{HH} obtained previously for $CH_4\cdots H_2$ and ε_{CO} and ε_{HO} obtained previously for $CH_4\cdots H_2O$. The resulting correction functions can be used in periodic systems for dispersion corrections to improve the DFT description of large systems that can only be computed at the DFT level. For example, the interaction between CH_4 and silica zeolite could, in principle, be corrected using correction functions obtained for the abovementioned reference sets. In this work, we employ the DFT/CC method for developing a force field that describes interactions between CH_4 and silica zeolite.

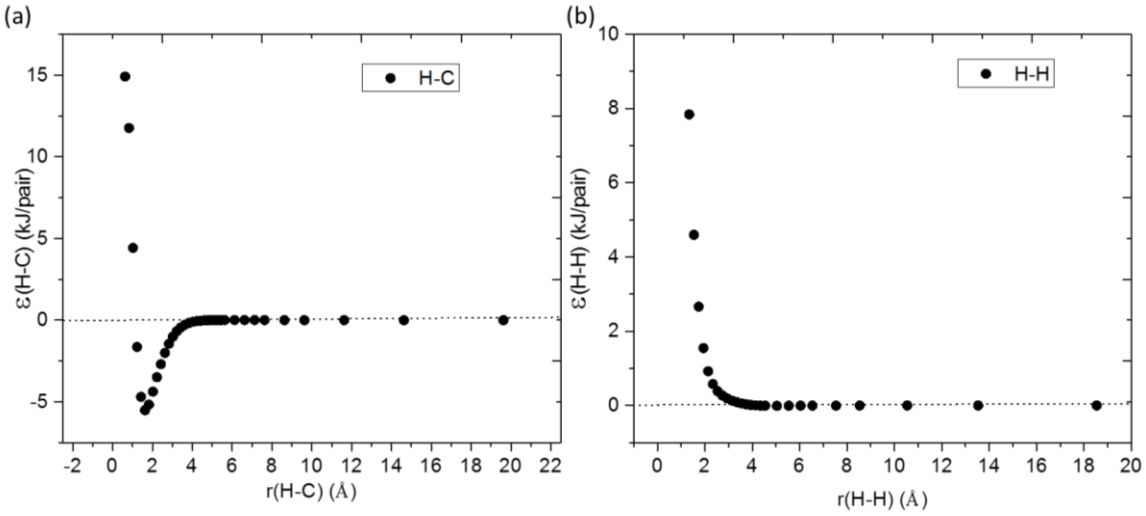

Figure 4.3 DFT/CC-correction curves for (a) H-C, (b) H-H interactions.

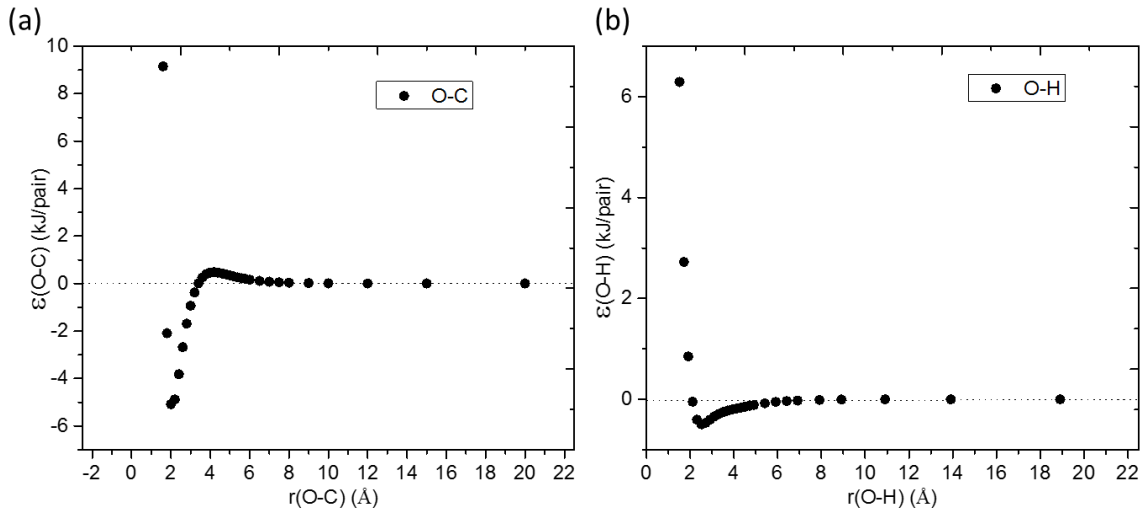

Figure 4.4 DFT/CC-correction curves for (a) O-C, (b) O-H interactions.

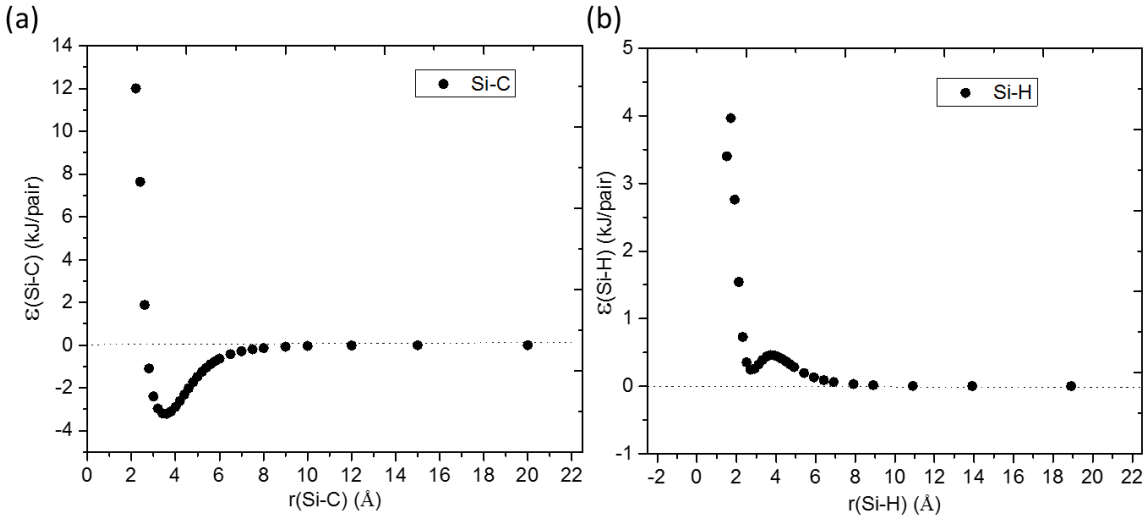

Figure 4.5 DFT/CC-correction curves for (a) Si-C, (b) Si-H interactions.

4.4 DFT/CC-derived Force fields for CH_4 in silica zeolite

As in most classical simulations of adsorption in zeolites, we assume that the zeolite frameworks are rigid as discussed in previous chapters. In order to fully specify the energy of adsorbed CH_4 molecules in zeolites, we need to define CH_4---zeolite, and CH_4---CH_4 interactions. It is important to use a CH_4---CH_4 potential that correctly

captures the phase behavior of pure CH_4, so we used the well-known Dubbeldam potential (ε= 158.5 K, σ= 3.72 Å),[55] which was developed for this purpose. In the following section, we focus on developing force field potentials that account for CH_4---zeolite interactions.

4.4.1 Classical form of force field

We assume the interactions between each atom in CH_4 and a silica zeolite atom are represented by pairwise van der Waals (vdW) and Coulombic terms

$$E_{FF}(R_{ij}) = E_{vdW} + E_{Coul} = s_{12}\frac{C_{12}^{ij}}{R_{ij}^{12}} - s_6\frac{C_6^{ij}}{R_{ij}^{6}} + \frac{q_i q_j}{R_{ij}} \tag{4.4}$$

where, R_{ij} is the distance between atoms i and j, C_6^{ij} and C_{12}^{ij} are the attractive and repulsive coefficients, q_i and q_j represent the charges for atoms i and j, respectively, and s_6 and s_{12} are global scaling factors that depend on the first-principles method used in the force field fitting. The attractive portion of the vdW interactions, $-s_6 C_6^{ij}/R_{ij}^6$, is based on Grimme's empirical dispersion expression in the DFT-D2 method. The damping function in the original dispersion expression, which was used to avoid near-singularities for small interatomic distances, is not considered here because the repulsive term, $s_{12}C_{12}^{ij}/R_{ij}^{12}$, is included.

The C_{12}^{ij} parameters were defined by

$$\frac{C_{12}^{ij}}{C_6^{ij}} = \frac{(R_0^i + R_0^j)^6}{2} \tag{4.5}$$

where R_0^i and R_0^j are the van der Waals radii of atoms i and j. A set of parameters for C_6 and R_0 from elements H to Pu are available in Grimme's work,[138] and these values were

adopted in our force field fitting. This relation is based on the fact that the vdW terms in our force field are similar to the Lennard-Jones (LJ) 12-6 potential with the form

$$E_{LJ}(R_{ij}) = 4\varepsilon_{ij}\left[\left(\frac{\sigma_{ij}}{R_{ij}}\right)^{12} - \left(\frac{\sigma_{ij}}{R_{ij}}\right)^{6}\right] = \frac{A_{ij}}{R_{ij}^{12}} - \frac{B_{ij}}{R_{ij}^{6}} \quad (4.6)$$

where ε_{ij} is the depth of the potential well and σ_{ij} is the interatomic distance at which the potential is zero. The repulsion coefficient A_{ij} is determined so that the potential has a minimum at the distance equal to the sum of the van der Waals radii of the atomic pair. Coulombic interactions between atoms in CH_4 and the zeolite were neglected as we used a neutral model for CH_4. To complete the specification of the CH_4-zeolite force field, the scaling factors s_6 and s_{12} must be defined. These factors are fitted to allow the closest correspondence between the first-principles results and the classical force field in a least-squares sense. This is similar to the concept in Grimme's work, where s_6 only depends on the density functional used and was determined by least-squares optimization of interaction energy deviations for standard benchmark sets.[137] Here, four cross species interactions should be considered, including C...Si, H…Si, C…O_z, and H…O_z.

4.4.2 Force field fitting procedures

We performed a large number of DFT calculations for CH_4 adsorption in Si-CHA in order to derive a classical force field. Si-CHA was chosen because its small unit cell ($Si_{12}O_{24}$ per unit cell) reduces the computational demands associated with periodic DFT calculations. The rhombohedral unit cell ($R\bar{3}m$ space group) of Si-CHA was first fully optimized at the DFT level. PBE-D2 gives lattice constants of a = b = c = 9.333 Å and α = β = γ = 94.34°, close to the experimentally determined data, a = b = c = 9.229 Å and α

= β = γ = 94.3°.[164] The optimized structure of CHA is shown in Fig. 4.6 (a). All single point DFT calculations to assess CH_4 binding energies were performed at the Γ-point to reduce computational cost with a loading of one CH_4 per unit cell.

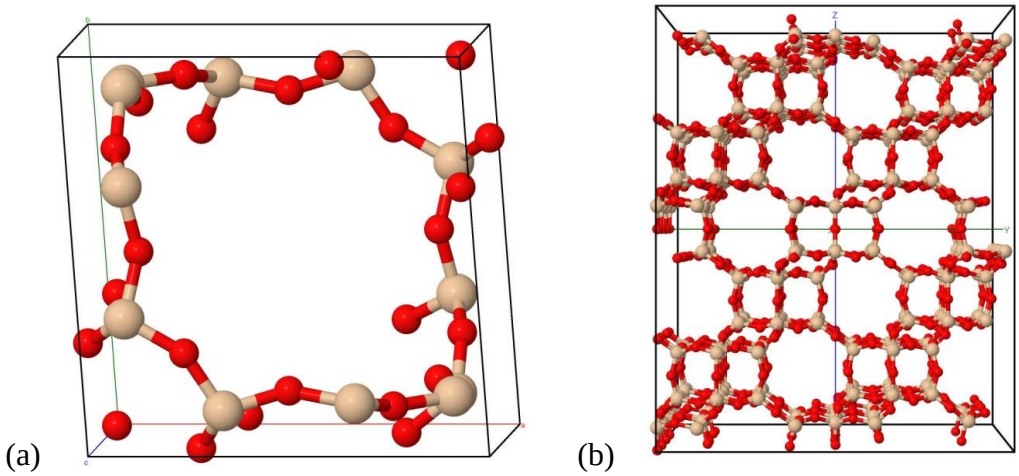

Figure 4.6 (a) primitive unit cell of silica CHA used in the DFT calculations. (b) Supercell of silica CHA used in the GCMC calculations. Si and O atoms depicted as light brown and red spheres, respectively.

The goal of our force field development strategy is to ensure that the force field parameters reproduce the DFT energy for various configurations of the adsorbates in silica CHA. Briefly, this is done by generating a number of configurations from an initial generic force field, calculating the DFT interaction energies for these configurations for the periodic system and fitting a classical force field to the DFT data to obtain the new force field. Next, this new force field is used to generate another set of adsorbate configurations and this process is repeated until sufficient convergence of the force field parameters is obtained.

To begin with, a total of 300 adsorption configurations of CH_4 within the zeolite framework were randomly generated with a restriction that there should be no interatomic overlap between the atoms of CH_4 and zeolite framework. More specifically, only configurations where the minimum interatomic distance satisfied $R_{min} > 2.2$ Å were used. The adsorption energies at the DFT/CC level were calculated for all 300 CH_4 configurations within the Si-CHA framework using

$$E_{ads} = E_{CH_4-zeolite} - (E_{CH_4} + E_{zeolite}) + \Delta E_{DFT/CC} \tag{4.7}$$

where $E_{CH_4-zeolite}$, E_{CH_4}, and $E_{zeolite}$ are the total energies for the adsorption complex, isolated CH_4 molecule, and isolated Si-CHA, respectively while $\Delta E_{DFT/CC}$ is DFT/CC correction applied. These DFT adsorption energies were then equated to classical form of adsorption energies as given in Eq. (4.4). The repulsive and attractive vdW terms without scaling factors, C_{12}^{ij}/R_{ij}^{12} and $-C_6^{ij}/R_{ij}^6$, were also determined separately for each CH_4 adsorption configuration. Table 1 gives the C_{12}^{ij} and C_6^{ij} coefficients for each cross species interaction between CH_4 and Si-CHA, which were derived from Grimme's work and Eq. (4.5). The distances ($1/R_{ij}^{12}$ and $1/R_{ij}^6$) for each cross species were measured and summed based on a finite $5 \times 5 \times 5$ model, where the CH_4 molecule is located near the center of the model and its position relative to the zeolite framework is the same as in the original $1 \times 1 \times 1$ model. This approximation is reasonable because the vdW contributions from the framework atoms that reside beyond the $5 \times 5 \times 5$ model are negligible.

Least-squares fitting was then used to determine values for the scaling factors s_{12} and s_6 that minimized the deviation between the adsorption energies defined by the force

field and the DFT/CC values. This gave scaling factors of s_{12} and s_6 of 9.08 and 1.83, respectively which in turn gives the initial force field. Since the vdW terms of the force field developed here have the same form as the 12-6 Lennard-Jones (LJ) potential, the $s_{12}C_{12}^{ij}$ and $s_6C_6^{ij}$ term in Eq. (4.1) can also be expressed with corresponding ε_{ij} and σ_{ij} values in Eq. (4.3) for each cross species interaction.

Table 4.1 Attractive and repulsive coefficients (C_6^{ij} and C_{12}^{ij}) and the sum of van der Waals radii ($R_0^i + R_0^j$) for each cross species for CH_4 in silica CHA and aluminophosphate (AlPO) and N_2 in silica CHA.

Cross species	C_{12}^{ij} ($Jnm^{12}\ mol^{-1}$)	C_6^{ij} ($Jnm^6\ mol^{-1}$)	$R_0^i + R_0^j$ (Å)
Si–C	2.03×10^{-3}	4.02	3.168
Si–H	2.29×10^{-4}	1.14	2.717
O_z–C	2.63×10^{-4}	1.11	2.794
O_z–H	2.59×10^{-5}	0.31	2.343
Al-C	1.89×10^{-3}	4.34	3.091
Al-H	2.08×10^{-3}	1.23	2.640
P-C	1.83×10^{-3}	3.70	3.157
P-H	2.06×10^{-4}	1.05	2.706
Si–N	1.53×10^{-3}	3.37	3.113
O_z–N	1.96×10^{-4}	0.93	2.739

Besides the random sampling of CH_4 configurations, 760 configurations generated using the GCMC technique were also included in the force field fitting using the initially obtained force field. After that, a certain number of CH_4 configurations from

the snapshots of simulations were randomly chosen. We refitted the force field using all (random + GCMC) configurations. We found that a total of 760 CH_4 configurations from GCMC simulations plus the original 300 random configurations can give converged force field parameters (the changes of ε_{ij} and σ_{ij} values relative to the initial FF are small). Table 4.2 shows the final fitted force field parameters. For simplicity, we will refer to the force field derived in this way as CCFF. The mean absolute deviation (MAD) and mean deviation (MD) is 0.85 kJ/mol (0.22 kJ/mol) for the CH_4 for the converged CCFF. The force field parameters for the DFT-D2 method (D2FF), which was developed earlier are also shown for comparison in Table 4.2.

Table 4.2 CCFF and D2FF Parameters for CH_4 in silica zeolites.

Cross species	CCFF		D2FF	
	ε/k_B (K)	σ (Å)	ε/k_B (K)	σ (Å)
Si–C	23.49	3.47	47.58	3.61
Si–H	98.99	3.64	33.82	3.10
O_z–C	9.37	2.89	27.84	3.19
O_z–H	5.52	3.25	22.65	2.67

A detailed comparison of the interaction energies predicted with the fitted force fields and the corresponding calculations at the DFT/CC level, is shown in Fig.4.7. As shown in Fig. 4.7, the total of 1060 DFT/CC calculations span a broad range of adsorption energies, from -17 to +30 kJ/mol. Randomly generating CH_4 configurations cannot effectively capture the energetically favorable interacting states, hence GCMC configurations of CH_4 molecules were used. As expected, the force field interaction

energies are reasonably consistent with the DFT/CC energies. Some deviations between force fields and DFT energies exist, especially when repulsive interactions are the dominating factor in determining the overall adsorption energy. In this case, the force fields somewhat overestimate the interaction energies.

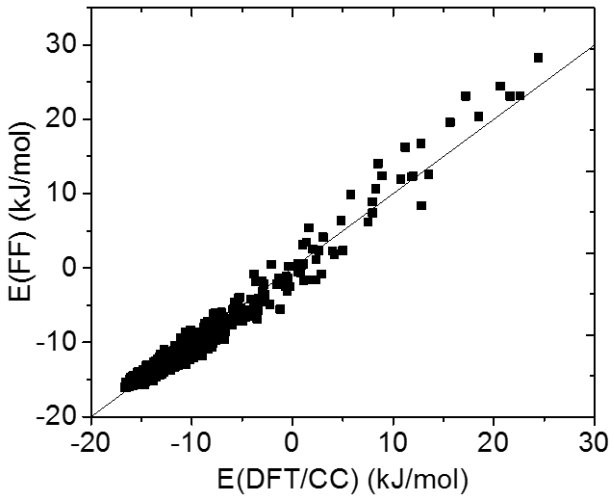

Figure 4.7 Comparison of the interaction energies of CH_4 in silica CHA for the CCFF and DFT/CC.

4.5 Classical simulations using DFT-derived force fields

To examine the applicability of the force fields developed above, we compared CH_4 adsorption properties predicted using the force fields with experimental data for several zeolites. Adsorption isotherms were predicted computationally using standard GCMC methods. We first focus on CH_4 adsorption in Si-CHA on which the force field fitting is based. GCMC simulations were performed at 298 and 323 K for pressures from 10 to 180 kPa. The simulated isotherms are shown in Figure 4.8 (a), along with experimental data[147]. The CCFF predicted the CH_4 adsorption in good agreement with the

experiments. This is in contrast to other DFT methods such as DFT-D2, DFT-D3, VDW-DF-CC, VDW-DF-CC as discussed earlier.

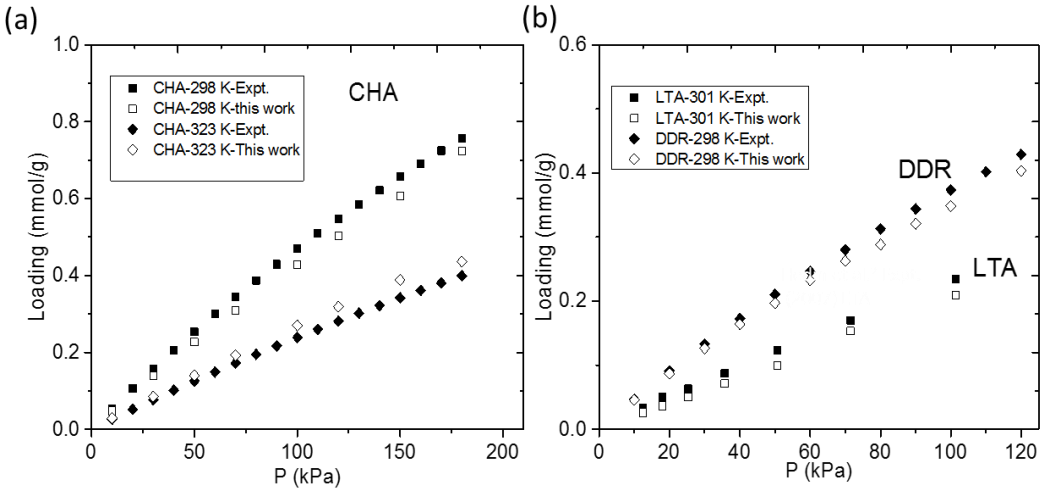

Figure 4.8 Comparison of simulated (CCFF) and experimental adsorption isotherms (a) at 298 K and 333 for CH_4 in silica CHA (b) at 298 K in silica DDR and at 301 K silica LTA respectively. The experimental data are from Maghsoudi *et al.*[147]for CHA, from Himeno *et al.*[148] for DDR and, from Hedin *et al.*[62] for LTA The lines are drawn to guide the eyes.

To validate the transferability of the developed force field, CCFF, we also performed GCMC simulations of CH_4 in two other silica zeolites, DDR and LTA. These materials were chosen because reliable experimental data in these two materials are available. Figure 4.8 (b) shows the comparison of simulated and experimental results for CH_4 adsorption in DDR at 298 K and in LTA at 301 K, under pressures from 10 to 120 kPa. It can be seen that the CCFF simulated isotherms agree very well with the experimental results, showing a good transferability of developed force field to silica zeolites.

4.6 Extension of DFT/CC to Aluminophosphates (AlPOs)

4.6.1 Overview of AlPOs

The synthesis of aluminophosphate molecular sieves (AlPOs) was first reported in 1982.[165] Aluminophosphates (AlPOs) are a class of zeolites with framework structures built of alternate AlO_4^- and PO_4^+ tetrahedral building units instead of SiO_4 units of silica zeolites. Aluminophosphates (AlPOs) are molecular sieves with a neutral framework and have no need for charge-balancing, exchangeable cations making the framework homogeneous. For cation-exchanged aluminosilicates used in the separation of gases containing polar molecules, the regeneration of the spent adsorbent due to the strong interaction is energy intensive. AlPOs don't have these problem even after containing both Lewis and protonic acid sites.[166-167] Even though aluminophosphate molecular sieves are considered globally neutral, adsorbate molecules featuring permanent electric moments can interact with a local non-zero framework electric field.[168] The stronger interactions existing in smaller-pore aluminophosphate molecular sieves have a greater effect on non-polar molecules like CH_4 than on polar molecules.[169] Aluminophosphate molecular sieves like the 10MR AIPO-11 feature permanent dipoles oriented according to the channel direction.[170] Because of the lower electronegativity of the Al atom with respect to the P atom, each pair of adjacent Al-P atoms represents a permanent dipole.[169] The polar properties .are less pronounced in the 8MR aluminophosphate molecular sieves AIPO-14 and AIPO-18, because of their 3D channel system which does not allow for the representation of framework as stacked 2-D nets alternately linked by Al and P atoms.[169] These characteristics may make AlPOs useful in the separation processes.

The rich variety of pore structures, both cavities and channels, as well as the cation sites that can be exchanged in the SAPO analogs, offer promising opportunities for their use as new sorbents for separations. The AlPOs (AlPO-14[171], AlPO-18[172],AlPO-11[173], and AlPO-5[174]) listed in Table 4.3 have been studied for CO_2/CH_4 separation. Although there are numerous simulation studies on the adsorption and diffusion of gaseous adsorbates in silica zeolites and cation exchanged aluminosilicates, theoretical studies in AlPOs are scarce, mainly due to the absence of suitable force fields. For CH_4, only two theoretical studies of adsorption are available, one in AlPO-5[175] and one in AlPO-11[176]. All these studies use different force field parameters to model CH_4-AlPO interactions. As a result there hasn't been a detailed investigation about the transferability of a given force field to AlPO materials.

Table 4.3 List of AlPO materials with available experimental CH_4 adsorption data.

AlPO	Zeolite topology	Ring size	Dimensionality
AlPO-14[171]	AFN	8MR	3
AlPO-18[172]	AEI	8MR	3
AlPO-11[173]	AEL	10MR	1
AlPO-5[174]	AFI	12MR	1

4.6.2 DFT/CC method

In case of AlPO materials, we need Al-C, Al-H, P-C, and P-H CC-correction curves. The calculation details for obtaining DFT/CC correction functions are similar to that for CH_4 with $Si(OH)_4$. Here, we have just replaced $Si(OH)_4$ with $Al(OH)_3$ for Al-C and Al-H while with $P(OH)_5$ for P-C and P-H corrections. For AlPO, N_a and N_b in Eq.

(4.1) are the numbers of atoms of the CH_4 and of the monomer b ($Al(OH)_3$ or $P(OH)_5$) , ε_{ij} are the DFT/CC correction functions, and R_{ij} is the intermolecular atomic distance between atom *i* (C, H) and *j* (Al or P). The correction functions are obtained again using the RP-RKHS interpolation scheme from a set of energies calculated at CCSD(T)/CBS and DFT/AV5Z levels for a suitable reference clusters $Al(OH)_3$--CH_4 (65 grid points in total) or $P(OH)_5$--CH_4 (63 grid points in total) as shown in Fig. 4.9. All other calculation details are similar to that for CH_4--$Si(OH)_4$ cluster and are summarized above. The $\varepsilon_{Al\text{-}C}$, $\varepsilon_{Al\text{-}H}$, $\varepsilon_{P\text{-}C}$ and $\varepsilon_{P\text{-}H}$ correction functions are shown in Fig. 4.10. The numerical values of ε_{ij} and α_k are reported in Appendix C. The resulting correction functions then are used to improve the DFT energies in FF fitting for CH4 in periodic aluminophosphates, in particular AlPO-5.

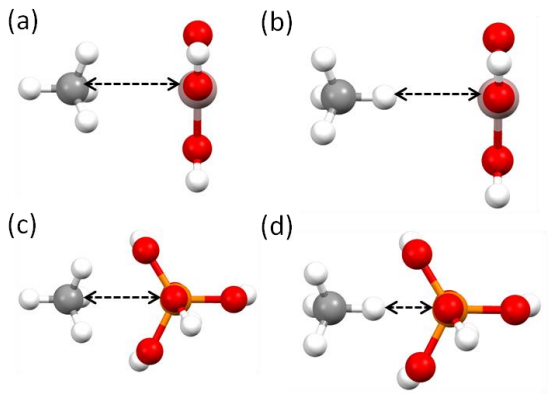

Figure 4.9 Definition of the reference set used for the generation of the DFT/CC correction functions for Al and P: $Al(OH)_3\cdots CH_4$ (a, b), $P(OH)_5\cdots CH_4$ (c, d). The *C2v* symmetry constraints were applied. C, H, Al, P, and O atoms depicted as grey, white, rosybrown, orange, and red spheres, respectively.

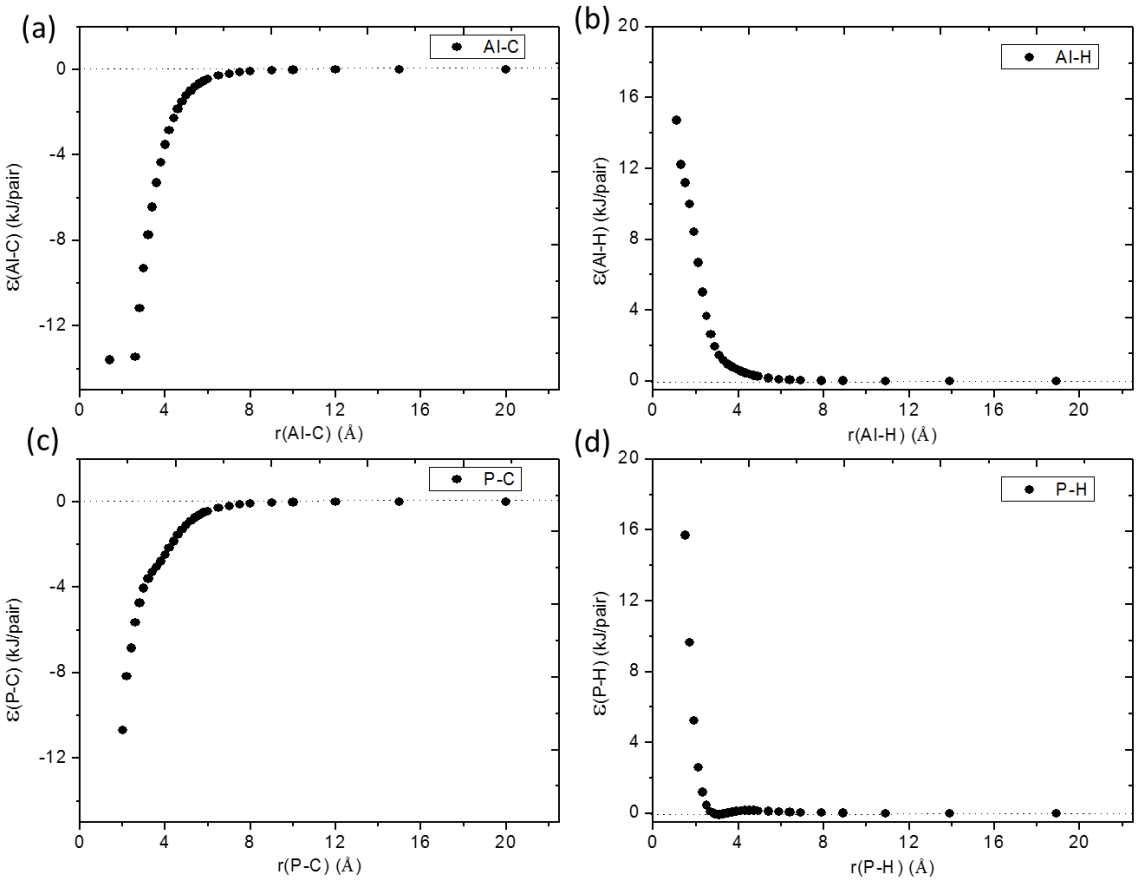

Figure 4.10 DFT/CC correction curves for (a) Al-C, (b) Al-H, (c) P-C, and (d) P-H interactions.

4.6.3 FF fitting for CH_4 in aluminophosphate (AlPO)

AlPO-5 ($Al_{12}P_{12}O_{48}$) was chosen as a model adsorbent for FF fitting. The unit cell (P6/mcc space group) of AlPO-5 was first fully optimized at the DFT level as implemented in Vienna ab-initio Simulation Package (VASP). For this, the GGA functional of Perdew, Burke and Ernzerhof [177] (PBE) was used with Grimme's D2[137] corrections to include dispersion interactions with the PAW method[178]. The lattice constants were optimized at a plane wave cutoff of 700 eV while, the internal coordinates were energy minimized at a 400 eV cutoff. The energy minimization was terminated

when the individual atomic forces are less than 0.03 eV/Å. To reduce the computational cost, the DFT calculations were performed at the Γ-point. The lattice constants obtained for AlPO-5 using PBE-D2 are a = b = 13.991 Å, c = 8.710 Å and α = β = 90.0°, and γ = 120.0°, which are close to the experimentally determined lattice constants, a = b = 13.725 Å, c = 8.473 Å and α = β = 90.0°, and γ = 120.0°.[179] The optimized primitive unit cell of AlPO-5 is shown in Fig. 5.11 (a).

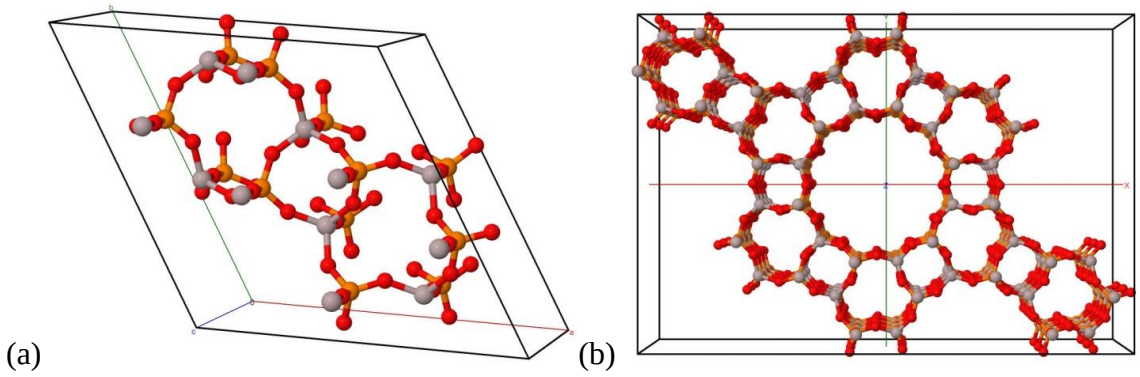

Figure 4.9 (a) Primitive unit cell of AlPO-5 used in the DFT calculations. (b) Supercell of AlPO-5 used in the GCMC calculations. Al, P, and O atoms depicted as rosy brown, orange, and red spheres, respectively.

The calculation details for each step of the FF development algorithm are same as in case of silica CHA discussed above. We first calculate the interaction energies for a 200 randomly generated adsorbate configurations using Density Functional Theory (DFT) in the primitive unit cell of AlPO-5. To obtain an initial version of the force field, these interaction energies are fit to a classical potential form given in Eq. (6). We use the new FF parameters in a Grand Canonical Monte Carlo (GCMC) simulation to generate isotherms and a larger set (400) of adsorbate configurations. Again, DFT interaction energies are obtained for the new configurations and the FF parameters are recalculated

using a least-square fit to yield the final, DFT-consistent version of the force field. The dimensionless, s12 and s6 parameters obtained are 4.35 and 0.848. The final FF parameters for CH_4- AlPO-5 interactions are given in Table 4.4 and are compared with DFT-D2 parameters obtained using PBE-D2 functional. Fig. 4.12 compares the CCFF predicted energies for 600 CH_4 configurations with the DFT/CC energies. The MAD (MD) is 1.90 kJ/mol (0.32 kJ/mol) for the CH_4 for the converged FF.

Table 4.4 CCFF and D2FF Parameters for CH_4 in AlPO-5.

Cross species	CCFF		D2FF	
	ε/k_B (K)	σ (Å)	ε/k_B (K)	σ (Å)
Al–C	49.52	3.62	57.88	3.56
Al–H	36.09	3.09	42.17	3.04
P-C	37.19	3.69	43.46	3.63
P-H	26.52	3.17	31.00	3.11
O_z–C	23.13	3.27	27.03	3.21
O_z–H	18.81	2.74	21.98	2.70

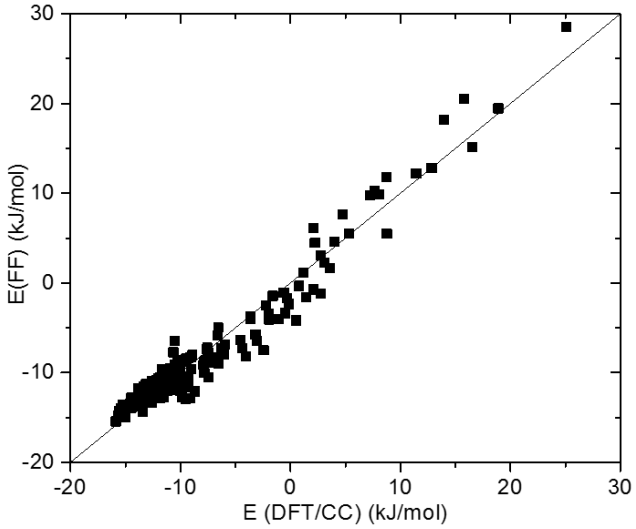

Figure 4.10 Comparison of the adsorption energies of CH_4 obtained using CCFF with DFT/CC in the primitive unit cell of AlPO-5.

4.6.4 Classical simulations and CCFF transferability

Figure 4.13 compares the predicted adsorption isotherms for various aluminophosphates with corresponding experimental data indicating excellent agreement.

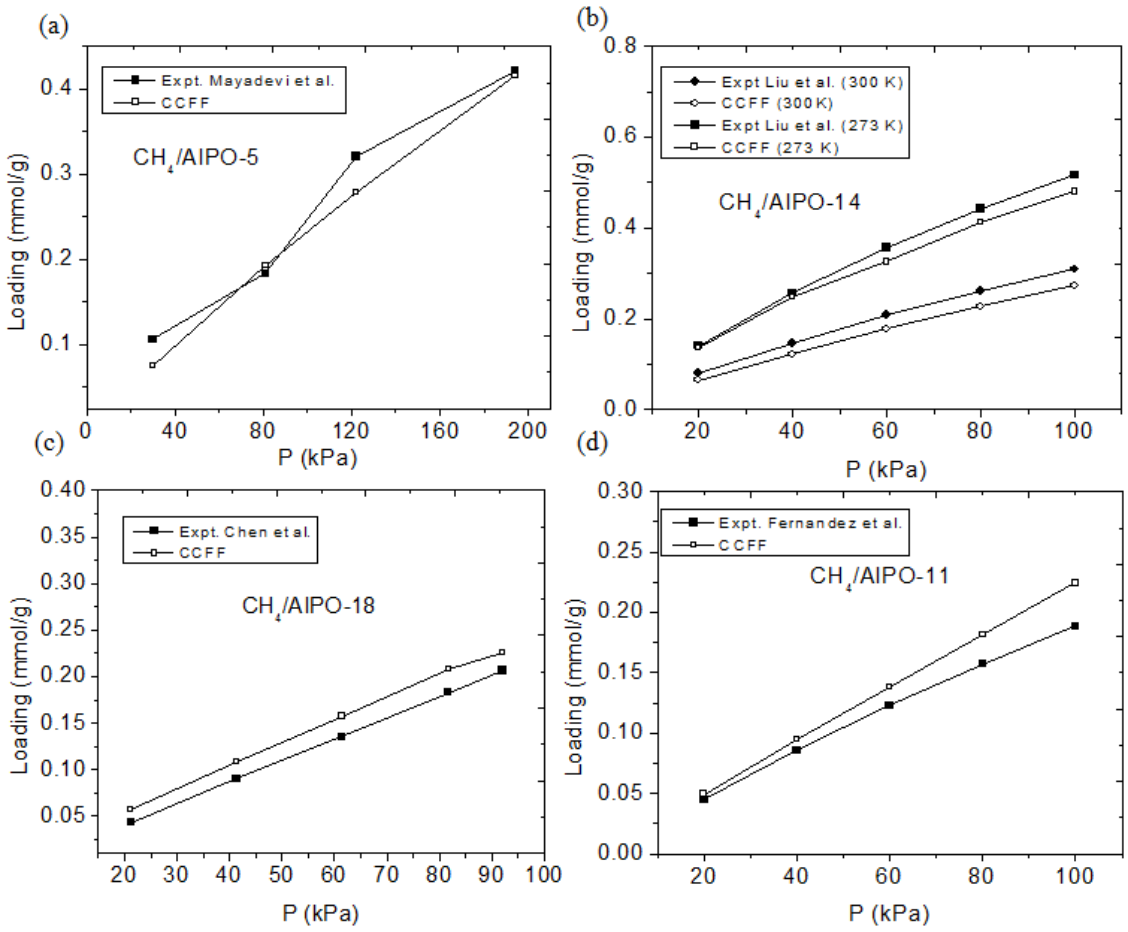

Figure 4.11 Comparison of simulated (CCFF) and experimental adsorption isotherms for CH_4 (a) at 305 K in AlPO-5, (b) at 273 K and 300 K in AlPO-14, (c) at 323 K in AlPO-18, and (d) at 308 K in AlPO-11, respectively. The experimental data are from Mayadevi et al.[174] for AlPO-5, Liu et al.[171] for AlPO-14, Chen et al.[172] for AlPO-18, and Fenandez et al.[173] for AlPO-11. The lines are drawn to guide the eyes.

4.7 Extension of DFT/CC to N_2

4.7.1 FF fitting summary for N_2

In case of N_2, the calculation details for obtaining DFT/CC correction functions are similar to that for CH_4 with H_2, H_2O, and $Si(OH)_4$. Here, we have just replaced CH_4 with N_2. For N_2, N_a and N_b in Eq. (4.1) are the numbers of atoms of the N_2 and of the monomer b (H_2, H_2O, or $Si(OH)_4$) , ε_{ij} are the DFT/CC correction functions, and R_{ij} is the intermolecular atomic distance between atom i(N) and j(H, O, or Si). The correction functions are obtained again using the RP-RKHS interpolation from a set of energies calculated at CCSD(T)/CBS and DFT/AV5Z levels for a suitable reference clusters N_2--H_2 (34 grid points), N_2--H_2O (33 grid points), and N_2--$Si(OH)_4$ (31 grid points) as shown in Fig. 4.14. All other calculation details are similar to that for CH_4 and are summarized above. The $N_2\cdots H_2$, $N_2\cdots H_2$, and $N_2\cdots Si(OH)_4$ reference systems (Fig. 4.14) provides the ε_{NH} , ε_{NO} and ε_{NSi} correction functions as shown in Fig. 4.15. The numerical values of ε_{ij} and α_k are reported in Table C5 in Appendix C. The resulting correction functions then are used to improve the DFT energies in FF fitting for N2 in periodic zeolites.

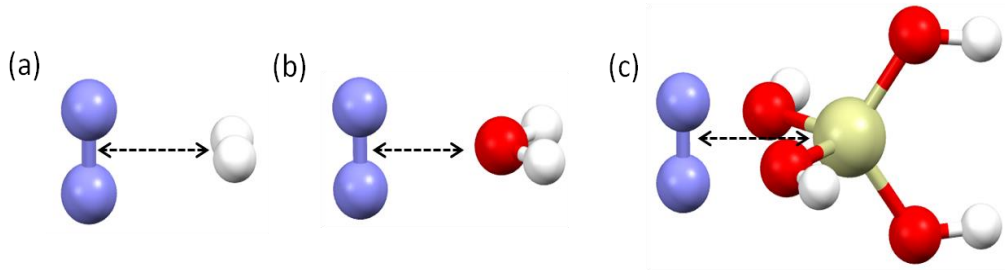

Figure 4.12 Definition of the reference set used for the generation of the DFT/CC correction functions for N_2: $N_2\cdots H_2$ (a), $N_2\cdots H_2O$ (b), and $N_2\cdots Si(OH)_4$ (c). The *C2v* symmetry constraints were applied. The N, O, H, and Si atoms are depicted in blue, red, white, and yellow, respectively**.**

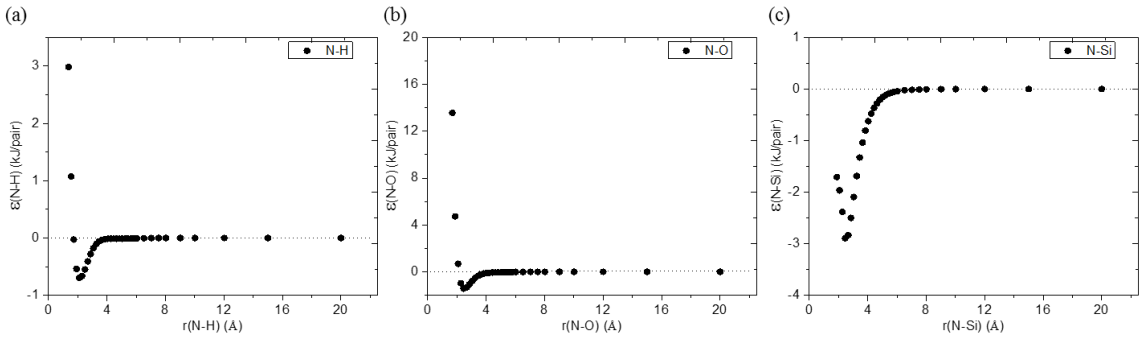

Figure 4.13 DFT/CC correction curves for (a) N-H, (b) N-O, and (c) N-Si interactions

The calculation details for each step of the FF development algorithm are same as in case of silica CHA except we use charges on N_2 and hence on the zeolite. We used the 2LJ3CB.MSKM potential[180] proposed by Theodorou *et al.* for N_2 whose LJ parameters for bulk N_2-N_2 interaction are given in Table 4.5 . For N_2, the magnitude of the charge on each N is -0.40484. A point charge of magnitude $-2q_N$ so that the total molecule charge is zero is located in the middle between the two atoms (pseudoatom). We used DDEC charges[27] for O_z (-1.025) and Si (+2.1) of zeolite. We first calculate the interaction energies for a 100 randomly generated adsorbate configurations using Density Functional Theory (DFT) in the primitive unit cell of CHA. The Coulombic interactions for each configurations are measured and summed based on a finite $3 \times 3 \times 3$ model, where the N_2 molecule is located in the central unit cell of the model and its relative position is kept same as in the $1 \times 1 \times 1$ model. These DFT interaction energies after subtracting the Coloumbic energies are fit using least square method to a LJ 12-6 form given in Eq. (4.6) to derive initial FF parameters. This FF is used in a GCMC calculation to generate 450 adsorbate configurations. Again, DFT and Coloumbic interaction energies are obtained for the new configurations and the FF parameters are refit to yield the final, converged force field. The final FF parameters for N_2-CHA interactions are given in Table 4.5 and

are compared with DFT-D2 parameters obtained using PBE-D2 functional. Figure 4.16 compares the CCFF predicted energies for 550 N_2 configurations with the DFT/CC energies. The mean absolute deviation (mean deviation) is 1.58 kJ/mol (-0.14 kJ/mol) for the N_2 for the converged FF.

Table 4.5 CCFF and D2FF Parameters for N_2 in silica zeolites.

Cross species	CCFF		D2FF	
	ε/k_B (K)	σ (Å)	ε/k_B (K)	σ (Å)
N-N[180]	36.4	3.32	-	-
N-Si	46.00	3.57	48.53	3.58
N-O_z	27.31	3.14	28.81	3.15
N-O_z[181]	58.25	3.06	FF used in earlier studies	

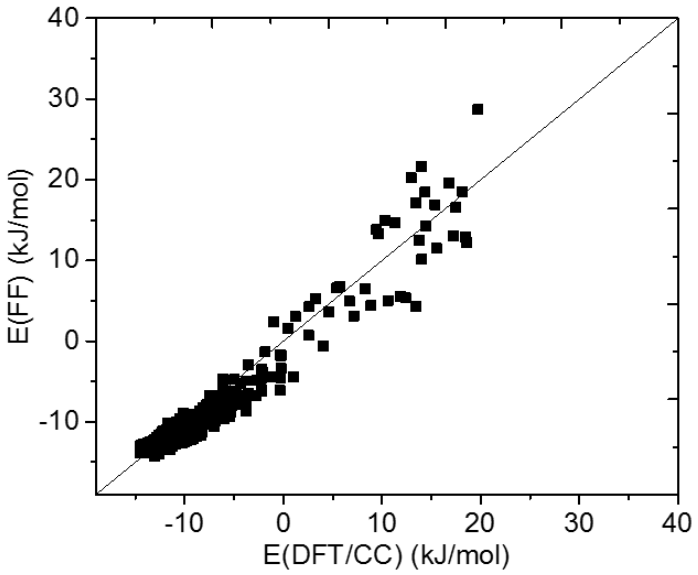

Figure 4.14 Comparison of the adsorption energies of N_2 obtained using CCFF with DFT/CC in the primitive unit cell of silica CHA.

4.7.2 Classical simulations and CCFF transferability

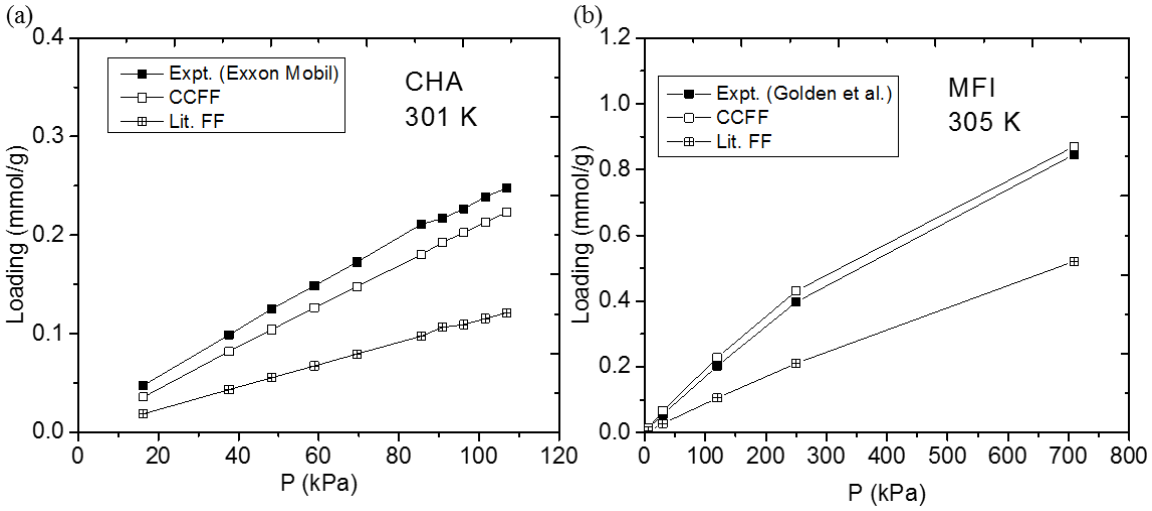

Figure 4.15 Comparison of simulated (CCFF and literature FF[181]) and experimental adsorption isotherms (a) at 301 K for N_2 in silica CHA, (b) at 305 K for N_2 in silica MFI. The experimental data are provided by our experimental collaborator, Exxon Mobil. for CHA and are taken from Golden *et al.*[182] for MFI. The lines are drawn to guide the eyes.

We first calculate N_2 adsorption in silica CHA in which the force field is developed. GCMC simulations were performed at 301 K, under pressures from 10 to 107 kPa. The simulated isotherms are shown in Figure 4.17 (a), with a comparison of experimental data from our experimental collaborator Exxon Mobil Research and Engineering. It is clear from the figure that the CCFF predicted the CH_4 adsorption in good agreement with the experimental data. We also performed GCMC calculation with the FF proposed by Theodorou[180] which is the only FF available in literature to best of our knowledge. The adsorption isotherms obtained using this FF deviated from the experimental data. This indicates the importance of first-principles method in the force field development for describing interactions between N_2 and zeolite. We also performed

GCMC simulations in zeolites DDR and MFI to test the transferability of the force field. As seen from Fig. 4.17 (b) and 4.18, the performance of CCFF is excellent while FF by Theodorou underestimates the adsorption of N_2.

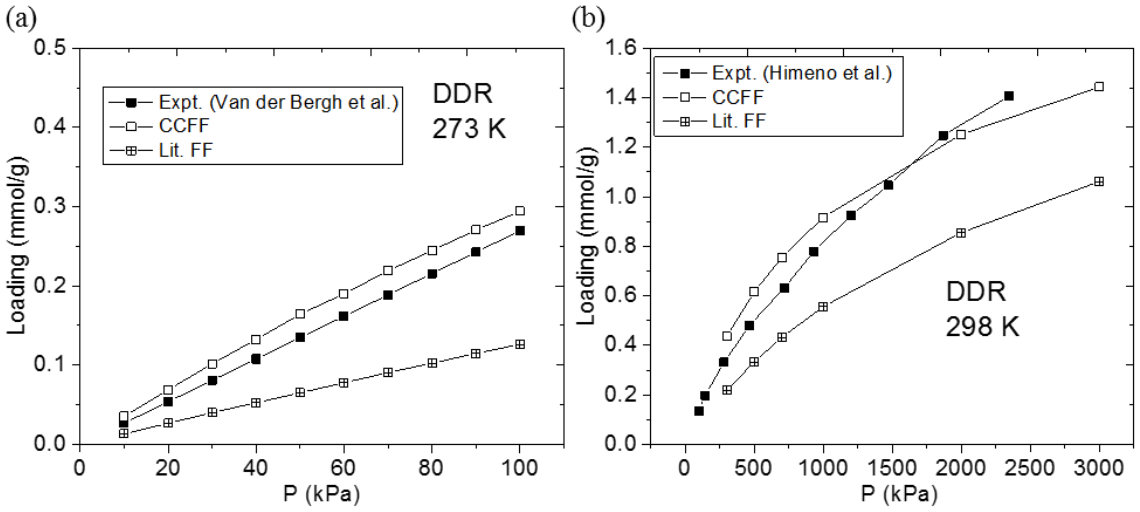

Figure 4.16 Comparison of simulated (CCFF and Theodorou FF) and experimental adsorption isotherms at 273 K and 298 K for N_2 in silica DDR. The experimental data are from Van der Bergh et al.[98] The lines are drawn to guide the eyes.

4.8 CH_4 and N_2 in cationic zeolites

Now we want to extend our DFT/CC methodology to cation-exchanged (especially, Na^+ and K^+) zeolites, known as aluminosilicates. For developing coupled cluster force field for CH4 and N_2 in aluminosilicates, we require CC correction parameters for CH_4 and N_2 with Al, Si. CH_4-Al, CH_4-Si, N_2-Al, and N_2-Al CC corrections are already available as given in the previous sections. For cation-zeolite interactions, we used potential developed by Fang *et al.*[146] Here, extra-framework cation as shown in Fig. 4.19 interacts with two interactions: (i) a Coulombic interaction between

all the atoms using the charges given in Table 4.6 and (ii) a Buckingham interaction instead of LJ-12-6 between Na and O_z atoms of a zeolite given by

$$E_{Buck}(R_{ij}) = A_{ij}\exp(-\frac{R_{ij}}{B_{ij}}) - \frac{C_{ij}}{R_{ij}^6} \tag{4.8}$$

where, A_{ij}, B_{ij}, and C_{ij} are the Buckingham parameters for cross species i and j given in Table 4.6 for Na-O_z and K-O_z. The Buckingham terms for Na-Si, Na-Al, and Na-Na interactions are not explicitly considered, but taken into account through the effective potential with the oxygen atoms.[146]

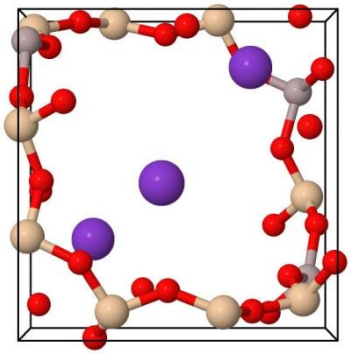

Figure 4.19 Primitive unit cell of M-CHA (M= Na or K) with Si/Al=3 ($Si_9Al_3O_{24}M_3$) used in the DFT calculations. Al, Si, O, and Na (K) atoms depicted as rosy brown, orange, red and violet spheres, respectively.

Using the CC corrections developed for CH_4 in pure silica zeolites, the DFT/CC force field was developed for Na-exchanged zeolites by Dr. Hanjun Fang in our group. Here we fitted DFT/CC energies of random (600) and GCMC generated (600) configurations of CH_4 in Na-CHA after subtracting Coulombic interactions. The FF parameters for Al-C, Al-H, Na-C, and Na-H are given in Table 4.7 and the predicted adsorption isotherms along with the experimental data are given in Appendix C (Fig. C1)

showing outstanding agreement. Then, in case of K-CHA, we only developed K-C and K-H LJ-12-6 parameters (see Table 4.7) by keeping the parameters for other cross species interactions the same as in Na-CHA to develop a self-consistent force field. We again used random (600) and GCMC generated (600) configurations of CH_4 in K-CHA. For N_2, the strategy is repeated with first obtaining LJ-12-6 interaction parameters for N-Al and N-Na in Na-CHA and then for N-K using K-CHA (see Table 4.7).

Table 4.6 Buckingham parameters for Na/K–framework interactions along with charges used on framework atoms and on extra-framework cations.

Cross species	Buckingham potential			Coulombic potential		
	A (eV)	B (Å)	C (eV)	Charge (e)		
Na-O_z	3261.6	0.2597	45.4	Na (0.99)	Si (2.21)	O_z^{Si}(-1.105)
K-O_z	5258.3	0.2916	193.7	K (0.99)	Al (2.08)	O_z^{Al}(-1.32)

Table 4.7 CCFF Parameters for CH_4 and N_2 in Na^+ and K^+ exchanged zeolites.

Cross species	CCFF		Cross species	CCFF	
	ε/k_B (K)	σ (Å)		ε/k_B (K)	σ (Å)
Al–C	61.90	3.258	Al–H	45.10	2.782
Na–C	128.31	2.736	Na–H	114.04	2.261
K–C	48.21	3.30	K–H	37.08	2.79
Al–N	19.74	3.05	Na–N	41.78	2.55
K–N	47.98	3.23			

To check the performance of the developed force fields and its transferability to other cationic zeolites with different Si/Al ratios, we performed GCMC simulations. Getting good initial positions of a cations is essential and hence we used a parallel tempering procedure.[183-184] In this procedure, we run simulations at different temperatures simultaneously for a given a framework of aluminosilicate with randomly distributed extra-framework cations equilibrating and generating framework copies at each

temperature. Then, based on the Metropolis criterion, configurations at different temperatures are swapped known as replica exchange move. The idea of this method is to make configurations at high temperatures available to the simulations at low temperatures. In the end, we obtain equilibrated cationic zeolites that can be used in GCMC simulations. We have generated GCMC predicted adsorption isotherms for CH_4 in K-CHA (Si:Al=2.62) and K-KFI (Si:Al=4.59) at 298 K, at pressures between 0 to 10 bar (see Fig. 4.20). Even though, the agreement with the experimental data from Li *et al.*[185] is good, small errors are still existed. This may be due to the fact that zeolites are considered pure crystal in simulations, while structural defects and/or impurities exist in synthesized crystal, especially in cationic zeolites. Similarly, the predicted adsorption isotherms for N_2 (Fig. 4.21) in Na(K)-CHA (Si:Al=2.62) and in Na(K)-KFI (Si:Al=4.59) agree well with the experimental adsorption isotherms[185].

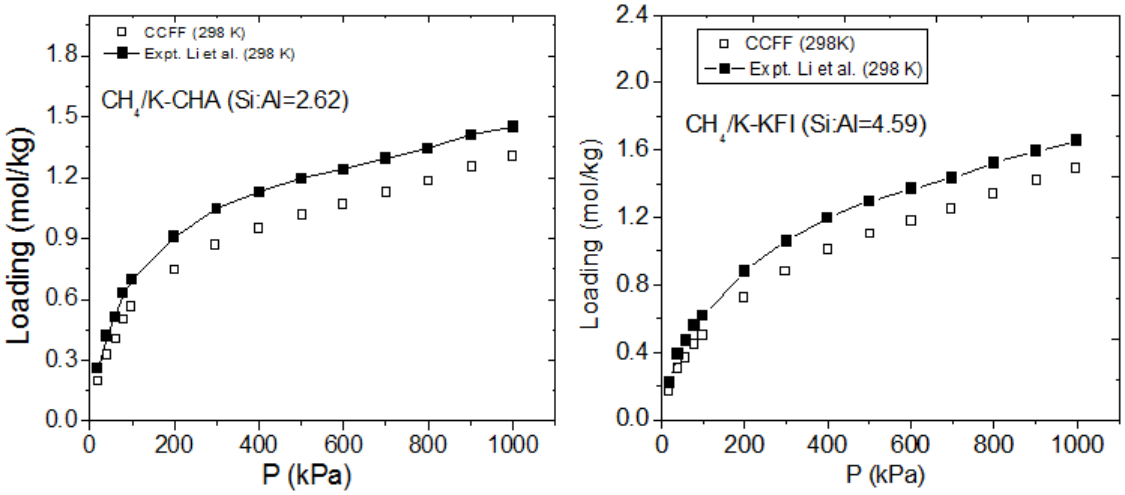

Figure 4.20 Comparison of simulated (using CCFF) and experimental adsorption isotherms at 298 K for CH_4 in (a) K-CHA (Si:/Al=2.62) and (b) K-KFI (Si:/Al=4.59) . The experimental data are from Li *et al.*[185] The lines are drawn to guide the eyes.

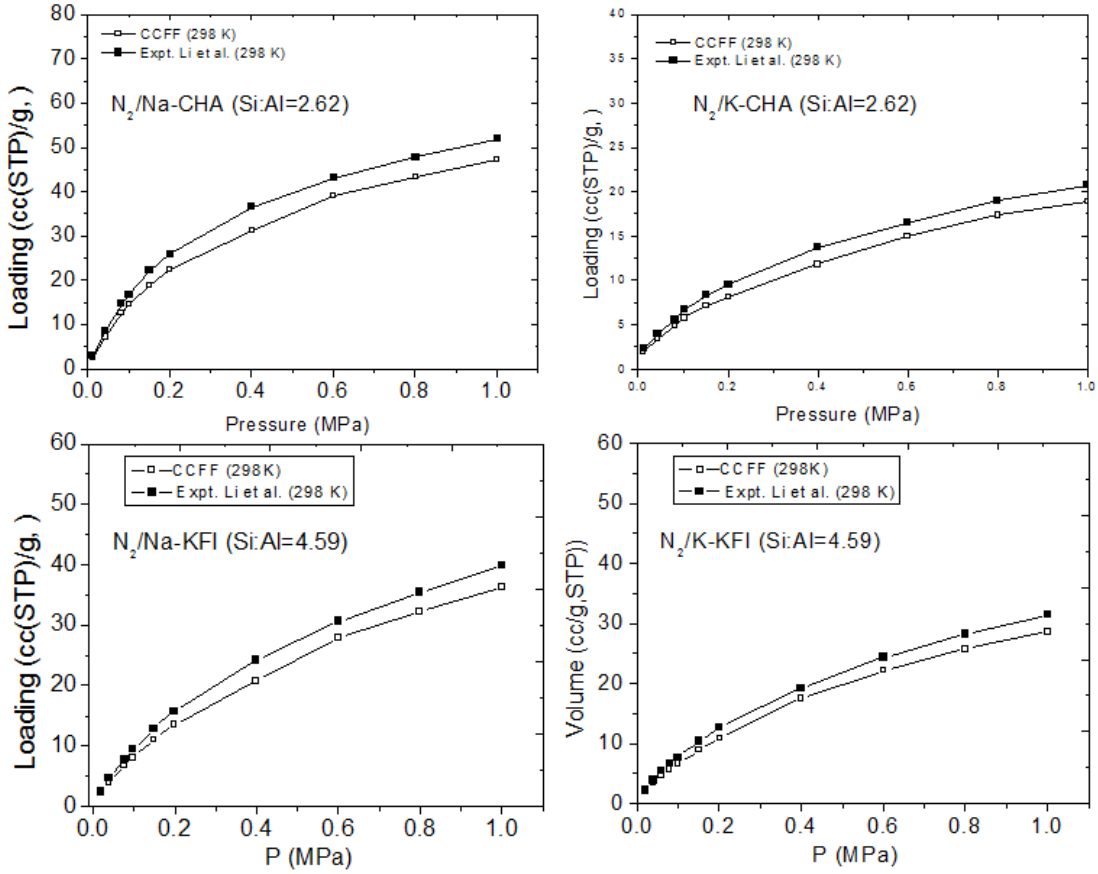

Figure 4.21 Comparison of simulated (using CCFF) and experimental adsorption isotherms at 298 K for N_2 in (a) Na-CHA (Si:/Al=2.62), (b) K-CHA (Si:/Al=2.62), (c) Na-KFI (Si:/Al=4.59), and (d) K-KFI (Si:/Al=4.59) . The experimental data are from Li *et al.*[185] The lines are drawn to guide the eyes.

4.9 Conclusions

We developed a transferrable, first-principles derived force field using the DFT/CC method to first predict CH_4 adsorption in silica zeolites without taking any inputs from experimental adsorption isotherms. The choice of first-principle method has a significant influence on the ability of force fields to accurately describe CH_4–zeolite interactions. The PBE-D2 derived force field, which performed well for CO_2 adsorption in silica

zeolites, does not perform well for CH_4 in silica zeolites. Other DFT methods like PBE-D3, VDW-DF2, and VDW-DF-CC derived force fields also fail in predicting adsorption isotherms of CH_4 in silica zeolites. A force field derived from the higher level of theory, the DFT/CC method, performed well. Good agreement with experimental data in different silica zeolites indicate the transferability of the force field.

A similar approach was extended to aluminopshosphates and aluminosilicates and also to N_2 to see the application of the DFT/CC method for different adsorbents and adsorbates. A transferable first-principle derived FF for CH_4-aluminophosphates, CH_4-aluminosilicate, N_2-silica zeolite, and N_2-aluminosilicate interactions using DFT/CC method are obtained.

CHAPTER 5

DFT Derived Force Fields for Modeling Hydrocarbon Adsorption in Silica Zeolites

5.1 Introduction and Literature Review

There is significant industrial interest in hydrocarbon separations, especially olefin/paraffin separations. Many nanoporous materials such as zeolites have been studied for such separations based on their adsorption and diffusion properties.[186-192] In particular, 8 member ring (8MR) zeolites such as DDR, CHA, and ITQ-12 are potential materials for such olefin/paraffin separations because of their small pore size.[186-188, 191] The wide range of possible framework topologies, chemical compositions, and extra-framework cations has allowed for the fine-tuning of zeolite structures to meet specific separation tasks. Therefore, it is important to explore the adsorption and diffusion behaviors of hydrocarbons in as many zeolites as possible to find the best candidates for such separations. The rational design and optimization of zeolite-based adsorptive separation processes (e.g., pressure/temperature swing adsorption) requires the ability to predict and understand the sorption characteristics of a given adsorbate−adsorbent system. However, the rich structural and chemical diversity of zeolites and sorbent molecules makes this a challenging task for predictive modeling.

In addition to experiment, molecular simulation has proved to be a useful tool to investigate the adsorption and diffusion properties of gas and liquid molecules confined in porous materials.[193] Multiple united-atom (UA) force fields[34, 55, 194-196] have been

proposed to describe the adsorption and diffusion properties of alkanes in nanoporous framework structures. A force field proposed by Dubbeldam *et al.*[55] is one of the most widely used FFs for molecular simulations of linear and branched alkanes in silica zeolites. This force field was parameterized so as to reproduce experimentally determined isotherms on MFI-type zeolite. It reproduces adsorption isotherms and other thermodynamic properties and was shown to be extended to other nanoporous framework topologies.[55] TraPPE-zeo is a relatively new FF in which adsorbate-zeolite interaction is obtained using Lorentz-Berthelot mixing rule and the already available TraPPE potential for bulk phase gas adsorbates.[117] For this purpose, TraPPE-zeo developed a generalized force field for Si and O atoms of a zeolite to match experimental adsorption isotherms of n-heptane, carbon dioxide, and ethanol in silicalite-1 (MFI topology) and propane in theta-1 (TON topology). This FF allows for accurate predictions for both adsorption and diffusion of alkanes, alcohols, carbon dioxide, and water over a wide range of pressures and temperatures. The FF gives reasonable agreement with the experimental data for the training set as expected. The FF gives good agreement for adsorption of CH_4 and ethane but its performance deteriorates for other branched alkanes[117], raising questions about its generality. The transferability of this FF to other zeolite topologies has not been studied in depth; instead only a single example of methanol adsorption in faujasite (FAU) is demonstrated where it underpredicts adsorption isotherms at lower pressure.[117]

There are few reliable UA force fields available in literature that deals with the adsorption of alkenes in zeolites.[118, 197] The first FF was developed by Jakobtorweihen *et al.* This force field accurately describes the adsorption properties of alkenes in the silicalite-1 as well as in the Theta-1 and DD3R (DDR) zeolites.[197] This FF, however uses

tail corrections, which make it less practical to use in inhomogeneous systems.[198-199] As most of the accurate alkane models do not use these tail corrections for doing proper adsorption and diffusion in this type of systems, it would be useful to have a similar type of model for both alkanes and alkenes. Another FF is an extended version of the Jakobtorweihen FF to include the effects of sodium cations by Granato *et al.*[200] Next, Calero *et al.* developed an UA FF for the linear alkenes by using the strategy of fitting inflection point on the adsorption isotherms in silicalite-1.[118] The same strategy was previously used by Dubbeldam *et al.*[55] to develop force field for alkanes in zeolites as mentioned above. The empirical UA force field developed in this fashion is claimed to describe the adsorption properties of linear alkenes in several pure silica zeolites, such as MFI, TON, ITQ-29, ITQ-3, ITQ-32, CHA, and DD3R. Even though the results show that this force field is applicable to most pure silica zeolites, some discrepancies can be observed in predicting adsorption isotherms in silica CHA and DDR.

The FFs listed above were developed via fitting to experimental data. An approach that avoids potential pitfalls associated with using experimental data is to use force fields that have been developed from quantum chemical calculations (such as the DFT/CC method described in the previous chapter) to model interactions with nanoporous materials.[136, 140, 146] A recent review from Fang et al.[136] provides a summary of the work in this area. A reasonable trade-off between computational cost and accuracy in many circumstances is provided by using Density Functional Theory (DFT). Force fields obtained from DFT have been previously used for modeling diverse systems including CO_2/silica zeolites[27, 136], CO_2/Na-exchanged zeolites[136, 146], water/HKUST-1[201], CH_4/HKUST-1[144], CO_2/MOF-74[202], and H_2O/MOF-74[202]. After successful

implementation of DFT/CC method for CH_4 as described in the previous chapter, it is natural to extend the methodology to other long chain hydrocarbons.

In this chapter, we extend our previous force field development methodology for developing transferable force fields for modeling adsorption of alkanes and alkenes in zeolites using periodic Density Functional Theory (DFT) calculations. By calculating the interaction energies for a large number of adsorbate configurations using DFT, we obtain force fields that give good predictions of adsorption isotherms and heats of adsorption for alkanes and alkenes in zeolites. Our results suggest that the force field is transferable to other silica zeolites and hence in the future it can be used to screen a large number of available and hypothetical zeolites to identify top performing candidates for various olefin/paraffin separations.

The Chapter is organized as follows. The overview of DFT/CC method is provided in section 5.2. Sections 5.3 and 5.4 gives a brief overview of our algorithm and the computational methods and describes the derivation of force fields for C_2 and C_3 hydrocarbons from periodic DFT calculations in silica CHA. Next, in Section 5.5, the performance of the developed FF and the transferability of the FF to other zeolite topologies as well as to longer hydrocarbons is discussed. In Section 5.6, we conclude this chapter by final remarks and future work.

5.2 DFT/CC method

As explained in previous chapter, the DFT/CC method is based on estimating the DFT error relative to CC calculations, and then correcting the DFT energies for periodic systems. Here $\Delta E^{\mathrm{DFT/CC}}$ is defined as the difference between DFT and accurate CCSD(T)

interaction energies on a molecular cluster. For ethane and propane, the DFT/CC correction functions developed earlier for CH_4 are used as it is assumed that the CC corrections for C^{sp3} is transferable. This was shown by Nachtigall *et al.* for propane in the MOF CuBTC.[151, 153] However, these CC correction curves are not transferrable to ethene or propene as these molecules contain C^{sp2} instead of C^{sp3}.[153] As a result, we aim to develop CC-corrections for ethene, which is then assumed to be transferrable to propene. Here, transferability will be tested when we compare computed adsorption isotherms with experimental adsorption isotherms. For ethene, the calculation details for obtaining DFT/CC correction functions are similar to that for CH_4 with H_2, H_2O, and $Si(OH)_4$. Here, we have just replaced CH_4 with C_2H_4. The main assumption of the method is that $\Delta E^{\mathrm{DFT/CC}}$ can be represented as pairwise representation using

$$\Delta E^{DFT/CC} = \sum_{i}^{N_{C_2H_4}} \sum_{j}^{N_b} \varepsilon_{ij}(R_{ij}) \tag{5.1}$$

where N_a and N_b are the numbers of atoms of the C_2H_4 and monomer b (H_2, H_2O, or $Si(OH)_4$) , ε_{ij} are the DFT/CC correction functions, and R_{ij} is the intermolecular atomic distance between atom i (H or C^{sp2}) and j(H, O, or Si). The correction functions are obtained using the reciprocal power reproducing kernel Hilbert space (RP-RKHS) interpolation from a set of energies calculated at CCSD(T)/CBS (CBS= complete basis sets) and DFT/AV5Z levels for a suitable reference set of clusters C_2H_4--H_2 (67 grid points), C_2H_4--H_2O (70 grid points), and C_2H_4--$Si(OH)_4$ (61 grid points) as shown in Fig. 5.1. These reference sets are chosen because precise calculations at the CCSD(T) level with sufficiently flexible basis sets are feasible. The DFT and CCSD(T)/CBS energies were calculated using Dunning's correlation consistent valence-X-ζ basis sets with

polarization functions for H, C, O, and Si atoms. Other calculation details are summarized in the previous chapter.

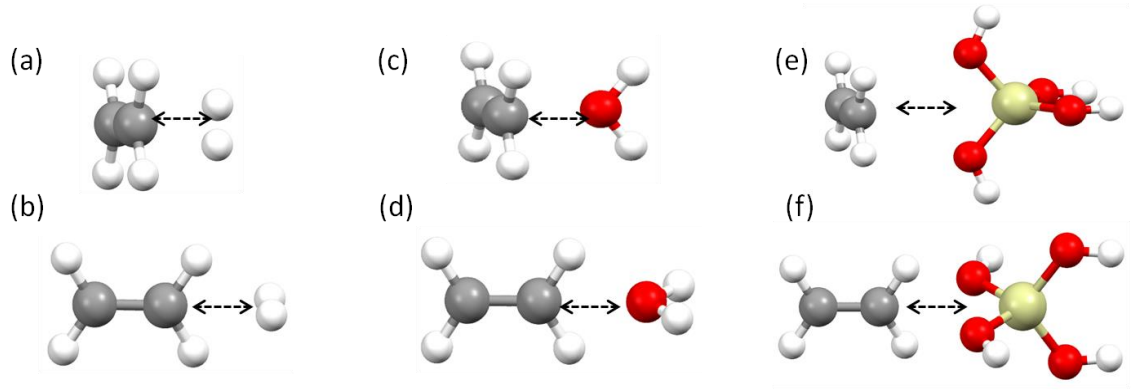

Figure 5.1 Definition of the reference set used for the generation of the DFT/CC correction functions for Ethene: $C_2H_4\cdots H_2$ (a, b), $C_2H_4\cdots H_2O$ (c, d), and $C_2H_4\cdots Si(OH)_4$ (e, f). The *C2v* symmetry constraints were applied. The C^{sp2}, O, H, and Si atoms are depicted in grey, red, white, and yellow, respectively.

The $C_2H_4\cdots H_2$ reference system (Fig. 5.1(a) and 5.1(b)) provides the $\varepsilon_C{}^{sp2}{}_H$ and ε_{HH} correction functions as shown in Fig. 5.2. The $C_2H_4\cdots H_2O$ reference system (Fig. 5.1(c) and 5.1(d)) provides $\varepsilon_C{}^{sp2}{}_O$ and ε_{HO} correction functions as shown in Fig. 5.3, using $\varepsilon_C{}^{sp2}{}_H$ and ε_{HH} obtained previously for $C_2H_4\cdots H_2$. The $C_2H_4\cdots Si(OH)_4$ reference system (Fig. 5.1(e) and 5.1(f)) provided $\varepsilon_C{}^{sp2}{}_{Si}$ and ε_{OSi} correction functions as shown in Fig. 5.4, using $\varepsilon_C{}^{sp2}{}_H$ and ε_{HH} obtained previously for $C_2H_4\cdots H_2$ and $\varepsilon_C{}^{sp2}{}_O$ and ε_{HO} obtained previously for $C_2H_4\cdots H_2O$. The numerical values of ε_{ij} and α_k are reported in Appendix D. The resulting correction functions then can be used to improve dispersion interactions in the DFT calculations of ethene or propene molecules in periodic zeolites.

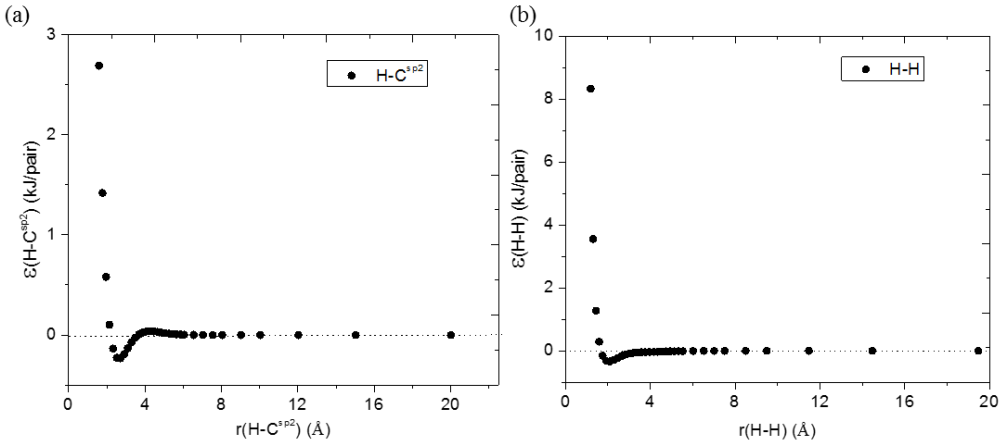

Figure 5.2 DFT/CC-correction curves for (a) H-C^{sp2}, (b) H-H interactions

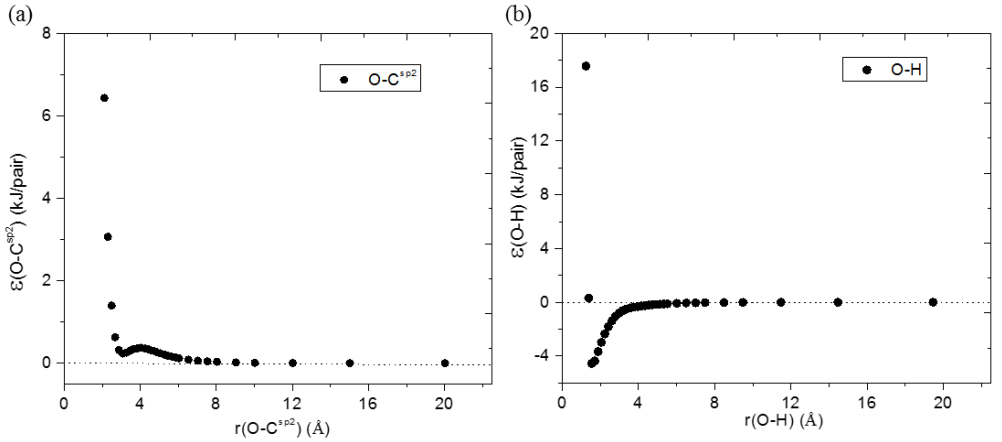

Figure 5.3 DFT/CC-correction curves for (a) O-C^{sp2}, (b) O-H interactions

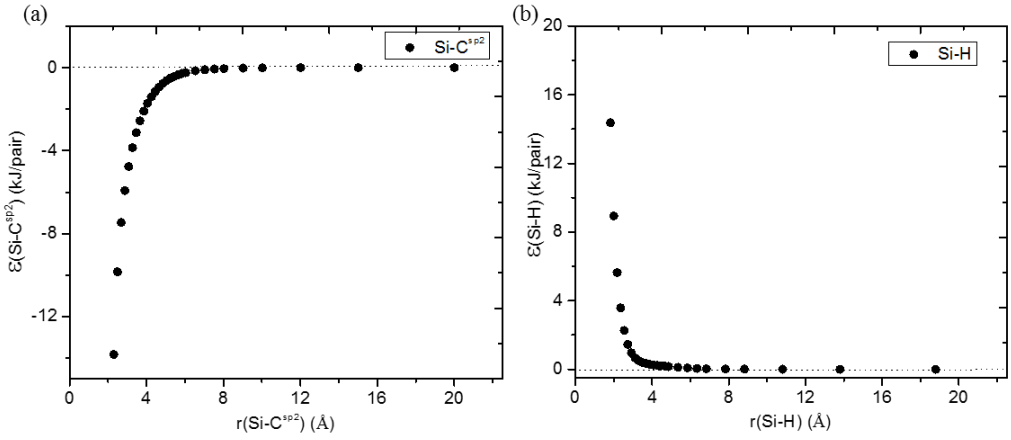

Figure 5.4 DFT/CC-correction curves for (a) Si-C^{sp2}, (b) Si-H interactions

5.3 Force Field Development for Ethane and Ethene

5.3.1 Overview

The force field development approach used here is similar to the one used in Chapter 4. We first calculate the interaction energies for a 200 randomly generated adsorbate configurations using Density Functional Theory (DFT) in primitive unit cell of silica CHA. These interaction energies are fit to a classical potential form to obtain an initial version of the force field. We use the new FF parameters in a Grand Canonical Monte Carlo (GCMC) simulation to generate isotherms and a larger set (600 - 1200) of adsorbate configurations. DFT interaction energies are obtained for the new configurations and the FF parameters are recalculated using a least-squares fit to yield the final, DFT-consistent version of the force field. The calculation details for each step of the FF development algorithm are discussed below. Briefly, the goal of our force field development strategy is to ensure that the force field parameters reproduce the DFT energy for various configurations of the adsorbates in silica CHA.

5.3.2 Structure optimization

Silica CHA was chosen as a adsorbent because it has the smallest primitive unit cell ($Si_{12}O_{24}$ per unit cell) among zeolites, which reduces the computational time for the periodic DFT calculations. The rhombohedral unit cell ($R\bar{3}m$ space group) of Si-CHA was first fully optimized at the DFT level as implemented in Vienna ab-initio Simulation Package (VASP). The GGA functional of Perdew, Burke and Ernzerhof [177] (PBE) was used with Grimme's D2[137] corrections to include dispersion interactions with the PAW method[178]. The lattice constants were optimized at a plane wave cutoff of 700 eV while the internal coordinates were energy minimized at a 400 eV cutoff. The energy

minimization is terminated when the individual atomic forces are less than 0.03 eV/Å. To reduce the computational cost, the DFT calculations were performed at the Γ-point. The lattice constants obtained for silica CHA using PBE-D2 are a = b = c = 9.333 Å and α = β = γ = 94.34°, which are close to the experimentally determined lattice constants, a = b = c = 9.229 Å and α = β = γ = 94.3°.[164] The optimized primitive unit cell of silica CHA is shown in Fig. 5.5 (a).

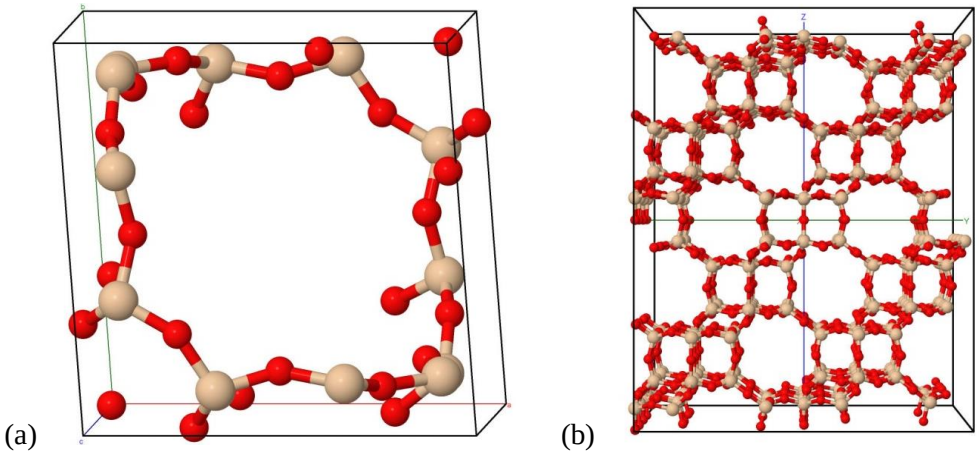

Figure 5.5 (a) Primitive unit cell of silica CHA used in the DFT calculations. (b) Supercell of silica CHA used in the GCMC calculations. Si and O atoms depicted as light brown and red spheres, respectively.

5.3.3 Single point energy DFT calculations

Our FF development approach is based on fitting the interaction energies obtained from periodic DFT calculations to a classical potential form. In the first part, the adsorption energy is defined as

$$E_{ads} = E_{CHA+ads} - E_{CHA} - E_{ads} + \Delta E_{DFT/CC} \tag{5.2}$$

where E_{CHA} and E_{ads} refer to the DFT energies of the empty CHA framework and the

hydrocarbon molecule, respectively, while $E_{CHA+ads}$ is the DFT energy of the CHA-adsorbate complex. All the DFT single point energy (SPE) calculations using PBE functional are performed with reciprocal space sampled at the Γ point to reduce the computational cost. The interaction of hydrocarbons with zeolite is dominated by dispersion interactions and a DFT method that accounts for these interactions is required. Within DFT, the electron exchange-correlation can be described by different functionals that may result in different interaction energies for the given configuration of the adsorbate. After the excellent performance of the DFT/CC method for CH_4 (chapter 4), we decided to extend the methodology to long chain alkanes and alkenes because the similar nature of the dispersion interactions. Our previous results (Chapter 4) for CH_4 adsorption in zeolites suggest that FFs derived from the PBE-D2, PBE-D3, vdW-DF2, VDW-DF-CC functionals give isotherms that are not in agreement with the experimental isotherms. Thus, we only use the DFT/CC method for the force field development using the correction functions described in section 5.2.

The total DFT/CC correction used in Eq. 5.2 for a given adsorbate configuration with the periodic zeolite is measured using

$$\Delta E_{DFT/CC} = \sum_{R_{CSi}} \varepsilon_{CSi} + \sum_{R_{HSi}} \varepsilon_{HSi} + \sum_{R_{CO}} \varepsilon_{CO} + \sum_{R_{HO}} \varepsilon_{HO} \tag{5.3}$$

where C is carbon atom in either sp^3-CH_3 or sp^2-CH_2 depending upon the hydrocarbon. Intermolecular atomic distances, R_{ij}, for each cross species are calculated over a finite $5 \times 5 \times 5$ model. This approximation is realistic because the CC contribution, which can be perceived as dispersion interaction plus DFT error, outside the $5 \times 5 \times 5$ model are negligible. Then using the RP-RKHS interpolation scheme and CC-corrections given in

Fig. 5.3-5.4 for sp^2-CH_2 and Fig. 4.4-4.5 for sp^3-CH_3, total the DFT/CC correction is calculated. Numerical values of CC-corrections are provided in Appendix C and D.

5.3.4 Parameter fitting and functional forms

A majority of the molecular simulation studies for adsorption in zeolites published to date have used the so-called Kiselev model[203]: (i) atoms in the zeolite framework are fixed at their crystallographically determined positions; (ii) the host−guest interactions can be approximated as a sum of pair interactions between all atoms; and (iii) since silicon atoms have small polarizability and are shielded by the surrounding oxygen atoms, their effects can therefore be taken into account effectively by considering only interactions with the oxygen atoms. The last assumption leads to a greatly reduced parameter space for a force field describing guest−host interactions. In our work, we used the Kiselev description of the zeolite for the classical part of the FF fitting along with the TraPPE united atom description of alkanes[204] and alkenes[205]. Hence, we have (sp^3-CH_3)-O (for ethane) and (sp^2-CH_2)-O (for ethene) as a cross-species interactions. The TraPPE united atom description does not include point charges on the adsorbate atoms and only considers Lennard-Jones terms to model the intermolecular dispersion interactions. To be consistent with the TraPPE FF, we do not explicitly consider any Coulombic interactions in our calculations. It is important to note that the TraPPE force field was obtained by fitting to experimental fluid phase properties.[204-205] Details of the force field parameters for the TraPPE FF are presented in Table 5.1.

Table 5.1 Parameters for the united atom TraPPE[204-205] FF for alkanes and alkenes.

Atom Type (sp^3)	ε (K)	σ (Å)	Atom Type (sp^2)	ε (K)	σ (Å)
CH_3	98	3.75	CH_2	85	3.675
CH_2	46	3.95	CH	47	3.73
CH	10	4.65			

The DFT energies obtained from random and GCMC configurations of hydrocarbons (hereafter, either ethane or ethene) as explained above are fitted to Lennard-Jones (LJ) 12-6 potential form of a force field,

$$E_{ads.} = E_{LJ}(R_{ij}) = 4\varepsilon_{ij}\left[\left(\frac{\sigma_{ij}}{R_{ij}}\right)^{12} - \left(\frac{\sigma_{ij}}{R_{ij}}\right)^{6}\right] = \frac{A_{ij}}{R_{ij}^{12}} - \frac{B_{ij}}{R_{ij}^{6}} \tag{5.4}$$

where ε_{ij} is the depth of the potential well and σ_{ij} is the interatomic distance at which the potential is zero. The repulsion coefficient, $A_{ij}=4\times\varepsilon_{ij}\times\sigma_{ij}^{12}$ and attractive coefficient, $B_{ij}=4\times\varepsilon_{ij}\times\sigma_{ij}^{6}$ are determined in a least squares sense where the parameter fitting calculations are done in MATLAB. The A_{ij} and B_{ij} in above equation then are converted into ε_{ij} and σ_{ij}.

Here, the pairwise interactions of the adsorbates with the zeolites are modeled using only Van der Waals terms to be consistent with the TraPPE-UA force field. Hence, the Coulombic interactions between atoms in hydrocarbons and the zeolite were neglected. The distances ($1/R_{ij}^{12}$ and $1/R_{ij}^{6}$) for each cross species were measured and summed based on a finite $5 \times 5 \times 5$ model, where the hydrocarbon molecule is located near the center of the model and its position relative to the zeolite framework is the same as in the original $1 \times 1 \times 1$ model.

Table 5.2 CCFF and D2FF Parameters for ethane and ethene in silica CHA.

Cross species	CCFF		D2FF	
	ε/k_B (K)	σ (Å)	ε/k_B (K)	σ (Å)
(sp^3-CH_3)–O	107.00	3.306	133.42	3.26
(sp^2-CH_2)–O	101.45	3.301	115.09	3.10

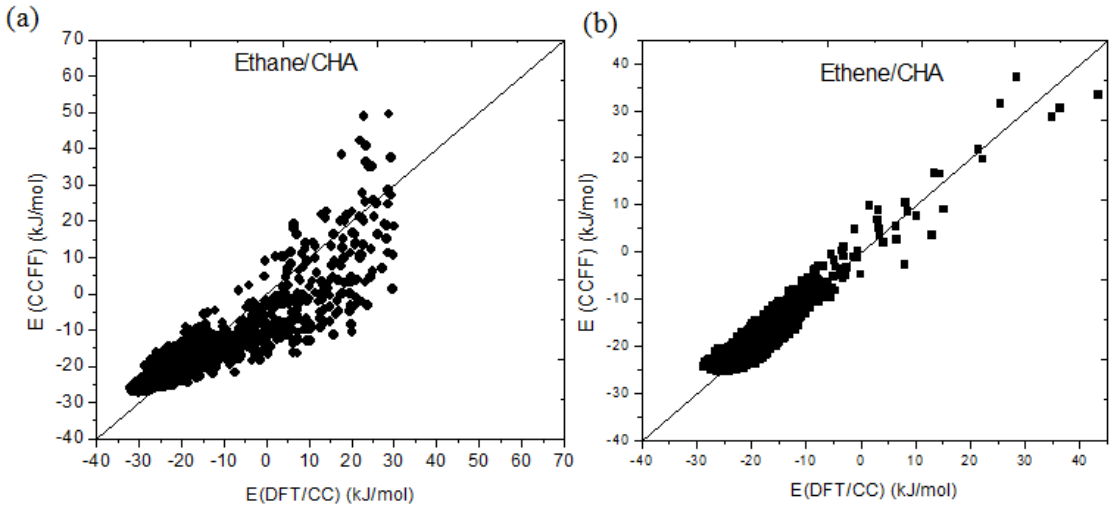

Figure 5.6 Comparison of the adsorption energies obtained using CCFF with DFT/CC of (a) 1000 configurations of ethane and (b) 1600 configurations of ethene in the primitive unit cell of silica CHA.

Typically, we use 600 - 1600 adsorbate configurations to derive a set of force field parameters. Note that only united atom positions are obtained from GCMC snapshots. Thus, hydrogen atoms must be correctly added to carbon chains prior to the next iteration of the DFT calculations. The final FF parameters (CCFF) for (sp^3-CH_3)–O (in ethane) and (sp^2-CH_2)–O (in ethene) interactions are given in Table 5.2 and are compared with DFT-D2 parameters obtained using PBE-D2 functional. Figure 5.6 compares the CCFF predicted energies for 1000 ethane (1600 ethene) configurations with the DFT/CC energies. The MAD (MD) is 4.4 kJ/mol (0.38 kJ/mol) for the ethane and

1.35 kJ/mol (0.05 kJ/mol) for the ethene for the converged FF. It also shows a systematic underestimation of ~3 kJ/mol for low energy configurations for ethane which can be attributed to fitting to simple and commonly used UA model instead of a more realistic all-atom model.

5.4 Force Field Development for Propane and Propene

In the previous section, we have outlined our force field development algorithm for ethane and ethylene adsorption in silica CHA using periodic DFT calculations. We now turn to extending the same approach for higher hydrocarbons such as propane and propylene. From the ethane and ethylene results in Section 5.4, we now have LJ 12-6 force field parameters for (sp^2-CH_2) UA (ethene) and (sp^3-CH_3) UA (ethane) interactions with the O atoms of the framework. To describe adsorption of propane and propene, additional (sp^3-CH_2) (propane) and (sp^2-CH) (propene) interaction parameters are required. The steps involved in this calculation are similar to the previous section and only a brief description of the method is provided here. Using a similar strategy as in section 4.4, we performed single point energy calculations for random plus GCMC generated adsorbate configurations of propane and propene in silica CHA. The contribution of the unknown (sp^3-CH_2) (propane) and (sp^2-CH) (propene) interactions with the O atom of the zeolite are obtained by subtracting the known components from the total DFT interaction energy. These known terms include (sp^3-CH_3)-O (from ethane) and (sp^2-CH_2)-O (from ethene).

Table 5.3 CCFF and D2FF Parameters for propane and propene in silica CHA.

Cross species	CCFF		D2FF	
	ε/k_B (K)	σ (Å)	ε/k_B (K)	σ (Å)
(sp^3-CH_2)–O	97.85	3.350	125.23	3.28
(sp^2-CH)–O	81.89	3.246	97.34	3.198

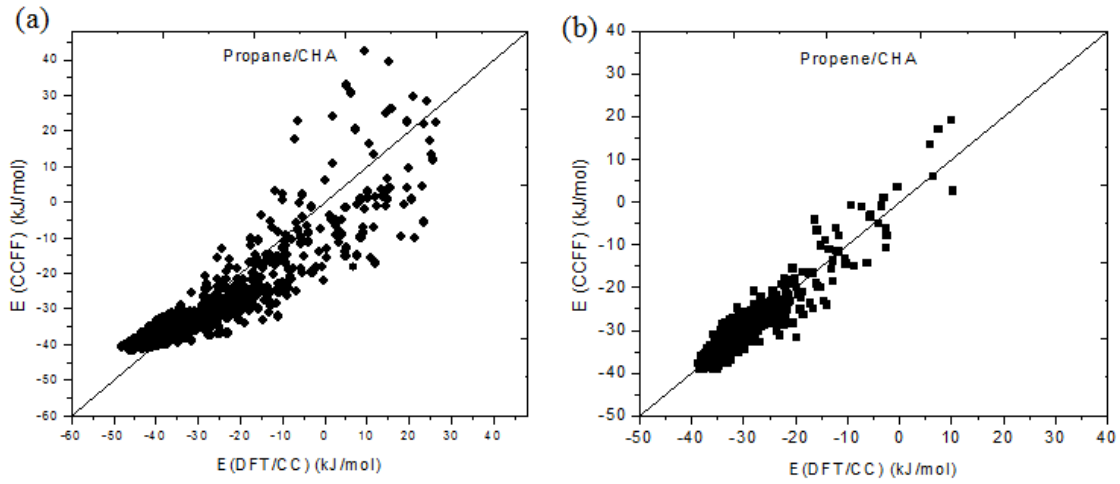

Figure 5.7 Comparison of the adsorption energies obtained using CCFF with DFT/CC of (a) 800 configurations of propane and (b) 600 configurations of propene in the primitive unit cell of silica CHA.

Similar to the previous calculations for ethane and ethene, FF fitting is performed using 200 (200) random plus 600 (400) GCMC generated configurations of propane (propene) in silica CHA. Note that only united atom positions are obtained from GCMC snapshots. Thus, hydrogen atoms must be correctly added to carbon chains prior to the next iteration of the DFT calculations. The final FF parameters (CCFF) for (sp^3-CH_2)–O (in propane) and (sp^2-CH)–O (in propene) interactions are given in Table 5.3 and are compared with DFT-D2 parameters (D2FF). Figure 5.7 compares the CCFF predicted energies for 800 propane (600 propene) configurations with the DFT/CC energies. The

MAD (MD) is 6.46 kJ/mol (-0.46 kJ/mol) for the propane and 2.9 kJ/mol (0.22 kJ/mol) for the propene for the converged FF. It also shows a systematic underestimation of ~4-5 kJ/mol for low energy configurations for propane. Compared to the MAD for C2 hydrocarbons, the slightly higher MAD for C3 hydrocarbons is due to the increasing complexity of the adsorbate molecule and the additional degree of freedom from the (sp^3-CH_3) united atom.

These results are encouraging and indicate the transferability and versatility of our FF development approach for modeling increasingly complex adsorbates. Since we now have interaction parameters for (sp^3-CH_3), (sp^3-CH_2), (sp^2-CH_2), and (sp^2-CH) with the zeolite, the DFT-derived CCFF are used for modeling adsorption of higher linear alkanes and alkenes as shown in the following section.

5.5 Classical simulations and CCFF transferability

All GCMC simulations were performed within the RASPA simulation code developed by Dubbeldam and co-workers.[206-207] For adsorption simulations involving longer hydrocarbons (propane/propene and above) configurational-bias Monte Carlo (CBMC)[208] was employed. The pairwise interaction potentials were truncated at a spherical cutoff of 12.0 Å. For each simulation, a simulation box was chosen to ensure that the minimum length in each of the direction was larger than 24 Å (twice the cutoff radius of the LJ potentials). An example of the simulation box of silica CHA used in the GCMC calculations is shown in Fig. 5.5 (b). The CBMC calculations were carefully equilibrated using at least 50,000 cycles, and production runs of 200,000 cycles were used for measuring the macroscopic properties.

5.5.1 C2 hydrocarbon adsorption isotherms

We performed GCMC simulations for ethane and ethene in silica zeolites to test the performance of the DFT/CC derived force field (CCFF) as shown in figures 5.8 and 5.9. The figures 5.8 and 5.9 compare the predicted adsorption isotherms with corresponding experimental data for ethane and ethene showing good agreement at all the conditions. An underprediction of adsorption for ethane in CHA can be attributed to the slight underprediction of lower energy configurations for ethane. Note that the isotherms from GCMC shown in Fig. 5.8 and 5.9 for both ethane and ethene are obtained purely from computational methods and do not include any fitting or adjustments based on the experimental measurements and hence these FFs are truly first-principle derived.

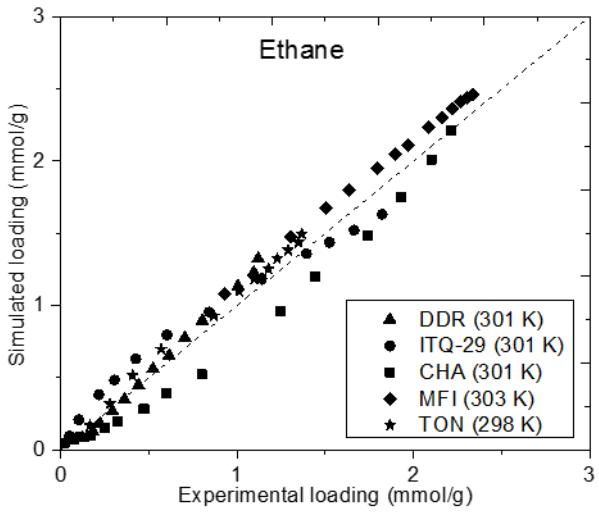

Figure 5.8 GCMC predicted adsorption isotherms for ethane in CHA at 301 K, in ITQ-29 (LTA topology) at 301 K, in DDR at 301 K, in MFI at 303 K, and in TON at 298 K. The experimental adsorption isotherms are shown by filled symbols and are obtained from Hedin *et al.*[62] for CHA, ITQ-29, and DDR, Zhu *et al.*[209] for MFI, and Hampson and Rees[210] for TON.

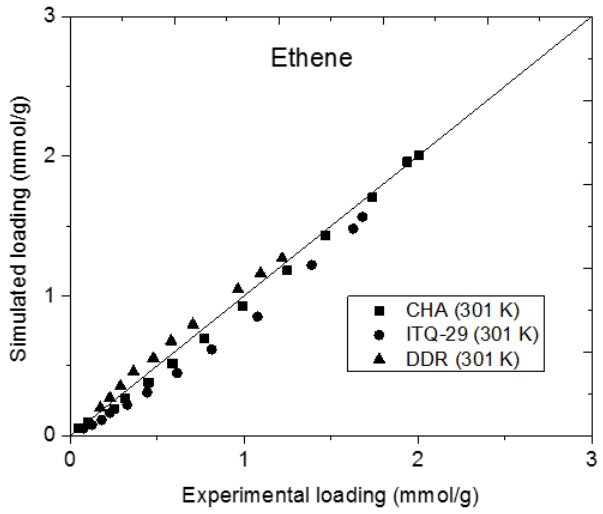

Figure 5.9 GCMC predicted adsorption isotherms for ethene in CHA, ITQ-29 (LTA topology), and DDR at 301 K using the CCFF to test the FF transferability. The experimental adsorption isotherms are obtained from Hedin *et al.*[62] shown by filled circles.

5.5.2 C3 hydrocarbon adsorption isotherms

Experimental data for propane adsorption in silica CHA is not available in literature because of the very slow equilibration[188, 211-212] of zeolite with propane in 8MR zeolites. This is because of the large activation energy and hence slow diffusion of propane through 8MR window of CHA.[191] Thus, we used a 10MR silica zeolite MFI, for GCMC simulations using the FF parameters in Table 5.3 for propane, which simultaneously tests the transferability of the CCFF. Figure 5.10 compares the predicted adsorption isotherms with corresponding experimental data from Zhu et al.[209] for propane showing excellent agreement. Then, to test if the developed FF parameters for (sp^3-CH_3)-O for ethane and (sp^3-CH_2)-O for propane are transferable to higher liner alkanes, we performed GCMC simulation of n-butane in MFI. The adsorption isotherms from GCMC

agrees well with the experimental data for n-butane. This indicates that CCFF not only works for propane but also works for higher linear alkanes like n-butane.

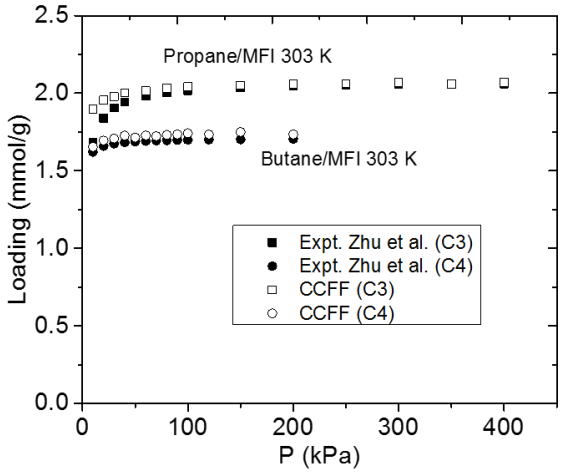

Figure 5.10 GCMC predicted adsorption isotherms for propane and n-butane in silica MFI using the DFT/CC FF for the framework-adsorbate interactions. The experimental adsorption isotherms are taken from Zhu et al.[209] and shown by filled circles.

Next, we performed GCMC simulations for propene in silica zeolites: CHA, DDR, ITQ-29, and ITQ-12. Even though propane and propene seem very similar, the diffusion of propene is much faster than propane in 8MR zeolites because of the smaller cross section of propene than propane.[191] As a result, the estimated activation energies for diffusion are 10 and 73 kJ/mol, respectively, for propene and propane in silica CHA.[191] This indicates that the propene diffusion through 8MR is much faster than that for propane causing no concerns for equilibration. The results for adsorption isotherms are shown in Fig. 5.11 and excellent agreement is obtained when compared to experimental adsorption isotherms from various sources given in Fig. 5.11. Again, the isotherms from GCMC for both propane and propene are obtained purely from computational methods and do not include any fitting or adjustments based on the experimental measurements

and hence these FFs are truly first-principle derived. Then, to test if the developed FF parameters for (sp^3-CH_3)-O, (sp^3-CH_2)-O, (sp^2-CH_2)-O, and (sp^2-CH)-O are transferable to higher liner alkenes, we performed GCMC simulation for 1-butene in MFI at 300 K and for trans-2-butene in DDR at 303 K. As seen from the Fig. 5.12, the adsorption isotherms from GCMC agrees with the experimental data except at lower pressure where slight discrepancy is observed.

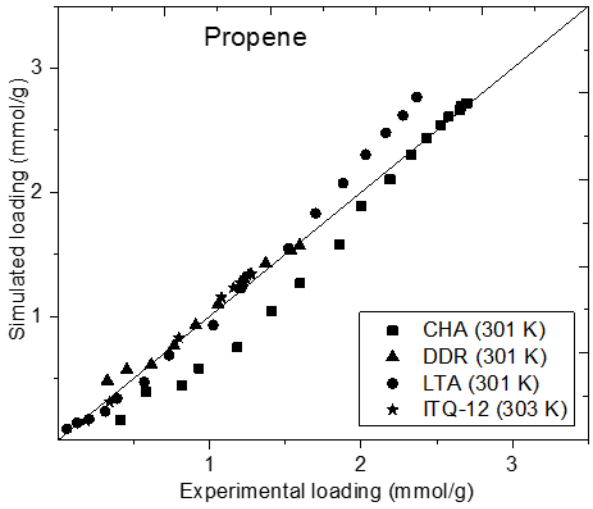

Figure 5.11 GCMC predicted adsorption isotherms for propene in CHA at 301 K, in DDR at 301 K, in ITQ-29 at 301 K, and in ITQ-12 at 303 K using the CCFF. The experimental adsorption isotherms are shown by filled circles obtained from Hedin et al.[62] (for CHA, DDR, and ITQ-29) and from Olson et al.[188] (for ITQ-12).

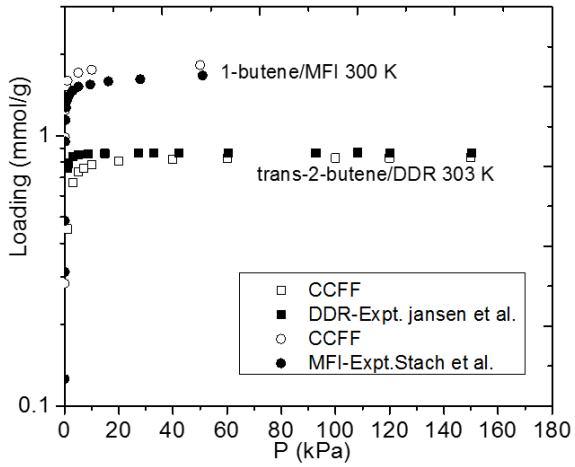

Figure 5.12 CCFF predicted isotherms for (a)1-butene in MFI at 300 K (Expt. data from Stach et al.[213]) and (b) trans-2-butene at 303 K in DDR (Expt. data from Jansen et al.[214]).

5.6 Conclusions

A novel united atom force field is developed using first principle methods that accurately describes the quantitative reproduction of the adsorption properties of linear alkanes and alkenes in nanoporous framework structures. Pure silica zeolites, especially small-pore 8MR zeolites, have been recognized as promising candidates for olefin/paraffin separation. Although various pure silica 8MR zeolites have been experimentally characterized for their alkene adsorption and olefin/paraffin separation capability, theoretical studies concerning the diffusion and adsorption of alkenes in these kinds of zeolites are scarce. Considering that there are many zeolites that can be prepared as pure silica and their potential application for olefin separation, it is worth performing a systematic screening of them for olefin/paraffin separation, for which molecular simulation is the most suitable tool. Our newly developed force field provides critical information that will enable this task.

CHAPTER 6

CONCLUSIONS AND SUGGESTIONS FOR FUTURE WORK

Zeolites are important nanoporous materials that possess wide range of possible framework topologies, chemical compositions, porosity, and extra-framework cations. These characteristics allow for the fine-tuning of zeolite structures to meet specific applications such as storage, separation, purification, as well as catalysis. Therefore, it is important to explore as many zeolites as possible to find the best candidates for such applications. The selection of a suitable zeolite has become a significant challenge because of the huge number of possible structures due to various combinations of the topologies, cation types and quantity, and chemical composition. As a result, experimental investigation of adsorption and diffusion is time consuming and hence computational modeling have been used to predict macroscopic properties of gases in zeolites, screen large number of materials, and provide information not available through experiments. As the large scale synthesis and characterization of zeolites is time consuming and tedious, experimental screening of zeolites will be limited to only a handful of materials. Moreover, the rational design and optimization of zeolite-based adsorptive separation processes (e.g., pressure/temperature swing adsorption) requires the ability to predict and understand the sorption characteristics of a given adsorbate−adsorbent system.

Classical simulation methods like GCMC is used to predict adsorption properties, while diffusivities are calculated from MD simulations. The accuracy of the GCMC and

MD predicted properties are highly dependent on the assumptions about the intramolecular and intermolecular interactions used to describe the energetics of the system. Generally, intramolecular interactions are ignored to keep the zeolite framework rigid to cut down the huge computational cost. Thus, it is a new direction for the research to understand when a rigid framework approximation is justified and when framework flexibility is important for correctly describing adsorbate adsorption and diffusion. Traditional or generic intermolecular force fields are not transferrable and are found to be severely lacking in correctly describing the complex chemical environments in nanoporous materials. Moreover, force fields fitted to one set of experimental data may not be able to predict adsorption in similar materials, rendering them unsuitable for material screening. For the atomistic simulations to be useful for screening applications, it is essential for the force field to have predictive capabilities. Hence, it is desired to develop first-principles derived, transferable intermolecular force fields for different gases in zeolites.

6.1 Thesis Summary

The overall objective of this thesis has been to develop accurate computational methods for the diffusion and adsorption of small gases in zeolites. In Chapter 2 and 3, we discuss the effect of the zeolite framework flexiblity on the single component and binary diffusion of various gases. This study presents the first detailed analysis of different types of zeolite framework flexibilities and how they depend upon the zeolite topology. We show that for molecules with kinetic diameters comparable (or larger) to the size of the window the rigid framework approximation can produce order(s) of magnitude difference in diffusivities as compared to the simulations performed with a

fully flexible framework. We also proposed two simple methods in which the flexible structure of a zeolite is approximated as a set of discrete rigid snapshots. Both methods are orders of magnitude more efficient than the simulations with the fully flexible structure. The new methods are broadly applicable for the fast and accurate predictions of both infinite dilution and finite loading diffusivities of simple molecules in zeolites.

In Chapter 4, we use a combined classical and quantum chemistry based approach to systematically develop the force fields based on DFT calculations for interactions of simple molecules like CH_4 and N_2 with silica and cationic zeolites. We also studied CH_4 adsorption in aluminophosphates, the zeolite analogues. We used a higher level of theory known as the DFT/CC method to correct DFT energies that were used in the periodic DFT calculations to develop force fields. In Chapter 5, this approach was further extended to studying more complex adsorbates like linear alkanes and alkenes in zeolites. The united atom force fields developed for C2 and C3 alkanes and alkenes are transferable to higher linear alkanes and alkenes. Our results in both the chapters show that DFT-derived force fields give good predictions of macroscopic properties like adsorption isotherms in zeolites. The force fields are transferrable across zeolites and hence can be further used to screen materials for different storage and separation applications. Overall, this thesis provides a framework for computing the adsorption and diffusion properties of industrially important gases using a multiscale computational approach.

6.2 Future Challenges and Opportunities

6.2.1 Zeolite framework flexibility

Though the changing snapshots and the TST methods we developed to account for the framework flexibility have been described for the 8MR zeolites, they can be applied to other topologies of zeolites and similar nanoporous materials such as MOFs etc. One limitation of the classical simulations in MOFs is that the computed diffusivities depend strongly on the intramolecular force field employed during the MD simulations.[74] This requires development and parameterization of new force fields for each new MOF to be studied. In such circumstances, one can use our methods about framework flexibility that are efficient, reliable, and depend only on intermolecular interactions. If a reliable force field is unavailable, the set of snapshots that are required for the can be generated using short *ab-initio* MD trajectories[52].

6.2.2 Material screening for storage and separations

6.2.2.1 CH_4 storage

Increasing atmospheric CO_2 concentration leading to the global warming is now regarded as one of the most pressing environmental issues. In the long run, use of less carbon-intensive fuels, for example, natural gas, will help in reducing overall CO_2 emissions. The major component of natural gas is CH_4, and thus it is essential to find a suitable adsorptive material for the CH_4 storage. The volume available for gas storage is often limited. However, the storage capacity at moderate pressures can be enhanced through the use of adsorbents because the density of the adsorbed gas is greater than the bulk gas phase above it. A comparison of different adsorption materials showed that carbon materials are difficult to have a balance of small pores and large pores, for

optimum balance between capacity and dynamics, and MOFs had lower thermal stability, but zeolites have very homogeneous structures with a moderate surface area and good thermal stability.[185] Thus, zeolites remain the most commonly used adsorbents in the field. Hence, it is appealing to screen silica zeolites, cationic zeolites, aluminophosphates for CH_4 storage using DFT/CC FF developed for CH_4 in chapter 4 from low pressures of 1 and 10 bar to high pressures of 50 and 100 bar.

6.2.2.2 CH_4/CO_2 and $CH_4/CO_2/N_2$ separations

CO_2 is often found as a major impurity in natural gas,[215] and its presence can reduce the energy content of natural gas. Consequently, before the storage of pure CH_4 using adsorbents, it is important to separate CO_2 from their mixture. By a careful selection of the zeolites, CO_2 and CH_4 can be effectively separated on the basis of the different adsorption affinities. Next, the removal of CO_2 from gaseous mixtures such flue gas, biogas, or landfill gases is important for reducing CO_2 emission. These sources contain N_2 in addition to CH_4 and CO_2. The separation of CO_2, CH_4, and N_2 mixtures can upgrade low quality natural gas and also mitigate the problem of excess CO_2 emissions.[216]

A first principle derived and transferable force field for CO_2 in silica and cationic zeolites have been proposed by Fang *et al.*[27, 136, 146] By combining the FFs for CO_2 by Fang *et al.* and for CH_4 and N_2 as described in chapter 4, the library of silica and cationic zeolites can be screened for CH_4/CO_2 and $CH_4/CO_2/N_2$ separations. Furthermore, we can screen the zeolites for the cyclic processes such as pressure swing adsorption (PSA) and temperature swing adsorption (TSA) for CH_4/CO_2 as well as $CH_4/CO_2/N_2$ separations.

6.2.2.3 Olefin/paraffin separation

There is significant industrial interest in olefin/paraffin separations. Many zeolites have been studied for such separations based on their adsorption and diffusion properties.[186-192] In particular, 8MR zeolites are potential materials for such olefin/paraffin separations because of their small pore size.[186-188, 191] Although various pure silica 8MR zeolites have been experimentally characterized for their alkene adsorption and olefin/paraffin separation capability, theoretical studies concerning the diffusion and adsorption of alkenes in these kinds of zeolites are rare. Considering that there are many zeolites that can be prepared as pure silica and their potential application for olefin separation, a systematic screening of them for olefin/paraffin separation using the force field developed in chapter 5 will be valuable.

The performance of such processes is also influenced by the diffusion of these large hydrocarbon molecules through the small zeolite pores, especially through 8MR.[191] Due to the very slow diffusion and the effect of zeolite framework flexibility, a traditional MD simulation is not appropriate for these adsorbates in zeolites.[217] To tackle this problem, a new approach was proposed by Boulfelfel *et al.* based on the transition path sampling (TPS) and transition interface sampling.[217] The DFT/CC FF, combined with the TPS method, can give diffusivities and diffusion selectivities for the mixture calculations which will be helpful for the screening of zeolites for kinetic separations.

6.2.3 Extending the DFT/CC method to other adsorbates and adsorbents

The DFT/CC method has a potential to accurately describe interactions between different adsorbate-adsorbent complexes.[140, 146, 150, 154, 201] Few such examples of adsorbates include O_2, H_2S, NH_3, CO, and COS in the adsorbents such as silica zeolites,

cationic zeolites, aluminophosphate, and also MOFs. Furthermore, cationic zeolites have different varieties of cations such as Na, K, Ca, Li, and Mg and MOFs have numerous metal centers like Cu, Mn, V, Cd, Ni etc. The DFT/CC method is applicable for all these diverse materials providing a universal procedure for the FF development. In many situations, the flexibility of the zeolite framework in important and combined intramolecular and intermolecular force fields will be necessary for correctly modeling these systems.[103]

APPENDIX A

1. Modeling Intra- and Inter-molecular interactions

To model the internal degrees of freedom of zeolite, various potential types as described in the Table A1 were used given by,

$$V_{total} = V_{bonds} + V_{angles} + V_{torsions} + V_{bond-bond} + V_{angle-angle} + V_{bond-angle} + V_{angle-angle-torsion} + V_{LJ} + V_{coulomb} \quad \text{(i)}$$

The intermolecular interaction between adsorbate and zeolite was modeled by Lennard-Jones potential given as,

$$V_{LJ}^{ij,12-6} = 4\varepsilon_{ij}\left[\left(\frac{\sigma_{ij}}{r_{ij}}\right)^{12} - \left(\frac{\sigma_{ij}}{r_{ij}}\right)^{6}\right] \quad \text{(ii)}$$

where, i is CH_4 and j is either CH_4, O, or Si. Corresponding intramolecular and intermolecular potential parameters are listed in Tables A2 and A3.

Table A1. Hill-Sauer FF used to model zeolite framework dynamics.

$V_{bond}(r) = k_2\left(r - r_{eq}\right)^2 + k_3\left(r - r_{eq}\right)^3 + k_4\left(r - r_{eq}\right)^4$	(iii)
$V_{angle}(\theta) = k_{\theta 2}\left(\theta - \theta_{eq}\right)^2 + k_{\theta 3}\left(\theta - \theta_{eq}\right)^3 + k_{\theta 4}\left(\theta - \theta_{eq}\right)^4$	(iv)
$V_{bond-bond}(r, r') = k(r - r_{eq})(r' - r'_{eq})$	(v)
$V_{bond-angle}(r, \theta, r') = (\theta - \theta_{eq})\left[k_r(r - r_{eq}) + k_{r'}(r' - r'_{eq})\right]$	(vi)
$V_{angle-angle}(\theta, \theta') = k_{\theta\theta'}(\theta - \theta_{eq})(\theta' - \theta'_{eq})$	(vii)
$V_{torsion}(\varphi) = \left[k_1(1-\cos\varphi) + k_2(1-\cos 2\varphi) + k_3(1-\cos 3\varphi)\right]$	(viii)
$V_{angle-angle-torsion}(\theta, \varphi, \theta') = k_{\theta\varphi\theta'}\cos\varphi(\theta - \theta_{eq})(\theta' - \theta'_{eq})$	(ix)
$V_{LJ}^{ij,9-6} = \frac{A_{ij}}{r_{ij}^9} - \frac{B_{ij}}{r_{ij}^6}$, where i, j = O or Si	(x)

$V_{coul} = \frac{q_i q_j}{\varepsilon_0 r_{ij}^2}$, where i, j = O or Si (xi)

Table A2. Bonded potential parameters for zeolite framework.

Potential type	**Force constants**			**Equilibrium quantity**
Bond-Stretch (Si-O)	K_2=459.0786 (kcal/mol/Å^2)	K_3=-672.4445 (kcal/mol/Å^3)	K_4=443.3651 (kcal/mol/Å^4)	r_{eq}=1.6104Å
Angle-Bend (O-Si-O)	$K_{\theta 2}$ =81.9691 (kcal/mol/rad^2)	$K_{\theta 3}$=-36.5814 (kcal/mol/rad^3)	$K_{\theta 4}$= 116.9558 (kcal/mol/rad^4)	θ_{eq}=112.02°
Angle-Bend (Si-O-Si)	$K_{\theta 2}$ =20.7015 (kcal/mol/rad^2)	$K_{\theta 3}$=27.5506 (kcal/mol/rad^3)	$K_{\theta 4}$=10.9930 (kcal/mol/rad^4)	θ_{eq}=173.7651°
Bond-Bond (Si-O~Si-O)	K_r =151.8742 (kcal/mol/Å^2)			r_{eq}=1.6104 Å r'_{eq}=1.6104 Å
Bond-Angle (Si-O~O-Si-O)	K_r=78.1239 (kcal/mol/Å/rad)	$K_{r'}$=78.1239 (kcal/mol/Å/rad)		$\theta_{eq=}$112.02° r_{eq}=1.6104Å r'_{eq}=1.6104 Å
Bond-Angle (Si-O~Si-O-Si)	K_r=9.2390 (kcal/mol/Å/rad)	$K_{r'}$=9.2390 (kcal/mol/Å/rad)		θ_{eq}=173.7651° r_{eq}=1.6104Å $r'_{eq=}$1.6104Å
Angle-Angle (O-Si-O~O-Si-O)	$K_{\theta\theta'}$=-6.3030 (kcal/mol/rad^2)			θ_{eq}=112.02° θ'_{eq}=112.02°
Torsion	K_1=0.0306	K_2=-0.0105	K_3=0.0804	
Angle-Angle-Torsion	$K_{\theta\phi\theta'}$= -4.5150 (kcal/mol/rad^2)			θ_{eq}=112.02° θ'_{eq}= 173.7651°

Table A3. Non-bonded (LJ) potential parameters for framework and adsorbate molecules.

Site	**Potential**	**A (kcalÅ$^{1/9}$/mol)**	**B (kcalÅ$^{1/6}$/mol)**	**Charge (e)**
Si	LJ 9-6	186910.958	0.00	0.5236
O	LJ 9-6	57412.473	0.00	-0.2618
Si-O	LJ 9-6	103590.638	0.00	-
Site	**Potential**	**ε (K)**	**σ (Å)**	
CH_4	LJ 12-6	158.50	3.72	
O-CH_4	LJ 12-6	115.02	3.47	
Si-CH_4	LJ 12-6	0.00	0.00	

2. Explaining $d_{min}^{mean} < d_{min}^{TA}$ ($d_{min}^{mean} \approx d_{min}^{TA}$) for zeolites with multiple (single) directions

The minimum window dimensions of the energy minimized (d_{min}^{OPT}), time averaged structures (d_{min}^{TA}) as well as instantaneous minimum window dimension of the flexible structure ($d_{min}(t)$), and the mean of the distribution of window dimensions ($\langle d_{min}(t) \rangle$) are given by,

$$d_{min}^{OPT} = \min\left[d_1, d_2, d_3, d_4\right] \quad \text{(xii)}$$

$$d_{min}^{TA} = \min\left[\langle d_1(t)\rangle, \langle d_2(t)\rangle, \langle d_3(t)\rangle, \langle d_4(t)\rangle\right] \quad \text{(xiii)}$$

$$d_{min}(t) = \min\left[d_1(t), d_2(t), d_3(t), d_4(t)\right] \quad \text{(xiv)}$$

$$\langle d_{min}(t)\rangle = \langle \min\left[d_1(t), d_2(t), d_3(t), d_4(t)\right]\rangle \quad \text{(xv)}$$

where, $\langle \ldots \rangle$ indicates time averaging over a simulation time. In the time averaged structure if d_1 corresponds to minimum window dimension then equation (xiii) becomes,

$$d_{min}^{TA} = \langle d_1(t)\rangle \quad \text{(xvi)}$$

The minimum among the multiple distances is always less than or equal to one of the individual distances:

$$\langle \min\left[d_1(t), d_2(t), d_3(t), d_4(t)\right]\rangle \leq \langle d_1(t)\rangle \quad \text{(xvii)}$$

Comparing equations (xv), (xvi), and (xvii) shows that $\langle d_{min}(t)\rangle \leq d_{min}^{TA}$. The equality holds true only if d_1 corresponds to minimum window dimension (i.e. a single minimum window dimension), while the inequality holds only if the minimum window dimension

fluctuates between multiple distances d_1, d_2, d_3, or d_4 (i.e. multiple minimum window dimensions). In the case of LTA and CHA, $\langle d_{min}(t) \rangle < d_{min}^{TA}$ because the minimum window dimension fluctuates between multiple pairs of oxygen while for BIK and ERI, $\langle d_{min}(t) \rangle \approx d_{min}^{TA}$ because the minimum window dimension does not fluctuate between multiple pairs of oxygen.

3. Mean square displacement plots to obtain diffusivity in all zeolites

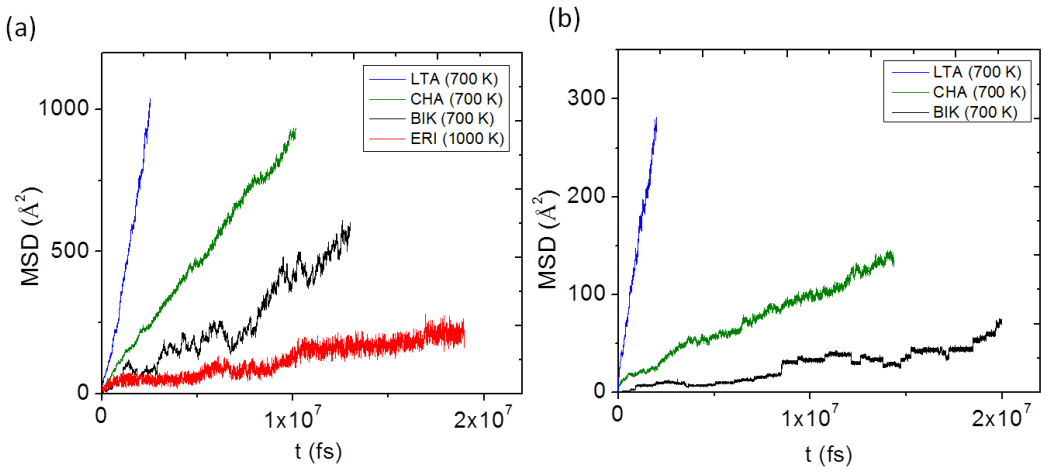

Figure A1. Mean square displacement (MSD) plots for (a) CH_4, (b) hypothetical CH_4 diffusion in respective zeolites. Loadings used were 9, 10, 0.25, and 1.5 molecules/unit cell respectively in LTA, CHA, BIK, and ERI. Diffusion coefficients were determined by fitting straight lines to the MSD. The data in (b) for BIK shows an example of the lowest diffusivity that can be routinely measured with our methods.

Table A4. The percentage overlaps that occurred while swapping frameworks at a frequency of 200 fs.

Loading	LTA	CHA	ERI	BIK
Low loading	0.72	0.68	0.76	1.12
High loading	1.34	1.46	-	-

4. Vibrational density of states (VDOS) plots

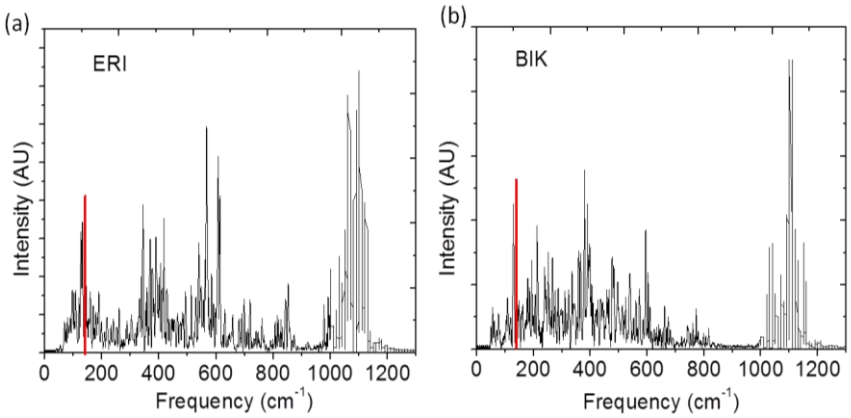

Figure A2. Vibrational density of states (VDOS) for one of the 8MR oxygen atoms from a single window belonging to d_{min} in (a) ERI and (b) BIK. The red line indicates the frequency of 150 cm^{-1}.

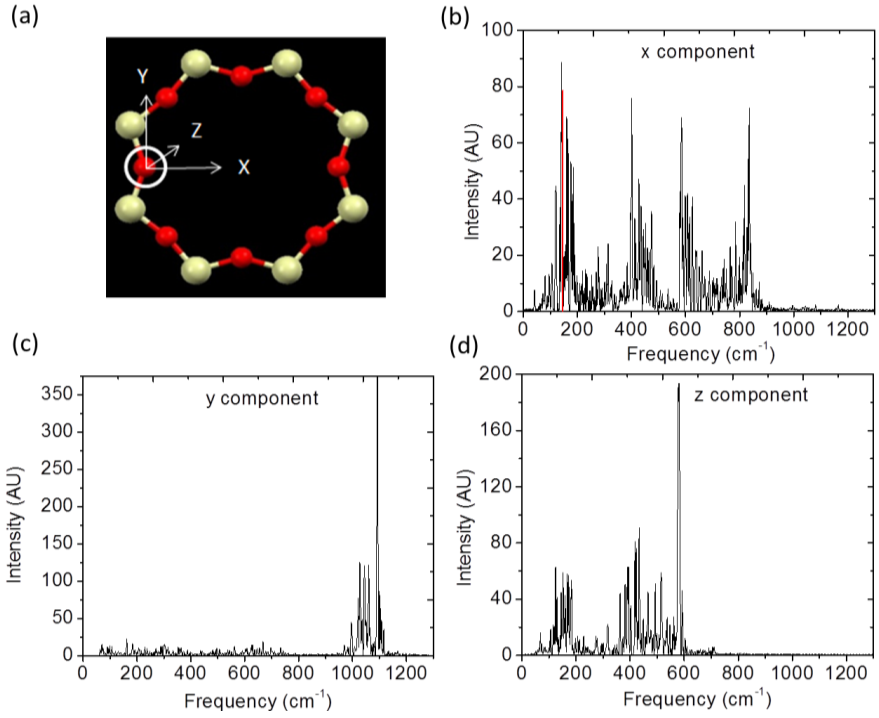

Figure A3. (a) 8MR oxygen atom (circled) in the xy plane belonging to d_{min} in the LTA. (b), (c), and (d) respectively shows the x, y, and z components of the VDOS for the same oxygen atom. The red line indicates the frequency of 150 cm^{-1}.

Table A5. Actual temperatures (in K) used in the simulations involving method 1, method 2, and lower temperature using method 2. In the corresponding figures, higher diffusivities correspond to higher temperatures.

Zeolite	Method 1		Method 2			Method 2 at Lower T
	Fig. 8 (a)	Fig. 8 (b)	Fig. 9 (a)	Fig. 9 (b)	Fig. 10	Fig. 11
LTA	300, 400, 500, 600, 700, 800, 900, 1000, 500[a], 700[a], 900[a]	-	300, 400, 500, 600, 700, 800, 900, 1000	300, 400, 500, 600, 700, 800, 900, 1000	300, 400	50, 100, 200, 300
CHA	300, 500, 700, 900, 700[a], 900[a]	300, 700[a], 900[a], 1100[a]	300, 400, 500, 600, 700, 800, 900, 1000	500, 700, 900, 1100	-	200[a], 300[a]
ERI	1100, 1300, 1500, 1700, 1900, 2100	1100, 1300, 1500, 1700	1100, 1300, 1500, 1700, 1900, 2100	1100, 1300, 1500, 1700, 1900, 2100	1100, 1300, 1500, 1700	700, 800 ,900, 1000
BIK	500, 700, 900, 1100, 700[a], 900[a], 1100[a]	700[a]	-	-	-	-

[a]Hypothetical CH_4 ($\sigma_{CH_4-O} = 3.7$ Å).

Appendix B

Table B1. Temperatures (in K) used in the simulations involving changing snapshot method, TST/snapshot method, and rigid structures, OPT and TA. In the corresponding figures, higher diffusivities correspond to higher temperatures.

Adsorbate/Zeolite	Temperatures used in simulations (K)	Adsorbate/Zeolite	Temperatures used in simulations (K)
Ne/ERI	200, 300, 500	Ar/ERI	500, 700, 900
Ne/DFT	200, 300, 500	Ar/DFT	200, 300, 500
Ne/EAB	200, 300, 500	Ar/EAB	200, 300, 500
Kr/CHA	300, 500, 700	Xe/CHA	900, 1100, 1300
Kr/LTA	200, 300, 500	Xe/LTA	700, 900, 1100
Kr/SAS	200, 300, 500	Xe/SAS	500, 700, 900
Kr/RHO	300, 500, 700	Xe/RHO	700, 900, 1100
Kr/BIK	300, 500, 700	CF_4/LTA	1500, 1700, 1900
Rn/LTA	900, 1100, 1300	CF_4/SAS	1300, 1500, 1700
Rn/SAS	700, 900, 1100	CF_4/RHO	1500, 1700, 1900
Rn/RHO	1100, 1300, 1500		

Table B2. Classification of 63 8MR zeolites*

Multiple d_{min}				Single d_{min}			
Harmonic		Anharmonic		Harmonic		Anharmonic	
zeolite	d_{min}^{OPT}	zeolite	d_{min}^{OPT}	zeolite	d_{min}^{OPT}	zeolite	d_{min}^{OPT}
ACO (3)	3.490	ATN (1)	3.195	ABW (1)	3.433	EAB (2)	3.278
AEI (3)	3.790	AWW (1)	3.710	AFN (3)	3.150	ERI (3)	3.001
AEN (2)	3.496	CDO (2)	3.414	AFT (3)	3.535	GIS (3)	3.157
CHA (3)	3.750	DDR (2)	3.400	AFX (3)	3.491	ITW (2)	2.878
EDI (3)	3.406	ESV (1)	3.646	APC (2)	2.685	SAT (3)	2.696
MER (3)	3.433	IHW (2)	3.693	APD (2)	2.551	BRE (2)	2.764
MON (2)	3.608	KFI (3)	3.688	ATT (2)	3.526	RWR (1)	2.315
PAU (3)	3.571	LTA (3)	3.720	ATV (1)	3.150	SIV (3)	2.199
PHI (3)	3.538	LTN (0)	3.745	AWO (1)	2.702		
SAS (1)	4.097	RHO (3)	3.822	BIK (1)	3.550		
THO (3)	3.575	RTE (1)	3.668	CAS (1)	2.564		
TSC (3)	3.557	SAV (3)	3.656	DFT (3)	2.725		
NPT (3)	3.543	UFI (2)	3.511	ITE (2)	3.368		

	VNI (3)	3.290	JBW (1)	3.452	
	YUG (2)	3.773	LEV (2)	3.243	
	GOO (3)	3.243	LTJ (2)	2.912	
	SBN (3)	3.753	MTF (1)	2.208	
	EPI (2)	3.454	NSI (2)	3.233	
			OWE (2)	2.408	
			RTH (2)	3.371	
			UEI (2)	2.679	
			BCT (1)	2.548	
			ZON (2)	2.933	
			ANA (3)	2.425	
# of zeolites= 13	# of zeolites= 18		# of zeolites= 24		# of zeolites= 8

*Each structure was optimized using the Hill-Sauer force field. The dimensionality of the pore structure is shown in the parentheses. The d_{min}^{OPT} is in Å.

Table B3. Numerical values of diffusivities and standard deviation (in m^2/s) in Fig 3.1.

System	Flexible		TST/Snapshot method		Changing Snapshot method	
	$D_s(m^2/s)$	$SD(m^2/s)$	$D_s(m^2/s)$	$SD(m^2/s)$	$D_s(m^2/s)$	$SD(m^2/s)$
1. LTA/Rn/1300 K	2.76E-11	9.27E-12	5.01E-11	--	3.24E-11	1.69E-11
2.RHO/Rn/1500 K	4.29E-11	4.57E-11	5.88E-11	--	3.92E-11	1.89E-11
3. LTA/Xe/1100 K	4.73E-11	2.15E-11	7.94E-11	--	8.19E-11	3.14E-11
4. RHO/Xe/1100 K	5.73E-11	4.20E-11	7.88E-11	--	7.15E-11	2.30E-11
5. CHA/Xe/1300 K	5.75E-11	7.17E-11	4.93E-11	--	7.25E-11	3.03E-11
6. EAB/Ar/500 K	9.85E-11	3.15E-11	--	--	1.44E-10	5.97E-11
7. ERI/Ar/700K	1.79E-10	8.23E-11	2.74E-10	--	2.47E-10	1.46E-10
8. SAS/Kr/500 K	1.99E-10	2.00E-10	3.66E-10	--	2.67E-10	1.00E-10
9. CHA/Kr/ 700 K	2.18E-10	1.80E-10	2.04E-10	--	2.29E-10	1.07E-10
10. LTA/Kr/700 K	3.19E-10	9.49E-11	3.57E-10	--	3.31E-10	7.43E-11
11. RHO/Kr/700 K	6.33E-10	2.83E-10	4.02E-10	--	5.45E-10	2.41E-10
12. DFT/Ar/500 K	6.43E-10	4.95E-10	--	--	7.14E-10	5.31E-10
13. ERI/Ne/500K	4.97E-09	2.61E-09	4.64E-09	--	5.77E-09	2.71E-09
14. EAB/Ne/500K	4.85E-09	2.46E-09	--	--	4.90E-09	2.01E-09
15. DFT/Ne/500K	1.32E-08	8.57E-09	--	--	1.31E-08	9.26E-09

Window size distribution of selected 8MR zeolites

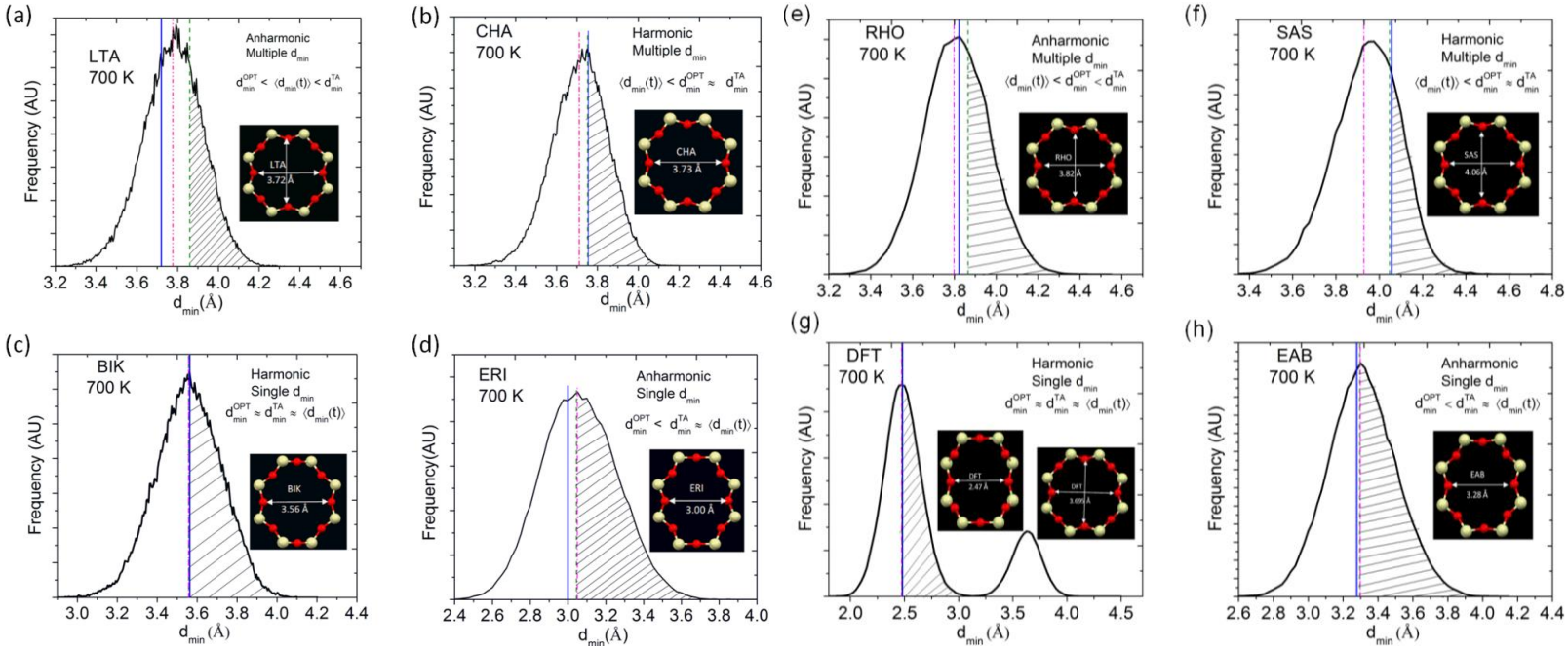

Figure B1. Window size distribution, $\mathbf{d_{min}^{OPT}}$(solid, blue), $\mathbf{d_{min}^{TA}}$ (dash, green), $\langle \mathbf{d_{min}(t)} \rangle$ (dot-dash, pink), and the tail of the distribution (shaded region) are shown for a) LTA, b) CHA, c) BIK, d) ERI, e) RHO, f) SAS, g) DFT, and h) EAB. Some of the characteristic dimensions are not visible because of the overlapping. In inset, 8MR windows of respective zeolites in the energy minimized geometries are shown with $\mathbf{d_{min}^{OPT}}$ labeled. Si (O) atoms are shown as yellow (red) spheres. [Note: In case of DFT, there are two different types of windows with $\mathbf{d_{min}^{OPT} = 2.47}$, 3.695 Å. The 8MR windows with $\mathbf{d_{min}^{OPT} = 2.47}$ Å has single d_{min} and is harmonic. Considering the size of Ne and Ar, the other window with $\mathbf{d_{min}^{OPT} = 3.695}$ Å is bigger and also less in numbers compared to smaller windows. Hence, the contribution of these windows in overall D_s is same for OPT, TA, and fully flexible structure and is not useful for comparison. Therefore, we consider zeolite DFT as defined by smaller windows with single d_{min} and harmonic behavior for our analysis in the chapter 3.]

Single component and binary adsorption isotherms for inert gases and CF_4

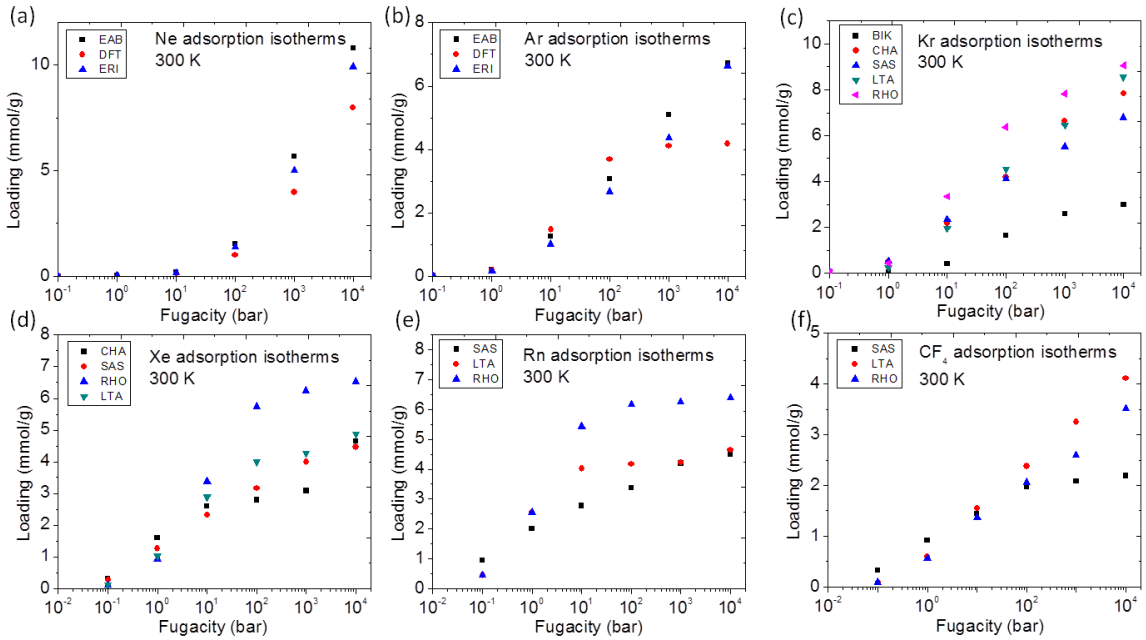

Figure B2. Single component adsorption isotherms for all the adsorbate-zeolite combinations studied.

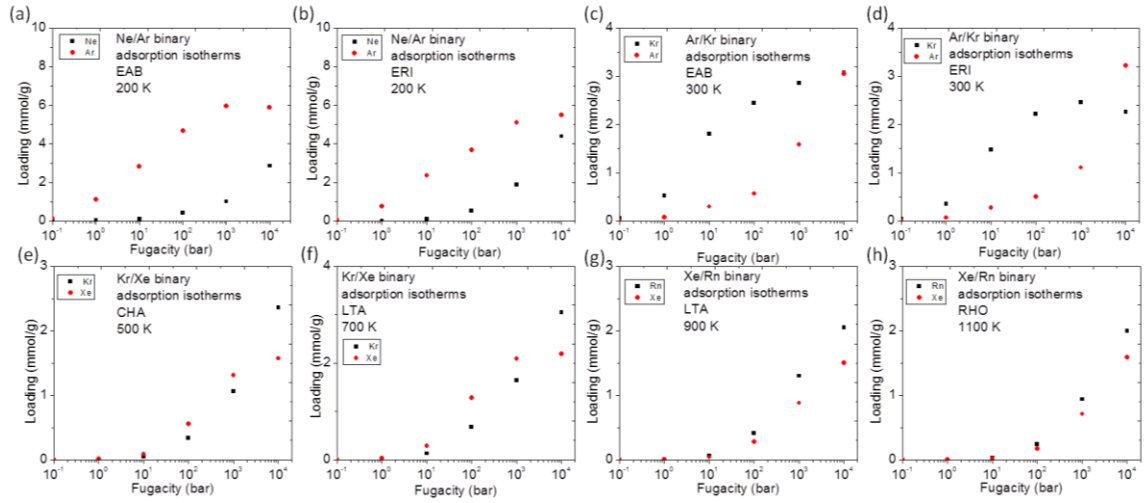

Figure B3. Binary adsorption isotherms (at 50:50 gas phase composition) for adsorbate-zeolite systems studied

Gas diffusivities in 8MR zeolites at 3 different temperatures and 3 different loadings

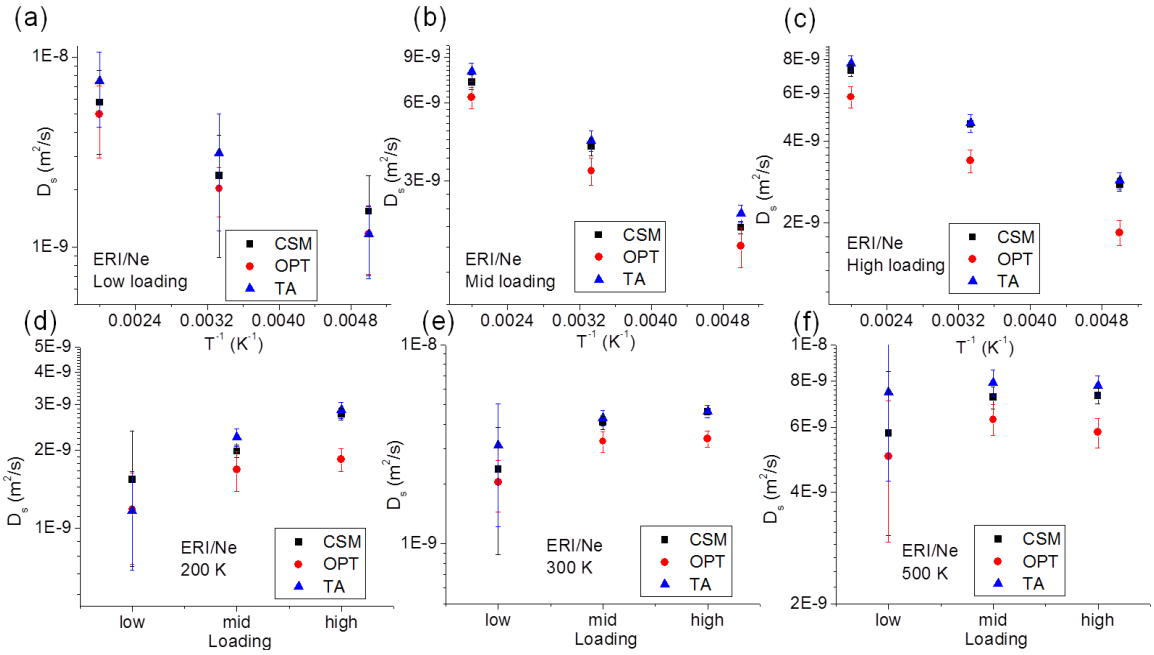

Figure B4. Self-diffusivities of Ne in ERI calculated using OPT, TA, and changing snapshot method (CSM) at 3 different loadings and 3 different temperatures. The data is plotted as a function of temperature (a-c) and as a function of adsorbate loading (d-f).

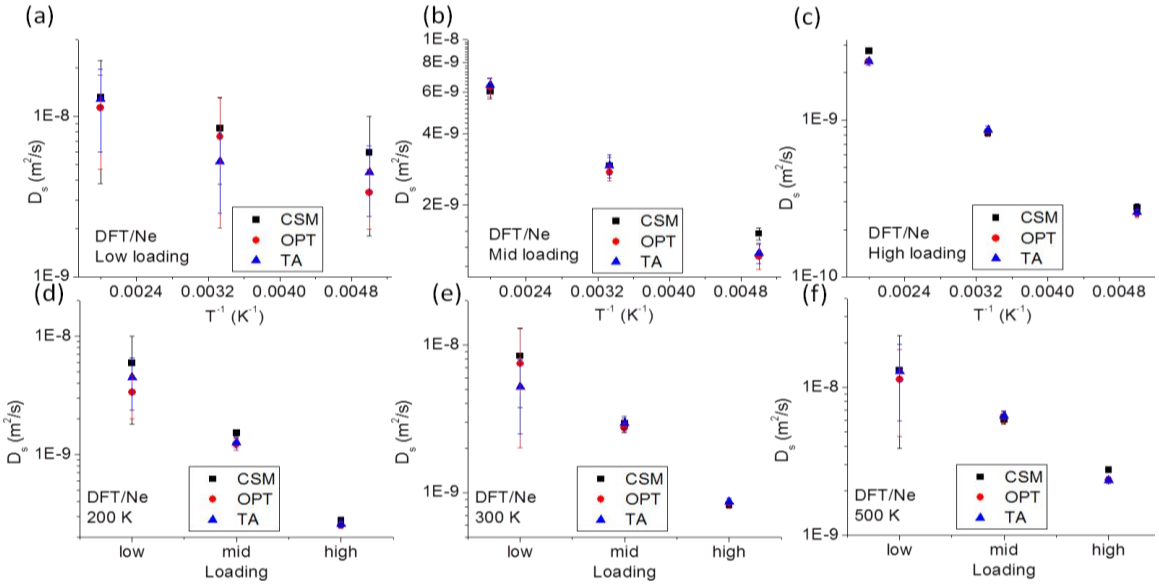

Figure B5. Self-diffusivities of Ne in DFT calculated using OPT, TA, and changing snapshot method (CSM) at 3 different loadings and 3 different temperatures. The data is plotted as a function of temperature (a-c) and as a function of adsorbate loading (d-f).

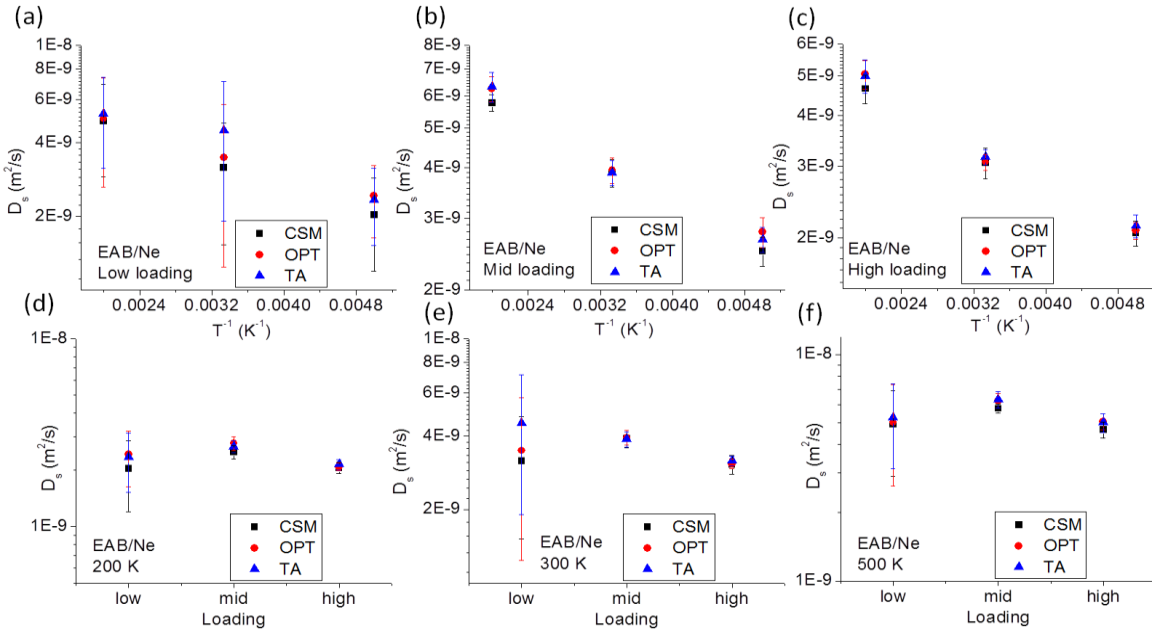

Figure B6. Self-diffusivities of Ne in EAB calculated using OPT, TA, and changing snapshot method (CSM) at 3 different loadings and 3 different temperatures. The data is plotted as a function of temperature (a-c) and as a function of adsorbate loading (d-f).

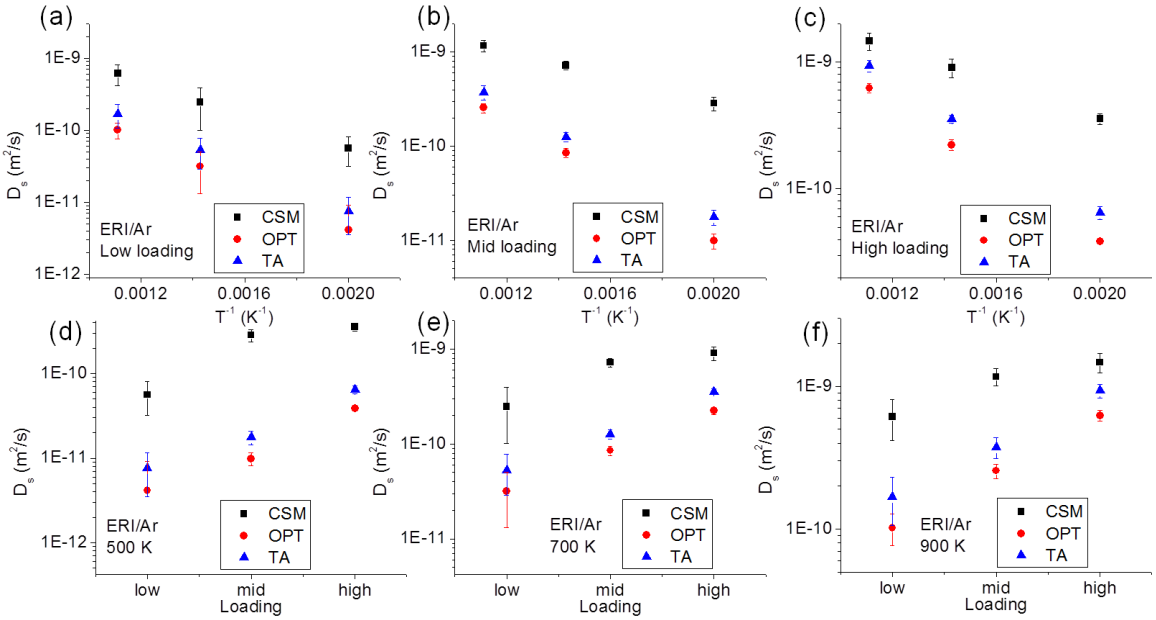

Figure B7. Self-diffusivities of Ar in ERI calculated using OPT, TA, and changing snapshot method (CSM) at 3 different loadings and 3 different temperatures. The data is plotted as a function of temperature (a-c) and as a function of adsorbate loading (d-f).

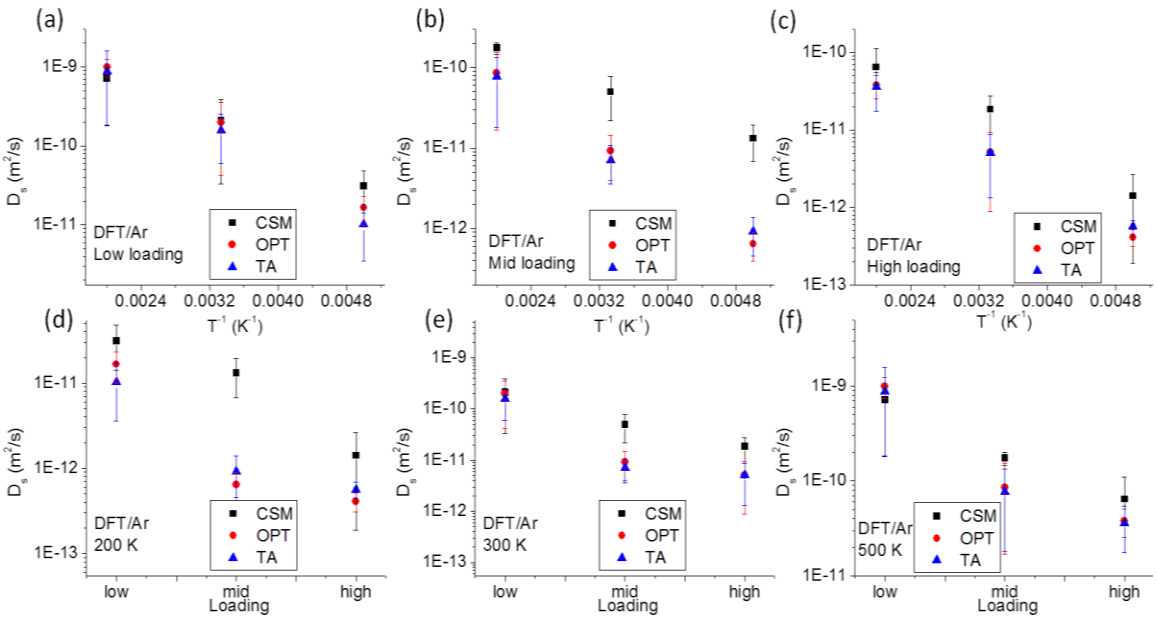

Figure B8. Self-diffusivities of Ar in DFT calculated using OPT, TA, and changing snapshot method (CSM) at 3 different loadings and 3 different temperatures. The data is plotted as a function of temperature (a-c) and as a function of adsorbate loading (d-f).

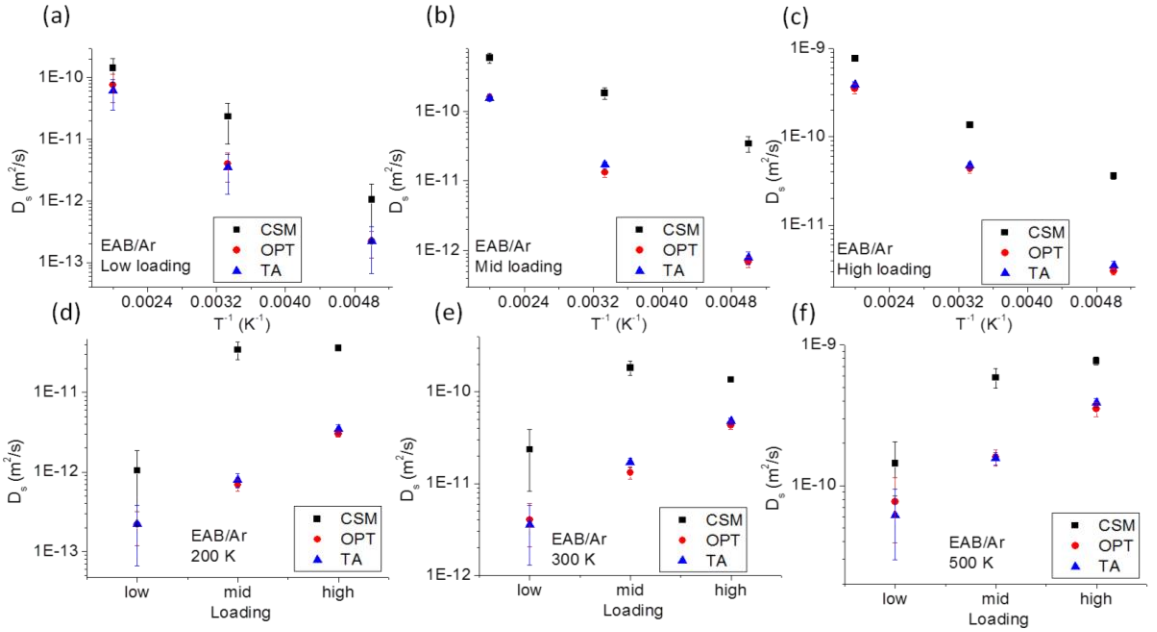

Figure B9. Self-diffusivities of Ar in EAB calculated using OPT, TA, and changing snapshot method (CSM) at 3 different loadings and 3 different temperatures. The data is plotted as a function of temperature (a-c) and as a function of adsorbate loading (d-f).

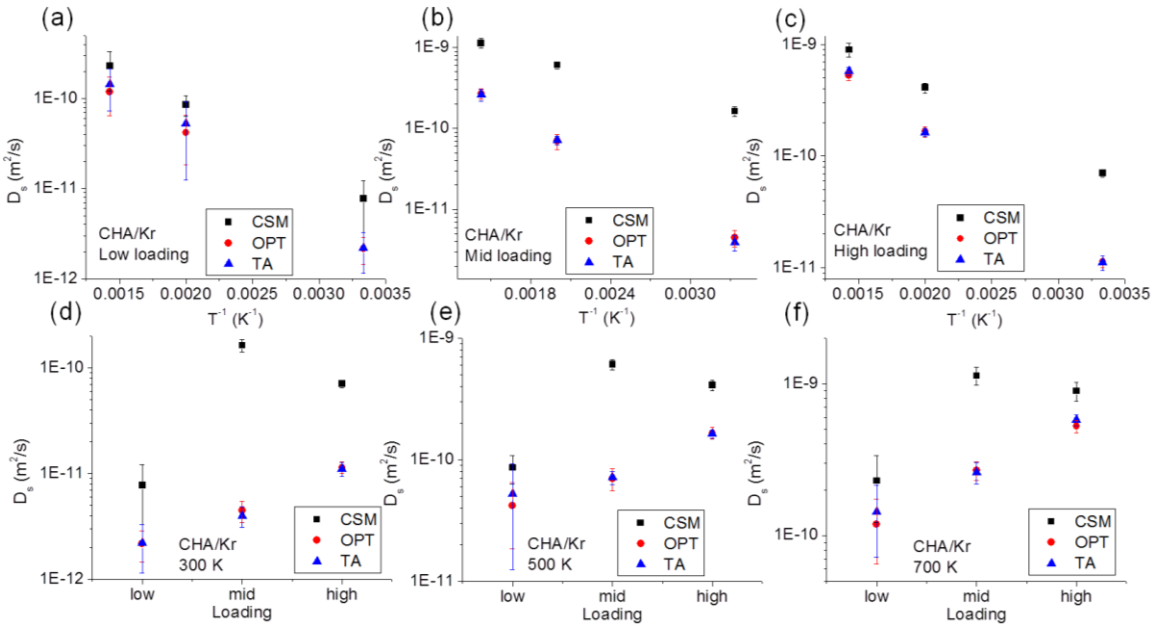

Figure B10. Self-diffusivities of Kr in CHA calculated using OPT, TA, and changing snapshot method (CSM) at 3 different loadings and 3 different temperatures. The data is plotted as a function of temperature (a-c) and as a function of adsorbate loading (d-f).

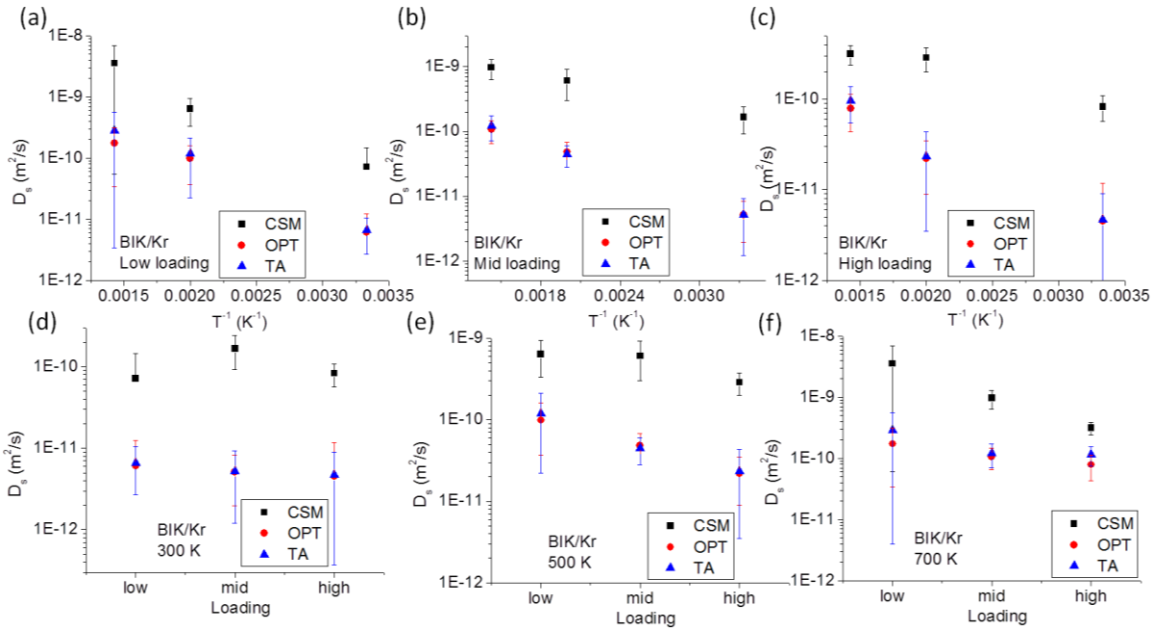

Figure B11. Self-diffusivities of Kr in BIK calculated using OPT, TA, and changing snapshot method (CSM) at 3 different loadings and 3 different temperatures. The data is plotted as a function of temperature (a-c) and as a function of adsorbate loading (d-f).

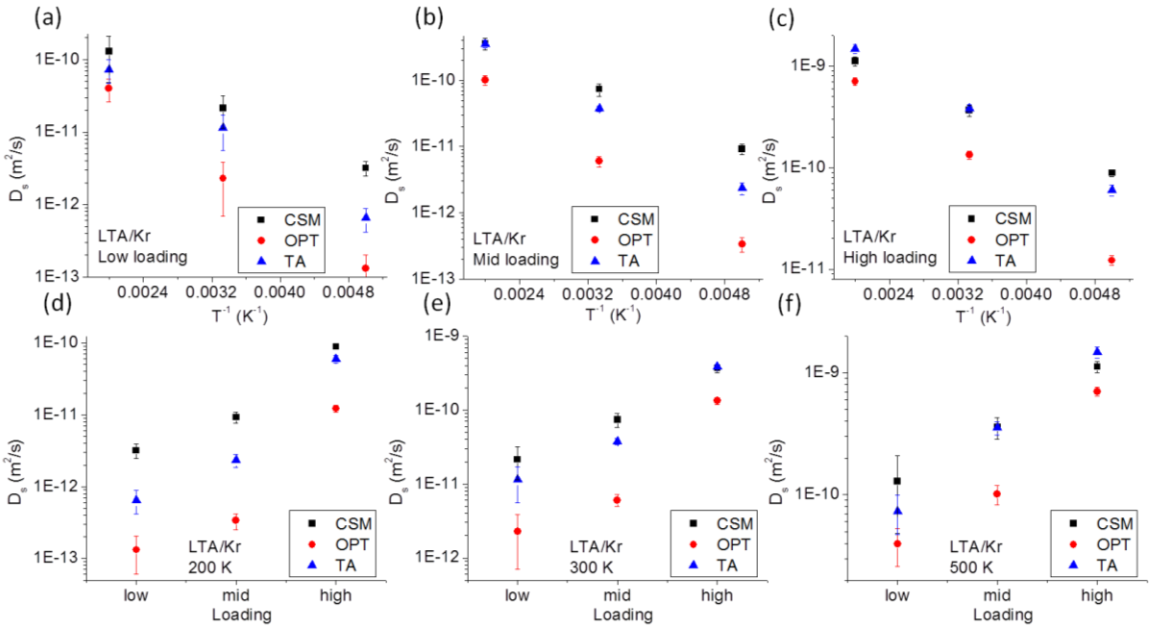

Figure B12. Self-diffusivities of Kr in LTA calculated using OPT, TA, and changing snapshot method (CSM) at 3 different loadings and 3 different temperatures. The data is plotted as a function of temperature (a-c) and as a function of adsorbate loading (d-f).

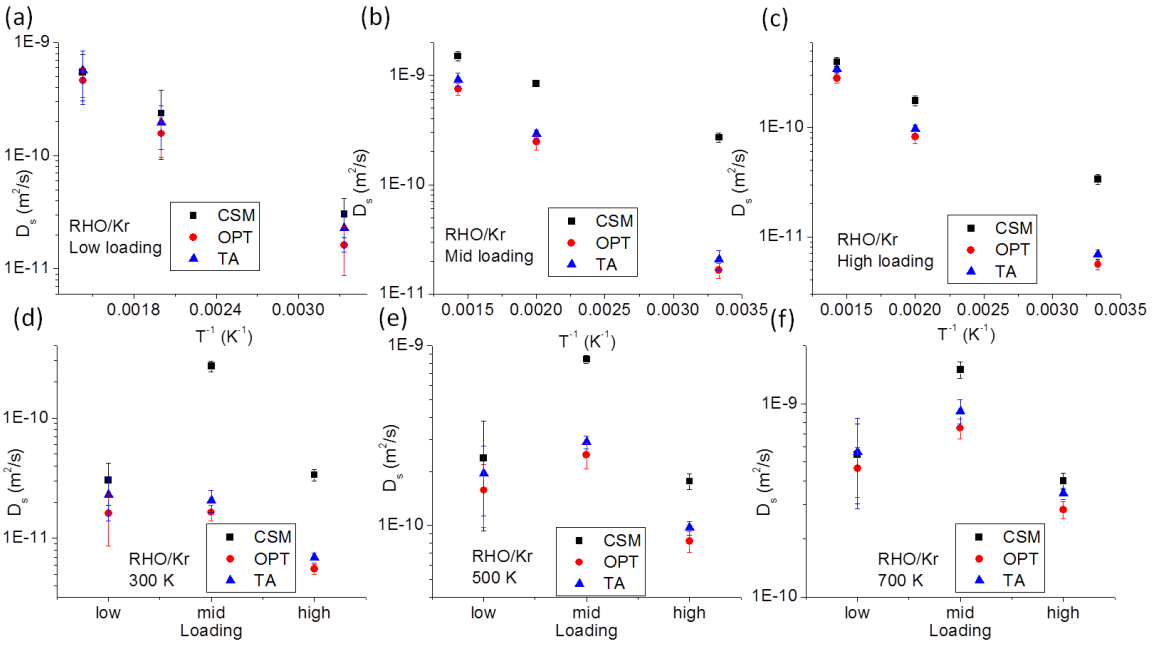

Figure B13. Self-diffusivities of Kr in RHO calculated using OPT, TA, and changing snapshot method (CSM) at 3 different loadings and 3 different temperatures. The data is plotted as a function of temperature (a-c) and as a function of adsorbate loading (d-f).

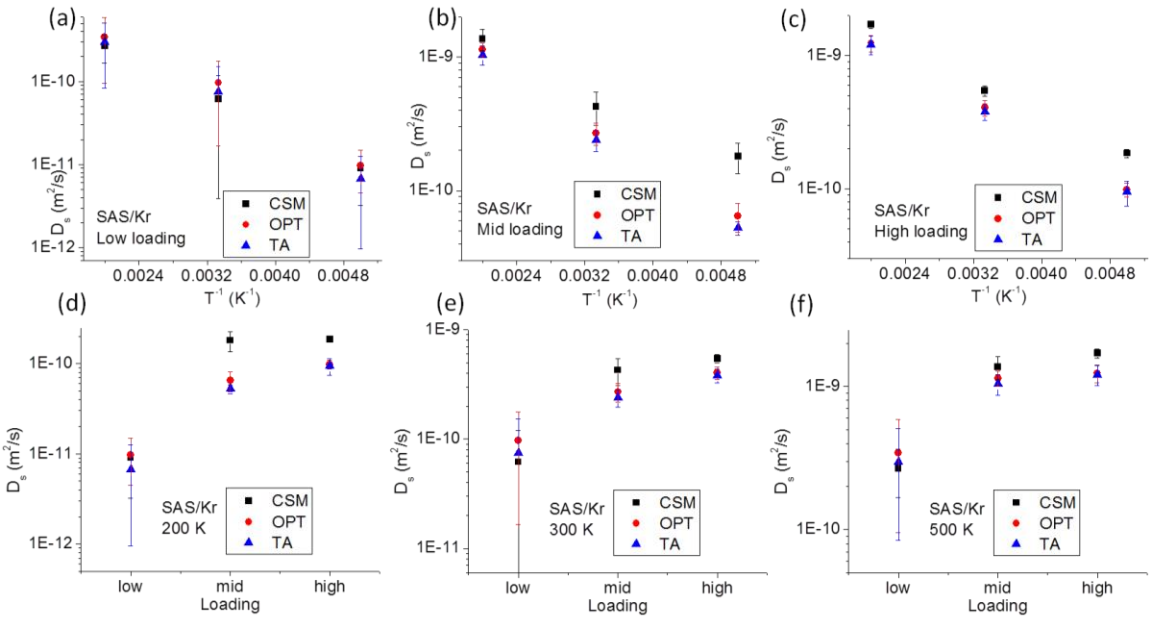

Figure B14. Self-diffusivities of Kr in SAS calculated using OPT, TA, and changing snapshot method (CSM) at 3 different loadings and 3 different temperatures. The data is plotted as a function of temperature (a-c) and as a function of adsorbate loading (d-f).

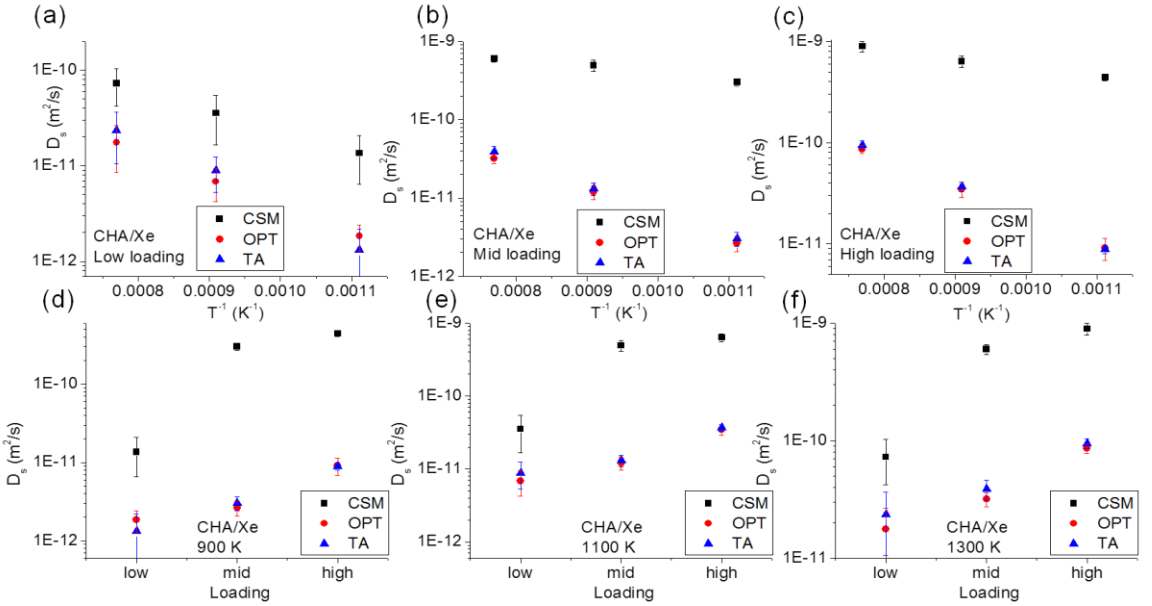

Figure B15. Self-diffusivities of Xe in CHA calculated using OPT, TA, and changing snapshot method (CSM) at 3 different loadings and 3 different temperatures. The data is plotted as a function of temperature (a-c) and as a function of adsorbate loading (d-f).

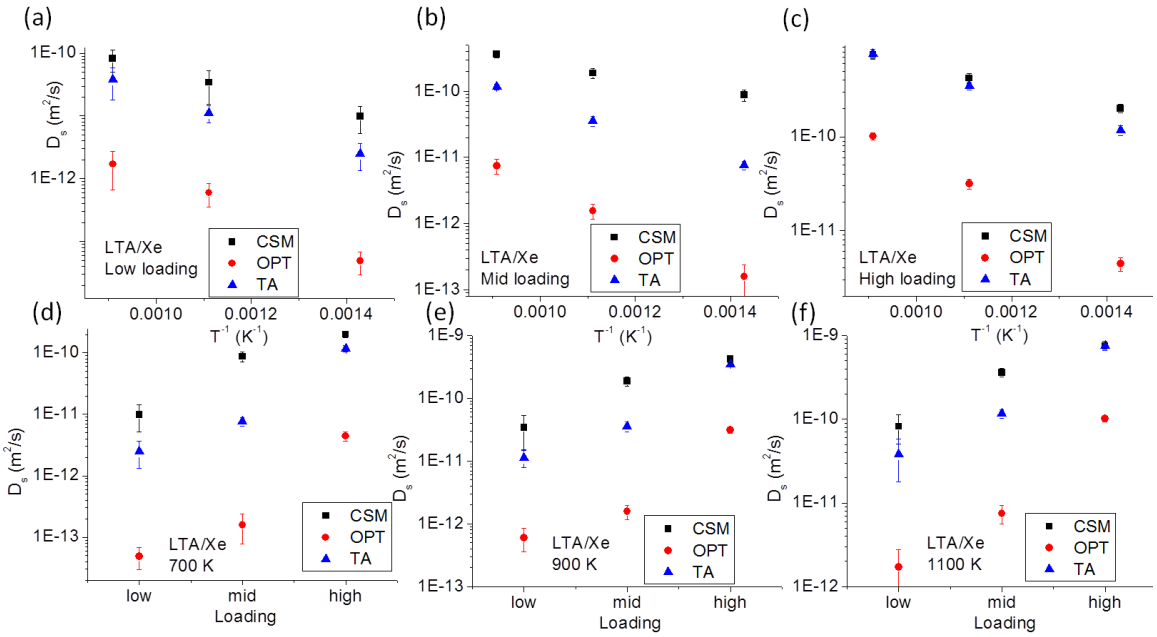

Figure B16. Self-diffusivities of Xe in LTA calculated using OPT, TA, and changing snapshot method (CSM) at 3 different loadings and 3 different temperatures. The data is plotted as a function of temperature (a-c) and as a function of adsorbate loading (d-f).

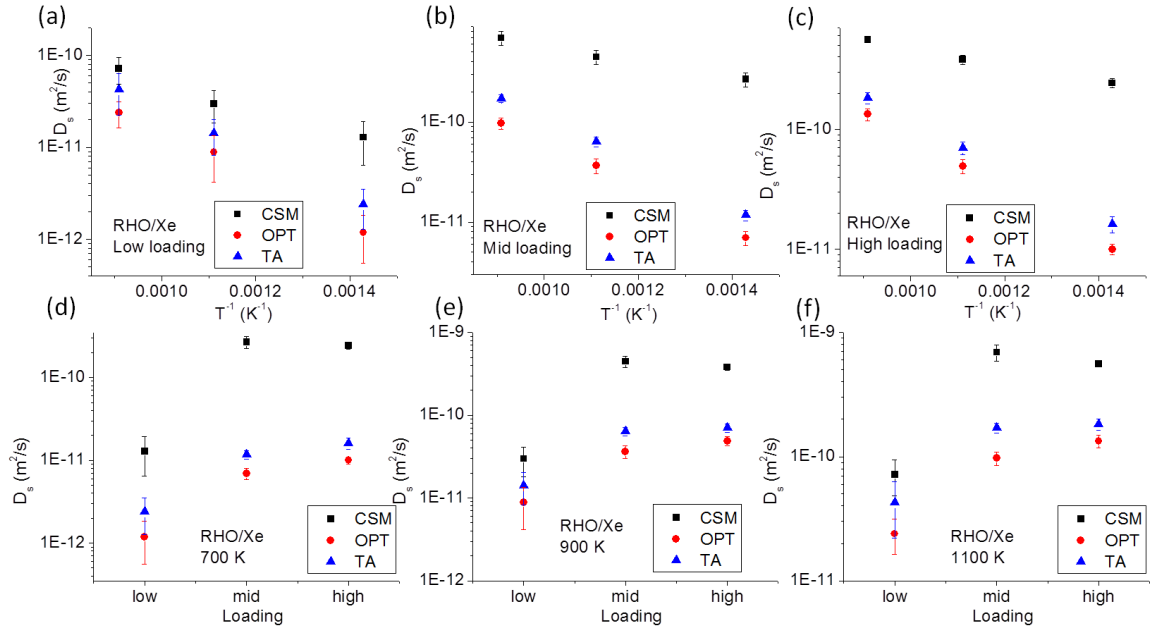

Figure B17. Self-diffusivities of Xe in RHO calculated using OPT, TA, and changing snapshot method (CSM) at 3 different loadings and 3 different temperatures. The data is plotted as a function of temperature (a-c) and as a function of adsorbate loading (d-f).

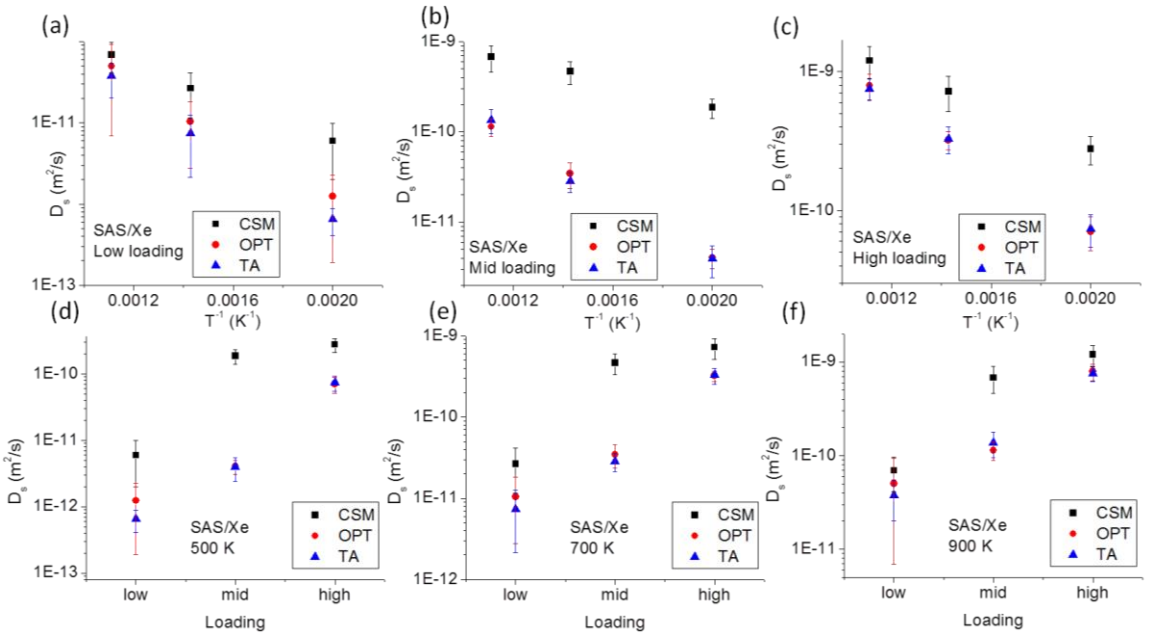

Figure B18. Self-diffusivities of Xe in SAS calculated using OPT, TA, and changing snapshot method (CSM) at 3 different loadings and 3 different temperatures. The data is plotted as a function of temperature (a-c) and as a function of adsorbate loading (d-f).

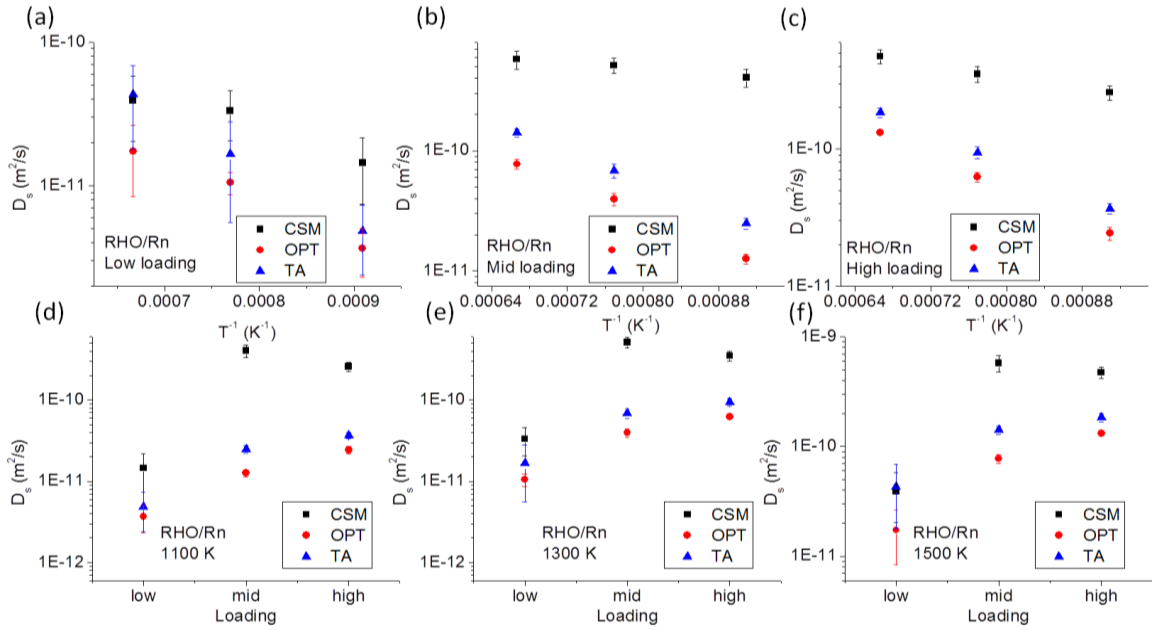

Figure B19. Self-diffusivities of Rn in RHO calculated using OPT, TA, and changing snapshot method (CSM) at 3 different loadings and 3 different temperatures. The data is plotted as a function of temperature (a-c) and as a function of adsorbate loading (d-f).

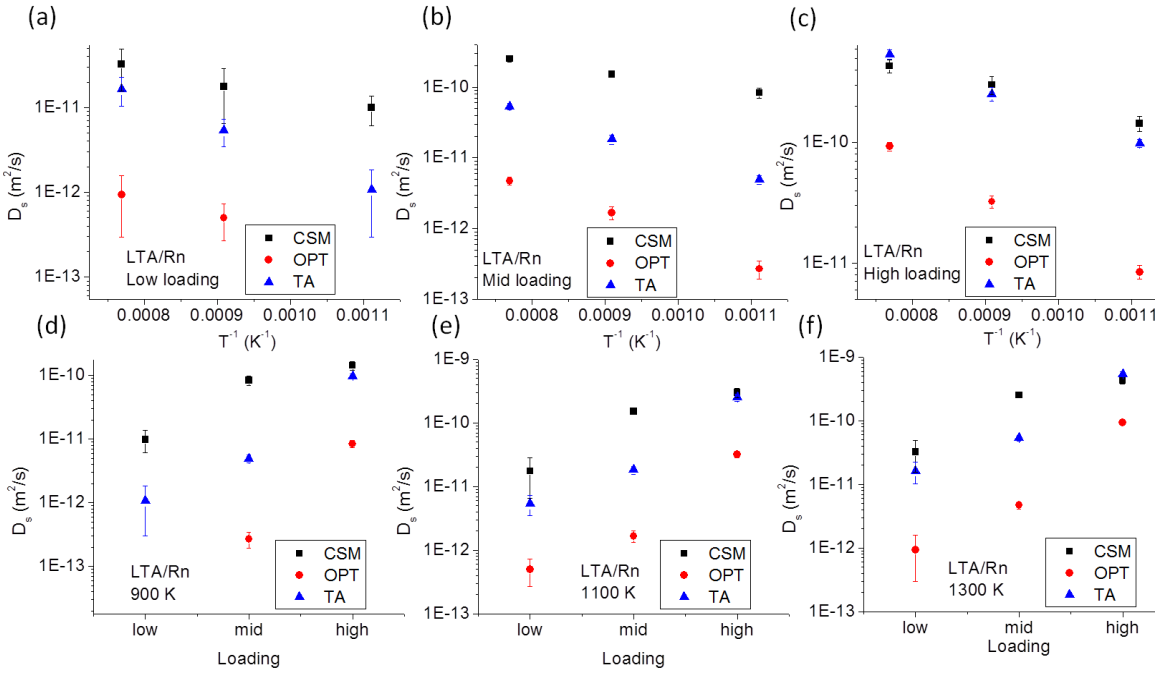

Figure B20. Self-diffusivities of Rn in LTA calculated using OPT, TA, and changing snapshot method (CSM) at 3 different loadings and 3 different temperatures. The data is plotted as a function of temperature (a-c) and as a function of adsorbate loading (d-f).

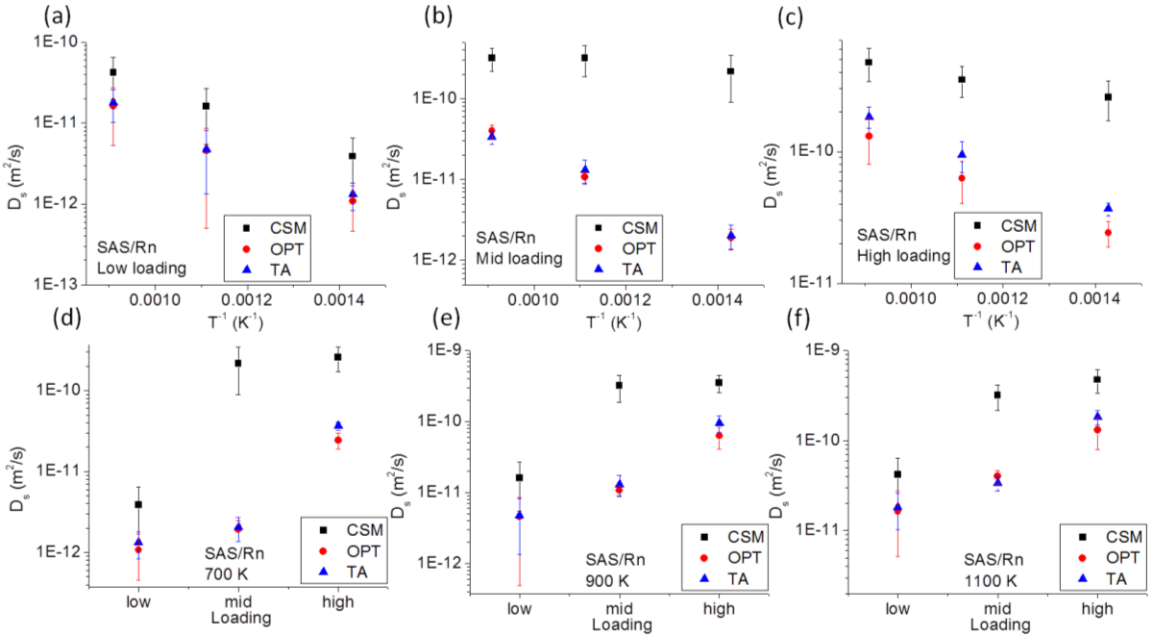

Figure B21. Self-diffusivities of Rn in SAS calculated using OPT, TA, and changing snapshot method (CSM) at 3 different loadings and 3 different temperatures. The data is plotted as a function of temperature (a-c) and as a function of adsorbate loading (d-f).

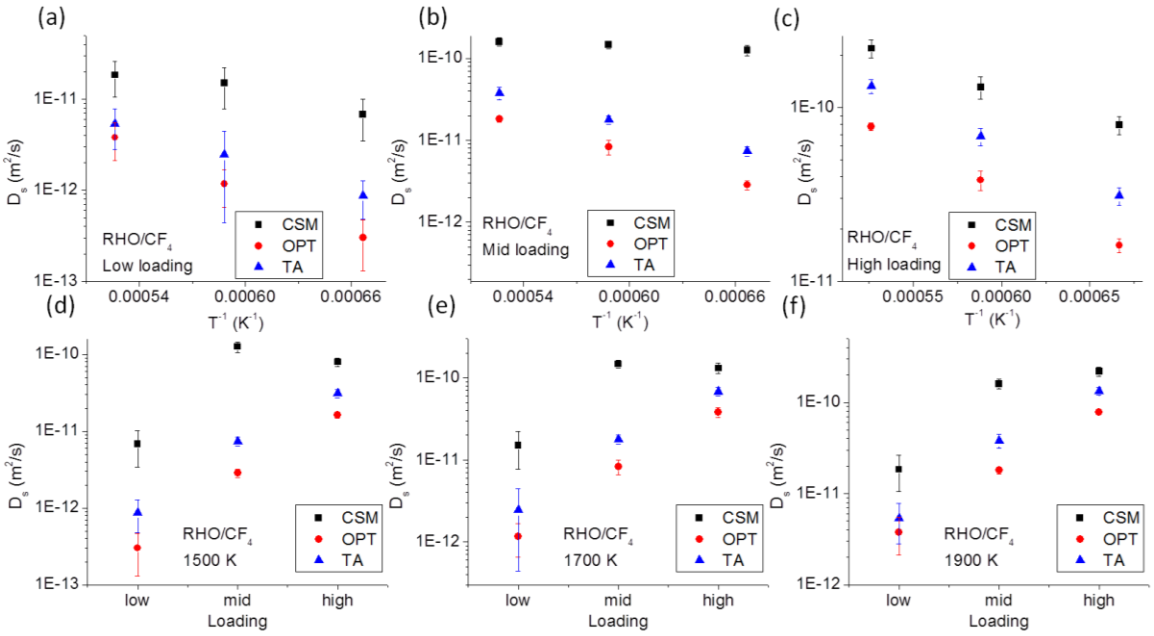

Figure B22. Self-diffusivities of CF_4 in RHO calculated using OPT, TA, and changing snapshot method (CSM) at 3 different loadings and 3 different temperatures. The data is plotted as a function of temperature (a-c) and as a function of adsorbate loading (d-f).

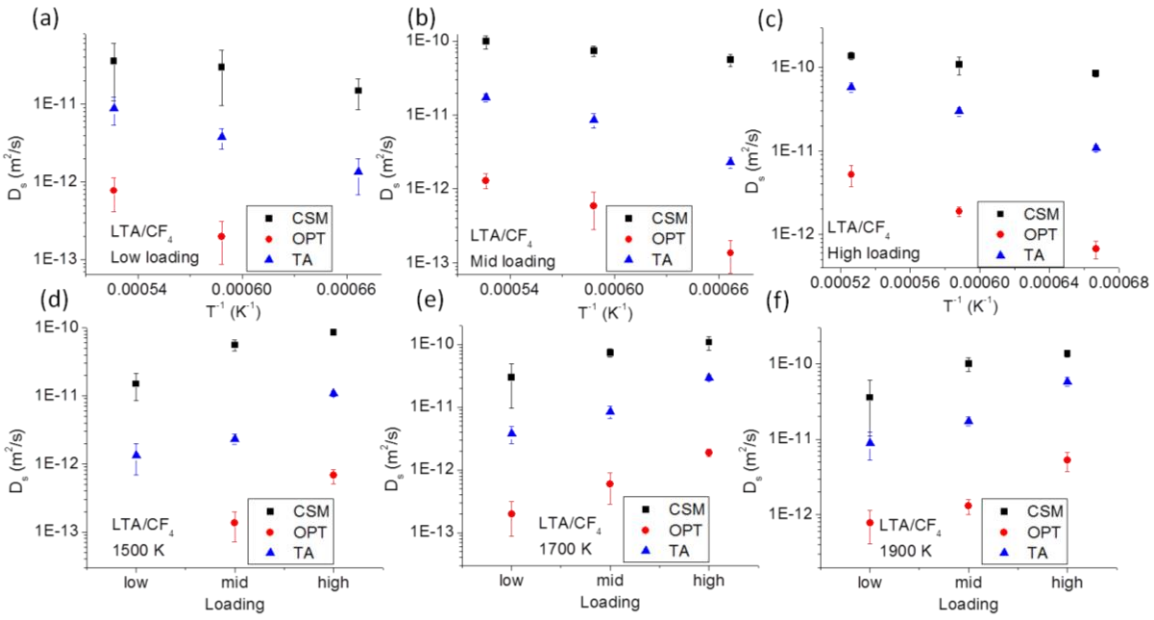

Figure B23. Self-diffusivities of CF_4 in LTA calculated using OPT, TA, and changing snapshot method (CSM) at 3 different loadings and 3 different temperatures. The data is plotted as a function of temperature (a-c) and as a function of adsorbate loading (d-f).

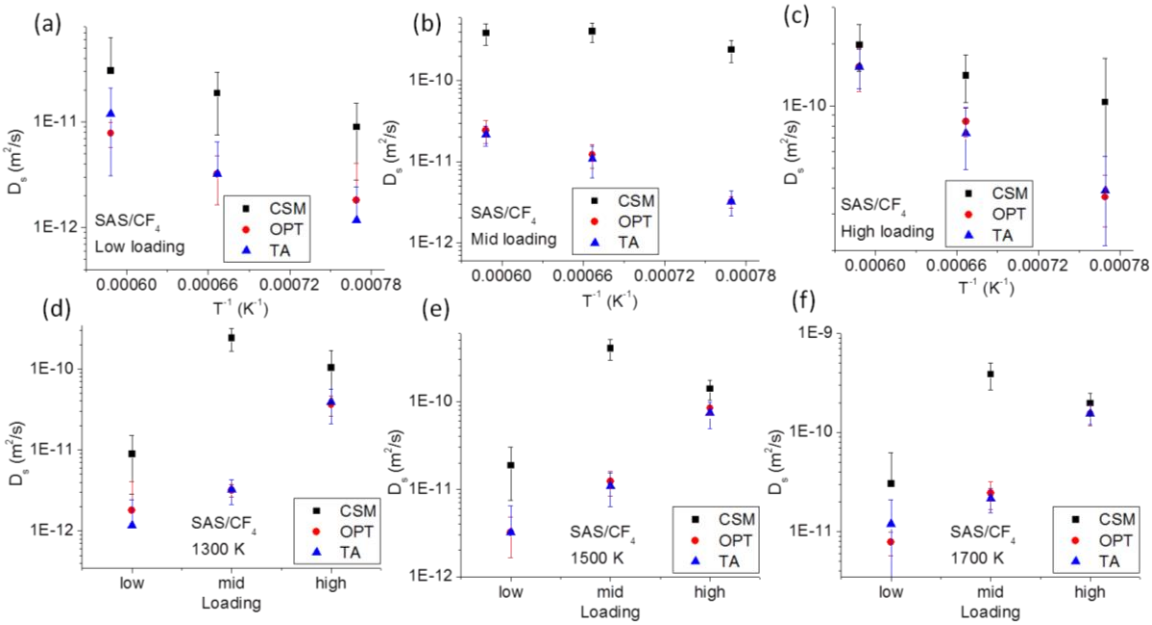

Figure B24. Self-diffusivities of CF_4 in SAS calculated using OPT, TA, and changing snapshot method (CSM) at 3 different loadings and 3 different temperatures. The data is plotted as a function of temperature (a-c) and as a function of adsorbate loading (d-f).

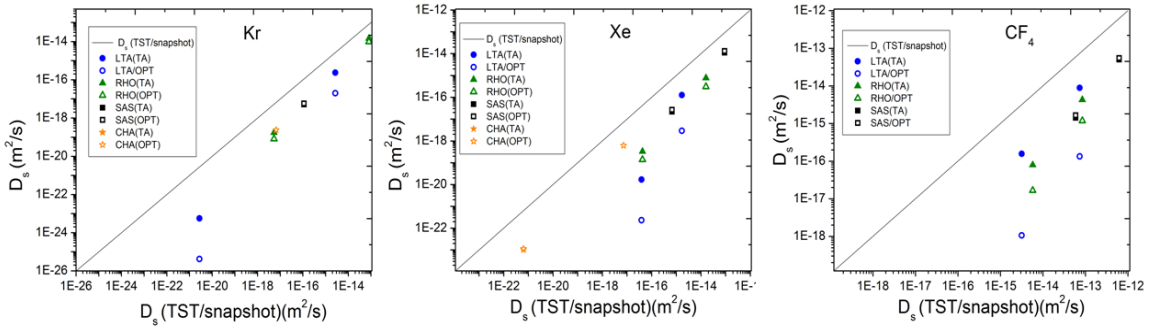

Figure B25. TST calculations to obtain D_s at low temperatures in the time averaged and optimized structures compared with D_s from TST/snapshot method for various adsorbates in variety of 8MR zeolites. For harmonic zeolites (CHA, SAS), the data for OPT and TA structures overlaps and hence is hard to visualize in the figure for some cases.

Table B4. Numerical values of diffusivities (in m^2/s) in Fig 3.2.

a) Ne/ERI-D_s(m^2/s)				b) Ar/ERI-D_s(m^2/s)			
T	Flexible	OPT	TA	T	Flexible	OPT	TA
200	1.539E-09	1.175E-09	1.165E-09	500	5.616E-11	4.125E-12	7.577E-12
300	2.037E-09	2.372E-09	3.127E-09	700	2.468E-10	3.160E-11	5.308E-11
500	5.773E-09	5.000E-09	7.461E-09	900	4.140E-10	1.016E-10	1.677E-10
c) Kr/CHA-D_s(m^2/s)				d) Xe/CHA-D_s(m^2/s)			
T	Flexible	OPT	TA	T	Flexible	OPT	TA
300	7.750E-12	2.162E-12	2.210E-12	900	1.355E-11	1.843E-12	1.318E-12
500	8.586E-11	4.180E-11	5.225E-11	1100	3.551E-11	6.841E-12	8.867E-12
700	2.289E-10	1.191E-10	1.434E-10	1300	7.246E-11	1.755E-11	2.352E-11
e) Rn/RHO-D_s(m^2/s)				f) CF_4/RHO-D_s(m^2/s)			
T	Flexible	OPT	TA	T	Flexible	OPT	TA
1100	1.448E-11	3.653E-12	4.848E-12	1500	6.757E-12	3.006E-13	8.76E-13
1300	3.319E-11	1.054E-11	1.667E-11	1700	1.503E-11	1.164E-12	2.46E-12
1500	3.916E-11	1.728E-11	4.311E-11	1900	1.838E-11	3.787E-12	5.34E-12

Table B5. Numerical values of diffusivities (in m^2/s) in Fig 3.3.

a) Ne/ERI-D_s(m^2/s)				b) Ar/ERI-D_s(m^2/s)			
Loading	Flexible	OPT	TA	Loading	Flexible	OPT	TA
Low	1.539E-09	1.175E-09	1.165E-09	Low	5.616E-11	4.125E-12	7.577E-12
Mid	1.68E-09	1.98E-09	2.24E-09	Mid	2.85E-10	9.87E-12	1.76E-11
High	1.84E-09	2.76E-09	2.86E-09	High	3.57E-10	3.84E-11	6.49E-11
c) Kr/CHA-D_s(m^2/s)				d) Xe/RHO-D_s(m^2/s)			
Loading	Flexible	OPT	TA	Loading	Flexible	OPT	TA
Low	7.750E-12	2.162E-12	2.210E-12	Low	1.278E-11	1.185E-12	2.392E-12
Mid	1.63E-10	4.47E-12	3.94E-12	Mid	2.66E-10	6.94E-12	1.17E-11
High	7.06E-11	1.14E-11	1.11E-11	High	2.42E-10	9.99E-12	1.61E-11
e) Rn/RHO-D_s(m^2/s)				f) CF_4/RHO-D_s(m^2/s)			
Loading	Flexible	OPT	TA	Loading	Flexible	OPT	TA
Low	1.448E-11	3.653E-12	4.848E-12	Low	6.757E-12	3.006E-13	8.76E-13
Mid	4.06E-10	1.26E-11	2.49E-11	Mid	1.26E-10	2.84E-12	7.338E-12
High	2.58E-10	2.42E-11	3.67E-11	High	7.95E-11	1.61E-11	3.103E-11

Table B6. Numerical values of diffusivities (in m^2/s) in Fig 3.5.

Ar/ERI-D_s(m^2/s)				Kr/CHA-D_s(m^2/s)			
T	Flexible	OPT	TA	T	Flexible	OPT	TA
100	3.63E-21	6.65E-24	1.12E-23	50	3.41E-26	1.68E-28	1.47E-28
200	1.63E-14	1.83E-16	3.54E-16	100	6.61E-18	2.37E-19	2.35E-19
Xe/CHA-D_s(m^2/s)				Rn/LTA-D_s(m^2/s)			
T	Flexible	OPT	TA	T	Flexible	OPT	TA
200	6.4E-21	1.2E-23	1E-23	200	2.15E-19	4.33E-27	8.26E-25
300	7.3E-17	6.20E-19	6.2E-19	300	1.63E-17	1.60E-21	2.02E-19
Rn/RHO-D_s(m^2/s)				Rn/SAS-D_s(m^2/s)			
T	Flexible	OPT	TA	T	Flexible	OPT	TA
200	1.1E-19	3.3E-24	1.1E-23	200	4.17E-18	9.59E-21	7.50E-21
300	3.1E-16	1.7E-19	5.8E-19	300	4.27E-15	5.75E-17	4.68E-17

Table B7. Numerical values of diffusivities (in m^2/s) in Fig 3.6.

System Index	D_s (Smaller Adsorbate)			
	Flexible	CSM	OPT	TA
1	1.47E-09	1.90E-09	2.52E-09	2.73E-09
2	7.43E-10	1.51E-09	2.19E-09	2.66E-09
3	5.22E-11	7.67E-11	1.26E-11	1.58E-11
4	1.41E-10	2.53E-10	1.41E-11	2.72E-11
5	4.97E-10	5.72E-10	1.56E-10	5.64E-10
6	4.54E-10	7.93E-10	4.59E-10	5.24E-10
7	8.56E-11	1.35E-10	1.15E-12	2.86E-11
8	1.44E-10	2.78E-10	5.57E-11	1.11E-10
System Index	D_s (Larger Adsorbate)			
	Flexible	CSM	OPT	TA
1	4.42E-12	5.96E-12	7.20E-13	7.20E-13
2	--	6.15E-11	1.63E-12	2.05E-12
3	1.22E-12	1.94E-12	7.20E-13	7.20E-13
4	--	2.06E-11	2.00E-13	2.00E-13
5	--	1.70E-11	1.64E-13	1.64E-13
6	--	9.83E-11	8.05E-13	8.90E-13
7	--	3.24E-11	1.86E-13	4.48E-12
8	3.98E-11	4.75E-11	8.14E-12	1.77E-11

Table B8. Numerical values of diffusivities (in m^2/s) in Fig 3.4.

Ne/ERI-D_s(m^2/s)			Ar/ERI-D_s(m^2/s)			Kr/CHA-D_s(m^2/s)			Xe/CHA-D_s(m^2/s)		
T	CSM	TST/ Snapshot	T	CSM	TST/ Snapshot	T	CSM	TST/ Snapshot	T	CSM	TST/ Snapshot
200	1.54E-09	1.03E-09	500	5.62E-11	5.07E-11	300	7.75E-12	5.60E-12	900	1.36E-11	8.43E-12
300	2.04E-09	2.13E-09	700	2.47E-10	2.74E-10	500	8.59E-11	5.74E-11	1100	3.55E-11	2.65E-11
500	5.77E-09	4.64E-09	900	4.14E-10	7.44E-10	700	2.29E-10	2.04E-10	1300	7.25E-11	4.93E-11
Kr/LTA-D_s(m^2/s)			Xe/LTA-D_s(m^2/s)			Rn/LTA-D_s(m^2/s)			CF_4/LTA-D_s(m^2/s)		
T	CSM	TST/ Snapshot	T	CSM	TST/ Snapshot	T	CSM	TST/ Snapshot	T	CSM	TST/ Snapshot
200	3.19E-12	3.66E-12	700	9.81E-12	6.98E-12	900	9.91E-12	5.13E-12	1500	1.49E-11	9.13E-12
300	2.15E-11	2.54E-11	900	3.41E-11	2.63E-11	1100	2.76E-11	2.09E-11	1700	2.97E-11	2.18E-11
500	1.29E-10	1.99E-10	1100	8.19E-11	7.94E-11	1300	3.24E-11	5.01E-11	1900	3.57E-11	3.74E-11
Kr/RHO-D_s(m^2/s)			Xe/RHO-D_s(m^2/s)			Rn/RHO-D_s(m^2/s)			CF_4/RHO-D_s(m^2/s)		
T	CSM	TST/ Snapshot	T	CSM	TST/ Snapshot	T	CSM	TST/ Snapshot	T	CSM	TST/ Snapshot
300	3.03E-11	4.58E-11	700	1.28E-11	1.15E-11	1100	1.45E-11	1.64E-11	1500	6.76E-12	6.75E-12
500	2.37E-10	2.10E-10	900	2.97E-11	3.34E-11	1300	3.32E-11	3.17E-11	1700	1.50E-11	1.44E-11
700	5.45E-10	4.02E-10	1100	7.15E-11	7.88E-11	1500	3.92E-11	5.88E-11	1900	1.84E-11	3.05E-11
Kr/SAS-D_s(m^2/s)			Xe/SAS-D_s(m^2/s)			Rn/SAS-D_s(m^2/s)			CF_4/SAS-D_s(m^2/s)		
T	CSM	TST/ Snapshot	T	CSM	TST/ Snapshot	T	CSM	TST/ Snapshot	T	CSM	TST/ Snapshot
200	9.03E-12	1.60E-11	500	5.95E-12	3.58E-12	700	3.86E-12	3.38E-12	1300	8.95E-12	8.09E-12
300	6.16E-11	7.80E-11	700	2.65E-11	2.56E-11	900	1.61E-11	1.65E-11	1500	1.87E-11	2.10E-11
500	2.67E-10	3.66E-10	900	6.91E-11	9.18E-11	1100	4.19E-11	4.80E-11	1700	3.04E-11	4.94E-11

Appendix C

Table C1. The numerical values for ε_{CH}, α_{CH}, ε_{HH}, and α_{HH} for CH_4 in silica zeolite

C-H			H-H		
R (Å)	α	ε (kJ/pair)	R (Å)	α	ε (kJ/pair)
0.6285	-0.0013	14.9141	0.5403	0.0001	38.5420
0.8285	0.0061	11.7619	0.7403	0.0025	29.5553
1.0285	0.0294	4.4213	0.9403	0.0109	20.3072
1.2285	0.0325	-1.6414	1.1403	0.0254	12.9513
1.4285	-0.0035	-4.6968	1.3403	0.0391	7.8438
1.6285	-0.0486	-5.5184	1.5403	0.0353	4.5993
1.8285	-0.1581	-5.1801	1.7403	0.0366	2.6626
2.0285	-0.1742	-4.3782	1.9403	0.0082	1.5451
2.2285	-0.1303	-3.5002	2.1403	-0.0470	0.9206
2.4285	-0.5711	-2.6974	2.3403	0.0009	0.5772
2.6285	-0.0175	-2.0085	2.5403	-0.1017	0.3829
2.8285	-0.9735	-1.4525	2.7403	0.0637	0.2669
3.0285	-0.3080	-1.0147	2.9403	0.1574	0.1890
3.2285	0.1202	-0.6864	3.1403	-0.0704	0.1321
3.4285	-0.2504	-0.4511	3.3403	0.3762	0.0894
3.6285	0.5336	-0.2877	3.5403	-0.0815	0.0567
3.8285	0.6184	-0.1784	3.7403	0.1112	0.0326
4.0285	0.7802	-0.1077	3.9403	-0.1214	0.0157
4.2285	0.5927	-0.0632	4.1403	-0.2718	0.0044
4.4285	0.4770	-0.0359	4.3403	-0.0395	-0.0026
4.6285	0.3436	-0.0194	4.5403	-0.2823	-0.0066
4.8285	0.0650	-0.0097	5.0403	-0.3629	-0.0095
5.0285	-0.0914	-0.0039	5.5403	-0.3358	-0.0081
5.2285	-0.0689	-0.0005	6.0403	-0.0173	-0.0060
5.4285	-0.0635	0.0014	6.5403	0.1637	-0.0042
5.6285	-0.0805	0.0025	7.5403	0.1277	-0.0020
6.1285	0.0117	0.0032	8.5403	0.0524	-0.0010
6.6285	0.0471	0.0028	10.5403	-0.0292	-0.0003
7.1285	0.0392	0.0023	13.5403	-0.0625	-0.0001
7.6285	0.0258	0.0018	18.5403	-0.0307	0.0000
8.6285	0.0116	0.0010			
9.6285	0.0018	0.0006			
11.6285	-0.0127	0.0002			
14.6285	-0.0145	0.0001			
19.6285	-0.0062	0.0000			

Table C2. The numerical values for ε_{CO}, α_{CO}, ε_{HO}, and α_{HO} for CH_4 in silica zeolite

C-O			H-O		
R (Å)	α	ε (kJ/pair)	R (Å)	α	ε (kJ/pair)
1.0000	-0.0926	39.2268	0.5118	-0.0023	19.2871
1.2000	-0.2876	41.6228	0.7118	-0.0007	43.3212
1.4000	2.3065	29.9847	0.9118	0.0326	36.4829
1.6000	-0.2788	9.1459	1.1118	0.0356	22.5773
1.8000	-1.8813	-2.0933	1.3118	0.0694	12.5345
2.0000	-0.6777	-5.0824	1.5118	0.0736	6.2911
2.2000	-0.4760	-4.8819	1.7118	0.0231	2.7228
2.4000	-0.4087	-3.8197	1.9118	0.0205	0.8490
2.6000	-1.3995	-2.6771	2.1118	-0.1421	-0.0487
2.8000	0.9501	-1.6923	2.3118	-0.1560	-0.4053
3.0000	-2.2560	-0.9367	2.5118	-0.1763	-0.4949
3.2000	-0.0018	-0.3766	2.7118	-0.3727	-0.4687
3.4000	0.3317	0.0114	2.9118	-0.0378	-0.4040
3.6000	0.8660	0.2587	3.1118	0.4060	-0.3411
3.8000	1.5260	0.4000	3.3118	-0.2690	-0.2920
4.0000	2.5856	0.4653	3.5118	0.4101	-0.2544
4.2000	2.4368	0.4796	3.7118	0.4091	-0.2261
4.4000	2.6894	0.4624	3.9118	-0.4654	-0.2033
4.6000	2.3949	0.4275	4.1118	-0.1455	-0.1830
4.8000	1.8647	0.3847	4.3118	-0.2148	-0.1640
5.0000	1.4925	0.3399	4.5118	-0.7781	-0.1459
5.2000	1.1101	0.2966	4.7118	-0.8043	-0.1287
5.4000	0.7565	0.2569	4.9118	-0.7446	-0.1125
5.6000	0.5327	0.2213	5.4118	-1.2728	-0.0783
5.8000	0.3830	0.1902	5.9118	-0.5720	-0.0533
6.0000	0.2696	0.1632	6.4118	0.0929	-0.0361
6.5000	0.0801	0.1114	6.9118	0.2081	-0.0246
7.0000	-0.0095	0.0767	7.9118	0.0351	-0.0120
7.5000	-0.0258	0.0536	8.9118	0.0724	-0.0062
8.0000	-0.0134	0.0379	10.9118	0.0902	-0.0019
9.0000	0.0137	0.0199	13.9118	0.0478	-0.0005
10.0000	0.0229	0.0110	18.9118	0.0130	-0.0001
12.0000	0.0190	0.0039			
15.0000	0.0090	0.0011			
20.0000	0.0025	0.0002			

Table C3. The numerical values for ε_{CSi}, α_{CSi}, ε_{HSi}, and α_{HSi} for CH_4 in silica zeolite

C-Si			H-Si		
R (Å)	α	ε (kJ/pair)	R (Å)	α	ε (kJ/pair)
2.0000	0.1190	-45.7233	0.5118	0.0011	78.5145
2.2000	12.0051	92.6899	0.7118	0.0079	36.4284
2.4000	7.6406	-20.2843	0.9118	0.0852	5.6178
2.6000	1.8745	-27.2930	1.1118	-0.2203	-7.2803
2.8000	-1.0933	-3.6255	1.3118	-0.2066	-1.5987
3.0000	-2.3981	2.6360	1.5118	0.3058	3.4014
3.2000	-2.9677	0.5424	1.7118	0.4603	3.9653
3.4000	-3.1865	5.7556	1.9118	0.0971	2.7607
3.6000	-3.2135	-0.5741	2.1118	0.4374	1.5411
3.8000	-3.1039	-5.3521	2.3118	-0.6259	0.7269
4.0000	-2.8933	-9.7879	2.5118	-0.5401	0.3528
4.2000	-2.6190	-11.1688	2.7118	-0.0890	0.2454
4.4000	-2.3165	-9.0323	2.9118	-0.7817	0.2591
4.6000	-2.0143	-7.2763	3.1118	0.1345	0.3198
4.8000	-1.7302	-5.8006	3.3118	-2.4423	0.3855
5.0000	-1.4739	-4.7614	3.5118	1.8927	0.4374
5.2000	-1.2487	-3.2200	3.7118	0.8407	0.4601
5.4000	-1.0547	-1.5283	3.9118	1.5657	0.4565
5.6000	-0.8899	-0.0914	4.1118	0.4835	0.4345
5.8000	-0.7510	0.9232	4.3118	0.7302	0.4016
6.0000	-0.6347	1.4029	4.5118	2.1281	0.3631
6.5000	-0.4210	1.1242	4.7118	2.7263	0.3222
7.0000	-0.2843	0.3621	4.9118	2.4505	0.2817
7.5000	-0.1956	-0.0834	5.4118	-0.0588	0.1941
8.0000	-0.1371	-0.1962	5.9118	0.6876	0.1317
9.0000	-0.0708	-0.0724	6.4118	0.8964	0.0896
10.0000	-0.0389	0.0357	6.9118	0.4733	0.0615
12.0000	-0.0135	0.0716	7.9118	-0.5321	0.0301
15.0000	-0.0037	0.0402	8.9118	-0.2392	0.0156
20.0000	-0.0007	0.0119	10.9118	0.2754	0.0050
			13.9118	0.2056	0.0012
			18.9118	0.0615	0.0002

Table C4. The numerical values for ε_{CAl}, α_{CAl}, ε_{HAl}, α_{HAl}, ε_{CP}, α_{CP}, ε_{HP}, and α_{HP} for CH_4 in aluminophosphates

C-Al			H-Al		
R (Å)	α	ε (kJ/pair)	R (Å)	α	ε (kJ/pair)
1.4000	0.8940	-13.5989	0.5118	-0.0009	53.6209
1.6000	-0.8343	-21.4910	0.7118	0.0113	42.3547
1.8000	0.3096	-23.2786	0.9118	0.0105	23.1311
2.0000	-1.4700	-21.9645	1.1118	-0.0147	14.7099
2.2000	-1.2221	-19.1831	1.3118	-0.0404	12.2117
2.4000	-0.6634	-16.1582	1.5118	-0.0055	11.1824
2.6000	-1.1908	-13.4516	1.7118	0.0341	9.9893
2.8000	-0.6397	-11.1751	1.9118	0.3833	8.4289
3.0000	-0.2525	-9.3007	2.1118	0.4569	6.6756
3.2000	-1.8277	-7.7485	2.3118	0.8917	5.0291
3.4000	-4.4568	-6.4351	2.5118	0.4830	3.6596
3.6000	-6.2040	-5.3067	2.7118	-0.1605	2.6416
3.8000	-6.5563	-4.3388	2.9118	-0.9433	1.9452
4.0000	-5.0083	-3.5205	3.1118	-0.1744	1.4857
4.2000	-2.5847	-2.8421	3.3118	0.3922	1.1751
4.4000	-0.5158	-2.2899	3.5118	-0.9347	0.9554
4.6000	0.4983	-1.8464	3.7118	-0.2264	0.7935
4.8000	0.7430	-1.4929	3.9118	1.6964	0.6658
5.0000	0.6412	-1.2120	4.1118	2.2991	0.5583
5.2000	0.3717	-0.9886	4.3118	1.4436	0.4654
5.4000	0.0578	-0.8103	4.5118	0.5924	0.3857
5.6000	-0.2350	-0.6674	4.7118	0.7652	0.3182
5.8000	-0.4446	-0.5524	4.9118	1.0912	0.2618
6.0000	-0.5438	-0.4593	5.4118	-0.4678	0.1604
6.5000	-0.4274	-0.2952	5.9118	-1.6522	0.1002
7.0000	-0.0628	-0.1946	6.4118	-1.1335	0.0649
7.5000	0.2795	-0.1313	6.9118	0.0935	0.0438
8.0000	0.4923	-0.0906	7.9118	2.0034	0.0221
9.0000	0.5778	-0.0456	8.9118	2.3022	0.0121
10.0000	0.4523	-0.0246	10.9118	1.2297	0.0042
12.0000	0.1882	-0.0084	13.9118	0.2836	0.0011
15.0000	0.0405	-0.0022	18.9118	0.0216	0.0002
20.0000	0.0030	-0.0004			

C-P			H-P		
R (Å)	α	ε (kJ/pair)	R (Å)	α	ε (kJ/pair)
1.8000	-8.7172	-20.2255	0.5118	0.0018	64.2762
2.0000	16.4045	-10.6764	0.7118	0.0138	24.3397
2.2000	-8.4426	-8.1869	0.9118	-0.0469	11.8449
2.4000	-1.3862	-6.8456	1.1118	-0.1113	18.1528
2.6000	0.2683	-5.6550	1.3118	0.2329	20.5021
2.8000	-2.5996	-4.7219	1.5118	0.4356	15.6974
3.0000	2.3109	-4.0357	1.7118	0.1810	9.6327
3.2000	6.7609	-3.5880	1.9118	0.1605	5.2276
3.4000	2.2867	-3.2969	2.1118	-0.4326	2.5892
3.6000	-3.1889	-3.0493	2.3118	0.0054	1.1884
3.8000	-7.2889	-2.7810	2.5118	0.0914	0.4636
4.0000	-10.5655	-2.4802	2.7118	-0.1226	0.1044
4.2000	-9.6389	-2.1623	2.9118	-0.9308	-0.0425
4.4000	-6.3141	-1.8503	3.1118	-0.3258	-0.0680
4.6000	-3.5461	-1.5623	3.3118	-0.5219	-0.0369
4.8000	-1.8470	-1.3079	3.5118	-0.4120	0.0149
5.0000	-0.7196	-1.0897	3.7118	-1.4391	0.0689
5.2000	0.1415	-0.9061	3.9118	-1.5596	0.1158
5.4000	0.7529	-0.7535	4.1118	2.4288	0.1491
5.6000	1.0199	-0.6276	4.3118	3.4158	0.1658
5.8000	0.9871	-0.5240	4.5118	0.9166	0.1689
6.0000	0.7935	-0.4389	4.7118	0.2456	0.1635
6.5000	0.2348	-0.2861	4.9118	1.6458	0.1532
7.0000	0.0204	-0.1906	5.4118	2.6421	0.1203
7.5000	0.1001	-0.1297	5.9118	1.0250	0.0890
8.0000	0.2676	-0.0901	6.4118	0.4863	0.0645
9.0000	0.4604	-0.0459	6.9118	0.3563	0.0467
10.0000	0.4153	-0.0249	7.9118	1.2579	0.0252
12.0000	0.1823	-0.0086	8.9118	1.8462	0.0141
15.0000	0.0320	-0.0023	10.9118	1.1772	0.0050
20.0000	-0.0014	-0.0004	13.9118	0.2509	0.0013
			18.9118	0.0004	0.0002

Table C5. The numerical values for ε_{NH}, α_{NH}, ε_{NO}, α_{NO}, ε_{NSi}, and α_{NSi} for N_2 in silica zeolite

N-H			N-O			N-Si		
R (Å)	α	E (kJ/pair)	R (Å)	α	ε (kJ/pair)	R (Å)	α	ε (kJ/pair)
1.3714	0.1344	2.9846	1.5043	2.9082	31.656	1.8822	-0.0689	-1.7074
1.5494	-0.0658	1.0731	1.6920	-2.9023	13.565	2.0743	-0.8364	-1.9651
1.7323	0.0308	-0.0268	1.8822	0.9771	4.783	2.2678	6.5041	-2.3842
1.9185	-0.0461	-0.5393	2.0743	-0.5493	0.6797	2.4623	-7.6183	-2.8948
2.1073	-0.0716	-0.6967	2.2678	-0.6204	-0.9725	2.6576	0.7563	-2.8345
2.2980	-0.1306	-0.6647	2.4623	-0.5748	-1.4243	2.8536	-0.4750	-2.5027
2.4901	-0.1696	-0.5485	2.6576	-1.2218	-1.3430	3.0500	-2.1575	-2.0948
2.6834	-0.2470	-0.4096	2.8536	-0.5516	-1.0667	3.2470	-1.4922	-1.6874
2.8776	-0.1288	-0.2811	3.0500	0.2416	-0.7717	3.4442	1.6262	-1.3292
3.0726	-0.0753	-0.1790	3.2470	-0.9004	-0.5266	3.6418	-0.8755	-1.0385
3.2681	0.2609	-0.1064	3.4442	1.1570	-0.3441	3.8396	-0.0082	-0.8072
3.4642	0.0293	-0.0598	3.6418	1.0284	-0.2217	4.0377	-0.4244	-0.6245
3.6607	0.6173	-0.0328	3.8396	1.1372	-0.1458	4.2359	-1.1198	-0.4803
3.8576	0.3887	-0.0192	4.0377	0.8075	-0.1012	4.4343	-1.5702	-0.3665
4.0547	0.1613	-0.0137	4.2359	0.3983	-0.0756	4.6328	-0.4268	-0.2773
4.2522	0.0991	-0.0121	4.4343	0.0230	-0.0608	4.8314	1.0023	-0.2085
4.4498	-0.0119	-0.0121	4.6328	-0.2164	-0.0515	5.0302	1.8405	-0.1565
4.6477	-0.2376	-0.0124	4.8314	-0.5035	-0.0450	5.2290	1.9540	-0.1179
4.8457	-0.3306	-0.0125	5.0302	-0.6733	-0.0397	5.4280	1.6135	-0.0895
5.0439	-0.3452	-0.0121	5.2290	-0.6688	-0.0350	5.6270	1.0960	-0.0687
5.2422	-0.3217	-0.0114	5.4280	-0.5992	-0.0307	5.8260	0.5748	-0.0534
5.4407	-0.2535	-0.0104	5.6270	-0.4930	-0.0268	6.0252	0.1693	-0.0421
5.6392	-0.1733	-0.0093	5.8260	-0.3556	-0.0232	6.5232	-0.3771	-0.0244
5.8379	-0.1013	-0.0082	6.0252	-0.2150	-0.0199	7.0216	-0.4944	-0.0151
6.0366	-0.0387	-0.0071	6.5232	0.0621	-0.0135	7.5202	-0.4538	-0.0098
6.5338	0.0729	-0.0049	7.0216	0.2121	-0.0090	8.0189	-0.3763	-0.0066
7.0314	0.1261	-0.0033	7.5202	0.2660	-0.0061	9.0168	-0.2387	-0.0033
7.5293	0.1378	-0.0022	8.0189	0.2647	-0.0042	10.015	-0.1501	-0.0017
8.0275	0.1272	-0.0015	9.0168	0.2050	-0.0021	12.012	-0.0629	-0.0006
9.0245	0.0886	-0.0007	10.015	0.1418	-0.0011	15.010	-0.0199	-0.0002
10.022	0.0564	-0.0004	12.012	0.0641	-0.0004	20.007	-0.0041	0.0000
12.018	0.0223	-0.0001	15.010	0.0212	-0.0001			
15.014	0.0063	0.0000	20.007	0.0046	0.0000			
20.011	0.0012	0.0000						

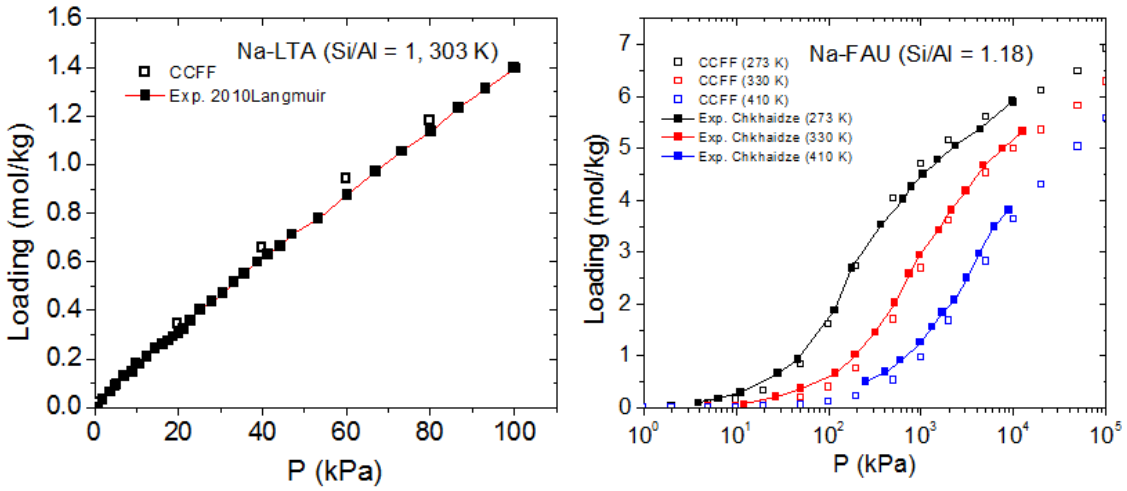

Figure C1. Comparison of simulated (CCFF) and experimental adsorption isotherms at 273 K and 298 K for N_2 in silica DDR. The experimental data are from Palomino et al.[218] for Na-LTA and Chkhaidze et al.[219] for Na-FAU. The simulations were performed by Dr. Hanjun Fang. The lines are drawn to guide the eyes.

Appendix D

Table D1. The numerical values for ε_{CH}, α_{CH}, ε_{HH}, and α_{HH} for C_2H_4 in silica zeolite

C^{sp2}-H			H-H		
R (Å)	α	ε (kJ/pair)	R (Å)	α	ε (kJ/pair)
1.5949	0.2457	2.6909	1.1813	0.3088	8.3239
1.7730	-0.1063	1.4188	1.2999	-0.4012	3.5545
1.9554	0.0374	0.5801	1.4367	0.1033	1.2711
2.1409	-0.0313	0.1019	1.5869	0.0104	0.2883
2.3289	-0.0252	-0.1370	1.7472	-0.0087	-0.1557
2.5186	-0.1368	-0.2281	1.9149	-0.0189	-0.3199
2.7099	-0.1798	-0.2321	2.0883	-0.0374	-0.3419
2.9023	-0.3433	-0.1911	2.2661	-0.0702	-0.2984
3.0957	-0.2892	-0.1328	2.4474	-0.0206	-0.2333
3.2899	-0.3657	-0.0751	2.6313	-0.1280	-0.1712
3.4848	0.3737	-0.0277	2.8175	0.1713	-0.1215
3.6802	-0.2486	0.0056	3.0054	-0.1177	-0.0880
3.8760	0.6017	0.0262	3.1948	0.2774	-0.0667
4.0723	0.7287	0.0360	3.3854	0.0586	-0.0546
4.2689	0.5561	0.0380	3.5771	0.0107	-0.0476
4.4658	0.9127	0.0353	3.7696	-0.0411	-0.0428
4.6630	0.4853	0.0301	3.9628	-0.1304	-0.0387
4.8604	-0.1412	0.0241	4.1567	0.1648	-0.0349
5.0580	-0.0129	0.0184	4.3511	-0.4622	-0.0311
5.2558	-0.0739	0.0136	4.5461	-0.2870	-0.0272
5.4538	-0.5387	0.0097	4.7414	0.1315	-0.0234
5.6519	-0.7250	0.0067	4.9371	-0.2219	-0.0199
5.8501	-0.5954	0.0045	5.1332	-0.2184	-0.0167
6.0484	-0.4661	0.0030	5.3295	0.1911	-0.0140
6.5447	-0.2508	0.0010	5.5261	0.0606	-0.0117
7.0416	-0.0714	0.0002	6.0186	0.0479	-0.0074
7.5388	0.1205	0.0000	6.5123	0.1162	-0.0048
8.0364	0.2137	-0.0001	7.0068	-0.0511	-0.0032
9.0324	0.1737	-0.0001	7.5021	-0.0434	-0.0021
10.0291	0.0749	0.0000	8.4942	0.1292	-0.0010
12.0243	0.0008	0.0000	9.4881	0.1346	-0.0005
15.0194	-0.0017	0.0000	11.4789	0.0108	-0.0001
20.0146	0.0013	0.0000	14.4700	-0.0050	0.0000
			19.4612	0.0026	0.0000

Table D2. The numerical values for ε_{CO}, α_{CO}, ε_{HO}, and α_{HO} for C_2H_4 in silica zeolite

C^{sp2}-O			H-O		
R (Å)	α	ε (kJ/pair)	R (Å)	α	ε (kJ/pair)
1.2023	-0.3945	24.2310	1.0214	45.1961	-0.0344
1.3732	-0.9666	34.8142	1.1214	34.1336	-0.0075
1.5510	3.2757	35.5161	1.2457	17.5672	1.6041
1.7337	2.2285	24.3372	1.3878	0.3060	-2.0963
1.9198	-2.7530	13.0065	1.5428	-4.5550	-0.1028
2.1084	-0.3920	6.4315	1.7072	-4.3644	0.6333
2.2990	-0.1868	3.0652	1.8785	-3.6709	-0.1859
2.4911	-0.5565	1.3979	2.0550	-2.9728	-0.0190
2.6843	-0.5243	0.6277	2.2355	-2.3454	-0.2319
2.8785	-0.4824	0.3179	2.4190	-1.8085	-0.1584
3.0734	-1.5885	0.2349	2.6050	-1.3728	-0.4053
3.2689	-0.1542	0.2535	2.7929	-1.0366	0.2902
3.4649	-0.6013	0.3002	2.9824	-0.7927	-0.3929
3.6614	0.5755	0.3418	3.1731	-0.6197	0.5342
3.8582	0.8699	0.3651	3.3650	-0.5006	0.1498
4.0553	1.6252	0.3686	3.5577	-0.4180	0.5317
4.2527	1.9410	0.3559	3.7512	-0.3586	-0.2813
4.4503	1.8045	0.3323	3.9454	-0.3125	-0.1458
4.6482	1.5381	0.3027	4.1401	-0.2744	-0.6185
4.8462	1.1811	0.2711	4.3352	-0.2415	-0.3347
5.0444	0.8724	0.2399	4.5309	-0.2126	-0.3942
5.2427	0.6776	0.2106	4.7268	-0.1869	-0.4838
5.4411	0.5929	0.1840	4.9231	-0.1639	-0.5414
5.6396	0.5890	0.1602	5.1197	-0.1434	-0.7365
5.8383	0.6260	0.1392	5.3166	-0.1251	-0.9743
6.0370	0.6800	0.1208	5.5136	-0.1088	-1.1665
6.5342	0.7971	0.0849	6.0071	-0.0760	-1.1972
7.0318	0.7941	0.0600	6.5016	-0.0529	-0.7171
7.5296	0.6620	0.0429	6.9969	-0.0369	-0.1878
8.0278	0.4768	0.0309	7.4928	-0.0260	0.1766
9.0247	0.1725	0.0166	8.4861	-0.0133	0.2637
10.0223	0.0244	0.0094	9.4808	-0.0072	0.0784
12.0186	-0.0428	0.0034	11.4729	-0.0025	-0.0845
15.0148	-0.0269	0.0009	14.4652	-0.0006	-0.0612
20.0111	-0.0077	0.0002	19.4576	-0.0001	-0.0175

Table D3. The numerical values for ε_{CSi}, α_{CSi}, ε_{HSi}, and α_{HSi} for C_2H_4 in silica zeolite

C^{sp2}-Si			H-Si		
R (Å)	α	ε (kJ/pair)	R (Å)	α	ε (kJ/pair)
1.9198	1.9555	-22.2530	1.2016	0.5688	55.1999
2.1084	-7.2416	-18.5646	1.3383	-0.8808	40.9163
2.2990	-5.8973	-13.8277	1.4894	0.9618	30.8111
2.4911	13.3657	-9.8397	1.6509	0.0481	21.7653
2.6843	-1.8887	-7.4665	1.8200	1.4031	14.3630
2.8785	-3.5927	-5.9276	1.9949	-1.8789	8.9335
3.0734	-1.0595	-4.7708	2.1741	0.8529	5.6423
3.2689	-1.6744	-3.8618	2.3567	0.3978	3.5794
3.4649	-1.6792	-3.1371	2.5419	-0.5813	2.2649
3.6614	1.0001	-2.5579	2.7292	0.1790	1.4549
3.8582	-0.5776	-2.0945	2.9181	0.1318	0.9598
4.0553	-2.9474	-1.7187	3.1085	-1.6898	0.6648
4.2527	-4.1109	-1.4088	3.3000	-0.1268	0.4977
4.4503	-3.4210	-1.1515	3.4924	0.5173	0.3999
4.6482	-2.0491	-0.9386	3.6857	-0.8551	0.3376
4.8462	-0.3220	-0.7642	3.8796	0.9114	0.2944
5.0444	0.7242	-0.6227	4.0741	0.6278	0.2605
5.2427	1.0370	-0.5086	4.2692	-0.0679	0.2316
5.4411	0.9793	-0.4170	4.4646	-0.0133	0.2061
5.6396	0.7399	-0.3434	4.6605	0.9460	0.1831
5.8383	0.4770	-0.2841	4.8567	1.6649	0.1618
6.0370	0.2826	-0.2362	5.3484	2.5576	0.1156
6.5342	-0.0171	-0.1520	5.8415	1.4099	0.0800
7.0318	-0.1481	-0.1005	6.3357	0.0908	0.0544
7.5296	-0.1245	-0.0681	6.8307	-0.6118	0.0370
8.0278	-0.0628	-0.0472	7.8227	-0.7336	0.0176
9.0247	-0.0052	-0.0240	8.8165	-0.3138	0.0090
10.0223	-0.0120	-0.0130	10.8075	-0.0813	0.0028
12.0186	-0.0282	-0.0045	13.7989	-0.0475	0.0007
15.0148	-0.0177	-0.0012	18.7907	-0.0140	0.0001
20.0111	-0.0052	-0.0002			

REFERENCES

(1) Lu, G. Q.; Zhao, X. S.; Wei, T. K., *Nanoporous materials: science and engineering*; Imperial College Press, 2004; Vol. 4.

(2) Wang, Q. M.; Shen, D. M.; Bulow, M.; Lau, M. L.; Deng, S. G.; Fitch, F. R.; Lemcoff, N. O.; Semanscin, J., Metallo-organic molecular sieve for gas separation and purification. *Microporous and Mesoporous Materials* **2002**, *55*, 217-230.

(3) Christensen, A. N.; Jensen, T. R.; Norby, P.; Hanson, J. C., In Situ Synchrotron X-ray Powder Diffraction Studies of Crystallization of Microporous Aluminophosphates and Me2+-Substituted Aluminophosphates. *Chemistry of materials* **1998**, *10*, 1688-1693.

(4) Tang, L.; Shi, L.; Bonneau, C.; Sun, J.; Yue, H.; Ojuva, A.; Lee, B.-L.; Kritikos, M.; Bell, R. G.; Bacsik, Z., A zeolite family with chiral and achiral structures built from the same building layer. *Nature materials* **2008**, *7*, 381-385.

(5) Peterson, B. K., A simulated annealing method for determining atomic distributions from NMR data: silicon and aluminum in faujasite. *The Journal of Physical Chemistry B* **1999**, *103*, 3145-3150.

(6) Baerlocher, C.; McCusker, L. B.; Olson, D. H., *Atlas of zeolite framework types*; Elsevier, 2007.

(7) Castillo, J., *Molecular simulations in microporous materials: adsorption and separation*; TU Delft, Delft University of Technology, 2010.

(8) Zhou, W., Microscopic study of crystal defects enriches our knowledge of materials chemistry. *J. Mater. Chem.* **2008**, *18*, 5321-5325.

(9) Ramachandran, C. E.; Chempath, S.; Broadbelt, L. J.; Snurr, R. Q., Water adsorption in hydrophobic nanopores: Monte Carlo simulations of water in silicalite. *Microporous and mesoporous materials* **2006**, *90*, 293-298.

(10) Baerlocher, C.; McCusker, L. B., Database of Zeolite Structures. International Zeolite Association: 2002.

(11) Al'tshuler, G.; Shkurenko, G. Y., Equilibrium cation exchange on natural heulandite. *Russian Chemical Bulletin* **1990**, *39*, 1331-1334.

(12) Watanabe, Y.; Yamada, H.; Tanaka, J.; Komatsu, Y.; Moriyoshi, Y., Ammonium ion exchange of synthetic zeolites: The effect of their open- window sizes, pore structures, and cation exchange capacities. *Separation science and technology* **2005**, *39*, 2091-2104.

(13) Willhammar, T.; Sun, J.; Wan, W.; Oleynikov, P.; Zhang, D.; Zou, X.; Moliner, M.; Gonzalez, J.; Martínez, C.; Rey, F., Structure and catalytic properties of the most complex

intergrown zeolite ITQ-39 determined by electron crystallography. *Nature chemistry* **2012**, *4*, 188-194.

(14) Kurup, A. S.; Hidajat, K.; Ray, A. K., Optimal operation of an industrial-scale Parex process for the recovery of p-xylene from a mixture of C8 aromatics. *Industrial & engineering chemistry research* **2005**, *44*, 5703-5714.

(15) Santos, J.; Cruz, P.; Regala, T.; Magalhaes, F.; Mendes, A., High-purity oxygen production by pressure swing adsorption. *Industrial & engineering chemistry research* **2007**, *46*, 591-599.

(16) Reut, S.; Prakash, A., Evaluation of sorbents for thiophene removal from liquid hydrocarbons. *Fuel processing technology* **2006**, *87*, 217-222.

(17) Chambellan, A.; Chevreau, T.; Khabtou, S.; Marzin, M.; Lavalley, J., Acidic sites of steamed HY zeolites, active for benzene self-alkylation and hydrogenation. *Zeolites* **1992**, *12*, 306-314.

(18) Komaromine, M. K.; Loksa, G.; Csereklye, K. E.; Bardoczyne, E. S.; Kallai, S., Use of zeolite to improve soil amelioration and takes effects on microclimate. *Cereal Research Communications* **2008**, *36*, 1783-1786.

(19) Fragoulis, D.; Chaniotakis, E.; Stamatakis, M. G., Zeolitic tuffs of Kimolos Island, Aegean Sea, Greece and their industrial potential. *Cement and Concrete Research* **1997**, *27*, 889-905.

(20) Frenkel, D.; Smit, B., *Understanding Molecular Simulation, Second Edition: From Algorithms to Applications (Computational Science)*; Academic Press, 2001.

(21) Garcia-Sanchez, A.; Dubbeldam, D.; Calero, S., Modeling Adsorption and Self-Diffusion of Methane in LTA Zeolites: The Influence of Framework Flexibility. *J. Phys. Chem. C* **2010**, *114*, 15068-15074.

(22) Krishna, R.; van Baten, J. M., Comment on "Modeling Adsorption and Self-Diffusion of Methane in LTA Zeolites: The Influence of Framework Flexibility". *J. Phys. Chem. C* **2010**, *114*, 18017-18021.

(23) Combariza, A. F.; Sastre, G.; Corma, A., Propane/Propylene Diffusion in Zeolites: Framework Dynamics. *The Journal of Physical Chemistry C* **2009**, *113*, 11246-11253.

(24) Leroy, F.; Rousseau, B., Self-diffusion of n-alkanes in MFI type zeolite using molecular dynamics simulations with an anisotropic united atom (AUA) forcefield. *Mol. Simul.* **2004**, *30*, 617-620.

(25) Seminario, J. M., *Recent developments and applications of modern density functional theory*; Elsevier, 1996; Vol. 4.

(26) Geerlings, P.; De Proft, F.; Langenaeker, W., Conceptual density functional theory. *Chemical Reviews* **2003**, *103*, 1793-1874.

(27) Fang, H.; Kamakoti, P.; Zang, J.; Cundy, S.; Paur, C.; Ravikovitch, P. I.; Sholl, D. S., Prediction of CO2 Adsorption Properties in Zeolites Using Force Fields Derived from Periodic Dispersion-Corrected DFT Calculations. *The Journal of Physical Chemistry C* **2012**, *116*, 10692-10701.

(28) June, R. L.; Bell, A. T.; Theodorou, D. N., Transition-state studies of xenon and SF_6 diffusion in silicalite. *Journal of Physical Chemistry* **1991**, *95*, 8866-8878.

(29) Maginn, E. J.; Bell, A. T.; Theodorou, D. N., Dynamics of long n-alkanes in silicalite: A hierarchical simulation approach. *Journal of Physical Chemistry* **1996**, *100*, 7155-7173.

(30) Forester, T. R.; Smith, W., Bluemoon simulations of benzene in silicalite-1 - Prediction of free energies and diffusion coefficients. *Journal of the Chemical Society-Faraday Transactions* **1997**, *93*, 3249-3257.

(31) Beerdsen, E.; Smit, B.; Dubbeldam, D., Molecular simulation of loading dependent slow diffusion in confined systems. *Physical Review Letters* **2004**, *93*.

(32) Krishna, R.; van Baten, J. M., A molecular dynamics investigation of the diffusion characteristics of cavity-type zeolites with 8-ring windows. *Micropor. Mesopor. Mat.* **2011**, *137*, 83-91.

(33) Keil, F. J.; Krishna, R.; Coppens, M. O., Modeling of diffusion in zeolites. *Reviews in Chemical Engineering* **2000**, *16*, 71-197.

(34) Calero, S.; Dubbeldam, D.; Krishna, R.; Smit, B.; Vlugt, T. J. H.; Denayer, J. F. M.; Martens, J. A.; Maesen, T. L. M., Understanding the Role of Sodium during Adsorption: A Force Field for Alkanes in Sodium-Exchanged Faujasites. *Journal of the American Chemical Society* **2004**, *126*, 11377-11386.

(35) Dubbeldam, D.; Beerdsen, E.; Calero, S.; Smit, B., Dynamically corrected transition state theory calculations of self-diffusion in anisotropic nanoporous materials. *Journal of Physical Chemistry B* **2006**, *110*, 3164-3172.

(36) Dubbeldam, D.; Beerdsen, E.; Vlugt, T. J. H.; Smit, B., Molecular simulation of loading-dependent diffusion in nanoporous materials using extended dynamically corrected transition state theory. *Journal of Chemical Physics* **2005**, *122*.

(37) Dubbeldam, D.; Beerdsen, E.; Calero, S.; Smit, B., Molecular path control in zeolite membranes. *Proceedings of the National Academy of Sciences of the United States of America* **2005**, *102*, 12317-12320.

(38) Snurr, R. Q.; Bell, A. T.; Theodorou, D. N., Investigation of the dynamics of benzene in silicalite using Transition-State Theory. *The Journal of Physical Chemistry* **1994**, *98*, 11948-11961.

(39) Kärger, J.; Ruthven, D. M.; Theodorou, D. N., *Diffusion in Nanoporous Materials*; Wiley-VCH Verlag: Weinheim, 2012; Vol. 1.

(40) Tagliabue, M.; Farrusseng, D.; Valencia, S.; Aguado, S.; Ravon, U.; Rizzo, C.; Corma, A.; Mirodatos, C., Natural gas treating by selective adsorption: Material science and chemical engineering interplay. *Chemical Engineering Journal* **2009**, *155*, 553-566.

(41) Smit, B.; Siepmann, J. I., Computer Simulations of the Energetics and Siting of n-Alkanes in Zeolites. *The Journal of Physical Chemistry* **1994**, *98*, 8442-8452.

(42) June, R. L.; Bell, A. T.; Theodorou, D. N., Molecular dynamics studies of butane and hexane in silicalite. *The Journal of Physical Chemistry* **1992**, *96*, 1051-1060.

(43) Demontis, P.; Suffritti, G. B., Sorbate-loading dependence of diffusion mechanism in a cubic symmetry zeolite of type ZK4. A molecular dynamics study. *Journal of Physical Chemistry B* **1997**, *101*, 5789-5793.

(44) Vlugt, T. J. H.; Schenk, M., Influence of framework flexibility on the adsorption properties of hydrocarbons in the zeolite silicalite. *Journal of Physical Chemistry B* **2002**, *106*, 12757-12763.

(45) Deem, M. W.; Newsam, J. M.; Creighton, J. A., Fluctuations in zeolite aperture dimensions simulated by crystal dynamics. *Journal of the American Chemical Society* **1992**, *114*, 7198-7207.

(46) Nicholas, J. B.; Hopfinger, A. J.; Trouw, F. R.; Iton, L. E., Molecular modeling of zeolite structure .2. Structure and dynamics of silica sodalite and silicate force-field. *Journal of the American Chemical Society* **1991**, *113*, 4792-4800.

(47) Hill, J. R.; Sauer, J., Molecular mechanics potential for silica and zeolite catalysts based on ab-initio calculations .1. Dense and microporous silica. *J. Phys. Chem.* **1994**, *98*, 1238-1244.

(48) Hill, J. R.; Sauer, J., Molecular mechanics potential for silica and zeolite catalysts based on ab-initio calculations .2. Aluminosilicates. *J. Phys. Chem.* **1995**, *99*, 9536-9550.

(49) Vanbeest, B. W. H.; Kramer, G. J.; Vansanten, R. A., Force-fields for silicas and aluminophosphates based on abinitio calculations. *Physical Review Letters* **1990**, *64*, 1955-1958.

(50) Pedone, A.; Malavasi, G.; Menziani, M. C.; Cormack, A. N.; Segre, U., A new self-consistent empirical interatomic potential model for oxides, silicates, and silica-based glasses. *Journal of Physical Chemistry B* **2006**, *110*, 11780-11795.

(51) Huth, A. J.; Stueve, J. M.; Guliants, V. V., A simulation study of the gas separation properties of decadodecasil 3R zeolite with emphasis on energy-related separations. *Journal of Membrane Science* **2012**, *403–404*, 236-249.

(52) Haldoupis, E.; Watanabe, T.; Nair, S.; Sholl, D. S., Quantifying Large Effects of Framework Flexibility on Diffusion in MOFs: CH_4 and CO_2 in ZIF-8. *ChemPhysChem* **2012**, *13*, 3449-3452.

(53) Watanabe, T.; Sholl, D. S., Accelerating Applications of Metal-Organic Frameworks for Gas Adsorption and Separation by Computational Screening of Materials. *Langmuir* **2012**, *28*, 14114-14128.

(54) Spyriouni, T.; Boulougouris, G. C.; Theodorou, D. N., Prediction of Sorption of CO_2 in Glassy Atactic Polystyrene at Elevated Pressures Through a New Computational Scheme. *Macromolecules* **2009**, *42*, 1759-1769.

(55) Dubbeldam, D.; Calero, S.; Vlugt, T. J. H.; Krishna, R.; Maesen, T. L. M.; Smit, B., United Atom Force Field for Alkanes in Nanoporous Materials. *Journal of Physical Chemistry B* **2004**, *108*, 12301-12313.

(56) Plimpton, S., Fast Parallel Algorithms for Short-Range Molecular Dynamics. *J. Comp. Phys.* **1995**, *117*, 1-19.

(57) Sholl, D. S., Understanding macroscopic diffusion of adsorbed molecules in crystalline nanoporous materials via atomistic simulations. *Accounts Chem Res* **2006**, *39*, 403-411.

(58) Borreguero, J. M.; He, J. H.; Meilleur, F.; Weiss, K. L.; Brown, C. M.; Myles, D. A.; Herwig, K. W.; Agarwal, P. K., Redox-Promoting Protein Motions in Rubredoxin. *Journal of Physical Chemistry B* **2011**, *115*, 8925-8936.

(59) Krishnan, M.; Kurkal-Siebert, V.; Smith, J. C., Methyl group dynamics and the onset of anharmonicity in myoglobin. *Journal of Physical Chemistry B* **2008**, *112*, 5522-5533.

(60) Tokuhisa, A.; Joti, Y.; Nakagawa, H.; Kitao, A.; Kataoka, M., Non-Gaussian behavior of elastic incoherent neutron scattering profiles of proteins studied by molecular dynamics simulation. *Physical Review E* **2007**, *75*.

(61) Jobic, H., Diffusion of linear and branched alkanes in ZSM-5. A quasi-elastic neutron scattering study. *Journal of Molecular Catalysis A: Chemical* **2000**, *158*, 135-142.

(62) Hedin, N.; DeMartin, G. J.; Roth, W. J.; Strohmaier, K. G.; Reyes, S. C., PFG NMR self-diffusion of small hydrocarbons in high silica DDR, CHA and LTA structures. *Microporous and Mesoporous Materials* **2008**, *109*, 327-334.

(63) Krishna, R.; van Baten, J. M., Influence of segregated adsorption on mixture diffusion in DDR zeolite. *Chemical Physics Letters* **2007**, *446*, 344-349.

(64) Iyer, K. A.; Singer, S. J., Local-mode analysis of complex zeolite vibrations: Zeolite-A. *J. Phys. Chem.* **1994**, *98*, 12679-12686.

(65) Karger, J.; Vasenkov, S.; Auerbach, S. M., Diffusion in Zeolites. In *Handbook of Zeolites Science and Technology*, Auerbach, S. M.; Carrado, K. A.; Dutta, P. K., Eds. Marcel Dekker: New York, 2003; p 401.

(66) Turaga, S. C.; Auerbach, S. M., Calculating free energies for diffusion in tight-fitting zeolite-guest systems: Local normal-mode Monte Carlo. *Journal of Chemical Physics* **2003**, *118*, 6512-6517.

(67) Ford, D. M.; Glandt, E. D., Molecular simulation study of the surface-barrier effect - dilute gas limit. *Journal of Physical Chemistry* **1995**, *99*, 11543-11549.

(68) Tunca, C.; Ford, D. M., A transition-state theory approach to adsorbate dynamics at arbitrary loadings. *Journal of Chemical Physics* **1999**, *111*, 2751-2760.

(69) Tunca, C.; Ford, D. M., Modeling cage-to-cage dynamics of adsorbates at arbitrary loadings with dynamically corrected transition-state theory. *Journal of Physical Chemistry B* **2002**, *106*, 10982-10990.

(70) Tunca, C.; Ford, D. M., A hierarchical approach to the molecular modeling of diffusion and adsorption at nonzero loading in microporous materials. *Chemical Engineering Science* **2003**, *58*, 3373-3383.

(71) Tunca, C.; Ford, D. M., Coarse-grained nonequilibrium approach to the molecular modeling of permeation through microporous membranes. *Journal of Chemical Physics* **2004**, *120*, 10763-10767.

(72) Jee, S. E.; Sholl, D. S., Carbon Dioxide and Methane Transport in DDR Zeolite: Insights from Molecular Simulations into Carbon Dioxide Separations in Small Pore Zeolites. *Journal of the American Chemical Society* **2009**, *131*, 7896-7904.

(73) Dubbeldam, D.; Calero, S.; Maesen, T. L. M.; Smit, B., Incommensurate Diffusion in Confined Systems. *Physical Review Letters* **2003**, *90*, 245901.

(74) Hertäg, L.; Bux, H.; Caro, J.; Chmelik, C.; Remsungnen, T.; Knauth, M.; Fritzsche, S., Diffusion of CH_4 and H_2 in ZIF-8. *Journal of Membrane Science* **2011**, *377*, 36-41.

(75) Marshall, J.; Bird, A. C., A Comparative Histopathological Study of Argon And Krypton Laser Irradiations of the Human Retina. *Br J Ophthalmol* **1979**, *63*, 657-668.

(76) Cullen, S. C.; Gross, E. G., The Anesthetic Properties of Xenon in Animals and Human Beings, with Additional Observations on Krypton. *Science* **1951**, *113*, 580-582.

(77) Cho, H. S.; Miyasaka, K.; Kim, H.; Kubota, Y.; Takata, M.; Kitagawa, S.; Ryoo, R.; Terasaki, O., Study of Argon Gas Adsorption in Ordered Mesoporous MFI Zeolite Framework. *The Journal of Physical Chemistry C* **2012**, *116*, 25300-25308.

(78) Saxton, C. G.; Kruth, A.; Castro, M.; Wright, P. A.; Howe, R. F., Xenon Adsorption in Synthetic Chabazite Zeolites. *Microporous and Mesoporous Materials* **2010**, *129*, 68-73.

(79) McCormick, A. V.; Chmelka, B. F., Xenon Adsorption in NaA Zeolite Cavities. *Molecular Physics* **1991**, *73*, 603-617.

(80) Jameson, C. J.; Jameson, A. K.; Lim, H. M., Competitive Adsorption of Xenon and Argon in Zeolite NaA. 129Xe Nuclear Magnetic Resonance Studies and Grand Canonical Monte Carlo Simulations. *The Journal of Chemical Physics* **1996**, *104*, 1709-1728.

(81) Ianovski, D.; Munakata, K.; Kanjo, S.; Yokoyama, Y.; Koga, A.; Yamatsuki, S.; Tanaka, K.; Fukumatsu, T.; Nishikawa, M.; Igarashi, Y., Adsorption of Noble Gases on H-Mordenite. *Journal of Nuclear Science and Technology* **2002**, *39*, 1213-1218.

(82) Jameson, C. J.; Jameson, A. K.; Lim, H.-M., Competitive Adsorption of Xenon and Krypton in Zeolite NaA:129Xe Nuclear Magnetic Resonance Studies and Grand Canonical Monte Carlo Simulations. *The Journal of Chemical Physics* **1997**, *107*, 4364-4372.

(83) Munakata, K.; Fukumatsu, T.; Yamatsuki, S.; Tanaka, K.; Nishikawa, M., Adsorption Equilibria of Krypton, Xenon, Nitrogen and Their Mixtures on Molecular Sieve 5A and Activated Charcoal. *Journal of Nuclear Science and Technology* **1999**, *36*, 818-829.

(84) Bazan, R. E.; Bastos-Neto, M.; Moeller, A.; Dreisbach, F.; Staudt, R., Adsorption Equilibria of O_2, Ar, Kr and Xe on Activated Carbon and Zeolites: Single Component and Mixture data. *Adsorption* **2011**, *17*, 371-383.

(85) Charkhi, A.; Kazemeini, M.; Ahmadi, S.; Ammari Allahyari, S., Adsorption and Diffusion of Xenon in a Granulated Nano-NaY Zeolite. *Adsorption* **2012**, *18*, 75-86.

(86) Mueller, U.; Schubert, M.; Teich, F.; Puetter, H.; Schierle-Arndt, K.; Pastre, J., Metal-organic Frameworks-Prospective Industrial Applications. *Journal of Materials Chemistry* **2006**, *16*, 626-636.

(87) Skoulidas, A. I.; Sholl, D. S., Transport Diffusivities of CH_4, CF_4, He, Ne, Ar, Xe, and SF_6 in Silicalite from Atomistic Simulations. *The Journal of Physical Chemistry B* **2002**, *106*, 5058-5067.

(88) Krishna, R.; van Baten, J. M., Insights Into Diffusion of Gases in Zeolites Gained from Molecular Dynamics Simulations. *Microporous and Mesoporous Materials* **2008**, *109*, 91-108.

(89) Kopelevich, D. I.; Chang, H.-C., Diffusion of Inert Gases in Silica Sodalite: Importance of Lattice Flexibility. *The Journal of Chemical Physics* **2001**, *115*, 9519-9527.

(90) Van Heest, T.; Teich-McGoldrick, S. L.; Greathouse, J. A.; Allendorf, M. D.; Sholl, D. S., Identification of Metal–Organic Framework Materials for Adsorption Separation of Rare Gases: Applicability of Ideal Adsorbed Solution Theory (IAST) and Effects of Inaccessible Framework Regions. *The Journal of Physical Chemistry C* **2012**, *116*, 13183-13195.

(91) Parkes, M. V.; Demir, H.; Teich-McGoldrick, S. L.; Sholl, D. S.; Greathouse, J. A.; Allendorf, M. D., Molecular Dynamics Simulation of Framework Flexibility Effects on Noble Gas Diffusion in HKUST-1 And ZIF-8. *Microporous and Mesoporous Materials* **2014**, *194*, 190-199.

(92) Greathouse, J. A.; Kinnibrugh, T. L.; Allendorf, M. D., Adsorption and Separation of Noble Gases by IRMOF-1: Grand Canonical Monte Carlo Simulations. *Industrial & Engineering Chemistry Research* **2009**, *48*, 3425-3431.

(93) Ryan, P.; Farha, O. K.; Broadbelt, L. J.; Snurr, R. Q., Computational Screening of Metal-Organic Frameworks for Xenon/Krypton Separation. *AIChE Journal* **2011**, *57*, 1759-1766.

(94) Thallapally, P. K.; Grate, J. W.; Motkuri, R. K., Facile Xenon Capture and Release at Room Temperature Using a Metal-Organic Framework: a Comparison With Activated Charcoal. *Chemical Communications* **2012**, *48*, 347-349.

(95) Dai, Y.; Johnson, J.; Karvan, O.; Sholl, D. S.; Koros, W., Ultem®/ZIF-8 Mixed Matrix Hollow Fiber Membranes for CO_2/N_2 Separations. *Journal of Membrane Science* **2012**, *401*, 76-82.

(96) Keskin, S.; Sholl, D. S., Selecting Metal Organic Frameworks as Enabling Materials in Mixed Matrix Membranes for High Efficiency Natural Gas Purification. *Energy & Environmental Science* **2010**, *3*, 343-351.

(97) Caro, J.; Noack, M., Zeolite Membranes–Recent Developments and Progress. *Microporous and Mesoporous Materials* **2008**, *115*, 215-233.

(98) Van den Bergh, J.; Zhu, W.; Gascon, J.; Moulijn, J.; Kapteijn, F., Separation and Permeation Characteristics of a DD3R Zeolite Membrane. *Journal of Membrane Science* **2008**, *316*, 35-45.

(99) Li, S.; Carreon, M. A.; Zhang, Y.; Funke, H. H.; Noble, R. D.; Falconer, J. L., Scale-up of SAPO-34 Membranes for CO_2/CH_4 Separation. *Journal of Membrane Science* **2010**, *352*, 7-13.

(100) Nair, S.; Lai, Z.; Nikolakis, V.; Xomeritakis, G.; Bonilla, G.; Tsapatsis, M., Separation of Close-Boiling Hydrocarbon Mixtures by MFI and FAU Membranes Made by Secondary Growth. *Microporous and Mesoporous Materials* **2001**, *48*, 219-228.

(101) Himeno, S.; Tomita, T.; Suzuki, K.; Nakayama, K.; Yajima, K.; Yoshida, S., Synthesis and Permeation Properties of a DDR-type Zeolite Membrane for Separation of CO_2/CH_4 Gaseous Mixtures. *Industrial & Engineering Chemistry Research* **2007**, *46*, 6989-6997.

(102) Bux, H.; Chmelik, C.; Krishna, R.; Caro, J., Ethene/Ethane Separation by the MOF membrane ZIF-8: Molecular Correlation of Permeation, Adsorption, Diffusion. *Journal of Membrane Science* **2011**, *369*, 284-289.

(103) Awati, R. V.; Ravikovitch, P. I.; Sholl, D. S., Efficient and Accurate Methods for Characterizing Effects of Framework Flexibility on Molecular Diffusion in Zeolites: CH4 Diffusion in Eight Member Ring Zeolites. *The Journal of Physical Chemistry C* **2013**, *117*, 13462-13473.

(104) Cygan, R. T.; Liang, J. J.; Kalinichev, A. G., Molecular Models of Hydroxide, Oxyhydroxide, and Clay Phases and the Development of a General Force Field. *Journal of Physical Chemistry B* **2004**, *108*, 1255-1266.

(105) Ruthven, D. M., *Principles of Adsorption and Adsorption Processes*; Wiley-Interscience: New York, 1984.

(106) Schuth, F.; Sing, K. S. W.; Weitkamp, J., *Handbook of Porous Solids*; Wiley-VCH: New York, 2002.

(107) Scott, M. A.; Kathleen, A. C.; Prabir, K. D., *Handbook of Zeolite Science and Technology*; Marcel Dekker: New York, 2003.

(108) Valtchev, V.; Mintova, S.; Tsapatsis, *Ordered Porous Solids: Recent Advances And Prospects*; Elsevier B.V.: Oxford, 2009.

(109) Vlugt, T. J. H.; Krishna, R.; Smit, B., Molecular simulations of adsorption isotherms for linear and branched alkanes and their mixtures in silicalite. *J Phys Chem B* **1999**, *103*, 1102-1118.

(110) Fuchs, A. H.; Cheetham, A. K., Adsorption of guest molecules in zeolitic materials: Computational aspects. *J Phys Chem B* **2001**, *105*, 7375-7383.

(111) Skoulidas, A. I.; Sholl, D. S., Transport diffusivities of CH4, CF4, He, Ne, Ar, Xe, and SF6 in silicalite from atomistic simulations. *J Phys Chem B* **2002**, *106*, 5058-5067.

(112) Smit, B.; Maesen, T. L. M., Molecular simulations of zeolites: Adsorption, diffusion, and shape selectivity. *Chem Rev* **2008**, *108*, 4125-4184.

(113) Keskin, S.; Liu, J.; Rankin, R. B.; Johnson, J. K.; Sholl, D. S., Progress, Opportunities, and Challenges for Applying Atomically Detailed Modeling to Molecular Adsorption and Transport in Metal-Organic Framework Materials. *Ind Eng Chem Res* **2009**, *48*, 2355-2371.

(114) Duren, T.; Bae, Y. S.; Snurr, R. Q., Using molecular simulation to characterise metal-organic frameworks for adsorption applications. *Chem Soc Rev* **2009**, *38*, 1237-1247.

(115) Rappe, A. K.; Casewit, C. J.; Colwell, K. S.; Goddard, W. A.; Skiff, W. M., UFF, a full periodic table force field for molecular mechanics and molecular dynamics simulations. *Journal of the American Chemical Society* **1992**, *114*, 10024-10035.

(116) Mayo, S. L.; Olafson, B. D.; Goddard, W. A., DREIDING - A generic force-field for molecular simulations. *Journal of Physical Chemistry* **1990**, *94*, 8897-8909.

(117) Bai, P.; Tsapatsis, M.; Siepmann, J. I., TraPPE-zeo: Transferable Potentials for Phase Equilibria Force Field for All-Silica Zeolites. *The Journal of Physical Chemistry C* **2013**, *117*, 24375-24387.

(118) Liu, B.; Smit, B.; Rey, F.; Valencia, S.; Calero, S., A New United Atom Force Field for Adsorption of Alkenes in Zeolites. *The Journal of Physical Chemistry C* **2008**, *112*, 2492-2498.

(119) Maurin, G.; Bourrelly, S.; Llewellyn, P. L.; Bell, R. G., Simulation of the adsorption properties of CH4 in faujasites up to high pressure: Comparison with microcalorimetry. *Micropor Mesopor Mat* **2006**, *89*, 96-102.

(120) Plant, D. F.; Maurin, G.; Deroche, I.; Llewellyn, P. L., Investigation of CO2 adsorption in Faujasite systems: Grand Canonical Monte Carlo and molecular dynamics simulations based on a new derived Na+鈥旳O2 force field. *Micropor Mesopor Mat* **2007**, *99*, 70-78.

(121) Liu, L.; Zhao, L.; Sun, H., Simulation of NH3 Temperature-Programmed Desorption Curves Using an ab Initio Force Field. *J Phys Chem C* **2009**, *113*, 16051-16057.

(122) Han, S. S.; Deng, W.-Q.; Goddard, W. A., Improved Designs of Metal–Organic Frameworks for Hydrogen Storage. *Angew Chem, Int Ed* **2007**, *46*, 6289-6292.

(123) Han, S. S.; Goddard, W. A., Lithium-Doped Metal-Organic Frameworks for Reversible H2 Storage at Ambient Temperature. *J Am Chem Soc* **2007**, *129*, 8422-8423.

(124) Han, S. S.; Mendoza-Cortes, J. L.; Goddard, W. A., Recent advances on simulation and theory of hydrogen storage in metal-organic frameworks and covalent organic frameworks. *Chem Soc Rev* **2009**, *38*, 1460-1476.

(125) Fu, J.; Sun, H., An Ab Initio Force Field for Predicting Hydrogen Storage in IRMOF Materials. *J Phys Chem C* **2009**, *113*, 21815-21824.

(126) Getman, R. B.; Miller, J. H.; Wang, K.; Snurr, R. Q., Metal Alkoxide Functionalization in Metal−Organic Frameworks for Enhanced Ambient-Temperature Hydrogen Storage. *J Phys Chem C* **2011**, *115*, 2066-2075.

(127) Getman, R. B.; Bae, Y.-S.; Wilmer, C. E.; Snurr, R. Q., Review and Analysis of Molecular Simulations of Methane, Hydrogen, and Acetylene Storage in Metal–Organic Frameworks. *Chem Rev* **2012**, *112*, 703-723.

(128) Han, S. S.; Furukawa, H.; Yaghi, O. M.; Goddard, W. A., Covalent Organic Frameworks as Exceptional Hydrogen Storage Materials. *J Am Chem Soc* **2008**, *130*, 11580-11581.

(129) Mendoza-Cortes, J. L.; Han, S. S.; Furukawa, H.; Yaghi, O. M.; Goddard, W. A., Adsorption Mechanism and Uptake of Methane in Covalent Organic Frameworks: Theory and Experiment. *J Phys Chem A* **2010**, *114*, 10824-10833.

(130) Cao, D.; Lan, J.; Wang, W.; Smit, B., Lithium-Doped 3D Covalent Organic Frameworks: High-Capacity Hydrogen Storage Materials. *Angew Chem, Int Ed* **2009**, *48*, 4730-4733.

(131) Lan, J.; Cao, D.; Wang, W., High Uptakes of Methane in Li-Doped 3D Covalent Organic Frameworks. *Langmuir* **2009**, *26*, 220-226.

(132) Lan, J.; Cao, D.; Wang, W., Li-Doped and Nondoped Covalent Organic Borosilicate Framework for Hydrogen Storage. *J Phys Chem C* **2010**, *114*, 3108-3114.

(133) Xiang, Z.; Cao, D.; Lan, J.; Wang, W.; Broom, D. P., Multiscale simulation and modelling of adsorptive processes for energy gas storage and carbon dioxide capture in porous coordination frameworks. *Energy Environ Sci* **2010**, *3*, 1469-1487.

(134) Han, S. S.; Choi, S.-H.; Goddard, W. A., Zeolitic Imidazolate Frameworks as H2 Adsorbents: Ab Initio Based Grand Canonical Monte Carlo Simulation. *J Phys Chem C* **2010**, *114*, 12039-12047.

(135) Han, S. S.; Choi, S.-H.; Goddard, W. A., Improved H2 Storage in Zeolitic Imidazolate Frameworks Using Li+, Na+, and K+ Dopants, with an Emphasis on Delivery H2 Uptake. *J Phys Chem C* **2011**, *115*, 3507-3512.

(136) Fang, H.; Demir, H.; Kamakoti, P.; Sholl, D. S., Recent developments in first-principles force fields for molecules in nanoporous materials. *Journal of Materials Chemistry A* **2014**, *2*, 274-291.

(137) Grimme, S., Semiempirical GGA-type density functional constructed with a long-range dispersion correction. *J Comput Chem* **2006**, *27*, 1787-1799.

(138) Grimme, S.; Antony, J.; Ehrlich, S.; Krieg, H., A consistent and accurate ab initio parametrization of density functional dispersion correction (DFT-D) for the 94 elements H-Pu. *Journal of Chemical Physics* **2010**, *132*.

(139) Lee, K.; Murray, E. D.; Kong, L. Z.; Lundqvist, B. I.; Langreth, D. C., Higher-accuracy van der Waals density functional. *Phys Rev B* **2010**, *82*, 081101.

(140) Bludský, O.; Rubeš, M.; Soldán, P.; Nachtigall, P., Investigation of the benzene-dimer potential energy surface: DFT/CCSD(T) correction scheme. *The Journal of Chemical Physics* **2008**, *128*, 114102.

(141) Li, W. L.; Grimme, S.; Krieg, H.; Mollmann, J.; Zhang, J. P., Accurate Computation of Gas Uptake in Microporous Organic Molecular Crystals. *J Phys Chem C* **2012**, *116*, 8865-8871.

(142) Lan, J.; Cheng, D.; Cao, D.; Wang, W., Silicon Nanotube as a Promising Candidate for Hydrogen Storage: From the First Principle Calculations to Grand Canonical Monte Carlo Simulations. *J Phys Chem C* **2008**, *112*, 5598-5604.

(143) Maurin, G.; Belmabkhout, Y.; Pirngruber, G.; Gaberova, L.; Llewellyn, P., CO2 adsorption in LiY and NaY at high temperature: molecular simulations compared to experiments. *Adsorption* **2007**, *13*, 453-460.

(144) Chen, L.; Morrison, C. A.; Düren, T., Improving Predictions of Gas Adsorption in Metal–Organic Frameworks with Coordinatively Unsaturated Metal Sites: Model Potentials, ab initio Parameterization, and GCMC Simulations. *J Phys Chem C* **2012**, *116*, 18899-18909.

(145) Dzubak, A. L.; Lin, L.-C.; Kim, J.; Swisher, J. A.; Poloni, R.; Maximoff, S. N.; Smit, B.; Gagliardi, L., Ab initio carbon capture in open-site metal–organic frameworks. *Nat Chem* **2012**, *4*, 810-816.

(146) Fang, H.; Kamakoti, P.; Ravikovitch, P. I.; Aronson, M.; Paur, C.; Sholl, D. S., First principles derived, transferable force fields for CO2 adsorption in Na-exchanged cationic zeolites. *Physical Chemistry Chemical Physics* **2013**, *15*, 12882-12894.

(147) Maghsoudi, H.; Soltanieh, M.; Bozorgzadeh, H.; Mohamadalizadeh, A., Adsorption isotherms and ideal selectivities of hydrogen sulfide and carbon dioxide over methane for the Si-

CHA zeolite: comparison of carbon dioxide and methane adsorption with the all-silica DD3R zeolite. *Adsorption* **2013**, *19*, 1045-1053.

(148) Himeno, S.; Tomita, T.; Suzuki, K.; Yoshida, S., Characterization and selectivity for methane and carbon dioxide adsorption on the all-silica DD3R zeolite. *Microporous and Mesoporous Materials* **2007**, *98*, 62-69.

(149) Rubes, M.; Nachtigall, P.; Vondrasek, J.; Bludsky, O., Structure and Stability of the Water-Graphite Complexes. *J Phys Chem C* **2009**, *113*, 8412-8419.

(150) Rubes, M.; Kysilka, J.; Nachtigall, P.; Bludsky, O., DFT/CC investigation of physical adsorption on a graphite (0001) surface. *Physical Chemistry Chemical Physics* **2010**, *12*, 6438-6444.

(151) Chen, L.; Grajciar, L.; Nachtigall, P.; Düren, T., Accurate Prediction of Methane Adsorption in a Metal–Organic Framework with Unsaturated Metal Sites by Direct Implementation of an ab Initio Derived Potential Energy Surface in GCMC Simulation. *The Journal of Physical Chemistry C* **2011**, *115*, 23074-23080.

(152) Grajciar, L.; Bludský, O.; Nachtigall, P., Water Adsorption on Coordinatively Unsaturated Sites in CuBTC MOF. *The Journal of Physical Chemistry Letters* **2010**, *1*, 3354-3359.

(153) Rubeš, M.; Wiersum, A. D.; Llewellyn, P. L.; Grajciar, L.; Bludský, O.; Nachtigall, P., Adsorption of Propane and Propylene on CuBTC Metal–Organic Framework: Combined Theoretical and Experimental Investigation. *The Journal of Physical Chemistry C* **2013**, *117*, 11159-11167.

(154) Pulido, A.; Delgado, M. R.; Bludsky, O.; Rubes, M.; Nachtigall, P.; Arean, C. O., Combined DFT/CC and IR spectroscopic studies on carbon dioxide adsorption on the zeolite H-FER. *Energy & Environmental Science* **2009**, *2*, 1187-1195.

(155) Cejka, J.; Zukal, A.; Pulido, A.; Gil, B.; Nachtigall, P.; Bludsky, O.; Rubes, M., Experimental and theoretical determination of adsorption heats of CO(2) over alkali metal exchanged ferrierites with different Si/Al ratio. *Phys Chem Chem Phys* **2010**, *12*, 6413-6422.

(156) Arean, C. O.; Delgado, M. R.; Bibiloni, G. F.; Bludsky, O.; Nachtigall, P., Variable-Temperature IR Spectroscopic and Theoretical Studies on CO(2) Adsorbed in Zeolite K-FER. *ChemPhysChem* **2011**, *12*, 1435-1443.

(157) Zukal, A.; Arean, C. O.; Delgado, M. R.; Nachtigall, P.; Pulido, A.; Mayerova, J.; Cejka, J., Combined volumetric, infrared spectroscopic and theoretical investigation of CO(2) adsorption on Na-A zeolite. *Micropor Mesopor Mat* **2011**, *146*, 97-105.

(158) Nachtigall, P.; Delgado, M. R.; Nachtigallova, D.; Arean, C. O., The nature of cationic adsorption sites in alkaline zeolites-single, dual and multiple cation sites. *Phys Chem Chem Phys* **2012**, *14*, 1552-1569.

(159) Boys, S. F.; Bernardi, F., The calculation of small molecular interactions by the differences of separate total energies. Some procedures with reduced errors. *Molecular Physics* **1970**, *19*, 553-566.

(160) Ho, T. S.; Rabitz, H., A general method for constructing multidimensional molecular potential energy surfaces from ab initio calculations. *J Chem Phys* **1996**, *104*, 2584-2597.

(161) Soldan, P.; Hutson, J. M., On the long-range and short-range behavior of potentials from reproducing kernel Hilbert space interpolation. *J Chem Phys* **2000**, *112*, 4415-4416.

(162) Tikhonov, A.; Arsenin, V., Solutions of Ill-Posed Problems, translation ed. by F. *John (Winston/Wiley, Washington DC/New York 1977)* **1977**, *10*.

(163) Tikhonov, A. N.; Goncharsky, A.; Stepanov, V.; Yagola, A. G., *Numerical methods for the solution of ill-posed problems*; Springer Science & Business Media, 2013; Vol. 328.

(164) Diaz-Cabanas, M. J.; Barrett, P. A.; Camblor, M. A., Synthesis and structure of pure SiO2 chabazite: the SiO2 polymorph with the lowest framework density. *Chem Commun* **1998**, 1881-1882.

(165) Wilson, S. T.; Lok, B. M.; Messina, C. A.; Cannan, T. R.; Flanigen, E. M., Aluminophosphate molecular sieves: a new class of microporous crystalline inorganic solids. *Journal of the American Chemical Society* **1982**, *104*, 1146-1147.

(166) Bond, G. C.; Gelsthorpe, M. R.; Sing, K. S. W.; Theocharis, C. R., Incorporation of zinc in an aluminophosphate microporous phase. *Journal of the Chemical Society, Chemical Communications* **1985**, 1056-1057.

(167) Choudhary, V. R.; Akolekar, D. B., Site energy distribution and catalytic properties of microporous crystalline AlPO4-5. *Journal of Catalysis* **1987**, *103*, 115-125.

(168) Grillet, Y.; Llewellyn, P. L.; Reichert, H.; Coulomb, J. P.; Pellenq, N.; Rouquerol, J., Confinement in micropores and enthalpies of physisorption. In *Studies in Surface Science and Catalysis*, J. Rouquerol, F. R.-R. K. S. W. S.; Unger, K. K., Eds. Elsevier: 1994; Vol. Volume 87, pp 525-533.

(169) Predescu, L.; Tezel, F. H.; Chopra, S., Adsorption of nitrogen, methane, carbon monoxide, and their binary mixtures on aluminophosphate molecular sieves. *Adsorption* **1997**, *3*, 7-25.

(170) Martens, J. A.; Jacobs, P. A., ChemInform Abstract: Crystalline Microporous Phosphates: A Family of Versatile Catalysts and Adsorbents. *ChemInform* **1995**, *26*, no-no.

(171) Zhao, X.-X.; Xu, X.-L.; Sun, L.-B.; Zhang, L. L.; Liu, X.-Q., Adsorption Behavior of Carbon Dioxide and Methane on AlPO4-14: A Neutral Molecular Sieve. *Energy & Fuels* **2009**, *23*, 1534-1538.

(172) Wu, T.; Wang, B.; Lu, Z.; Zhou, R.; Chen, X., Alumina-supported AlPO-18 membranes for CO2/CH4 separation. *Journal of Membrane Science* **2014**, *471*, 338-346.

(173) Delgado, J. A.; Águeda, V. I.; Uguina, M. A.; Sotelo, J. L.; Fernández, P., Adsorption and diffusion of nitrogen, methane and carbon dioxide in aluminophosphate molecular sieve AlPO4-11. *Adsorption* **2013**, *19*, 407-422.

(174) Choudhary, V. R.; Mayadevi, S., Sorption Isotherms of Methane, Ethane, Ethylene, and Carbon Dioxide on ALPO-5 and SAPO-5. *Langmuir* **1996**, *12*, 980-986.

(175) Maris, T.; Vlugt, T. J. H.; Smit, B., Simulation of Alkane Adsorption in the Aluminophosphate Molecular Sieve AlPO4−5. *The Journal of Physical Chemistry B* **1998**, *102*, 7183-7189.

(176) Zhang, D.; Li, W.; Liu, Z.; Xu, R., Molecular simulation of methane adsorption in aluminophosphate molecular sieve AlPO4-11. *Journal of Molecular Structure: THEOCHEM* **2007**, *804*, 89-94.

(177) Perdew, J. P.; Burke, K.; Ernzerhof, M., Generalized Gradient Approximation Made Simple. *Physical Review Letters* **1996**, *77*, 3865-3868.

(178) Kresse, G.; Joubert, D., From ultrasoft pseudopotentials to the projector augmented-wave method. *Physical Review B* **1999**, *59*, 1758-1775.

(179) Guo, Z.; Guo, C.; Jin, Q.; Li, B.; Ding, D., Synthesis and Structure of Large AlPO4-5 Crystals. *J Porous Mater* **2005**, *12*, 29-33.

(180) Makrodimitris, K.; Papadopoulos, G. K.; Theodorou, D. N., Prediction of Permeation Properties of CO2 and N2 through Silicalite via Molecular Simulations. *The Journal of Physical Chemistry B* **2001**, *105*, 777-788.

(181) Krishna, R.; van Baten, J. M., Using molecular simulations for screening of zeolites for separation of CO2/CH4 mixtures. *Chemical Engineering Journal* **2007**, *133*, 121-131.

(182) Golden, T. C.; Sircar, S., Gas Adsorption on Silicalite. *Journal of Colloid and Interface Science* **1994**, *162*, 182-188.

(183) Beauvais, C.; Guerrault, X.; Coudert, F. X.; Boutin, A.; Fuchs, A. H., Distribution of sodium cations in faujasite-type zeolite: A canonical parallel tempering simulation study. *J Phys Chem B* **2004**, *108*, 399-404.

(184) Earl, D. J.; Deem, M. W., Parallel tempering: Theory, applications, and new perspectives. *Phys Chem Chem Phys* **2005**, *7*, 3910-3916.

(185) Yang, J.; Zhao, Q.; Xu, H.; Li, L.; Dong, J.; Li, J., Adsorption of CO2, CH4, and N2 on Gas Diameter Grade Ion-Exchange Small Pore Zeolites. *Journal of Chemical & Engineering Data* **2012**, *57*, 3701-3709.

(186) Zhu, W.; Kapteijn, F.; A. Moulijn, J., Shape selectivity in the adsorption of propane/propene on the all-silica DD3R. *Chemical Communications* **1999**, 2453-2454.

(187) Zhu, W.; Kapteijn, F.; Moulijn, J. A.; den Exter, M. C.; Jansen, J. C., Shape Selectivity in Adsorption on the All-Silica DD3R. *Langmuir* **2000**, *16*, 3322-3329.

(188) Olson, D. H.; Yang, X.; Camblor, M. A., ITQ-12: A Zeolite Having Temperature Dependent Adsorption Selectivity and Potential for Propene Separation. *The Journal of Physical Chemistry B* **2004**, *108*, 11044-11048.

(189) Grande, C.; Gigola, C.; Rodrigues, A., Propane–Propylene Binary Adsorption on Zeolite 4A. *Adsorption* **2003**, *9*, 321-329.

(190) Daems, I.; Leflaive, P.; Méthivier, A.; Denayer, J. F. M.; Baron, G. V., A study of packing induced selectivity effects in the liquid phase adsorption of alkane/alkene mixtures on NaY. *Microporous and Mesoporous Materials* **2005**, *82*, 191-199.

(191) Olson, D. H.; Camblor, M. A.; Villaescusa, L. A.; Kuehl, G. H., Light hydrocarbon sorption properties of pure silica Si-CHA and ITQ-3 and high silica ZSM-58. *Microporous and Mesoporous Materials* **2004**, *67*, 27-33.

(192) Rege, S. U.; Padin, J.; Yang, R. T., Olefin/paraffin separations by adsorption: π-Complexation vs. kinetic separation. *AIChE Journal* **1998**, *44*, 799-809.

(193) Catlow, C. R. A.; Smit, B.; van Santen, R., *Computer modelling of microporous materials*; Academic Press, 2004.

(194) Dubbeldam, D.; Calero, S.; Vlugt, T.; Krishna, R.; Maesen, T. L.; Beerdsen, E.; Smit, B., Force field parametrization through fitting on inflection points in isotherms. *Physical review letters* **2004**, *93*, 088302.

(195) Calero, S.; Lobato, M.; Garcia-Perez, E.; Mejias, J.; Lago, S.; Vlugt, T.; Maesen, T. L.; Smit, B. d.; Dubbeldam, D., A coarse-graining approach for the proton complex in protonated aluminosilicates. *The Journal of Physical Chemistry B* **2006**, *110*, 5838-5841.

(196) Garcia-Perez, E.; Dubbeldam, D.; Maesen, T. L.; Calero, S., Influence of cation Na/Ca ratio on adsorption in LTA 5A: a systematic molecular simulation study of alkane chain length. *The Journal of Physical Chemistry B* **2006**, *110*, 23968-23976.

(197) Jakobtorweihen*, S.; Hansen, N.; Keil, F. J., Molecular simulation of alkene adsorption in zeolites. *Molecular Physics* **2005**, *103*, 471-489.

(198) Martin, M. G.; Thompson, A. P.; Nenoff, T. M., Effect of pressure, membrane thickness, and placement of control volumes on the flux of methane through thin silicalite membranes: A dual control volume grand canonical molecular dynamics study. *The Journal of Chemical Physics* **2001**, *114*, 7174-7181.

(199) Wilding, N. B.; Schoen, M., Absence of simulation evidence for critical depletion in slit pores. *Physical Review E* **1999**, *60*, 1081.

(200) Granato, M. A.; Vlugt, T. J.; Rodrigues, A. E., Molecular simulation of propane-propylene binary adsorption equilibrium in zeolite 4A. *Industrial & engineering chemistry research* **2007**, *46*, 321-328.

(201) Zang, J.; Nair, S.; Sholl, D. S., Prediction of Water Adsorption in Copper-Based Metal–Organic Frameworks Using Force Fields Derived from Dispersion-Corrected DFT Calculations. *The Journal of Physical Chemistry C* **2013**, *117*, 7519-7525.

(202) Lin, L.-C.; Lee, K.; Gagliardi, L.; Neaton, J. B.; Smit, B., Force-Field Development from Electronic Structure Calculations with Periodic Boundary Conditions: Applications to Gaseous Adsorption and Transport in Metal–Organic Frameworks. *Journal of Chemical Theory and Computation* **2014**, *10*, 1477-1488.

(203) Avgul, N.; Kiselev, A.; Mirskii, Y. V.; Serdobov, M., Heats of adsorption of water vapour by NaX and NaA zeolites. *RUSSIAN JOURNAL OF PHYSICAL CHEMISTRY, USSR* **1968**, *42*, 768-&.

(204) Martin, M. G.; Siepmann, J. I., Transferable Potentials for Phase Equilibria. 1. United-Atom Description of n-Alkanes. *The Journal of Physical Chemistry B* **1998**, *102*, 2569-2577.

(205) Wick, C. D.; Martin, M. G.; Siepmann, J. I., Transferable Potentials for Phase Equilibria. 4. United-Atom Description of Linear and Branched Alkenes and Alkylbenzenes. *The Journal of Physical Chemistry B* **2000**, *104*, 8008-8016.

(206) Dubbeldam, D.; Calero, S.; Ellis, D. E.; Snurr, R. Q., RASPA: molecular simulation software for adsorption and diffusion in flexible nanoporous materials. *Mol Simul* **2015**, 1-21.

(207) Dubbeldam, D.; Torres-Knoop, A.; Walton, K. S., On the inner workings of Monte Carlo codes. *Mol Simul* **2013**, *39*, 1253-1292.

(208) Siepmann, J. I.; Frenkel, D., Configurational Bias Monte-Carlo - A New Sampling Scheme for Flexible Chains *Molecular Physics* **1992**, *75*, 59-70.

(209) Zhu, W.; Kapteijn, F.; Moulijn, J., Adsorption of light alkanes on silicalite-1: Reconciliation of experimental data and molecular simulations. *Physical Chemistry Chemical Physics* **2000**, *2*, 1989-1995.

(210) Hampson, J.; Rees, L., Adsorption of Lower Hydrocarbons in Zeolite NaY and Theta-1. Comparison of Low and High Pressure Isotherm Data. *Studies in Surface Science and Catalysis* **1994**, *83*, 197-208.

(211) Barrett, P. A.; Boix, T.; Puche, M.; Olson, D. H.; Jordan, E.; Koller, H.; Camblor, M. A., ITQ-12: a new microporous silica polymorph potentially useful for light hydrocarbon separations. *Chemical Communications* **2003**, 2114-2115.

(212) Palomino, M.; Cantín, A.; Corma, A.; Leiva, S.; Rey, F.; Valencia, S., Pure silica ITQ-32 zeolite allows separation of linear olefins from paraffins. *Chemical Communications* **2007**, 1233-1235.

(213) Stach, H.; Lohse, U.; Thamm, H.; Schirmer, W., Adsorption equilibria of hydrocarbons on highly dealuminated zeolites. *Zeolites* **1986**, *6*, 74-90.

(214) Zhu, W.; Kapteijn, F.; Moulijn, J.; Jansen, J., Selective adsorption of unsaturated linear C 4 molecules on the all-silica DD3R. *Physical Chemistry Chemical Physics* **2000**, *2*, 1773-1779.

(215) Singh, D.; Croiset, E.; Douglas, P. L.; Douglas, M. A., Techno-economic study of CO 2 capture from an existing coal-fired power plant: MEA scrubbing vs. O 2/CO 2 recycle combustion. *Energy Conversion and Management* **2003**, *44*, 3073-3091.

(216) Kikkinides, E.; Yang, R.; Cho, S., Concentration and recovery of carbon dioxide from flue gas by pressure swing adsorption. *Industrial & Engineering Chemistry Research* **1993**, *32*, 2714-2720.

(217) Boulfelfel, S.; Ravikovitch, P. I.; Sholl, D. S., Modeling Diffusion of Linear Hydrocarbons in Silica Zeolite LTA Using Transition Path Sampling. *The Journal of Physical Chemistry C* **2015**.

(218) Palomino, M.; Corma, A.; Rey, F.; Valencia, S., New Insights on CO2− Methane Separation Using LTA Zeolites with Different Si/Al Ratios and a First Comparison with MOFs. *Langmuir* **2009**, *26*, 1910-1917.

(219) Chkhaidze, E.; Fomkin, A.; Serpinskii, V.; Tsitsishvili, G., Adsorption of methane on NaX zeolite in the subcritical and supercritical regions. *Bulletin of the Academy of Sciences of the USSR, Division of chemical science* **1985**, *34*, 886-890.